

## Optical Characterization of Nanostructured Surfaces

**Feidenhans'l, Nikolaj Agentoft; Taboryski, Rafael J.; Petersen, Jan Conrad**

*Publication date:*  
2016

*Document Version*  
Publisher's PDF, also known as Version of record

[Link back to DTU Orbit](#)

*Citation (APA):*  
Feidenhans'l, N. A., Taboryski, R. J., & Petersen, J. C. (2016). Optical Characterization of Nanostructured Surfaces. DTU Nanotech.

## DTU Library

Technical Information Center of Denmark

---

### General rights

Copyright and moral rights for the publications made accessible in the public portal are retained by the authors and/or other copyright owners and it is a condition of accessing publications that users recognise and abide by the legal requirements associated with these rights.

- Users may download and print one copy of any publication from the public portal for the purpose of private study or research.
- You may not further distribute the material or use it for any profit-making activity or commercial gain
- You may freely distribute the URL identifying the publication in the public portal

If you believe that this document breaches copyright please contact us providing details, and we will remove access to the work immediately and investigate your claim.

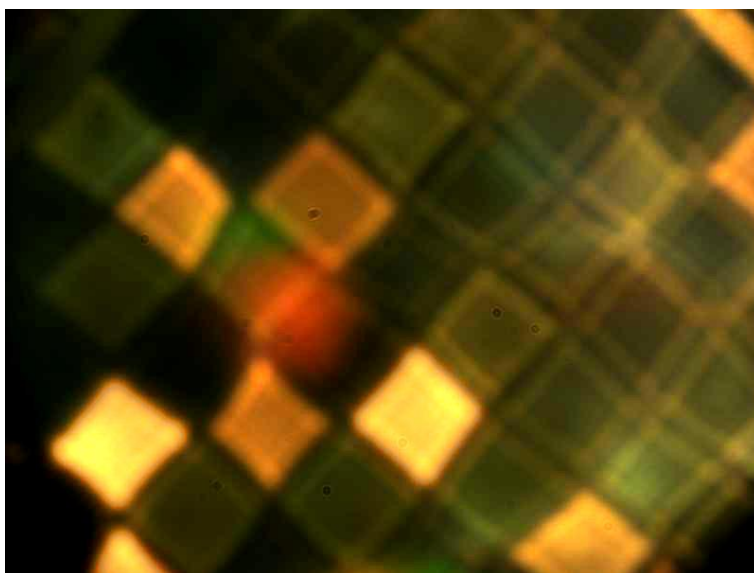


# Optical Characterization Of Nanostructured Surfaces

Nikolaj Agentoft Feidenhans'l  
PhD Thesis August 2016



# OPTICAL CHARACTERIZATION OF NANOSTRUCTURED SURFACES



Nikolaj Agentoft Feidenhans'l

PhD Thesis

August 2016

Supervisors

Jan C. Petersen, Danish Fundamental Metrology A/S

Rafael Taboryski, DTU Nanotech

Cover image: Photograph of nanopatterned polymer surface, structured with regions of line gratings with different periods and orientations. The polymer itself is black, while the gratings provide a range of structural colors in relation to the dimensions of each grating.

## PREFACE

This thesis is submitted as part of the requirements for obtaining the PhD degree from the Technical University of Denmark (DTU). The work has been carried out in the period from September 2013 to August 2016, in the group Polymer Micro & Nano Engineering (POLYMIC) at DTU Nanotech and in the optics team at Danish Fundamental Metrology A/S (DFM). The work has been sponsored by the Danish Agency for Science, Technology and Innovation (Forsknings- og Innovationsstyrelsen), through the Industrial PhD Programme. Part of the work was conducted under the NanoPlast project, funded by the Danish National Advanced Technology Foundation.

The PhD project has been supervised by Rafael Taboryski from DTU Nanotech and Jan C. Petersen from DFM. I would like to sincerely thank both supervisors for the many fruitful discussions and academic guidance during the last three years.

I would like to thank my colleagues at DFM, especially Morten Hannibal Madsen and Poul-Erik Hansen, for the great collaborations and for laying the foundations of scatterometry at DFM. Additionally, I would like to thank Lars Nielsen for assisting in the uncertainty calculations, something I have only realized the importance and complexity of by working in a metrology institute. Also a great thanks to Anders Bruschi and Mikael Ø. Lassen, for borrowing their equipment and for assistance with some critical measurements.

In the POLYMIC group, I would like to thank all present and former colleagues for the interesting discussions, the great travel company on several conferences, and the many great cakes! Swathi Murthy deserves a special thank for performing the FIB-SEM measurements and Mikkel Rønne Lotz for discussions of the numerical simulations.

Thanks to the entire Nanoplast project group, for introducing me to such an application-minded project, and for the very interesting visits to the industrial partners. These include the Concept Center at LEGO Group in Billund and the machine shop Michael Lundbech A/S in Ringsted, which both provided valuable insight into the requirements of industrial characterization instruments. Also special thanks to the other PhD students, Emil Højlund-Nielsen and Jeppe Clausen, for discussions and advices regarding scatterometry and colors.

Thanks to Lukáš Pilný from DTU MEK, for supplying the indispensable samples for the roughness analysis and the loan of equipment.

Also a thanks to my fellow alumni from MScEng Physics and Nanotechnology, for mutual whining about being PhD students, even with the great conditions we all had at DTU.

Lastly, a sincere thanks to my wife for always being supportive and understanding, and to my two kids, Sigrid and Asger, for ensuring I always woke up early, got the work done, and hurried back home.

Nikolaj Agentoft Feidenhans'1

Helsingør, August 2016

## ABSTRACT

Micro- and nanostructured surfaces are interesting due to the unique properties they add to the bulk material. One example is structural colors, where the interaction between surface structures and visible light produce bright color effects without the use of paints or dyes. Several research groups are investigating the manufacturing of these structures using established high-volume polymer fabrication methods, such as injection molding and roll-to-roll manufacturing. These methods are interesting as they can ease the industrial uptake of nanopatterning technology. However, for a successful industrial implementation, a range of complementing characterization methods is needed to perform high-speed quality control of the nanostructures.

This thesis concerns the development of a new method for fast in-line characterization of periodic nanostructures. The focus is on optical scatterometry, which uses inverse modeling to evaluate the dimensions of subwavelength gratings, by correlating the reflected light measured from the structures with a database of simulations. A new method is developed and termed *color scatterometry*, since compared to typical *spectroscopic scatterometry*, which evaluates the full reflection spectrum; the new method only evaluates the color of the reflected light using a standard RGB color camera. Color scatterometry provides the combined advantages of spectroscopic scatterometry, which provides fast evaluations, and *imaging scatterometry* that provides an overview image from which small regions can be analyzed independently. With color scatterometry, a single exposure with the camera is sufficient to evaluate the grating profile for thousands of individual regions spanning a millimeter-sized area. The accuracy of color scatterometry is evaluated on injection molded polymer line gratings, with trapezoidal profiles approximately ~200 nm high and with periods between 600 nm and 5000 nm. The heights and filling factors are determined with an accuracy of ~8 %, while the sidewall slopes have larger uncertainties due to a lower influence on the reflected light.

The thesis also evaluates the use of *angular scatterometry* for characterization of nanoscale surface roughness. This study is motivated by the need for highly polished surfaces for the production of master molds in injection molding and roll-to-roll manufacturing. Three characterization instruments are compared: a confocal optical profiler, a high-resolution laboratory scatterometer, and a simple commercial scatterometer designed for in-machine measurements. The study is focused on characterizing the commercial scatterometer, to support the implementation of in-situ roughness evaluation during polishing processes. We present an algorithm for expanding the length scale of evaluated surface structures, and a method for converting the standard output parameter, “Aq”, to the more widely used root-mean-square roughness parameter (Rq). The study also includes a detailed analysis of the range of spatial surface wavelengths correctly evaluated by each instrument, and a small study of the implications if the sample surface is covered with an interface layer, e.g. a thin liquid film.

For roughness evaluation on hard-to-reach surfaces, the thesis includes a study of surface replication using the thermosetting polymer PDMS.

## RESUMÉ (IN DANISH)

Mikro- og nanostrukturerede overflader er interessante på grund af de unikke egenskaber de kan tilføje et materiale. Et eksempel er strukturelle farver, hvor samspillet mellem overfladestrukturer og synligt lys resulterer i glitrende farveeffekter, uden brug af hverken maling eller farvestoffer. Flere forskningsgrupper arbejder med produktionen af denne type strukturer, typisk ved brug af allerede veletablerede metoder til storskala plastik fabrikation, fx sprøjtestøbning og rotationspresning. Disse metoder er interessante da de vil lette den industrielle implementering af nanostrukturerede produkter. For industriel implementering kræves dog også en række nye karakterisering metoder, der kan udføre kvalitetskontrol af nanostrukturene i dette høje produktions tempo.

Denne afhandling beskriver en ny metode til hurtig inline karakterisering af nanostrukturer. Fokus er på optisk skatterometri, der ved hjælp af inverse modellering bestemmer dimensionerne af nanoskala gitre. Dette gøres ved at sammenligne en måling af det reflekterede lys fra strukturerne med en database af simulerede værdier. En ny metode er udviklet og navngives *farve skatterometri*. Metoden skal ses i forhold til traditionel *spektroskopisk skatterometri*, hvor det fulde spektrum undersøges, hvorimod denne nye metode kun evaluerer farven af det reflekterede lys med et normalt RGB farvekamera. Farve skatterometri giver en kombination af fordelene ved spektroskopisk skatterometri, der har en høj målehastighed, og *billedannede skatterometri*, der giver et oversigtsbillede til udvælgelse af mindre områder for individuel analyse. Med farve skatterometri er et enkelt billede med kameraet nok for at bestemme dimensionerne af tusindvis af små områder fordelt over et areal i millimeter størrelsen. Nøjagtigheden af farve skatterometri undersøges på sprøjtestøbte plastik gitre, med trapezformet profiler cirka ~200 nm høje og med perioder mellem 600 nm og 5000 nm. Højden og fyldningsfaktoren bestemmes med en nøjagtighed på ~8 %, mens sidehældningen har større usikkerhed da denne dimension kun svagt påvirker det reflekterede lys.

Afhandlingen omhandler desuden brugen af *vinkel skatterometri* til karakterisering af nanoskala overfladeruheder. Denne undersøgelse er motiveret af behovet for blankpolerede overflader for fremstillingen af formene til sprøjtestøbning og rotationspresning. Tre karakteriserings instrumenter sammenlignes: et konfokalt optisk profilometer, et højtopløsnings laboratorie skatterometer og et simpelt kommercielt skatterometer designet til industrielle målinger. Undersøgelsen fokuserer på det kommercielle skatterometer, for derved at støtte udviklingen af in-situ ruhedsmålinger til brug i poleringsmaskiner. Vi præsenterer en algoritme til at udvide instrumentets måleområde ned til kortere perioder af overfladestrukturer, samt en formel til at konvertere den normale måleværdi, "Aq", til den mere velkendte root-mean-square ruhedsværdi (Rq). Undersøgelsen omfatter desuden en grundig analyse af hvert instruments reelle måleområde i forhold til bølgelængderne af overfladestrukturerne, samt en mindre undersøgelse af konsekvenserne hvis overfladen er dækket med et grænsefladelag, fx en tynd væskefilm.

Muligheden for ruhedsmålinger på svært tilgængelige overflader, undersøges med en analyse af overflade afstøbninger med den varmhærdende polymer PDMS.

# LIST OF PUBLICATIONS

## Journal papers

### Accepted

**N. A. Feidenhans'l**, P.-E. Hansen, L. Pilný, M. H. Madsen, G. Bissacco, J. C. Petersen, and R. Taboryski, Comparison of optical methods for surface roughness characterization, *Measurement Science and Technology*, vol. 26, no. 8, p. 085208, 2015.

M. H. Madsen\*, **N. A. Feidenhans'l**\*, P.-E. Hansen, J. Garnæs, and K. Dirscherl, Accounting for PDMS shrinkage when replicating structures, *Journal of Micromechanics Microengineering*, vol. 24, no. 12, p. 127002, 2014. \*Equal contributions

S. Murthy, M. Matschuk, Q. Huang, N. K. Mandsberg, **N. A. Feidenhans'l**, P. Johansen, L. Christensen, H. Pranov, G. Kofod, H. C. Pedersen, O. Hassager, and R. Taboryski. Fabrication of Nanostructures by Roll-to-Roll Extrusion Coating. *Advanced Engineering Materials*, 18(4):484–489, 2015. doi: 10.1002/adem.201500347.

### Under review

**N. A. Feidenhans'l**, S. Murthy, M. H. Madsen, J. C. Petersen, and R. Taboryski, Spatial characterization of nanotextured surfaces by visual color imaging, *Applied Optics*, 2016.

L. Schneider, **N. A. Feidenhans'l**, A. Telecka, R. Taboryski, One-step Maskless Fabrication and Optical Characterization of Silicon Surfaces with Antireflective Properties and a White Color Appearance, *Scientific Reports*, 2016.

## Peer-reviewed conference proceedings

**N. A. Feidenhans'l**, P.-E. Hansen, L. Pilný, M. H. Madsen, G. Bissacco, J. C. Petersen, and R. Taboryski, “Industrial characterization of nano-scale roughness on polished surfaces,” in *Proceedings of SPIE 9633*, Optifab 2015, 2015, vol. 9633, p. 96330B.

## Conference contributions

### Oral presentations

**N. A. Feidenhans'l**, P.-E. Hansen, L. Pilný, M. H. Madsen, G. Bissacco, J. C. Petersen, R. Taboryski, Industrial characterization of nano-scale roughness on polished surfaces, at: SPIE Optifab, Rochester, NY-USA, 2015.

**N. A. Feidenhans'l**, P.-E. Hansen, L. Pilný, J. C. Petersen, R. Taboryski, Optical characterization of roughness on polished steel surfaces, at: PRN 2015 (Polymer Replication on Nanoscale), DTU, Denmark, 2015.

**N. A. Feidenhans'l**, M. H. Madsen, P.-E. Hansen, J. Garnæs, J. C. Petersen, R. Taboryski, Visual appearance for validating nanostructure dimensions, at: PRN 2014, DTU, Denmark, 2014.

#### Poster presentations

**N. A. Feidenhans'l**, P.-E. Hansen, L. Pilný, M. H. Madsen, G. Bissacco, J. C. Petersen, R. Taboryski, Industrial Characterization of Nano-Scale Roughness on Polished Surfaces, at: PITTCON 2016, Chicago, IL-USA, 2016.

**N. A. Feidenhans'l**, J. C. Petersen, R. Taboryski, Topographic characterization of nanostructures on curved polymer surfaces, at: PITTCON 2014, Chicago, IL-USA, 2014.

#### Popular science articles

M. H. Madsen, **N. A. Feidenhans'l**, M. L. Madsen. Målinger på nanoskala – sådan ser man græsset gro. Dansk Kemi, vol. 8, page 12 – 15, 2014. <http://www.danskkemi-online.dk/files/DAK8-2014-s12-15.pdf>



## LIST OF ABBREVIATIONS

1D	1-dimensional
2D	2-dimensional
3D	3-dimensional
AFM	Atomic force microscopy
ARS	Angle resolved scatter
BRDF	Bidirectional reflectance distribution function
CCD	Charge-coupled device
CD-SEM	Critical dimension SEM
CFA	Color filter array
CI	Confidence interval
CIE	International Commission on Illumination
CM	Confocal microscopy
CMOS	Complementary metal-oxide-semiconductor
FDTD	Finite-difference time-domain method
FEM	Finite element method
FIB SEM	Focused ion beam SEM
FWHM	Full width at half maximum
GUM	Guide to the Expression of Uncertainty in Measurement
IM	Injection molding
ISO	International Organization for Standardization
ND	Neutral density
PDMS	Polydimethylsiloxane
PSD	Power spectral density
R2R	Roll-to-roll imprinting
Ra	Arithmetic average
Rdq	RMS slope
Rq	RMS profile
RCWA	Rigorous coupled-wave analysis
RGB	Red-green-blue
RMS	Root mean square
RR	Rayleigh-Rice
SE	Standard error
SEM	Scanning electron microscopy
SU	Standard uncertainty
TIS	Total integrated scatter
UV	Ultra violet
WLI	White light interferometry

# CONTENTS

Preface .....	iii
Abstract .....	iv
Resumé (in Danish).....	v
List of Publications .....	vi
List of Abbreviations .....	ix
<b>CONTENTS</b>	<b>x</b>
<b>PART 1 INTRODUCTION</b>	<b>1</b>
Chapter 1.1 Functional nanostructures.....	2
Chapter 1.2 High volume fabrication methods .....	4
1.2.1 Common structure defects .....	6
Chapter 1.3 Characterization of nanostructures .....	7
Chapter 1.4 Project goal.....	8
Chapter 1.5 Thesis outline .....	9
<b>PART 2 ROUGHNESS EVALUATION</b>	<b>11</b>
Chapter 2.1 Introduction to roughness evaluation .....	13
2.1.1 Angular scatterometry.....	13
2.1.2 Instrument presentation.....	13
2.1.3 Roughness calculations .....	15
2.1.4 Scattering theory .....	18
2.1.5 State of the art .....	23
Chapter 2.2 Paper 1, Optical evaluation of nanoscale roughness .....	25
2.2.1 Presentation of samples.....	25
2.2.2 Paper reprint.....	28
2.2.3 Comparison with stylus profiler.....	42
2.2.4 Accuracy of laboratory scatterometer .....	42
2.2.5 Industrial implementation of scatterometry .....	43
Chapter 2.3 Paper 2, Surfaces with interface layers.....	45
2.3.1 Paper reprint.....	46
2.3.2 Motivation for dividing the beam into segments .....	55
2.3.3 Validity of assumptions .....	55
2.3.4 Future work.....	57
Chapter 2.4 Paper 3, Replication of surface roughness.....	58
2.4.1 Paper reprint.....	59
2.4.2 Thickness dependency .....	68
2.4.3 Outlook .....	68

<b>PART 3 COLOR SCATTEROMETRY</b>	<b>71</b>
Chapter 3.1 Introduction .....	72
3.1.1 Scatterometry .....	72
3.1.2 Color perception.....	73
3.1.3 Simulation of reflection efficiencies .....	75
3.1.4 State of the art .....	77
Chapter 3.2 Paper 4 reprint .....	78
Chapter 3.3 Experimental setup .....	84
3.3.1 Imaging resolution .....	84
3.3.2 Polarization conversion.....	85
3.3.3 Relative scaling of colors.....	87
Chapter 3.4 Simulations .....	89
3.4.1 Simulation setup.....	89
3.4.2 Calculation of colors .....	93
3.4.3 Database resolution .....	94
Chapter 3.5 Calibrations .....	96
3.5.1 Camera .....	96
3.5.2 Light source .....	99
3.5.3 Beamsplitter .....	100
<b>CONCLUSION &amp; OUTLOOK</b>	<b>103</b>
<b>BIBLIOGRAPHY</b>	<b>107</b>
<b>APPENDICES</b>	<b>119</b>
A1 Detailed description of angular scatterometer setup .....	120
A1.1 Components .....	120
A1.2 Complete measurement workflow .....	121
A2 Convergence tests .....	124
A3 Supporting information for paper 4.....	128
A4 Instrument calibrations.....	133
A4.1 Spectrometer .....	133
A4.2 Camera warmup time .....	136
A4.3 LED warmup time.....	137
A5 Papers not included in thesis .....	138
A5.1 Paper 5.....	138
A5.2 Paper 6.....	145



# Part 1

## INTRODUCTION

# Chapter 1.1

## Functional nanostructures

---

The use of micro- and nanostructured surfaces is currently seeing increased research attention, due to the special properties they can provide without using chemical treatments. One example is structural colors, where the surface structures interact with visible light to produce bright color effects, without adding paints or dyes. This concept is well-known from nature, where many insects utilize this type of periodic patterns, one of the most famous example being the Morpho butterfly family<sup>[1]</sup>, shown in Figure 1a. Inspired by nature, this type of structures is currently being adapted for coloring different areas on plastic parts, using high volume fabrication methods such as injection molding and roll-to-roll manufacturing<sup>[2,3]</sup>. The advantages are that the colored regions can be defined directly in the manufacturing process, hereby removing post-processing steps and reduce production costs. One example of the use of this technology is for LEGO® Minifigures, as these are initially injection molded in one base color, and afterwards patterned in multiple steps to apply the different colors for the face, hair, and clothes. By including the coloring directly in injection molding process, the manufacturing cost would be significantly reduced. Structural colors also increases the prospects of plastic recycling, due to a reduced contamination of dye residues in the bulk material<sup>[3]</sup>. Another potential use for structural colors is in security holograms. Currently they are produced as metal-foil stickers that are subsequently attached to products like credit cards. By incorporating the holograms directly into the manufacturing process, the cost can be significantly reduced, hereby enabling the used in a much wider range of products. Potential applications are to protect high-quality brands from counterfeit goods, by having holograms on food packaging or even embedded into medical tablets.

Besides these colors effects, nature has developed several other functional micro- and nanostructured surfaces. Some examples are: the superhydrophobic effects known from Lotus leaves<sup>[4]</sup>, the anti-reflective surfaces of moth eyes<sup>[5]</sup>, and the dry adhesion of gecko feet<sup>[6]</sup>, see Figure 1. These structures all have different application areas, where superhydrophobic surfaces can provide self-cleaning and anti-fogging properties, while anti-reflective surfaces are essential for optical components such as camera lenses. However, before we can expect to see these functionalities implemented in everyday consumer products, the structures may not significantly increase the production cost, hence they should preferably be compatible with existing high volume fabrication methods.

The promising potentials of incorporating these functional surface structures into everyday products, have spun a considerable amount of research on high volume fabrication of such surfaces. DTU Nanotech alone has graduated six PhD scholars working within this topic during the last three years<sup>[2,3,7–10]</sup>. While these previous projects mainly focused on the production of the functional micro- and nanostructures, this thesis concerns the characterization of such structures, with a focus on methods suitable for high volume fabrication.

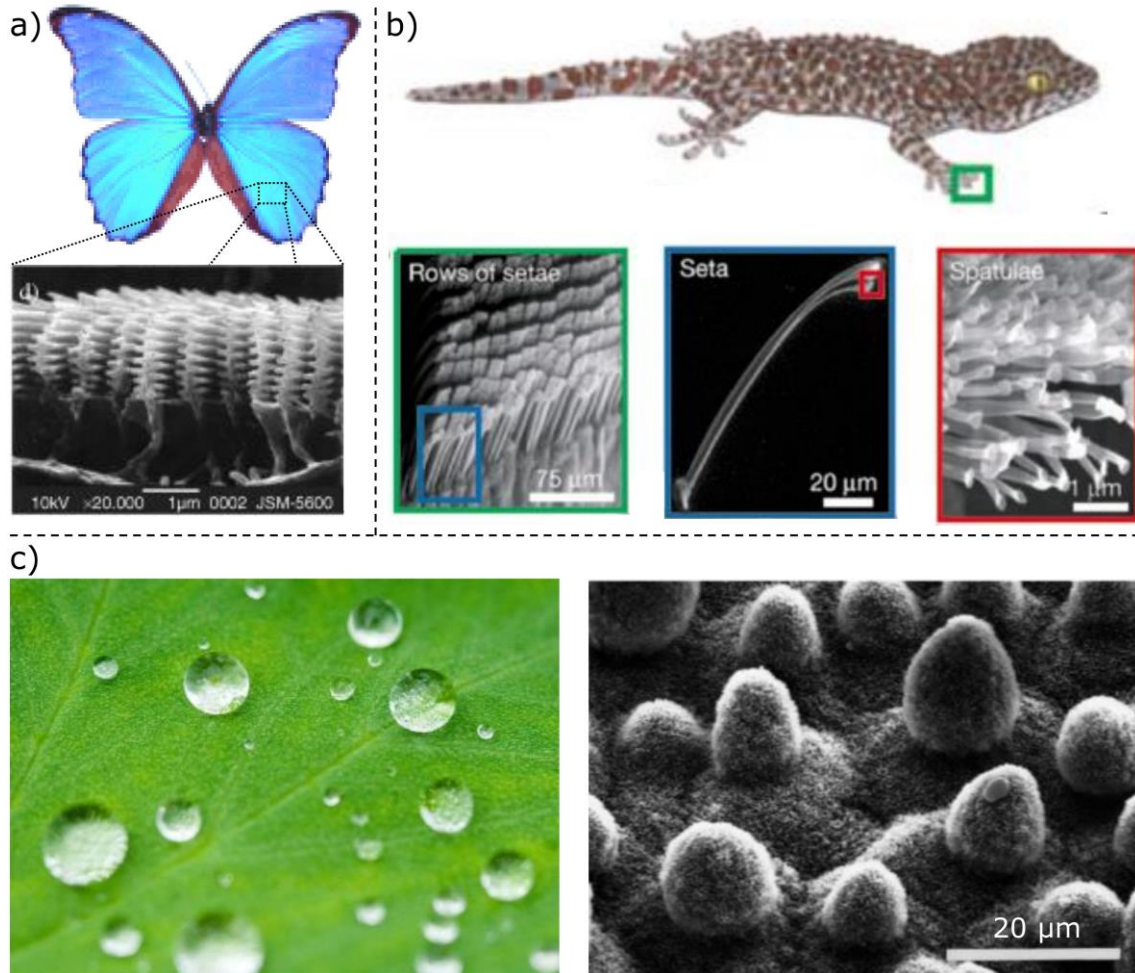


Figure 1: Examples of micro- and nanostructured surfaces found in nature. **a)** Morpho butterfly and scanning electron microscopy (SEM) image of structural color. Adapted from<sup>[1]</sup>. **b)** Gecko and SEM images of adhesive microstructures on feet. Adapted from<sup>[6]</sup>. **c)** Lotus leaf and SEM image of the super-hydrophobic micro- and nanostructures. Adapted from<sup>[4,11]</sup>.

# Chapter 1.2

## High volume fabrication methods

---

The largest high-volume producer of nanostructures is probably the semiconductor industry, which currently produces vast quantities of computer chips with feature sizes down to 14 nm<sup>[12]</sup>. However, while silicon is mainly suitable for electronic circuits, this thesis is focused on the growing field of high volume fabrication of nanostructured polymer surfaces. Plastics are one of most widely used materials in today's world, fueled by a low material cost and being easy to shape into a variety of forms<sup>[13]</sup>. Two promising methods for high volume manufacturing of nanostructured polymer products are injection molding (IM) and roll-to-roll manufacturing (R2R). Both are well-established methods for production of macroscale components, but are not specifically designed for producing nanostructures. However, by using already well-established fabrication methods, and tweaking them to also produce nanostructures, the functional nanostructured surfaces can more easily be implemented into existing production lines.

IM is used for producing solid plastic parts, with a typical setup seen in Figure 2. The general principle is to forcefully inject molten thermoplastic into a cold mold cavity, let the polymer solidify, then open the mold and remove the solid polymer part. This is a very cheap method for high volume fabrication, with typical cycle times in the order of seconds<sup>[14]</sup>. By structuring the inside of the mold master, micro- and nanostructures can be formed on the part surface, with reported feature sizes down to 50 nm<sup>[15]</sup>.

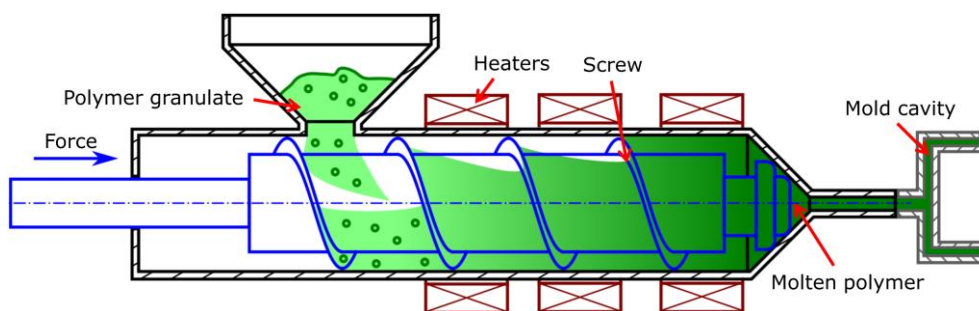


Figure 2: Illustration of typical injection molding machine. Adapted from<sup>[16]</sup>.

R2R, on the other hand, is designed for structuring polymer foils, e.g. for the interior of food packaging<sup>[14]</sup>. A typical setup is seen in Figure 3. The structures are defined by feeding a carrier foil in-between two rollers where one is structured and the other flat to supply counter pressure. The roller structures are transferred to the polymer foil with a speed of several meters per

second<sup>[17]</sup>. Several different R2R methods exist, two of them being R2R extrusion coating (R2R-EC) and R2R UV-assisted nanoimprint lithography (R2R-UV-NIL). For R2R-EC, a film of molten thermoplastic is extruded onto the carrier foil, and the structures defined by solidifying the polymer by a lower temperature of the structured roller. This method has been shown to reproduce nanostructures with feature sizes down to 80 nm and a foil speed of 1 m/s<sup>[18]</sup>. For R2R-UV-NIL, the thermoplastic is substituted with a film of UV-curable polymer, and the structures defined by curing the polymer with UV light while in contact with the structured roller. This method has been shown to achieve 70 nm structures, though the foil speed is limited to 1 m/min due to the slower UV curing step<sup>[19]</sup>.

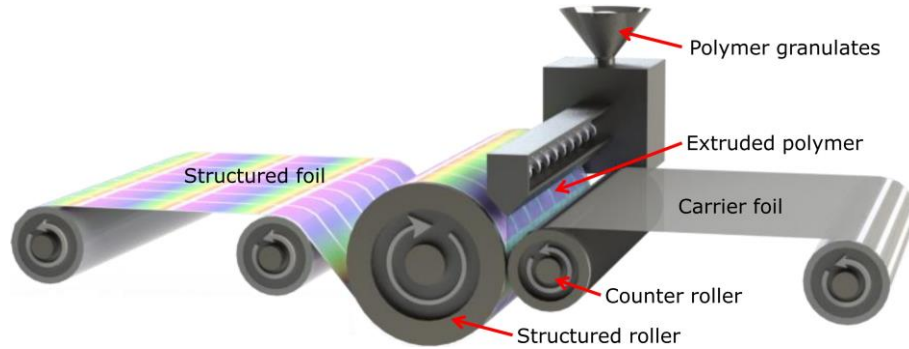


Figure 3: Illustration of typical roll-to-roll extrusion coating setup. Adapted from<sup>[18]</sup>.

For both methods, the fabrication of the master structures is a critical step, as these defines the best achievable structures for the manufactured parts. The macroscale mold shape is defined using the standard metalworking techniques of milling and polishing, while the nanostructures are defined lastly, e.g. using imprint lithography and an etch step<sup>[20]</sup> or by imprinting the structures into a thin coating layer such as hydrogen silsesquioxane (HSQ)<sup>[21]</sup>.

Other fabrication methods more specifically designed for nanostructuring are nanoimprint lithography (NIL)<sup>[22]</sup> and hot embossing (HE)<sup>[23]</sup>. These two methods are almost synonymous, and both work by imprinting a master tool into a thermoplastic heated above the softening temperature<sup>[24]</sup>. The difference is that NIL is designed to provide structured polymer thin films, typically on a substrate, whereas HE can produce larger sized components of solid polymer<sup>[24]</sup>. However, both methods only form planar components, and they often need long cycle times due to a slow polymer flow<sup>[24]</sup>. Hence, they are not as suitable for high volume manufacturing, as R2R and IM.

For defining the surface structures, the surface of the initial master tool needs to be flat on a length scale similar to the size of the structures. Hence, nano-patterning requires a nanoscale flat initial surface. For semiconductor fabrication, this is achieved by the atomically flat silicon wafer, but for steel molds, this level of surface finish demands a careful polishing of the mold. The polishing process can be a significant part of the overall manufacturing costs, and for staying within small tolerances, a good control of the material removal during polishing is needed<sup>[25]</sup>. Achieving this requires accurate and simple methods for monitoring the surface roughness, preferably together with a robot-assisted polishing process<sup>[25]</sup>.

### 1.2.1 Common structure defects

Two common defects often encountered with the previously mentioned fabrication methods are incomplete mold filling and sidewall scratches. Incomplete mold filling happens when the polymer solidifies before completely filling the structure cavities. Due to the low volume of a nanoscale cavity, the solidification time can be significantly shorter than the injection time, causing the polymer to block the cavity before complete filling<sup>[9,26,27]</sup>. The resulting structures then have lower heights than expected and typically more slanted sidewalls, though the shape also depends on the surface energy of the mold<sup>[27]</sup>, see Figure 4. Since the surface energy also influences how strongly the polymer sticks to the mold, the mold is often covered with an anti-stiction coating to ease the release without damaging the structures. Such coating results in a profile similar to the two leftmost illustrations in Figure 4.

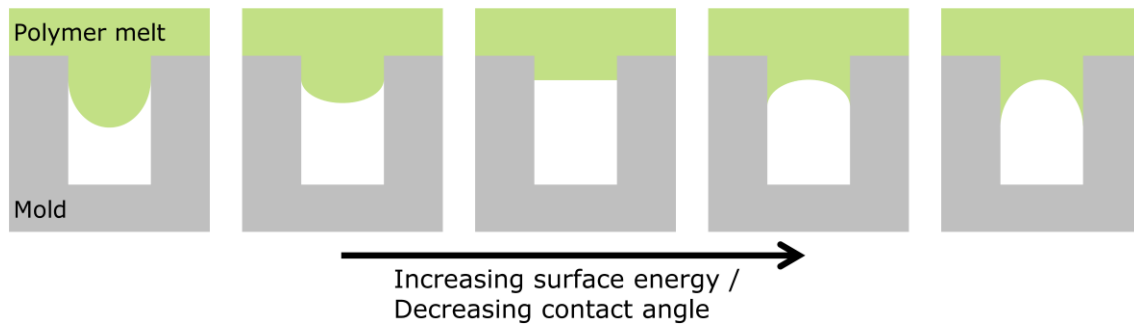


Figure 4: Illustration of the influence of the mold surface energy in relation to the shape of the advancing polymer melt front.

Sidewall scratches occur during the demolding step if the mold scrapes along one side of the polymer structures. This results in slanted sidewalls and the formation of a “tip” of excess material deposited along the rim of the structures<sup>[26,27]</sup>. The scratching is mainly caused by thermal contraction of the bulk polymer during the cooling phase; hence, the tips generally occur on the structure side facing the center of the part<sup>[26]</sup>. The shrinkage ratios of typical polymers are on the order of 1 %<sup>[27]</sup>, corresponding to a radial displacement of up to 250  $\mu\text{m}$  for a 5 cm diameter part. The formed tip typically only constitutes a small volume of the structure, but it can inhibit later bonding of the chip<sup>[26]</sup>. An example of a sidewall scratch and the formed tip is shown in Figure 5.

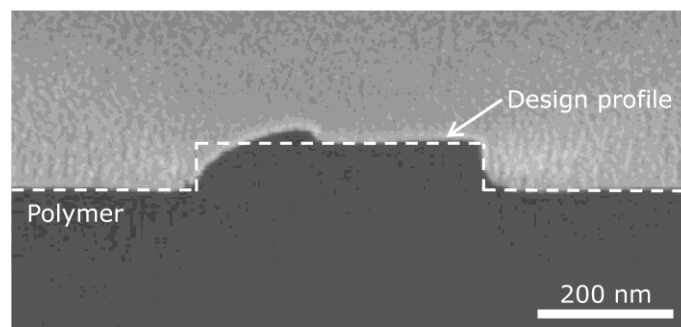


Figure 5: Illustration of sidewall scratches. FIB-SEM image of the structure profile, showing the tip deposited along one of the rims. Notice how the area of the tip corresponds to the void under the design profile.

# Chapter 1.3

## Characterization of nanostructures

---

Characterization of micro- and nanostructures is typically performed with atomic force microscopy (AFM) or scanning electron microscopy (SEM). For structures with a size of several micrometers, hence larger than the diffraction limit, optical techniques such as confocal microscopy (CM) and white light interferometry (WLI) are also increasingly being used<sup>[9,25,28]</sup>.

AFM works by tracing a sharp needle over the surface, and continuously evaluating the deflecting to obtain the 3-dimensional (3D) topography of the surface structures<sup>[29]</sup>. It is a very versatile research tool, as it does not impose any requirements on the material properties, and it can evaluate axial features with sub-nanometer resolution<sup>[29]</sup>. A disadvantage is that even though the tip has a radius of curvature of only a few nanometers<sup>[30]</sup>, the sidewalls of the tip are more slanted, resulting in the tip shape convoluting with the structures and distorting the lateral features<sup>[29]</sup>. Acquiring high precision AFM measurements is also time-consuming due to a slow tip scanning speed, and it requires a skilled operator.

With SEM, a focused electron beam is scanned across the sample and a contrast in structure topography generated by the number of backscattered electrons<sup>[28]</sup>. SEM has a high lateral resolution but does not provide axial information. By tilting the sample, SEM can also evaluate structure heights, but the tilt correction is non-trivial and can often lead to inaccurate values<sup>[31]</sup>. SEM images are generally faster to acquire than AFM images, but the technology requires the samples to be conductive and under vacuum. Obtaining high-quality images also require a skilled operator.

CM and WLI are both optical methods that provide 3D profiles of the sample. They both employ the concept of scanning the sample axially and determine the 3D profile from the stack of images. CM utilizes a pair of pinholes to illuminate only a small volume of the sample and by scanning this point across the plane, an image of each axial plane is formed. The 3D profile is then generated by determining the axial level of each pixel, based on the highest intensity in the stack<sup>[32]</sup>. WLI evaluates the interference fringes while scanning, and determines the axial position of each pixel from the intensity peak in the stack of images<sup>[33]</sup>.

A common problem for the methods mentioned above is that they are all serial techniques, where the image/3D-profile is generated either by the raster of a probe or from a sequence of images. This results in rather slow acquisition speeds, especially for the high-resolution methods of AFM and SEM. For quality control in high volume fabrication of nanostructures, faster evaluation methods are needed, and preferably implemented for automated in-line control.

# Chapter 1.4

## Project goal

---

The overall goal of the project is to develop a method for quality control of high volume fabrication of micro- and nanostructured surfaces. The method should provide a fast evaluation and work autonomously, to enable automatic in-line implementation. This focus might result in decreased accuracy compared to other state-of-the-art methods; however, for quality control applications a lower accuracy is typically tolerable. The control structures are expected to be periodic gratings, positioned next to the actual functional structures that might feature more complex geometries. The control structures then serve as indicators of the production quality.

The hypothesis is that optical methods can provide these characterization functionalities, due to a fast interaction with the sample compared to the mechanical interactions of AFM. The control structure dimensions are expected to be on the same length scale as visible light, as this provides an increased interaction between light and structures. This regime is typically also the interesting length scale for such functional surfaces. For dimensional characterization of 3D structures below the diffraction limit, methods such as CM or WLI cannot be used. Instead, scatterometry is seen as a promising technique for evaluating the 3D profile of sub-wavelength structures.

Besides the characterization of patterned micro- and nanoscale structures, the project also focused on new methods for characterizing nanoscale surface roughness. Such characterization is important when polishing the initial master mold for IM or R2R manufacturing as this surface must be smooth on a length scale smaller than the patterned structures. AFM can easily resolve nanoscale roughness, but AFM instruments are typically not compatible with industrial manufacturing conditions, e.g. due to vibrations. With an optical technique, the surface could potentially be evaluated without demounting from the metalworking machine, thereby optimizing the finishing process.

# Chapter 1.5

## Thesis outline

---

The thesis is structured into three parts, which emphasizes the two different fields covered by the project. Part 1 was a general introduction and motivation for the study. Part 2 concerns the evaluation of random roughness features using angular scatterometry, and Part 3 presents a new method for dimensional characterization of the nanostructured surfaces.

Part 2 is divided into four chapters:

Chapter 2.1 introduces the concepts of angular scatterometry and roughness evaluations.

Chapter 2.2 presents the first paper, including a more detail presentation of the samples, some additional analyses, and an outlook regarding future industrial implementations.

Chapter 2.3 and 2.4 presents the second and third paper. Both chapters include some additional analyses and expanded outlooks.

Part 3 is divided into five chapters:

Chapter 3.1 introduces the concepts of scatterometry for dimensional metrology, color theory, and numerical simulations of structure-light interactions.

Chapter 3.2 is a reprint of the fourth paper.

Chapter 3.3 contains a more detailed description of the experimental setup presented in the paper.

Chapter 3.4 expands on the numerical simulations in the paper.

Chapter 3.5 describes the calibration procedure of the setup.

Lastly, the thesis is concluded.



# Part 2

## ROUGHNESS EVALUATION

Evaluation of surface roughness is critical for most manufacturing processes. The first thing that comes to mind is a simple stylus profilometer in a mechanical workshop, but other industries, e.g. the manufacturing of optical components, are heavily dependent on proper evaluation methods of their products<sup>[34]</sup>. For the manufacturing of nano-patterned surfaces, the initial surface roughness needs to be smooth on this length scale, thereby requiring characterization instruments working in this regime. Part 1 will evaluate different methods for industrial evaluation of nanoscale roughness, with a focus on angular scatterometry.

Angular scatterometry is a non-contact optical technique that evaluates the roughness from the pattern of scattered light. A commercially available scatterometer is analyzed, called an “OptoSurf”, and compared with a high-resolution laboratory setup. The OptoSurf is designed for industrial use and can fit into common metalworking machines, one of its advantages is that it only takes a few milliseconds to evaluate each point, and it obtains both the roughness level and the surface form<sup>[35]</sup>. The fast measurement speed makes it possible to perform 2D scans of large surfaces, to provide a contour map of the roughness level that can help evaluate the homogeneity and discover defects<sup>[25]</sup>. Such detailed information can aid manufacturers in achieving better surface finish and provide products of higher grade.

Part 2 is divided into four chapters: first a general introduction and then three chapters organized around three published papers. In addition to a reprint of the papers, each chapter includes a more detailed description and a few extended analyses relating to the papers.

Short summary of papers:

Paper 1: The OptoSurf is compared with two other optical instruments, and a relation between the two roughness parameters  $A_q$  and  $R_q$  is presented. This relation is relevant because the  $A_q$  parameter is not standardized and largely unknown in the industry, its main advantage being that it is easy to calculate from the scatter distribution. In comparison, the  $R_q$  parameter is well known and defined by an ISO standard. The relation for converting  $A_q$  to  $R_q$  value is a step towards inline roughness metrology.

Paper 2: Continues the evaluation of scatterometry and the OptoSurf instrument for roughness measurements. With the goal of measuring on samples mounted inside metalworking machines, we investigate the effects on the scatter distribution under non-perfect measurement conditions. The analysis focuses on changes to the distribution when the sample is covered with a thin liquid film. Such film could be residues of the metalworking fluid or an unsuccessful cleaning step.

Paper 3: Concerns measurements on hard-to-reach surfaces that are not directly accessible with the evaluation instrument. Such surfaces are often evaluated by making a polymer cast of the surface structures and then measure on this replica instead. This method relies heavily on good replication fidelity, to trust that the values obtained from the replica correspond to the true values on the actual surface. In this paper, we study the shrinkage of replicas made with the polymer polydimethylsiloxane (PDMS), and presents a temperature dependent equation for correcting the measured replica dimensions

# Chapter 2.1

## Introduction to roughness evaluation

---

### 2.1.1 Angular scatterometry

Scatterometry is a non-destructive optical technique, where the intensity of light scattered from a sample is analyzed to provide information about the surface structures<sup>[36]</sup>. Typically scattering is characterized by the angular distribution, but one can also evaluate the polarization or wavelength dependency. For angular distributions, the intensity in each direction of the scattering hemisphere is evaluated, though a single arc on the hemisphere well describes many scattering patterns, known as a 1D scattering distribution. This reduced distribution can easily be evaluated by moving the detector in a circle around the sample, while an evaluation of the full hemisphere requires movements in three directions. The theory for analyzing the distributions is presented in Section 2.1.4.

### 2.1.2 Instrument presentation

The present section mainly concerns roughness measurements with two scatterometer instruments: the commercially available OptoSurf and a custom built laboratory setup. Beside the scatterometers, a confocal microscope is used for obtaining 3D surface profiles. These three instruments are introduced in the following, and an image of each show in Figure 6.

#### 2.1.2.1 OptoSurf

The “OptoSurf OS 500-32” (OptoSurf GmbH, Germany), is a simple scatterometer in a compact housing. It is designed for ease of use, robustness, measurement speed, and compatibility with common metalworking machinery<sup>[35]</sup>. The compatibility means that it fits into tool holders in the machines, hereby enabling in-machine measurements without needing to dismount the samples. By keeping the samples mounted, the cumbersome process of realigning them to the machine coordinate system is avoided. It is also possible to mount the OptoSurf in a corner of the machining volume, hereby also avoiding the tool dismount. With the term “common metalworking machinery”, we refer to machines such as polishing and milling machines, where the tool is mounted on a rotating spindle while the samples are moved around on a xyz-stage.

The evaluation principle is to probe the surface with a focused beam of monochromatic LED light, and determine the angular distribution of the backscattered light. The acquired distribution is a 1D distribution that spans a single arc on the scattering hemisphere, hereby only providing

information along one direction of the sample surface. The detector is an oblong CCD chip with 32 pixels covering an angular span of  $\pm 16^\circ$ ; hence, each pixel corresponds to an angular span of  $1^\circ$ . The low number of pixels enables a short measurement time, down to a few milliseconds, but also results in a low angular resolution that limits the possibilities for data analysis. On the other hand, the high measurement frequency enables the instrument to scan a larger area of the surface and produce a 2D map of the surface roughness. The CCD has a dynamic range of around three orders of magnitude.

#### 2.1.2.2 Laboratory scatterometer

The custom-built scatterometer setup is designed to obtain high angular resolution and provide reconfigurability. Compared to the OptoSurf it is significantly larger and more fragile. It evaluates the scattering distribution by scanning the detector in a circle around the sample, thereby obtaining the 1D scattering distribution. However, it is possible to tilt the sample in small increments and acquire several line scans, to obtain the full hemispherical scattering distribution. It has a fine angular resolution of  $0.01^\circ$ , can provide different incident angles on the sample, and evaluates the full angular range from the surface normal to beyond  $90^\circ$ . The detector is a single photodetector connected to a lock-in amplifier, providing a dynamic range of eight orders of magnitude. The fine angular resolution results in a long acquisition time of around two hours for a single scan. A detailed description is presented in Appendix A1.

#### 2.1.2.3 Confocal microscope

The confocal microscope is used to evaluate the 3D profiles of the samples. These profiles are used for comparing the roughness values obtained from the scattering distributions, with values calculated from line profiles by the ISO standardized methods presented in the following section. The microscope is a “Sensofar PLu Neox” (Sensofar Tech, Spain), and is also capable of performing white-light interferometry, though only the confocal part was used for the analysis. An example of the 3D profiles obtained can be seen in Figure 14 on page 26. The typical measurement time for the samples was below 30 s. The manufacturer states an  $x,y$ -resolution of 330 nm,  $z$ -resolution of 2 nm, and a field of view of  $255 \times 191 \mu\text{m}^{[37]}$ . However, an analysis of the effective bandwidth revealed that these resolutions could not be directly transferred to roughness calculations. Instead, a tighter set of boundaries had to be applied, especially on very smooth samples. This analysis is presented in Paper 1 in the section *Optical profiler*.

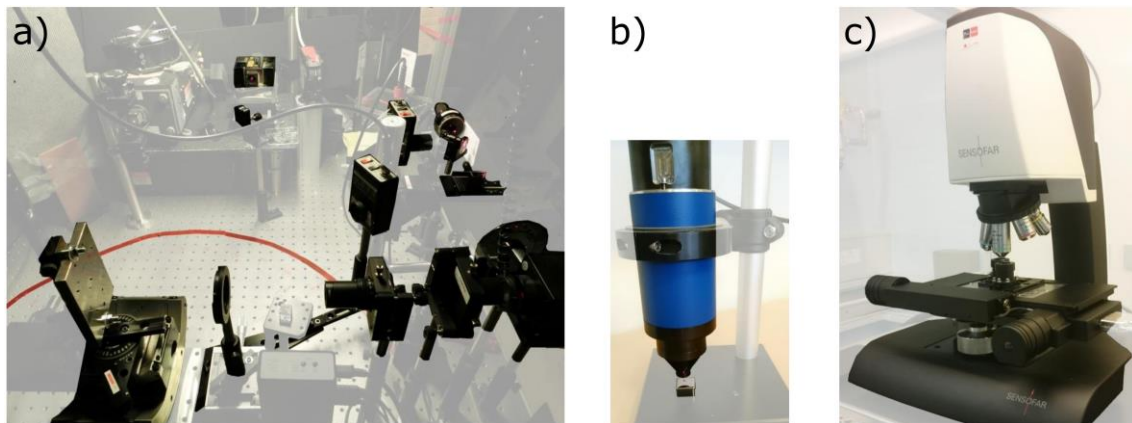


Figure 6: Photographs of the three instruments. **a)** The laboratory scatterometer (For a list of the components see Appendix A1), **b)** the OptoSurf, and **c)** the confocal microscope. The images are scaled to partially reflect their real-world sizes.

### 2.1.3 Roughness calculations

Evaluation of roughness parameters is routinely done in a wide range of industries. Generally, the parameters are calculated from line profiles of the surface topography, defined by the ISO standard 4287<sup>[38]</sup>. Classically, these profiles are determined with stylus profilers, but due to an increasing use of 3D characterization methods, such as AFM and WLI, a set of complimentary area parameters have been defined in ISO 25178-2<sup>[39]</sup>.

For the present analysis, it is not important which parameters are used, rather it is important to choose a parameter that is comparable between the instruments, and they should all be able to evaluate it in an overlapping frequency range. All parameters can be evaluated from the 3D confocal images, but since the laboratory scatterometer and the OptoSurf only evaluates scattering along one direction, a line parameter is most suitable. Of these parameters the RMS roughness ( $R_q$ ) and the RMS slope ( $R_{dq}$ ), are the only ones directly determinable from the angular scattering distribution. Hence, these parameters are chosen for the analysis. The corresponding ISO defined equations are seen in Figure 7. The main focus will be on  $R_q$ , as this is the most common of these parameters<sup>[40]</sup>. The most popular parameter is the arithmetic mean ( $R_a$ ), but some argue that  $R_q$  is often better at describing the properties of a surface<sup>[41]</sup>. This is due to the fact that the RMS formula, compared to the arithmetic mean, provides extra weight to large profile values, hereby increasing the output value if there are significant peaks or valleys on the surface<sup>[41]</sup>. Due to the increased weight,  $R_q$  values are generally around 10% larger than the corresponding  $R_a$  values, although this number depends on the specific surface profiles<sup>[41]</sup>.

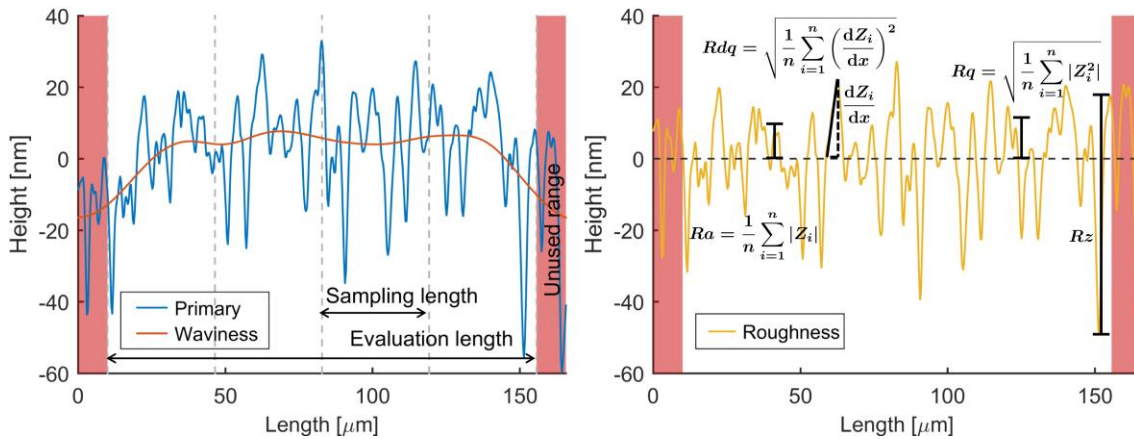


Figure 7: Illustration of roughness calculations based on ISO 4287<sup>[38]</sup>. Illustrations of the three profile derivatives, two of the length scales involved, and the equations for a few parameters.  $Z_i$  is the profile amplitude,  $\frac{dZ_i}{dx}$  the slope, and  $n$  the number of sample points.

When calculating the roughness parameters the line profile is bandwidth filtered by a noise ( $\lambda_s$ ) and a cut-off filter ( $\lambda_c$ ), defined by ISO 4287. The high frequent noise is removed by the noise filter, while the low frequent long-range waviness/form of the sample is separated from the roughness by the cut-off filter. The filters are also used to ensure that the evaluated parameters only cover the effective measurement range of the instrument. For an illustration of the filtering effects, see Figure 7.

The applied filters greatly influence the final roughness values, and they should always be specified along with the roughness values. For an example of how the filter length affects the roughness parameters, see Figure 8 where the  $R_q$  roughness is calculated from the same profile when filtered with different cut-off filter lengths. For stylus profile measurements, a guideline exists for choosing the filter lengths, see Table 1, though one should always also consider

whether the instrument is actually accurate in that regime. For other methods with higher resolution, e.g. AFM or WLI, no official guideline exists; hence, one must be aware of only comparing values obtained for similar bandwidths. In this study, we stay close to official ISO defined methods, though the guidelines for the filtering bandwidths are disregarded as the filters instead are used to match the common range covered by all three instruments. Otherwise, the obtained values can certainly not be expected to correlate.

Table 1: Guideline values for  $\lambda_s$  and  $\lambda_c$  given by ISO 3274:1996<sup>[42]</sup>. The values are defined by the radius of curvature of the probe and the sampling point spacing of the profile.

$\lambda_s$ [mm]	$\lambda_c$ [mm]	Probe radius [ $\mu\text{m}$ ]	Point spacing [ $\mu\text{m}$ ]
0.08	2.5	2	0.5
0.25	2.5	2	0.5
0.8	2.5	2	0.5
2.5	8.0	5	1.5
8.0	25	10	5.0

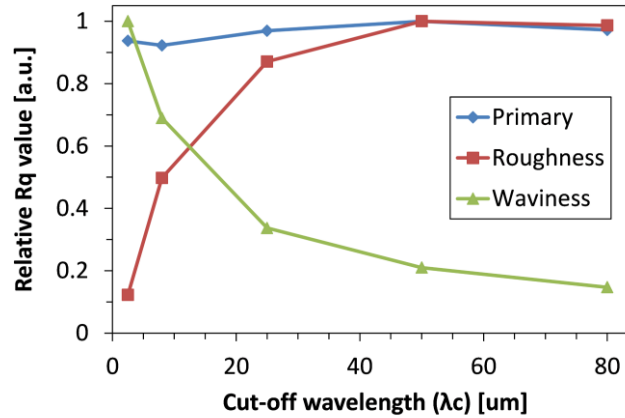


Figure 8: Calculation of the RMS roughness ( $R_q$ ) of the same sample profile but applying different filter cut-off wavelengths. The  $R_q$  values are calculated separately for each of the three profiles. This illustrates how the roughness value is transferred from the roughness to waviness profile depending on the cut-off filter length.

A common problem among almost all roughness parameters, both line and area parameters, are that they only describe variations normal to the surface. All information on lateral variations is then disregarded, although it can reveal which spatial wavelengths contribute most to the total roughness. This information is often useful when optimizing a manufacturing sequence and need to determine a combination of polishing methods to provide the desired surface finish<sup>[34]</sup>. When all lateral information is discarded, very differently shaped surface profiles can provide identical roughness values, as seen from the example profiles in Figure 9. There is only a single area parameter that concerns spatial variations, the “texture aspect ratio” ( $\text{Str}$ )<sup>[39]</sup>. But this is not an actual roughness value, rather an indicator to reveal if the sample is anisotropic<sup>[39]</sup>.

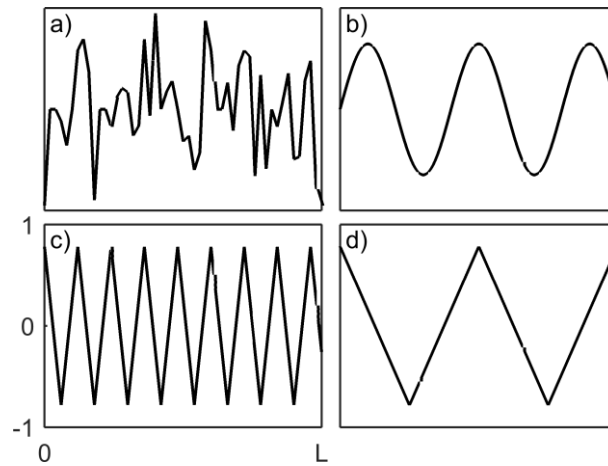


Figure 9: Illustration of four different roughness profiles with the same  $R_a$  and  $R_q$  roughness values. **a)** A sum of 10 sinusoidal curves, **b)** a pure sinus curve, **c)** and **d)** are sawtooth patterns with high and low spatial surface frequencies, respectively.

To provide more detailed information on the surface roughness, one should provide a graph of the roughness level as a function of spatial frequency, instead of only a single value for the entire surface. Unfortunately, such graphs would also make it harder to compare samples, and significantly more information would have to follow a sample, compared to the few numbers required for a single parameter and the frequency limits. A new approach currently under development by QED Technologies might prove as a good compromise. This method consists of a simple graph with only a few roughness values for some semi-wide bandwidths<sup>[34]</sup>. This provides an indication of the frequency range containing most roughness, while still being a rather simple graph, see Figure 10. Another advantage is the possibility to visualize the spatial distribution of roughness for each data point, to help determine where additional polishing is necessary.

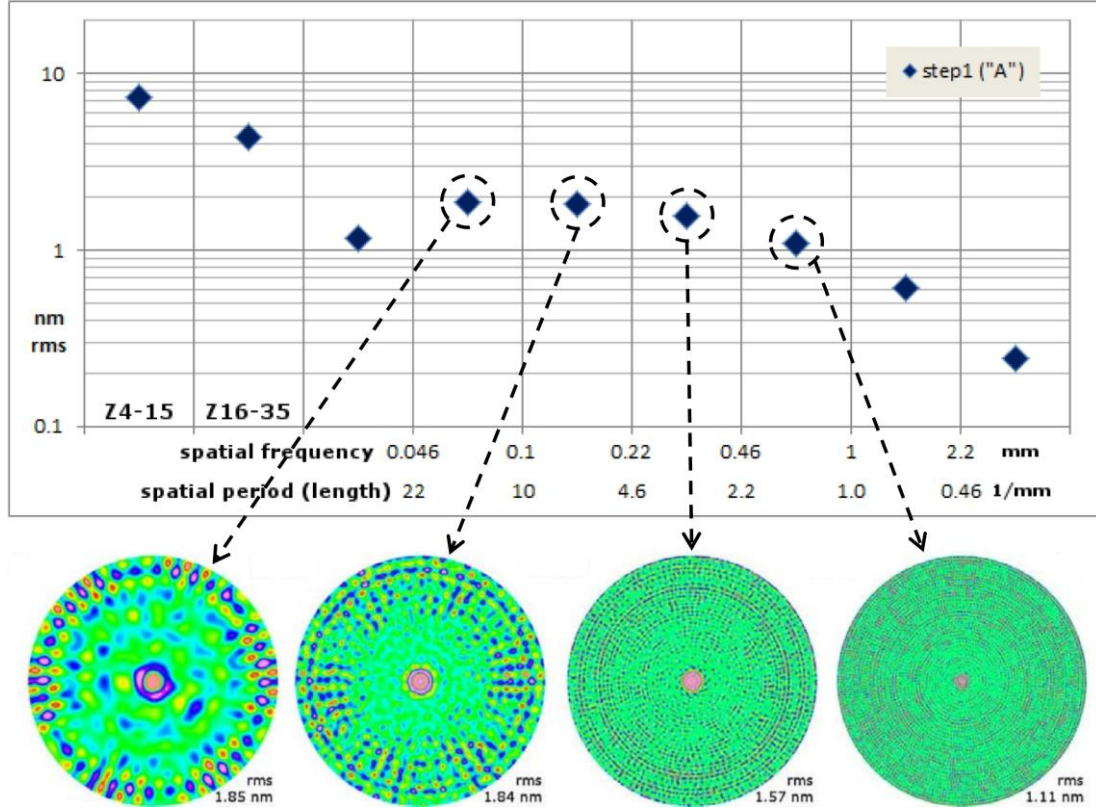


Figure 10: Graph of the RMS roughness for different bandwidths of spatial surface frequencies, and the corresponding 2D contour plots showing the distribution of roughness features on the sample surface. The x-axis tick marks defines the bandwidth of each data point is defined. Adapted from<sup>[34]</sup>.

## 2.1.4 Scattering theory

### 2.1.4.1 Scattering in general

Light incident on a surface can be reflected, scattered, transmitted, or absorbed, where the ratio between each depends on the material and surface properties. The two components of interest for this study are the reflected and scattered light. The reflected light is reflected like a mirror, hence  $\theta_r = \theta_i$ , while the scattered light is distributed on the hemisphere in a pattern relating to the surface structure. The scattering distribution is defined in the coordinate system sketched in Figure 11, and quantified by the bidirectional reflection distribution function (BRDF), which normalizes the scattering distribution to the incident intensity and corrects for angular variations along the hemisphere. It is given by<sup>[36]</sup>:

$$\text{BRDF} \equiv \frac{\text{differential radiance}}{\text{differential irradiance}} \cong \frac{dP_s/d\Omega_s}{P_i \cos \theta_s} \cong \frac{P_s/\Omega_s}{P_i \cos \theta_s}, \quad (1)$$

where  $P_i$  and  $P_s$  are the incident and scattered power, respectively,  $\Omega_s$  the solid angle through which the scattered light is detected, and  $\theta_s$  the scattering angle. The cosine factor corrects the illuminated area to its apparent size when viewed from the angle  $\theta_s$ . If the cosine factor is dropped it is called the cosine corrected BRDF (ccBRDF) or angle-resolved scatter (ARS). Due to the normalization, the unit of the BRDF is inverse steradians (a solid angle unit). For smooth samples and small detector solid angles the value can range over many orders of magnitude, from around  $10^6/\text{sr}$  at specular to the noise limit at  $10^{-9}/\text{sr}$ , due to scattering from ambient air molecules<sup>[36]</sup>.



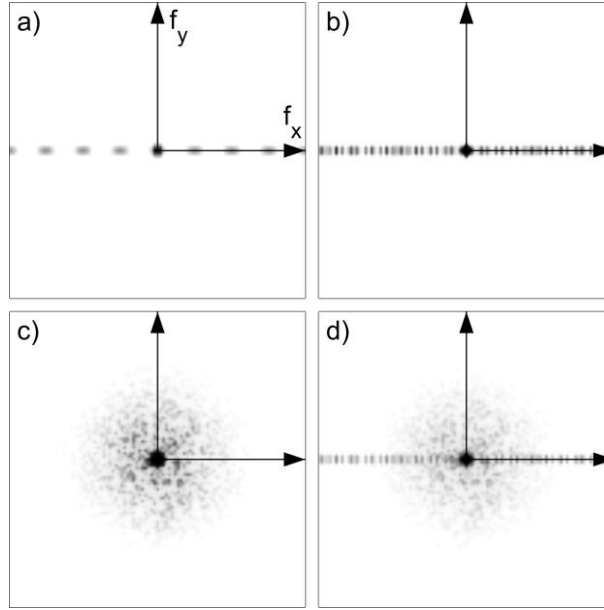


Figure 12: Illustrations of typical 2D PSD functions for various types of surface structures. **a)** Perfect sinusoidal line structures, **b)** 1D surface structures of parallel lines, resulting in a diffraction pattern combined of many different frequencies, **c)** perfectly isotropic sample scattering equally into all angles, and **d)** typical real surface with combination of isotropic and line scattering.

#### 2.1.4.3 Roughness calculations

Besides the indication of pronounced spatial surface wavelengths, the PSD also interesting due to a direct correlation with the RMS roughness ( $R_q$ ), obtained as the zeroth order moment<sup>[36]</sup>:

$$R_q^2 = 2 \int_{-\infty}^{\infty} (2\pi f_x)^0 S_1(f_x) df_x . \quad (5)$$

However, since real profiles are always sampled over a finite length, and the instrument is only sensitive within a finite bandwidth, the infinite boundaries should be replaced by the frequency limits  $f_{\min}$  and  $f_{\max}$ , and the resulting roughness termed *the relevant roughness* for the bandwidth,  $R_{q_{\text{rel}}}$ <sup>[43]</sup>. The second order moment provides the RMS slope of the surface ( $R_{dq}$ ), which should be determined over the same bandwidth:

$$R_{dq}^2 = 2 \int_{f_{\min}}^{f_{\max}} (2\pi f_x)^2 S_1(f_x) df_x . \quad (6)$$

The fourth order moment provides the surface curvature, but this parameter will not be used.

Similar to the cut-off frequency defined in ISO 4287, the frequency limits for the relevant roughness strongly affects the roughness values, hence it is important to use the correct bandwidth limits for each instrument and state them together with the roughness values. This might seem obvious but is often neglected<sup>[36]</sup>. For an illustration of the relations between the scattering distribution, the BRDF, the PSD, and the RMS roughness, see Figure 13.

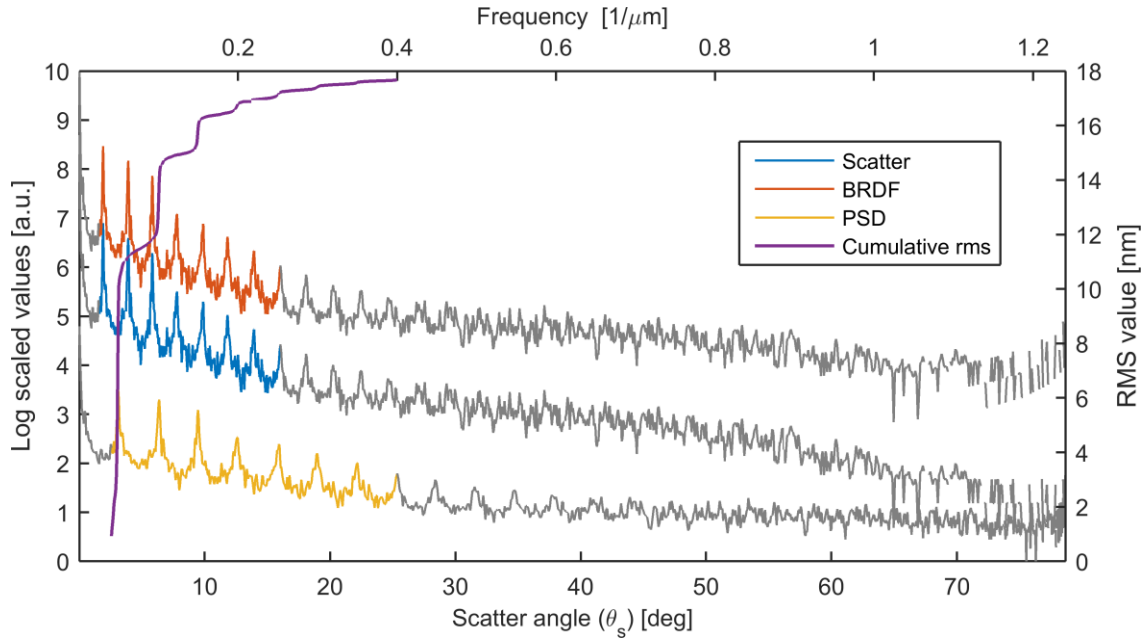


Figure 13: Illustration of the relation between measured scattering intensity (blue), the BRDF function (red), the PSD function (yellow), and the RMS roughness (purple). The PSD and RMS value are plotted on the frequency axis, while the others are on the angle axis. The gray parts of the graphs represent the regions outside the bandwidth limit, in this case defined as  $0.04 - 0.4 \mu\text{m}^{-1}$ , corresponding to  $1.6^\circ - 16^\circ$ . The RMS roughness is shown as a cumulative value, to illustrate how it is affected by the features on the PSD.

#### 2.1.4.4 Scattering models

Scattering distributions and BRDF functions are strongly coupled to the PSD, as they are all naturally functions in frequency space. However, different theories exist for converting the BRDF (or ccBRDF) to the surface PSD, mainly differing in the assumptions on roughness level and allowed scattering angles. In this work, the Rayleigh-Rice (RR) theory is used since this is the most established theory<sup>[36]</sup>. The RR theory is a perturbation theory, based on a perfectly smooth surface that is perturbed with a low degree of roughness. For this reason, it is inherently restricted to smooth surfaces<sup>[36]</sup>. One advantage over many other theories is that the perturbation does not impose angular constraints, hence RR theory is valid for larger incident and scattering angles than e.g. Kirchhoff diffraction theory<sup>[44]</sup>. Other methods of modeling rough surfaces include a shadowing function to account for light blocked by tall structures<sup>[45]</sup> and fitting of equations with up to 30(!) parameters to the scattering distribution<sup>[46]</sup>. Several other theories exist, for descriptions of these we refer to the reviews by Renhorn et al.<sup>[47]</sup>, Hoover and Gamiz<sup>[48]</sup>, and Elfouhaily and Guérin<sup>[49]</sup>. Based on their thorough review of 31 theories, Elfouhaily and Guérin concluded:

*At the present time, there does not seem to be a universal method that is to be preferred systematically. All the methods present a compromise between versatility, simplicity, numerical efficiency, accuracy and robustness, with a different weighting in these various fields.*

This quote illustrates the importance of critically choosing the theory for analyzing a given surface. Fortunately, most shortcomings of the theories are due to constraints on very rough surfaces and large scatter angles, but our samples are all fairly smooth and only evaluated close to normal incidence. A more recent theory not included in the reviews is the Generalized Harvey-Shack (GHS) model<sup>[50]</sup>, which have been under development since 1976<sup>[51]</sup>. This model

is designed to work on rougher surfaces than RR theory, something that is often the goal of these alternative theories. This theory describes the scattering by a surface transfer function, based on the RMS roughness and auto-covariance function. RR theory is used since all samples in the study are fairly smooth, and well described by this theory.

#### 2.1.4.5 Rayleigh-Rice theory

The following section will present the key relations in RR theory, while for a detailed description we refer to Section 3.3 in<sup>[36]</sup>. The main relation of RR theory, is the connection between the scattering distribution and the surface PSD, given as<sup>[36]</sup>:

$$\text{BRDF} = \frac{P_s/\Omega_s}{P_i \cos \theta_s} = \frac{16\pi^2}{\lambda^4} \cos(\theta_i) \cos(\theta_s) Q(\theta_i, \theta_s, \phi_s) S(f_x, f_y) , \quad (7)$$

where  $Q(\theta_i, \theta_s, \phi_s)$  is a polarization dependent reflection factor,  $S(f_x, f_y)$  the surface PSD, and  $\lambda$  the wavelength of the incident light. The spatial frequencies are defined from the scattering angles  $\theta_s$  and  $\phi_s$  shown in Figure 11, by the relations:

$$\begin{aligned} f_x &= \frac{\sin(\theta_s) \cos(\phi_s) - \sin(\theta_i)}{\lambda} \\ f_y &= \frac{\sin(\theta_s) \sin(\phi_s)}{\lambda} \end{aligned} \quad (8)$$

The  $Q$  factor in Equation (7) accounts for the reflection efficiencies of each polarization pair of  $s$  and  $p$  for both the incident and the scattered light. It is given by:  $Q = Q_{ss} + Q_{sp} + Q_{ps} + Q_{pp}$ , with the individual equations<sup>[36,52]</sup>:

$$\begin{aligned} Q_{ss} &= \left| \frac{(\varepsilon - 1) \cos(\phi_s)}{(\cos(\theta_i) + \sqrt{\varepsilon - \sin^2(\theta_i)})(\cos(\theta_s) + \sqrt{\varepsilon - \sin^2(\theta_s)})} \right|^2 \\ Q_{sp} &= \left| \frac{(\varepsilon - 1) \sqrt{\varepsilon - \sin^2(\theta_s)} \sin(\phi_s)}{(\cos(\theta_i) + \sqrt{\varepsilon - \sin^2(\theta_i)})(\cos(\theta_s) + \sqrt{\varepsilon - \sin^2(\theta_s)})} \right|^2 \\ Q_{ps} &= \left| \frac{(\varepsilon - 1) \sqrt{\varepsilon - \sin^2(\theta_i)} \sin(\phi_s)}{(\cos(\theta_i) + \sqrt{\varepsilon - \sin^2(\theta_i)})(\cos(\theta_s) + \sqrt{\varepsilon - \sin^2(\theta_s)})} \right|^2 \\ Q_{pp} &= \left| \frac{(\varepsilon - 1) (\sqrt{\varepsilon - \sin^2(\theta_s)} \sqrt{\varepsilon - \sin^2(\theta_i)} \cos(\phi_s) - \varepsilon \sin(\theta_i) \sin(\theta_s))}{(\cos(\theta_i) + \sqrt{\varepsilon - \sin^2(\theta_i)})(\cos(\theta_s) + \sqrt{\varepsilon - \sin^2(\theta_s)})} \right|^2 , \end{aligned} \quad (9)$$

where  $\varepsilon$  is the complex relative permittivity of the interface, and the subscripts  $Q_{ij}$  indicate incident  $i$  and scattered  $j$  polarization.

For our measurement setup, the only none zero component is  $Q_{ss}$ . The three others vanish due to the incident light being  $s$ -polarized, and the scattering only evaluated in the plane of incidence where  $\phi_s = 0$ .

#### 2.1.4.6 Model limitations

Since RR theory is based on a perturbation of a perfectly smooth surface, it is only valid for what is termed *optically smooth* surfaces<sup>[36]</sup>. A strict limit on the maximum roughness level does not exist, but it is generally taken as<sup>[36,43]</sup>:

$$\left(\frac{4\pi Rq \cos(\theta_i)}{\lambda}\right)^2 \ll 1. \quad (10)$$

This relation arises from a consideration of the total integrated scatter (TIS), which is the fraction of scattered to reflected light, given by<sup>[36,43]</sup>:

$$\text{TIS} = \frac{P_s}{P_s + P_r} = \frac{P_t - P_s}{P_t} = 1 - \exp\left[-\left(\frac{4\pi\sigma \cos(\theta_i)}{\lambda}\right)^2\right], \quad (11)$$

where  $P_s$  and  $P_r$  are the power of the scattered and specular reflected light, respectively, while  $P_t = P_s + P_r$ .

However, the limit in Equation (10) is unnecessarily strict, as the  $\ll$  limit simply arises from a Taylor expansion of the last term in Equation (11). This simplification might have been relevant in a time without calculators, and exponential functions should best be avoided, but today there is no need to use this approximation, as it merely constrains the theory with an artificial limit. Based on an analysis by Harvey et al.<sup>[43]</sup> the real limit for RR theory is rather  $\text{TIS} \leq 0.9$ , which corresponds to  $Rq \leq 0.12\lambda$  for normal incidence. For the present analysis, RR theory was found suitable for surfaces with  $Rq$  values up to 70 nm, corresponding to a TIS value of 0.82. One sample was found to be too rough to provide reliable RMS values from the scattering distributions, and since this sample was also too rough to acquired 3D profiles with the confocal microscope, it was omitted from the analysis.

### 2.1.5 State of the art

Roughness evaluation is a classic metrology discipline, likely dating back all the way to the first humans when they meticulously shaped blunt rocks into sharp axes<sup>[53]</sup>. They probably performed roughness metrology by feeling a finger over the surface, a method not that far from today's stylus profilers. Modern roughness evaluation methods can generally be classified as either mechanical or optical. The mechanical include methods such as stylus profilers and AFM, while the optical methods include angle resolved scatter (ARS), white light interferometry, and confocal microscopy. Comprehensive overviews of the currently available methods are found in the publications<sup>[54–58]</sup>.

The current workhorse in roughness evaluation is the stylus profiler<sup>[56]</sup>. In general, it works by tracing a sharp needle over the sample surface, and continuously measuring the x and z position to generate a line profile representing the surface topography. A downside is that it only provides a snapshot of the surface in a single position, making it difficult to discover individual scratches or digs. The physical contact between surface and needle is also known sometimes to damage the surface<sup>[56,59,60]</sup>. Stylus profilers are mainly used for roughly polished samples in the metalworking industry, while most research utilizes methods with a higher spatial resolution such as AFM or ARS<sup>[40,61]</sup>.

Comparison of instruments for roughness evaluation is often done by comparing the PSD instead of the actual roughness values, as this reduces the problem of different evaluation bandwidths for the instruments<sup>[61–65]</sup>. However, outside academia, the PSD spectrum is rarely used compared to the ISO defined roughness parameters<sup>[34,40]</sup>. One exception is the optics industry, where the manufacturing of high-grade optical components has induced a need for more precise specifications of the surface finish<sup>[34,66]</sup>. The specifications might then be

quantified as specific scattering properties or as a frequency dependent maximum value for the PSD spectrum<sup>[66]</sup>.

A few studies have compared the RMS roughness values obtained with different instruments, but these studies did either not correct for the different bandwidths<sup>[60,61,67]</sup>, or only analyzed a limited number of samples<sup>[68]</sup>. The issue with varying evaluation bandwidths is a well-known problem, but it is often overlooked<sup>[60,61,69]</sup>.

# Chapter 2.2

## Paper 1, Optical evaluation of nanoscale roughness

---

The main contributions of the paper presented in this chapter are a thorough comparison of roughness measurements using the three instruments presented in Section 2.1.2, and a relation between the two roughness values  $R_q$  and  $A_q$ . For each instrument, the effective measurement bandwidth is determined as the range of spatial surface wavelengths within which the roughness is accurately determined. These bandwidths are used to filter the measurements to only compare roughness values covering the same ranges. Additionally, we determined an empirical relation between the two roughness parameters  $R_q$  and  $A_q$ , which was previously not known to correlate. This relation could prove valuable for the OptoSurf instrument, as it enables an evaluation of the more commonly used  $R_q$  parameter.

### 2.2.1 Presentation of samples

The studied samples are all made of steel, but with different roughness levels achieved by a combination of fabrication methods and polishing process. 16 were fabricated by Lukáš Pilný for his PhD studies at DTU MEK<sup>[25]</sup>, while the last four are roughness standard for calibrating stylus profilers<sup>[70]</sup>.

The samples by Lukáš Pilný are polished by robotic uni-directional polishing, in a custom built setup where a small polishing pad oscillates quickly up and down while the samples moves slowly from side to side. The speeds of the two movements are 100 mm/s and 1 mm/s, respectively. The polishing sequence consisted of one initial pass with a grit size #600 stone pad, followed by multiple passes with a soft pad and diamond paste of 8  $\mu\text{m}$  grain size. For an illustration of the variations in surface quality see Figure 14a. Detailed description of the sample fabrication is available in<sup>[25,71]</sup>. Between measurements, the samples were covered with water displacing oil (CIMGUARD 20, CIMCOOL Fluid Technology, USA) to avoid corrosion. The samples were cleaned before each measurement by rinsing with isopropanol or ethanol and wiping with a non-woven cloth.

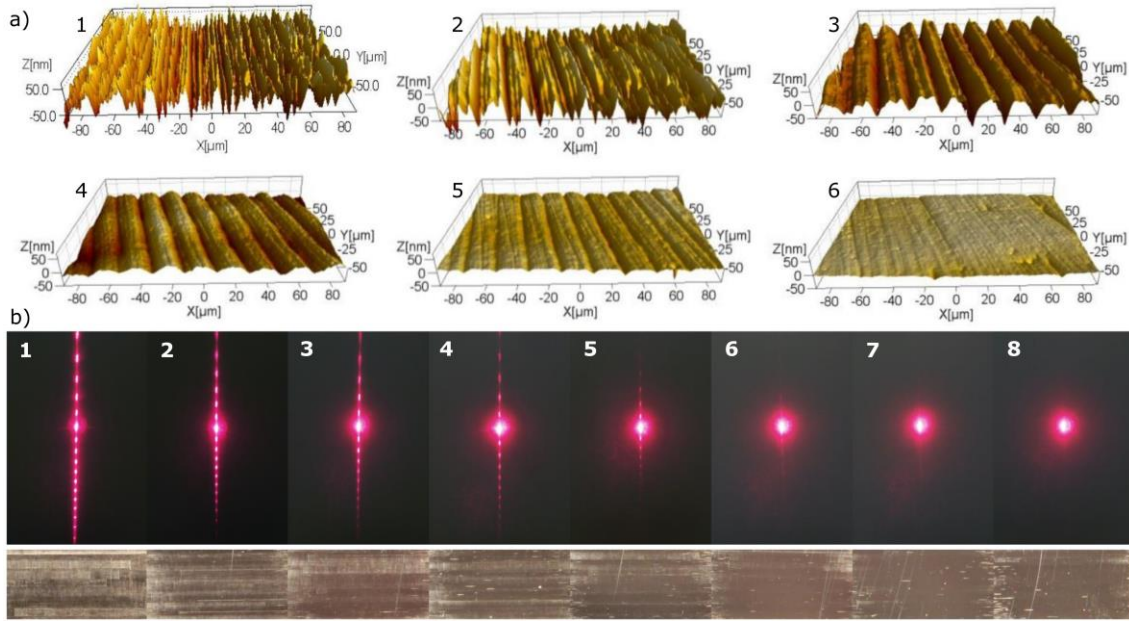


Figure 14: Overview of samples. **a)** 3D images of sample surfaces, adapted from<sup>[71]</sup>. **b)** top: Scattering patterns from samples, bottom: photographs of the surfaces acquired top down with tilted lighting. Numbers refer to the sample ids.

The scattering patterns shown in Figure 14b reveal a distinct diffraction pattern, corresponding to a surface period of 20 μm. This pattern is caused by the polishing motion, where the oscillation frequency of 100 mm/s and lateral motion of 1 mm/s, result in a sawtooth pattern with a periodicity of 20 μm. The parallel lines are also seen from the 3D profiles in Figure 14a, although only one side of the sawtooths are visible, probably due to a difference in the applied force during the forward and backward motion. These can be treated as 1D structures and are typical for directional processes, such as milling, grinding, and uni-directional polishing<sup>[25]</sup>. Together with isotropic surfaces, 1D surfaces are the best ones suited for roughness measurements, since a single line profile includes all roughness information of the surface, and a single line scan can completely describe the hemispherical scattering distribution<sup>[36]</sup>.

Unfortunately, the polishing setup did not provide consistent polishing levels, resulting in an inhomogeneous surface quality, especially for the rough samples. For some samples, resulting in significant variations in roughness levels for misalignments of only a few millimeters, see Figure 15. This increases the deviations when comparing the values from each instrument, as the evaluated areas might be slightly different.

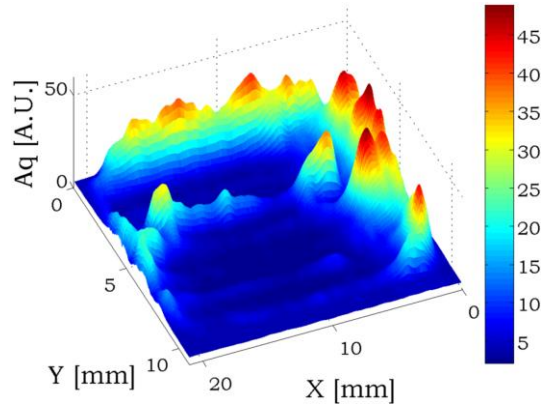


Figure 15: Surface plot illustrating the sample inhomogeneity on a typical sample. The tall peaks along the border of the image are outside the evaluated area, but the Aq value is seen to still vary between  $\sim 5$  and  $\sim 15$  in the center regions. Image from<sup>[71]</sup>.

The four roughness standards encompass three fairly rough standards by The Physikalisch-Technische Bundesanstalt (PTB) and a smoother one from HALLE Präzisions-Kalibriernormale GmbH, all with 1D patterns. Unfortunately, it was not possible to compare the calibrated and measured values, as they are only calibrated by the Ra value, which the scatterometers cannot evaluate, and the calibration cut-off filter ( $\lambda_c$ ) of 0.8 mm is too large for the measurement range of the confocal microscope.

### 2.2.2 Paper reprint

Published as Article in *Measurement Science and Technology* (IOP) in July 2015.

The article has currently received 6 citations (according to Scopus), and has been downloaded 4455 times (according to the journal webpage).

Citation:

**N. A. Feidenhans'l**, P.-E. Hansen, L. Pilný, M. H. Madsen, G. Bissacco, J. C. Petersen, and R. Taboryski, Comparison of optical methods for surface roughness characterization, *Measurement Science and Technology*, vol. 26, no. 8, p. 085208, 2015.

The published version is available online at: <http://dx.doi.org/10.1088/0957-0233/26/8/085208>

#### Title

Comparison of optical methods for surface roughness characterization

#### Abstract

We report a study of the correlation between three optical methods for characterizing surface roughness: a laboratory scatterometer measuring the Bi-directional Reflection Distribution Function (BRDF instrument), a simple commercial scatterometer (rBRDF instrument), and a confocal optical profiler. For each instrument, the effective range of spatial surface wavelengths is determined, and the common bandwidth used when comparing the evaluated roughness parameters. The compared roughness parameters are: the root-mean-square (RMS) profile deviation (Rq), the RMS profile slope (Rdq), and the variance of the scattering angle distribution (Aq). The twenty-two investigated samples were manufactured with several methods in order to obtain a suitable diversity of roughness patterns.

Our study shows a one-to-one correlation of both the Rq and the Rdq roughness values when obtained with the BRDF and the confocal instruments, if the common bandwidth is applied. Likewise, a correlation is observed when determining the Aq value with the BRDF and the rBRDF instruments.

Furthermore, we show that it is possible to determine the Rq value from the Aq value, by applying a simple transfer function derived from the instrument comparisons. The presented method is validated for surfaces with predominantly one-dimensional roughness, i.e. consisting of parallel grooves of various periods, and a reflectance similar to stainless steel. The Rq values are predicted with an accuracy of  $\pm 15$  nm at the 95% confidence interval.

#### Keywords

Angle-resolved scattering (ARS), scatterometry, surface roughness, Bi-directional Reflection Distribution Function (BRDF), optical profilometry, confocal microscopy

### Introduction

Accurate characterization of nanoscale surface roughness is important in many applications, and a number of techniques exist for this purpose<sup>[59,61]</sup>. The various characterization techniques, however, are often optimal for different applications or stages of a process<sup>[59]</sup>, hereby requiring that the measured values are comparable between the instruments. However, comparison of values obtained with different instruments is not a simple task, as the design of each instrument imposes different limitations to the measurement bandwidth<sup>[40,59]</sup>. This is an often overlooked

effect when comparing roughness values<sup>[36,61]</sup>. Hence, to perform a reliable comparison of values obtained with different instruments, a study of the accuracy and limits of each method is required.

Two methods often used for roughness measurements are stylus profilers and atomic force microscopy (AFM)<sup>[40,59–61]</sup>. Both are mechanical methods, where a sharp tip is traced along the surface and the surface profile assessed from its movement. AFMs generally have only weak interaction forces with the surface, while stylus profilers are known to damage the surface due to excessive forces, resulting in incorrect values and abrasion of the sample, which might not be realized<sup>[59,60]</sup>. Compared to mechanical methods, non-contact optical methods are advantageous due to their non-abrasive nature, and the feasibility of some methods to scan large areas in short time. The non-abrasive feature is particularly relevant for very smooth surfaces with roughness in the nanometer range.

In this study, three optical surface characterization methods are analyzed and compared. The comparison is performed in terms of the ISO standardized<sup>[38]</sup> roughness parameters  $R_q$  and  $R_{dq}$ , and the industry standard<sup>[72]</sup>  $A_q$ . The three characterized instruments are: 1) A laboratory scatterometer which measures the angular distribution of light scattered from a surface, quantified by the Bi-directional Reflection Distribution Function (BRDF). It evaluates all three roughness parameters. This instrument will be referred to as the “BRDF instrument”. 2) A commercial scatterometer also measuring the light scattering but in a restricted angular range and with lower resolution. By default it only determines the  $A_q$  parameter. It will be referred to as the “rBRDF instrument” (restricted-BRDF). 3) A commercial optical profiler which uses a confocal technique to acquire a three-dimensional (3D) map of the surface. It evaluates the  $R_q$  and  $R_{dq}$  parameters. BRDF and confocal instruments are well-known for roughness characterization<sup>[61,73–75]</sup>, while the rBRDF instrument is less known, but well described<sup>[72,76–79]</sup>.

Generally, all characterization methods perform an intrinsic filtering, which define the bandwidth of spatial surface wavelengths from which the measured values are evaluated<sup>[36,59]</sup>. For mechanical methods the bandwidth filtering is generally due to the tip radius and scan area<sup>[36,59]</sup>, while for optical methods it is mainly due to angular constraints in the detection system<sup>[36,61]</sup>. This study will determine the filtering bandwidths for each of the three methods, and ensure that values are only compared within common bandwidths. Without establishing the limiting bandwidth for each method, it is inappropriate to compare the measured values, since one method may describe the roughness on a different length scale than the others<sup>[36]</sup>.

Previous studies have mainly compared BRDF instruments with other methods using the power spectral density (PSD) curves rather than the roughness values<sup>[62–65]</sup>, while other studies used smoother samples<sup>[60,61]</sup>. One study compared  $R_q$  roughness obtained from BRDF and AFM<sup>[80]</sup>, but here only three samples were used and the bandwidth limitations not considered. Another study correlated the RMS roughness with the variance of the scattering distribution<sup>[81]</sup>, but the analyzed samples were all made from the same manufacturing process.

In this study, the three instruments are compared pairwise; as they do not all determine a common parameter. The BRDF and confocal instruments are compared by the  $R_q$  and  $R_{dq}$  parameters, while the BRDF and rBRDF instruments are compared by the  $A_q$  parameter. We find one-to-one correlations between the three instruments.

Additionally, we present a relation between the  $A_q$  and  $R_q$  values, which enables the simple rBRDF instrument to predict the ISO standardized roughness parameter  $R_q$ , instead of only the less known industry standard  $A_q$ . This is advantageous because the rBRDF instrument is better

suited than the two other instrument for applications where in-situ measurements are required, e.g. during a polishing process. The advantages of the rBRDF instrument includes: ease of use, faster and cheaper operation, and a more robust setup.

## Experimental methods

### Samples

A total of 22 samples were collected for the study. The samples include 4 steel roughness standards with roughness values certified by the Physikalisch-Technische Bundesanstalt (PTB), 16 samples made from one steel grade but polished to different smoothness levels, and 2 samples made with another steel grade and fabrication method. For characterizing the instruments, a silicon wafer (TP436 Si-100, Topsil Semiconductor Materials A/S, Denmark) was used. The specific manufacturing process of the 16 steel samples is described by Pilný et al.<sup>[71]</sup>

The samples are all one-dimensional surfaces, consisting of parallel grooves in a wide range of spatial frequencies. Such surfaces have all the roughness features along one dimension, resulting in a simple scattering pattern where all light is diffracted into one plane<sup>[36]</sup>.

The rougher samples have a quite inhomogeneous surface quality, resulting in a significant variation of roughness values on the surface. Even though care was taken to measure in the same position with all three instruments, this inhomogeneity will inevitably increase the uncertainty when comparing the roughness values.

### Roughness parameters

A wide range of roughness parameters can be used to describe a given surface<sup>[40]</sup>. The most common parameters are calculated from line profiles according to the ISO 4287 standard<sup>[38]</sup>, but due to an increased use of 3D profilers a set of complimentary area roughness parameters have been defined in the ISO 25178-2 standard<sup>[39]</sup>. In this study, the line parameters are used as these are more appropriate for the 1D surfaces analyzed.

The specific parameters used are: Rq, Rdq and Aq. The “R” parameters are defined in the ISO 4287 standard<sup>[38]</sup>, while the “Aq” parameter is defined in the VDA2009 directive<sup>[72]</sup>. The characteristics associated with each parameter are:

- Rq: the root mean square deviation (RMS) of the profile.
- Rdq: the root mean square of the local slope of profile.
- Aq: the variance of the scattered light distribution from a surface.

The formulas for the Rq and Rdq parameters are:

$$Rq = \sqrt{\frac{1}{n} \sum_{i=1}^n Z_i^2} \quad , \quad Rdq = \sqrt{\frac{1}{n} \sum_{i=1}^n \left( \frac{dZ_i}{dx} \right)^2} \quad , \quad (12)$$

where  $Z_i$  is the amplitude of point  $i$ ,  $n$  is the number of sample points, and  $dZ_i/dx$  is the local slope<sup>[38]</sup>. ISO 4287 further defines that the parameters must be calculated with suitable low-pass ( $\lambda_s$ ) and a high-pass ( $\lambda_c$ ) Gaussian filters, defined in spatial wavelengths. The low-pass filter removes noise from the profile, while the high-pass filter divides the profile into a long-ranged waviness pattern, assumed to be the form of the sample, and the actual roughness profile which is used to calculate Rq and Rdq.

The Aq parameter is defined in an industry directive by the German Association of the Automotive Industry (VDA), an association which includes most of the German car manufacturers and suppliers. This parameter is different from the R parameters, as it does not describe the surface profile but instead how the surface scatters light. It is defined as the variance of the distribution of scattered light<sup>[72]</sup>:

$$Aq = k \sum (\varphi' - M)^2 \cdot H(\varphi') , \quad (13)$$

where  $H(\varphi')$  is the normalized light distribution,  $M$  the center of mass for the distributions,  $k$  a scaling factor to ensure a maximum Aq value of 100, and  $\varphi' = \tan(\varphi)$  where  $\varphi$  is the scattering angle. However, as presented in a later section, a slight modification of Equation (13) is applied, where  $\varphi$  is used instead of  $\varphi'$ .

A low Aq value is a measure of low surface roughness, since smooth samples reflect a narrow beam, while rough samples scatter the light into larger angles.

### BRDF instrument

A scatterometer is used to measure the scattering spectrum from the samples, and from this calculate the Bi-directional Reflection Distribution Function (BRDF). The BRDF is a common way of describing the pattern of light scattered from a surface<sup>[82]</sup>. It is similar to the angle-resolved scatter (ARS), only difference being the cosine factor<sup>[36]</sup>. The BRDF is given as the ratio between the scattered surface radiance and the incident surface irradiance, corresponding to:

$$BRDF = \frac{P_s / \Omega_s}{P_i \cos(\theta_s)} , \quad (14)$$

where  $P_s$  is the scattering power in the scattering angle ( $\theta_s$ ),  $\Omega_s$  the detector solid angle,  $P_i$  the incident beam power, and  $\cos(\theta_s)$  a correction factor.

The BRDF instrument is illustrated in Figure 16. It consists of a 662 nm diode laser (LBX-660-100-CIR-PP, Oxixus, France), which is linearly polarized, shaped with an iris, and focused onto the detector plane with a 500 mm focal length lens (LA4184, Thorlabs Inc., USA). The incident polarization is  $s$  oriented, with the depolarization in the lens assumed negligible. The scattering intensity ( $P_s$ ) is detected with a photodetector (New Focus Model 2032, Newport, USA) and a lock-in amplifier (SR530, Stanford Research Systems, USA) locked to a chopper (SR540, Stanford Research Systems, USA). A rotary stage (NR360S/M, Thorlabs Inc., USA) scans the detector along the in-plane scattering direction, with steps between  $0.01^\circ$  and  $0.16^\circ$ . The detector is positioned 350 mm from the sample surface and shielded with a slit of  $215.5 \mu\text{m} \times 3.04 \text{ mm}$ , resulting in a detector solid angle of  $\Omega_s = 5.343 \mu\text{sr}$ . The laser intensity is monitored using a beam splitter and a photodetector (New Focus Model 2032, Newport, USA), while a step neutral density (ND) filter (NDL-10S-4, Thorlabs Inc., USA) decreases the beam intensity if needed. The resulting dynamic range is approximately 8 orders of magnitude, with a noise floor around  $10^{-4} \text{ sr}^{-1}$ . The measured intensities are scaled relative to the laser intensity and corrected for the ND filters used. The incident intensity ( $P_i$ ) is determined by a straight through scan without a sample. One scan, with an angle of incidence (AOI) of  $10^\circ$ , was acquired for each sample and the data analyzed in Matlab (Matlab R2014b, MathWorks, USA).

The dominant sources of uncertainty in the BRDF measurement are the ND filter transmissions, the angular accuracy of the detector, and the linearity of the detector and amplifier system.

The standard uncertainty (SU) on the intensity,  $P_s$ , were estimated to 5.7 %, 3.9 %, 1.0 %, for the three factors respectively. From error propagation<sup>[83]</sup>, this results in a combined SU of 6.1 %. This uncertainty was applied to all  $P_s$  and  $P_i$  values, and the resulting variation in Rq and Aq value assigned as the SU on these values.

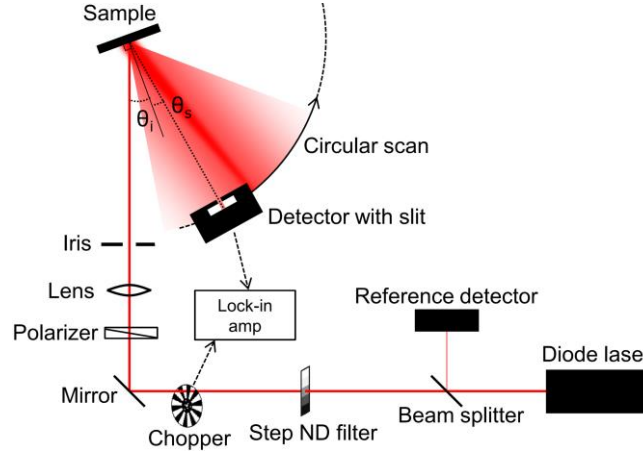


Figure 16: Diagram of BRDF instrument, see description in text.

#### Bandwidth limits

The BRDF instrument is bandlimited by six factors: the angular range of the scan, the laser wavelength, the beam size on the sample, the slit width, the angular resolution, and the beam width in the detector plane. The limits are mainly imposed by the diffraction angle of surface features with specific spatial wavelengths, governed by the diffraction equation<sup>[84]</sup>:

$$\sin\theta_s - \sin\theta_i = \lambda f, \quad (15)$$

where  $\theta_s$  is the scattering angle,  $\theta_i$  the incident angle,  $\lambda$  the incident wavelength, and  $f$  the spatial frequency of the scattering structures.

In the following, each limiting factor is presented and the final bandwidth of the BRDF instrument determined. A comparison of the limits for all three instruments is seen in Figure 18.

1: The angular scan range is a high frequency limit (low-pass filter), since high frequent structures scatter into large angles. The scan range limit is when the detector reaches the sample plane, which for an AOI of  $10^\circ$  is  $80^\circ$  from the specular angle. The corresponding frequency is found from Equation (4) to  $f_{\max, \text{range}} = (\sin(10^\circ + 80^\circ) - \sin(10^\circ)) / 662\text{nm} = 1.25 \mu\text{m}^{-1}$ . This limit could be increased by using a larger AOI and then measure the backwards reflected side of the spectrum, but a small AOI is preferred to ease comparison with the rBRDF instrument.

2: The laser wavelength is also a high frequency limit. It is based on the property of the diffraction equation, that spatial frequencies longer than  $1/\lambda_{\text{laser}}$  cannot scatter<sup>[85]</sup> because the angles would be above  $90^\circ$ . This results in  $f_{\max, \text{wave}} = 1/662\text{nm} = 1.51 \mu\text{m}^{-1}$ .

3: The beam size on the sample is a low frequency limit (high-pass filter), since spatial wavelengths longer than the spot diameter do not diffract. Actually, several periods within the spot are needed to provide a sufficiently intense diffraction pattern<sup>[86]</sup>. The beam width is determined to  $600 \mu\text{m}$  at the  $1/e^2$  intensity point, using a beam profiler (SP620U, Ophir Optonics, USA) placed at the sample position. Requiring five periods within this length results in  $f_{\min, \text{sample}} = 1/(600\mu\text{m}/5) = 0.0083 \mu\text{m}^{-1}$ .

4+5: The slit width and angular resolution both constitute low frequency limits, because scattering features below these limits are indistinguishable in the spectrum. In angular terms the limits are  $0.035^\circ$  and  $0.01^\circ$ , which from Equation (15) corresponds to the frequencies  $f_{\min, \text{slit}} = (\sin(10^\circ + 0.035^\circ) - \sin(10^\circ))/662\text{nm} = 0.00092 \mu\text{m}^{-1}$  and  $f_{\min, \text{resolution}} = (\sin(10^\circ + 0.01^\circ) - \sin(10^\circ))/662\text{nm} = 0.00026 \mu\text{m}^{-1}$ , respectively.

6: The beam width in the detector plane is also a low frequency limit, as scattering from long spatial wavelengths are buried in the intense specular peak. Based on a straight-through scan of the beam, the  $1/e^2$  width was found to:  $\theta_{\text{beam}} = 0.111^\circ$ , which by Equation (15) corresponds to  $f_{\min, \text{beam}} = (\sin(10^\circ + 0.111^\circ) - \sin(10^\circ))/662\text{nm} = 0.0029 \mu\text{m}^{-1}$ . However, during the further analysis this beam width was found too small, as the incident beam still held a significant intensity outside this range, which influenced the roughness calculations. Instead, the effective beam width was determined by comparing the straight-through beam with its reflection from a mirror (10Z20AL.2, Newport Corporation, USA), and estimating the angle where the two curves started to deviate. This width was found to  $f_{\min, \text{beam effective}} = 0.04 \mu\text{m}^{-1}$ , corresponding to  $\theta = 1.54^\circ$ . This limit was applied to all BRDF spectra, but it should be seen as a worst-case scenario mainly relevant for very smooth samples.

The resulting frequency bandwidth of the BRDF instrument is  $0.04 \mu\text{m}^{-1} - 1.25 \mu\text{m}^{-1}$ .

#### *Calculation of roughness parameters*

The root-mean-square roughness (Rq) and root-mean-square slope (Rdq) are calculated from the BRDF spectrum using the Rayleigh-Rice (RR) theory<sup>[36,87]</sup>. Other possibilities include the Generalized Harvey-Shack (GHS) theory<sup>[50]</sup> and the Beckmann-Kirchhoff theory<sup>[44]</sup>, but the RR theory is used because it is the most well-known and widely accepted scattering theory<sup>[36,50,88]</sup>. The analyzed samples have Rq values in the range 2 nm – 49 nm, which exceeds the traditional limit for the RR theory of the surface being “optically smooth”, defined as<sup>[84]</sup>:

$$\left( \frac{4\pi \cos(\theta_i) \sigma}{\lambda} \right)^2 \ll 1, \quad (16)$$

where  $\sigma$  is the total RMS roughness with no bandwidth limits,  $\theta_i$  the angle of incidence, and  $\lambda$  the wavelength of the incident light. However, Equation (16) is simply a Taylor expansion of the original equation<sup>[43,89]</sup>, and it is this approximation which introduces the assumption of  $Rq/\lambda \ll 1$ . Hence the surface roughness is not limited by Equation (16), as also found by other studies<sup>[43,90]</sup>

Because all samples are 1D surfaces with purely in-plane scattering, the PSD curves are evaluated from the BRDF as 1D PSD curves, as described by Stover<sup>[91]</sup>. From these, the Rq and Rdq values are determined by integration, with integration limits defined by the frequency bandwidth. For the refractive index of the steel samples, a tabular value of  $\tilde{n}_{\text{steel}} = 2.55 + 4.32i$  is used<sup>[92]</sup>. The value might be slightly different for our samples, but small changes in the refractive index were found to be negligible for calculating the Rq value. For the silicon sample a value of  $\tilde{n}_{\text{Si}} = 3.82 + 0.015i$  is used<sup>[93]</sup>.

The Aq value is determined from the scattering spectrum, as defined in the VDA directive<sup>[72]</sup>. However, for an AOI of  $10^\circ$  the BRDF instrument is limited to measure the one-sided scattering spectrum, hence the scattering spectrum is mirrored along the specular direction, to provide the full two-sided peak needed for the Aq calculation. When calculating the restricted angle Aq value, the scattering spectrum is cropped to the desired angular range.

### rBRDF instrument

The commercial scatterometer is an OptoSurf OS 500-32 (OptoSurf GmbH, Germany), referred to as the “rBRDF instrument” due to the restricted acceptance angle. It measures the same scattering spectra as the BRDF instrument, but it has a simpler design optimized to provide quality control in industrial manufacturing<sup>[35]</sup>.

The rBRDF instrument has previously been described by others<sup>[72,76–79]</sup>, and is comprised of a photodiode generating  $\sim 670$  nm light, a lens which focuses the light into a  $\sim 0.9$  mm spot on the sample and also collects the reflected light, and lastly a linear photodiode array for detecting the scattering spectrum, see illustration in Figure 17. It has an AOI of  $\sim 4^\circ$  perpendicular to the diode array, while the sample tilt is adjusted to ensure an AOI of  $0^\circ$  along the measuring direction. The major differences to the BRDF instrument are: a restricted acceptance angle of only  $\pm 16^\circ$  (corresponding to  $NA = 0.28$ ), a spectral resolution of  $1^\circ$  due to the angular size of the photodiodes, a dynamic range of around 3 orders of magnitude, the focus point on the sample instead of the detector.

These differences result in a lower resolution of the scattering spectra, and no information on the wide angle scattering from features with wavelengths below a few micrometers. The advantages on the other hand, are a more compact instrument and much faster measurements, in the range of milliseconds. Due to the high measurement speed, it is possible to measure the Aq value of many locations on a surface to generate a 2D map of the surface roughness<sup>[71]</sup>.

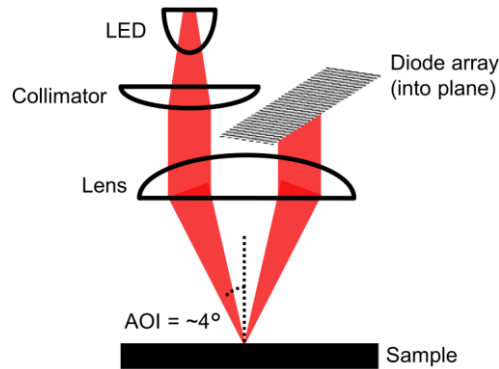


Figure 17: Approximate diagram of the rBRDF instrument, based on published device illustrations<sup>[72,76–79]</sup> and own analysis.

The standard measurement output is: the Aq value, the total light intensity detected, and the scattering distributions center of mass. In this study, however, the raw intensity data from the diode array was extracted, and the Aq value calculated using a custom Matlab script. For each sample, between five and ten measurements were performed close to the beam position in the BRDF measurement, the number depending on the homogeneity of the surface quality. From these measurements the average Aq value was determined, and the uncertainty estimated as the standard error of the mean (SEM).

During the analysis, a small correction was made to the Aq formula in Equation (13). Based on the raw rBRDF spectra, Aq values were calculated in Matlab as described in the VDA directive and compared to the Aq value provided by the OptoSurf control software. This revealed a consistently smaller Aq value than provided by the OptoSurf software, though the deviations did not exceeded 5 %. The deviation was reduced to below 0.4 %, by replacing the VDA defined  $x$  value of  $\tan(\varphi)$  with the angle  $\varphi$  directly. When calculating Aq values in the further analysis, the slightly modified formula using  $\varphi$  as  $x$  values is used.

### *Bandwidth limits*

The limiting factors in the rBRDF instrument are a high frequency limit imposed by the acceptance angle, and three low frequency limits imposed by the resolution of the diode array, the beam width on the detector, and the beam spot size on the sample.

The high frequency limit is determined by the  $\pm 16^\circ$  acceptance angle, which by Equation (15) corresponds to  $f_{\max, \text{angle}} = (\sin(16^\circ) - \sin(0^\circ))/670\text{nm} = 0.411 \mu\text{m}^{-1}$ . The low frequency limits are similarly found to:  $f_{\min, \text{res}} = (\sin(1^\circ) - \sin(0^\circ))/670\text{nm} = 0.0260 \mu\text{m}^{-1}$ ,  $f_{\min, \text{beam}} = (\sin(4^\circ) - \sin(0^\circ))/670\text{nm} = 0.104 \mu\text{m}^{-1}$ ,  $f_{\min, \text{sample}} = 1/(900\mu\text{m}/5) = 0.0056 \mu\text{m}^{-1}$ , for the resolution, the beam width on the detector and on the sample, respectively.

Since calculation of the Aq value requires the specular component, the spectra are not cropped with the low frequency limits.

### **Optical profiler**

The optical profiler is a 3D confocal interference microscope (Sensofar PLu Neox, Sensofar Tech, Spain) equipped with a 50x (NA 0.80) objective. It is capable of both confocal and white light interferometry, but only the confocal technique with 460 nm light is used in this study. The measurement output is a high resolution 3D profile of the surface, with a field of view of  $254.6 \mu\text{m} \times 190.9 \mu\text{m}$  and an image size of  $768 \text{ pixels} \times 576 \text{ pixels}$ <sup>[37]</sup>. All samples are aligned with the line structures perpendicular to the long image axis.

### *Bandwidth limits*

The confocal microscope is, like all profiling tools, restricted by the pixel resolution and the size of the scanned area<sup>[94]</sup>. The pixel resolution provides a high frequency limit, while the scan area limits the low frequencies. The scan area limit is determined by requiring two periods within the image  $f_{\min, \text{area}} = 1/(L_{\text{scan range}}/2) = 1/(254.6\mu\text{m}/2) = 0.0079 \mu\text{m}^{-1}$ . By applying the Nyquist sampling theorem of two samples per period, the pixel resolution limit is found to  $f_{\max, \text{Nyq}} = n_{\text{pixels}}/(2L_{\text{scan range}}) = 768/(2 \times 254.6\mu\text{m}) = 1.51 \mu\text{m}^{-1}$ . The microscope is also limited by the acceptance angle of the objective, as high frequency features scatter outside the objective. The numerical aperture (NA) describe the largest collection and incident angles of the objective, corresponding to a frequency limit found from Equation (15)  $f_{\max, \text{NA}} = (\text{NA} + \text{NA})/\lambda = (2 \times 0.8)/460\text{nm} = 3.48 \mu\text{m}^{-1}$ . In addition, the microscope might include apertures or other restrictions to the light path, which would lower the actual frequency limit.

However, the Nyquist frequency is the limiting frequency at which the spatial period information is just preserved, whereas the limit at which also the waveform is sufficiently preserved is somewhat higher. Hence the effective spatial frequency limit is lower than the Nyquist frequency, and was determined experimentally. PSD curves calculated from the confocal 3D profiles were compared with the BRDF scan and an AFM image (Park NX20, Park Systems, South Korea). At a frequency of approximately  $0.4 \mu\text{m}^{-1}$  and onwards, the confocal microscope was found to deviate significantly from the other PSDs, hence this is the effective frequency limit after which the waveform is not sufficiently preserved. An effective frequency limit of  $f_{\max, \text{eff}} = 0.4 \mu\text{m}^{-1}$  equals a spatial wavelength of  $2.5 \mu\text{m}$  with 7.6 pixels per period, which corresponds well with previous studies that found that around six to ten sample points (pixels) per period are needed to accurately determine the roughness values<sup>[60,95]</sup>.

The resulting bandwidth of the confocal microscope is  $0.0079 \mu\text{m}^{-1} - 0.4 \mu\text{m}^{-1}$ .

### Calculation of roughness parameters

Based on the 3D surface profiles the  $R_q$  and  $R_{dq}$  values are calculated as defined in ISO 4287, using the image processing software SPIP (SPIP ver. 6.3.2, Image Metrology, Denmark). The bandwidth limit is applied using the  $\lambda_s$  and  $\lambda_c$  filters, where  $\lambda = 1/f$ .

Confocal images were acquired from five positions on each sample. The positions were chosen close to the beam position during the BRDF measurement to decrease the effect of the inhomogeneous surface quality. The measurement uncertainty was estimated as the standard error of the mean (SEM).

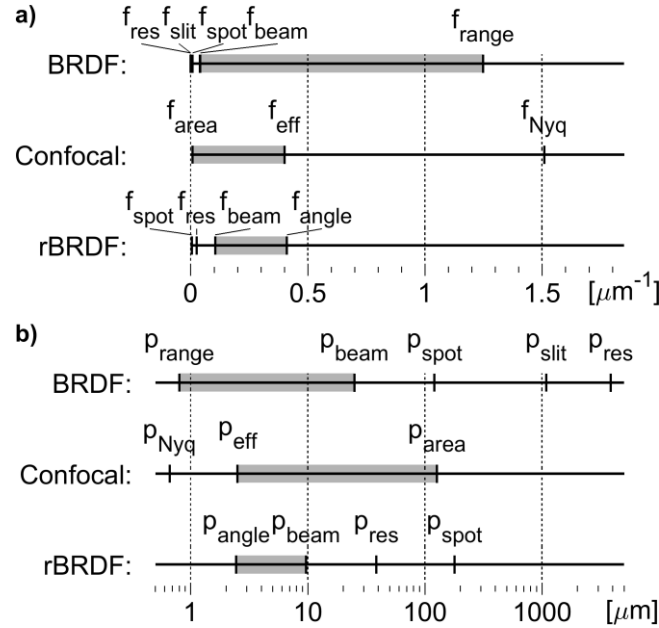


Figure 18: Comparison of the frequency limits of the three instruments, **a)** in spatial frequency unit, and **b)** in spatial wavelengths. The gray rectangles show the resulting bandwidth for each instrument. Note the log scale in b).

## Results and discussion

### BRDF and confocal comparison

The BRDF and confocal instruments are compared in terms of the  $R_q$  and  $R_{dq}$  parameters, evaluated in the bandwidth ( $f_{\text{min}} - f_{\text{max}}$ ):  $0.04 \mu\text{m}^{-1} - 0.4 \mu\text{m}^{-1}$ , corresponding to  $\lambda_s = 2.5 \mu\text{m}$  and  $\lambda_c = 25 \mu\text{m}$ . As seen in Figure 19, both the  $R_q$  and  $R_{dq}$  values show a one-to-one correlation between the two instruments. The large uncertainties on the confocal values are due to the inhomogeneous surface quality of the samples, resulting in noticeable deviations between the five measurement positions. The uncertainties on the BRDF values are more constant, as these are only measured in one position, and instead based on an estimation of the uncertainty of the intensity measurements.

To stress the importance of applying the correct filters,  $R_q$  values obtained using some improper filters are also shown in Figure 19, and the correlation is seen to be significantly reduced. These filters are determined as the FWHM diameter of the beam and the full scan range,  $0.0015 \mu\text{m}^{-1} - 1.25 \mu\text{m}^{-1}$ , while the confocal images are filtered to the minimum and maximum values allowed by ISO 4287,  $\lambda_s = 0.8 \mu\text{m}$  and  $\lambda_c = 80 \mu\text{m}$ .

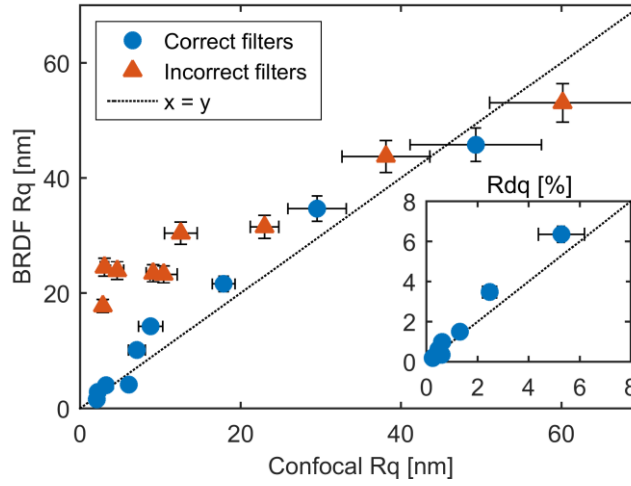


Figure 19: Comparison of Rq obtained from the BRDF and confocal instruments, with the corresponding Rdq comparison shown in the insert. One-to-one correlations between the instruments are seen, but only with correct filtering. For this comparison, a subset of only 9 samples was used. Error bars represent  $\pm 1$  SEM on the x values, and  $\pm 1$  standard uncertainty (SU) on the y values.

The good correlation reveal that the RR theory continues to provides correct roughness values for all samples in the study, hence this study supports the conclusions of Harvey et al.<sup>[43]</sup> and Stover et al.<sup>[90]</sup>, that the smoothness requirement is not limited by Equation (16).

#### BRDF and rBRDF comparison

The BRDF and rBRDF instruments are compared by the Aq parameter with the common frequency range defined by the restricted opening angle of  $\pm 16^\circ$ , corresponding to  $f_{\max} = 0.4 \mu\text{m}^{-1}$  and no minimum frequency. It is found that the frequency filter alone is not enough to ensure comparable values between the two instruments. Before calculating the Aq value, a smoothing function is required for the BRDF spectrum, to simulate the effects on the scattering spectra imposed by the different designs of the two instruments. The crucial differences in this context are the focus point and beam divergence of the incident light. In the BRDF instrument, the incident light is a laser beam focused into a small spot on the detector, where a slit limits the detector width to only  $0.035^\circ$  ( $215.5 \mu\text{m}$ ), hereby resulting in a very high resolution of the scattering spectrum. The rBRDF instrument on the other hand, uses an LED source which is focused onto the sample, thereby resulting in a significant beam divergence on the detector. Furthermore, the size of each diode in the detector array is around  $1^\circ$ . Consequently, for comparing the two instruments, the high resolution BRDF spectrum is smoothened and binned into  $1^\circ$  intervals.

The smoothing function is a sum of three Gaussians, as suggested by Karamehmedović et al.<sup>[96]</sup>, determined by a fit to the distribution of light reflected from a silicon wafer, which provides the narrowest peak measurable by the rBRDF instrument. The function has the form:

$$f(x) = \sum_{i=1}^3 A_i \exp\left(-\frac{(x - \mu_i)^2}{(2\sigma_i)^2}\right), \quad (17)$$

with the parameters:  $A_{1-3} = (0.295; 0.0562; 0.000621)$ ,  $\mu_{1-3} = (0.198; 0.0200; 0.102)$ ,  $\sigma_{1-3} = (1.41; 1.53; 5.55)$ . The filter is applied by convoluting the function with the raw scatter data, binning the spectrum into  $1^\circ$  intervals, and cropping it to a range of  $\pm 16^\circ$  from specular.

As seen in Figure 20, the raw spectra from the BRDF and rBRDF instruments are quite different, but by applying the Gaussian function to the BRDF data the two spectra become comparable. The change in Aq value for the spectrum shown in Figure 20 is from 10.7 to 15.3, between the raw and filtered spectrum, respectively.

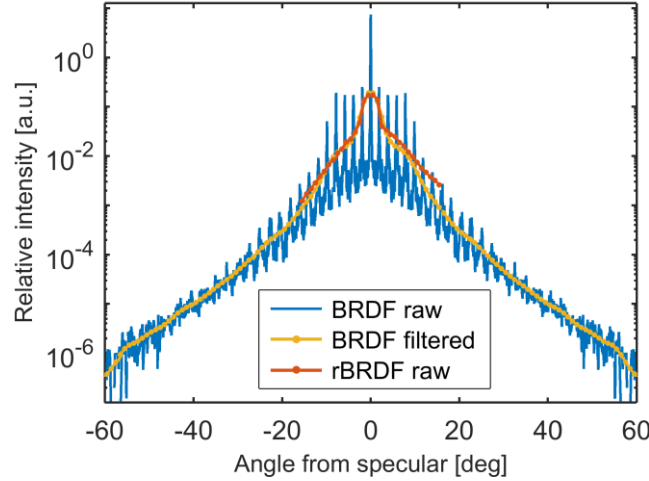


Figure 20: Scattering spectra obtained by BRDF and rBRDF instruments. The distinct spikes on the raw BRDF spectrum are caused by a periodic surface feature of  $20\text{ }\mu\text{m}$ , resulting from the polishing process. The spectra are scaled relative to the area under each curve, and the BRDF spectra shown before cropping.

A comparison of the Aq values obtained from the BRDF and rBRDF instruments is seen in Figure 21. The filtered values (triangular dots) show a good correlation between the two instruments, with only a single outlier at (62, 78), probably resulting from the inhomogeneous surface quality. If the Gaussian filter is not applied (round dots), the Aq values are consistently underestimated.

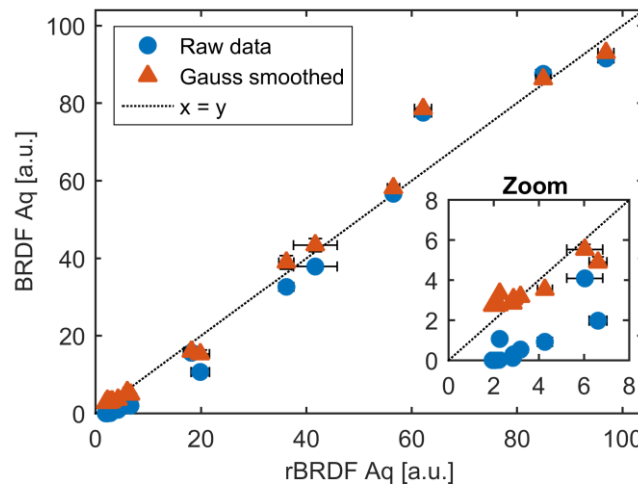


Figure 21: Comparison of Aq values obtained from the BRDF and rBRDF instruments. A strong correlation between the values is seen, but only after applying the Gaussian smoothing and the frequency filter of  $f_{\text{max}} = 0.4\text{ }\mu\text{m}^{-1}$ . Error bars represent  $\pm 1$  SEM on the x values, and  $\pm 1$  SU on the y values.

### Aq and Rq relation

With the strong correlation between the three instruments, we now turn to explore the capabilities of the simplest device: the rBRDF instrument.

The main limitations of this device are that it only evaluates the Aq parameter, and only for an angular range of  $\pm 16^\circ$ , which essentially removes all information of spatial wavelengths below  $2.5 \mu\text{m}$ . In the following, we present a method to predict the Rq value for a wider frequency range, using the rBRDF Aq value and a calibration of the incident light intensity. The first step is to extrapolate the full range Aq value from the restricted one, followed by a conversion to the full range Rq value. In this context, the “full range” refers to the full frequency bandwidth of the BRDF instrument of  $0.04 \mu\text{m}^{-1} - 1.25 \mu\text{m}^{-1}$ , while the “restricted range” is the  $\pm 16^\circ$  acceptance angle of the rBRDF instrument.

Figure 22a shows a comparison of the three Aq values: the rBRDF Aq values ( $Aq_{\text{rBRDF}}$ ), the BRDF restricted Aq values ( $Aq_{16\text{deg}}$ ), and the BRDF full range Aq values ( $Aq_{80\text{deg}}$ ). It is seen that while the  $Aq_{16\text{deg}}$  values corresponds linearly to the  $Aq_{\text{rBRDF}}$  values, as also shown in Figure 21, the  $Aq_{80\text{deg}}$  values diverge significantly from this trend. The rapid increase in  $Aq_{80\text{deg}}$  is caused by the rough samples scattering increasing amounts of light outside the  $\pm 16^\circ$  range, while the smooth samples with low  $Aq_{\text{rBRDF}}$  values scatter all light into the restricted angular range. The  $Aq_{80\text{deg}}$  values can exceed the normal limit of 100, because the  $k$  factor is kept constant while evaluating the wide angular range.

By calibrating the incident intensity of the rBRDF instrument, the intensity loss for each sample is determined from the detected intensity, and the loss compared to the difference in Aq value ( $Aq_{80\text{deg}} - Aq_{16\text{deg}}$ ), see Figure 22b. These two values are expected to correlate, as they both describe the scattering intensity outside the  $\pm 16^\circ$  interval. The incident intensity is calibrated from the reflected intensity of a silicon wafer, which is converted to incident intensity from the refractive index<sup>[93]</sup> and the Fresnel reflectance.

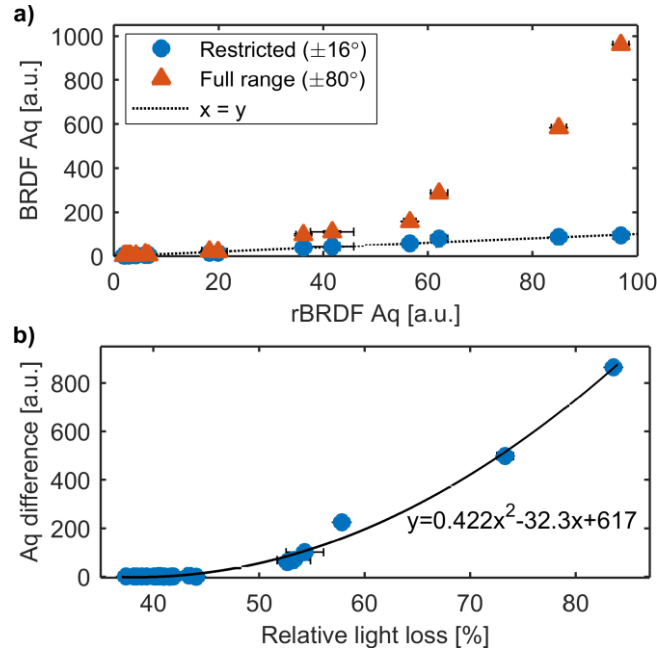


Figure 22: **a)** Relation between the  $Aq_{\text{rBRDF}}$ ,  $Aq_{16\text{deg}}$ , and  $Aq_{80\text{deg}}$  values. **b)** Comparison of the difference in Aq value ( $Aq_{80\text{deg}} - Aq_{16\text{deg}}$ ) with the relative intensity of light lost outside the restricted range. The lowest loss is not zero because the reflectance of the steel is only  $\sim 67\%$ . Error bars represent  $\pm 1$  SEM on the x values, and  $\pm 1$  SU on the y values.

Figure 22b reveals a strong correlation between the two values, fitted with a second order polynomial using least squares. This correlation enables an extrapolation from  $Aq_{rBRDF}$  to  $Aq_{80deg}$ , but it should only be applied to rough samples with significant scatter outside the  $\pm 16^\circ$  range, defined as  $Aq_{rBRDF} > 10$ . Since the relation in Figure 22b is based on the relative light loss of stainless steel samples, the presented polynomial coefficients are only valid for materials with a reflectance similar to  $R_{steel} = 33\%$ . However, by accounting for the material absorbance and using the “relative *scattering* loss” instead of the total (scattering + absorbance) loss, this procedure will also be valid for other materials.

Following the  $Aq$  extrapolation, Figure 23 shows a comparison of the full range  $Aq_{80deg}$  values with the  $Rq$  values from the full bandwidth of the BRDF instrument,  $0.04 \mu m^{-1} - 1.25 \mu m^{-1}$ . Figure 23 reveals a good correlation between the  $Aq_{80deg}$  and  $Rq$  values, with two regimes of linear correlations: for rough samples with  $Aq_{80deg} > 4.5$  nm, and for smooth samples with  $Aq_{80deg} < 4.5$  nm (the corresponding  $Rq$  limit is around 17 nm). The regimes are both fitted with first order polynomials using least squares. The presence of the two linear regimes could indicate a transition from mainly specular to more diffuse reflection, since the raw BRDF spectra of the smooth samples were significantly sharper and had a more pronounced specular peak, compared to the samples in the rough regime.

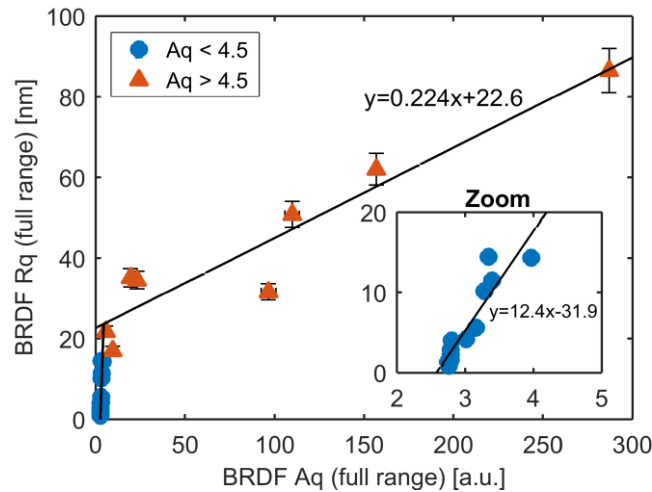


Figure 23: Comparison of  $Rq$  and  $Aq_{80deg}$  values obtained from the BRDF measurements, showing two regimes of linear correlation, fitted using least squares. Error bars represent  $\pm 1$  SU on both x and y values.

By combining the linear relations with the parabolic  $Aq$  extrapolation presented in Figure 22, the ISO standardized  $Rq$  roughness of a surface can be predicted from the  $Aq_{rBRDF}$  value and the total light intensity, both quantities provided by the rBRDF software. To our knowledge, such a relation has not been reported before, as previously the  $Aq$  parameter was only known to correlate with roughness parameters after a calibration to each specific process<sup>[72,77]</sup>. Since several samples with different roughness are analyzed in this study, we expect that the presented relations at least are valid for most 1D steel surfaces made by a directional processes, such as milling, grinding, or unidirectional polishing. This assumption is supported by the fact that many surfaces show similar scattering behavior<sup>[97–101]</sup>, described by general functions like the K-Correlation (also called the ABC model)<sup>[50,85]</sup> or the widely used ABg model<sup>[100]</sup>. For all samples in this study, the ABg model provides good fits to the spectra, hereby indicating that the results are applicable for other surfaces with similar scattering spectra. Extending the analysis to two-dimensional surfaces where the roughness features are no longer parallel but are randomly

distributed is straight forward. The scattering pattern then changes from a purely in-plane scattering to a two dimensional spectrum, in principle requiring a full hemispherical BRDF scan, and the Rq value must then be calculated along a certain direction or be replaced by the equivalent area parameter Sq defined in ISO 25178-2.

To test the accuracy of the Rq prediction, it is applied to the rBRDF data from the 22 samples, and the estimated Rq values compared to the full range BRDF Rq values ( $0.04 \mu\text{m}^{-1} - 1.25 \mu\text{m}^{-1}$ ). The average absolute deviation is 5.3 nm, with a standard deviation of 4.9 nm. Hence, the presented relations can determine the Rq value with an accuracy of  $\pm 15$  nm, at the 95% confidence interval.

## Conclusion

Three instruments for characterization of nanoscale surface roughness have been examined for correspondence between the parameters Rq, Rdq and Aq. For each instrument, the range of spatial surface wavelengths in-which the roughness values were correctly evaluated, was determined. The analysis is performed in spatial frequency space, hence the ranges are given as a frequency bandwidth for each instrument ( $f_{\min} - f_{\max}$ ): BRDF instrument:  $0.04 \mu\text{m}^{-1} - 1.25 \mu\text{m}^{-1}$ , rBRDF instrument:  $0.104 \mu\text{m}^{-1} - 0.41 \mu\text{m}^{-1}$ , confocal microscope:  $0.0196 \mu\text{m}^{-1} - 0.4 \mu\text{m}^{-1}$ , see overview in Figure 18. These bandwidths were applied to only compare roughness values within common frequency ranges.

The BRDF instrument and confocal microscope were compared in terms of the Rq and Rdq parameters, and showed a one-to-one correspondence in both parameters for the frequency range  $0.04 \mu\text{m}^{-1} - 0.4 \mu\text{m}^{-1}$ , see Figure 19.

The BRDF and rBRDF instruments were compared in terms of the Aq parameter. By including a Gaussian smoothing function to compensate for the instrument differences, the Aq values showed a one-to-one correspondence, see Figure 21.

A relation between the rBRDF Aq values and the BRDF Rq values was determined, hereby enabling the rBRDF instrument to also measure the Rq parameter. The conversion is based on a second order polynomial,  $y=ax^2+bx+c$ , to obtain the wide range  $Aq_{80\text{deg}}$  from the restricted range  $Aq_{\text{rBRDF}}$ , followed by a conversion of  $Aq_{80\text{deg}}$  to the Rq value through a first order polynomial relation,  $y=dx+e$ . The polynomial coefficients were found to be:  $a=0.422$ ,  $b=-32.3$ ,  $c=617$ ,  $d_{\text{smooth}}=12.4$ ,  $e_{\text{smooth}}=-31.9$ ,  $d_{\text{rough}}=0.224$ ,  $e_{\text{rough}}=22.6$ , where the “smooth” and “rough” subscripts refer to two regimes of linear correlation, see Figure 23. Note that the polynomials are only applicable for certain levels of surface roughness. The crossover between the “smooth” and “rough” linear regimes is at  $Aq_{80\text{deg}} = 4.5$ , while the second order polynomial should be applied to samples with  $Aq_{\text{rBRDF}} > 10$ . The conversion from  $Aq_{\text{rBRDF}}$  to Rq is achieved with an accuracy of  $\pm 15$  nm, at the 95% confidence interval.

## Acknowledgements

The authors acknowledge financial support from the Danish Ministry of Higher Education and Science through the Industrial PhD Programme, and the EC FP7 collaborative project “IFaCOM” (Project no. NMP-FoF 285489).

- - - End of paper reprint - - -

### 2.2.3 Comparison with stylus profiler

The paper focuses on roughness evaluation using optical methods, but as stated previously, the far majority of industrial roughness measurements are performed with stylus profilers. To also compare with this more standard method, the samples are evaluated with a stylus profiler (Surtronic 25, Taylor Hobson Ltd, UK). However, we found that this instrument is not sensitive enough for the smooth samples used in this study. The instrument is a small portable profiler, and as seen from the line scans in Figure 24a, the  $z$ -resolution is simply too low to resolve the nanoscale roughness features of the smooth samples. The  $z$ -resolution is only 20 nm, which is sufficient for rough samples with features in the  $\mu\text{m}$ , but for smooth samples with RMS roughness of a few nm, close to all features on the profile is lost, see Figure 24b.

The poor resolution could be due to the instrument being designed for portability and a small footprint instead of a high resolution. However, from the specifications of high-grade profilers, it seems that most profilers suffer from this low bit-resolution. For this reason, a stylus profiler was not included in the analysis. As an example, the *Form Talysurf Intra* (Taylor Hobson, UK) to a price of 400.000 DKK, has a  $z$ -resolution of 16 nm<sup>[102]</sup>. The very best profilers do have resolutions down to 0.8nm, but then the price also exceeds 1 million DKK, e.g. the *PGI 1200* (Taylor Hobson, UK)<sup>[103]</sup>.

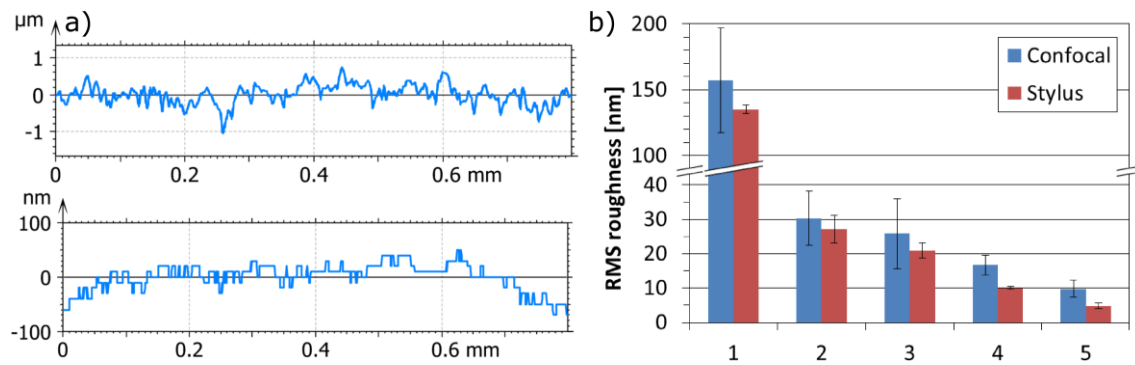


Figure 24: Evaluation of stylus profiler. **a)** Typical line scans from rough (upper) and smooth (lower) sample. The rough is sample number 1 in b), while the smooth is number 4. **b)** Comparison of RMS roughness values from confocal microscope and stylus profiler. Error bars represent one standard error of the mean. Sample 1 to 3 agrees well, while 4 to 5 are too smooth for the stylus profiler to evaluate.

### 2.2.4 Accuracy of laboratory scatterometer

For comparing the roughness values of each instrument, an estimate of the measurement uncertainties is required.

Due to the long measurement time of a BRDF scan, each sample was only measured once with this instrument. The confocal and OptoSurf measurements were then performed afterward, as close to the same positions as possible. The uncertainties for these instruments were then estimated as the standard error of the mean between the evaluations of slightly different positions. The uncertainties on the intensity values of the laboratory scatterometer are estimated by a Type B evaluation as defined by *The Guide to the Expression of Uncertainty in Measurement* (GUM)<sup>[83]</sup>. The estimate is based on the uncertainties of the three dominant factors:

- The linearity of the lock-in detector. Estimated to 1.0 % based on specifications from the manufacturer.

- The angular precision of the detector stage. Estimated to 3.9 % based on repeated measurements of the straight-through beam.
- The transmission of the ND filters. Estimated to 5.7 % based on a comparison of several calibrations performed for the filters.

The uncertainties of the intensity values are then determined using error propagation according to the GUM<sup>[83]</sup>, resulting in a standard uncertainty of 6.1 % ( $k=2$ ). The final confidence intervals on the roughness values are then determined from the resulting changes when applying the uncertainty of 6.1 % to each intensity value before the data processing. The error bars on the BRDF roughness values shown in the paper are calculated by this method, see Figures 19, 21–23.

Another approach is to perform a Type A evaluation<sup>[83]</sup>. Here multiple measurements are conducted on the same sample, and the uncertainty determined from the spread of these values. Such analysis is performed on 35 scans obtained for a stationary sample over a time span of 12.5 hours. From the differences between the intensities at each angular position, the standard uncertainty was estimated to 7.7 % ( $k=2$ ), which agrees well with the previous estimate of 6.1 %, see Figure 25.

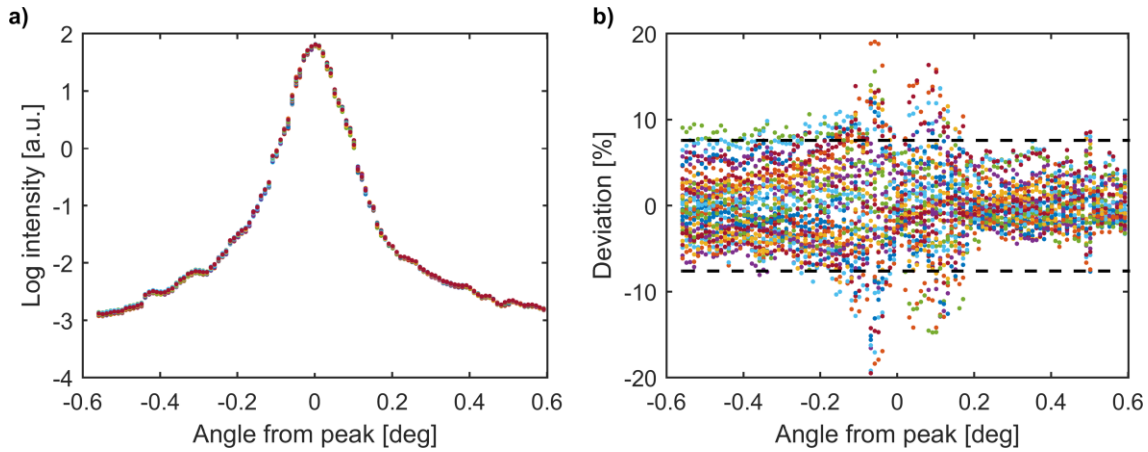


Figure 25: Uncertainty analysis. **a)** Graph of the 35 angular scans acquired. **b)** Deviations between the intensity values at each angle, with the dashed lines indicating the final uncertainty level. The marker colors correspond to the different scans.

### 2.2.5 Industrial implementation of scatterometry

The robustness of scatterometry with respect to vibrations makes this method well suited for roughness evaluations in industrial facilities. The OptoSurf is fast and easy to use, but the output parameter  $A_q$  is not adequate. According to an industry partner using the OptoSurf in a machine shop, the  $A_q$  value is largely unknown in the industry, and they always need to convince customers of its validity. The presented  $A_q$ -to- $R_q$  relation will help in this regard, but it would be even more beneficial to calculate the  $R_q$  value directly from the scattering distribution, as was done with the laboratory scatterometer. Such feature would substantially increase the value of the OptoSurf measurements, since then it could even provide a 2D contour map of the  $R_q$  roughness for different frequency bandwidths, similar to the method presented in Section 2.1.3. An added effect is that scatterometry easily detects periodic surface structures from the distinct diffraction peaks, which eases debugging if a vibration disturbs a polishing process<sup>[34]</sup>. Calculation of the  $R_q$  value requires an increased angular resolution and larger acceptance angle of the

OptoSurf instrument, both things that should be simple to implement in future models. The increased resolution can be achieved by using a high-resolution detector array, which can have several thousand pixels<sup>[104]</sup>. The acceptance angle can be increased by a higher numerical aperture lens. The downsides are that processing more pixels increases the evaluation time, and a high numerical aperture lens often requires a smaller tip-to-sample distance, hereby increasing the risk of collisions with the sample. Another possibility is to use camera-based systems, as reported by Herffurth et al.<sup>[68]</sup>. In these systems, a 2D CCD sensor captures the 2D scattering pattern of a part of the hemisphere, thereby also providing information on the anisotropy and orientation of the surface structures.

# Chapter 2.3

## Paper 2, Surfaces with interface layers

---

The previous chapter dealt with roughness measurements on clean surfaces, with a single interface from air to steel. It was assumed that any liquids or particles had been removed, and the scattering was solely caused by interactions with the surface structures. However, such perfect conditions might not always be achievable, especially if an instrument is to be used for in-line measurements inside a polishing machine. Thus, in this section, we analyze the consequences if the surface is covered with an interface layer, such as a thin liquid film.

In the following, the two terms *liquid film* and *interface layer* will be used interchangeably. *Interface layer* is the most general term, covering all thin layers on top of a substrate, while *liquid film* is the realization of such interface in the experiments. The effect on the scattering distribution is evaluated by comparing OptoSurf measurements of clean steel surfaces and covered with a liquid film. Two liquids are evaluated: pure water and a glycerol-water mixture. A real metalworking fluid is not used as these contain emulsion droplets that would interfere with the scattering, see discussion in Section 2.3.3.2. Instead, the glycerol-water mixture is designed with a refractive index similar to typical working fluids<sup>[105]</sup>, achieved by varying the ratio of glycerol and water<sup>[106]</sup>.

### 2.3.1 Paper reprint

Published as peer-reviewed conference proceedings after *SPIE Optifab 2015* in October 2015.

The article has currently received 0 citations (according to Scopus), and the journal webpage does not provide the number of downloads.

Citation:

**N. A. Feidenhans'l**, P.-E. Hansen, L. Pilný, M. H. Madsen, G. Bissacco, J. C. Petersen, and R. Taboryski, "Industrial characterization of nano-scale roughness on polished surfaces," in *Proceedings of SPIE 9633*, Optifab 2015, 2015, vol. 9633, p. 96330B.

The published version is available online at: <http://dx.doi.org/10.1117/12.2197242>

#### Title

Industrial characterization of nano-scale roughness on polished surfaces

#### Abstract

We report a correlation between the scattering value "Aq" and the ISO standardized roughness parameter Rq. The Aq value is a measure for surface smoothness, and can easily be determined from an optical scattering measurement. The correlation equation extrapolates the Aq value from a narrow measurement range of  $\pm 16^\circ$  from specular to a broader range of  $\pm 80^\circ$ , corresponding to spatial surface wavelengths of 0.8  $\mu\text{m}$  to 25  $\mu\text{m}$ , and converts the Aq value to the Rq value for the surface.

Furthermore, we present an investigation of the changes in scattering intensities, when a surface is covered with a thin liquid film. It is shown that the changes in the angular scattering intensities can be compensated for the liquid film, using empirically determined relations. This allows a restoration of the "true" scattering intensities which would be measured from a corresponding clean surface. The compensated scattering intensities provide Aq values within  $5.7\% \pm 6.1\%$  compared to the measurements on clean surfaces.

#### Keywords

polishing, roughness, scattering, BRDF, characterization, steel

### Introduction

Fabrication of very smooth steel surfaces is a long and costly process requiring several machining tools and polishing steps. Characterization between each step is necessary to obtain the best finishing and thus with in-line characterization the fabrication time can be shortened. Several techniques exist for roughness characterization<sup>[59,61]</sup> and different methods might be beneficial at the various process stages. However, it is not straightforward to compare roughness values obtained from different instruments, as they have different measurement bandwidths of the roughness features<sup>[40,59]</sup>, which is often not considered when comparing roughness values<sup>[36,61]</sup>. Hence, comparing values measured by different instruments require a study of the correlation between the instruments.

We have previously shown a comparison of three optical instruments<sup>[107]</sup>, which were analyzed for their effective measuring bandwidth and compared in terms of the ISO standardized roughness parameters Rq and Rdq<sup>[38]</sup>, along with an industry standard for surface smoothness Aq<sup>[72]</sup>. The "R" parameters were calculated as defined in ISO 4287<sup>[38]</sup>, which also defines two

bandwidth filters for the calculation: a long-pass wavelength filter ( $\lambda_s$ ) to remove noise, and a short-pass wavelength filter ( $\lambda_c$ ) to cut-off the long ranged form factor of the sample. These filters were used to restrict the bandwidths of each instrument, to ensure the instruments were only compared within a common bandwidth. The parameters and filtering effects are illustrated in Figure 26. The Aq value is defined in the VDA2009 standard<sup>[72]</sup>, maintained by the German Association of the Automotive Industry (German abbreviation: VDA). It describes the beam broadening due to scattering from surface roughness; hence a large Aq value indicates a rough surface with significant scatter.

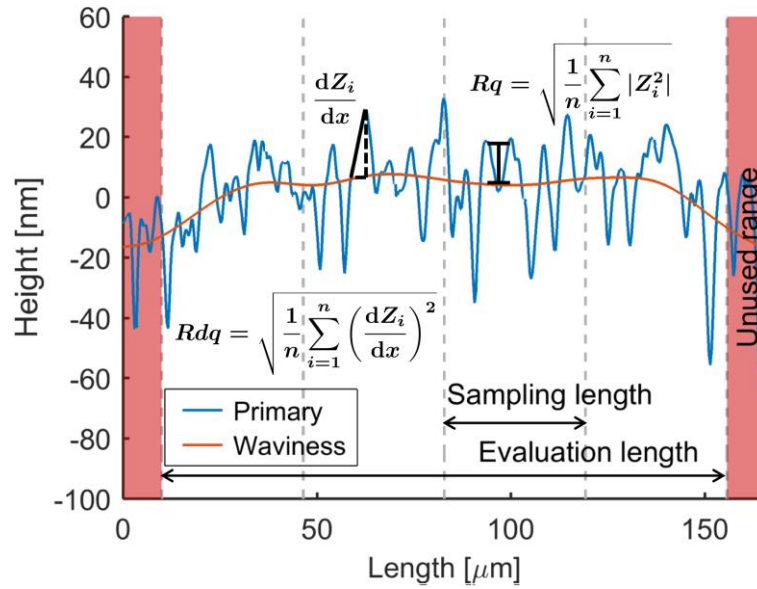


Figure 26: Illustration of the ISO 4287 roughness calculations, with the equations for the parameters: Rq (root-mean-square profile) and Rdq (root-mean-square slope). The primary profile is filtered with a noise and cut-off filter to obtain the roughness profile (not shown) and the waviness profile. The sampling and evaluation lengths are given from the width of the cut-off filter ( $\lambda_c$ ).

The three instruments in the previous comparison were: a laboratory scatterometer which measures the Bi-directional Reflection Distribution Function (BRDF), a simple commercial scatterometer with a restricted opening angle and lower resolution (OptoSurf OS 500-32, OptoSurf GmbH, Germany), and a confocal optical profiler which acquire a 3D image of the surface. The three instruments were compared pairwise as they did not all evaluate the same parameter. The BRDF and confocal instruments were compared by both the Rq and Rdq parameters, and the BRDF and OptoSurf by the Aq parameter. A one-to-one correlation was found between the instruments, when applying the correct bandwidth filters. Additionally, we presented a relation between the Aq and Rq values, enabling the calculation of the Rq value from any Aq value<sup>[107]</sup>. This is advantageous since the Aq value can be measured very rapidly by optical scattering, while the Rq value often requires a slower tactile instrument.

In this work, we extend the analysis of the Aq value to surfaces with an arbitrary interface layer. In the previous analysis the surfaces were thoroughly cleaned and all scattering assumed to originate from the surface structures of the sample. However, during metal processing a cutting fluid is normally used to ensure cooling and lubrication, this is often an oil-water emulsion<sup>[105]</sup>. These lubricants have to be removed before inspection, since any residues will significantly affect the measured values. It can be a challenging task to completely remove the lubricant<sup>[108]</sup>. In this work, we study the effects on the scattering distribution and Aq value when the steel

surface is covered with a thin liquid film. By compensating for the liquid film instead of removing it, it will be possible to avoid a thorough cleaning of the sample before each inspection, by instead rinsing with fresh working fluid to remove swarf and other contaminants. This would decrease overall processing time, and facilitate easier in-line inspection. The liquid film is assumed homogeneous, containing no particles, having a flat surface, hence covering all roughness features, and with complete filling of the roughness structures.

## Theory

In this section we consider how the angular scattering is altered due to the arbitrary interface layer. The general theory of optical scattering and BRDF spectra is described in<sup>[36]</sup>.

For a clean surface the incident light is scattered into an angular spectrum quantified by the  $BRDF_{air}$  spectrum, see Figure 27a, where the Rayleigh Rice theory assumes that the surface consists of a superposition of infinitely many sinusoidal structures, each resulting in a diffraction pattern given by the diffraction equation:

$$\sin(\theta_s) - \sin(\theta_i) = \lambda f, \quad (18)$$

where  $\theta_s$  is the scattering angle,  $\theta_i$  the incident angle,  $\lambda$  the wavelength of the light, and  $f$  the spatial surface frequency.

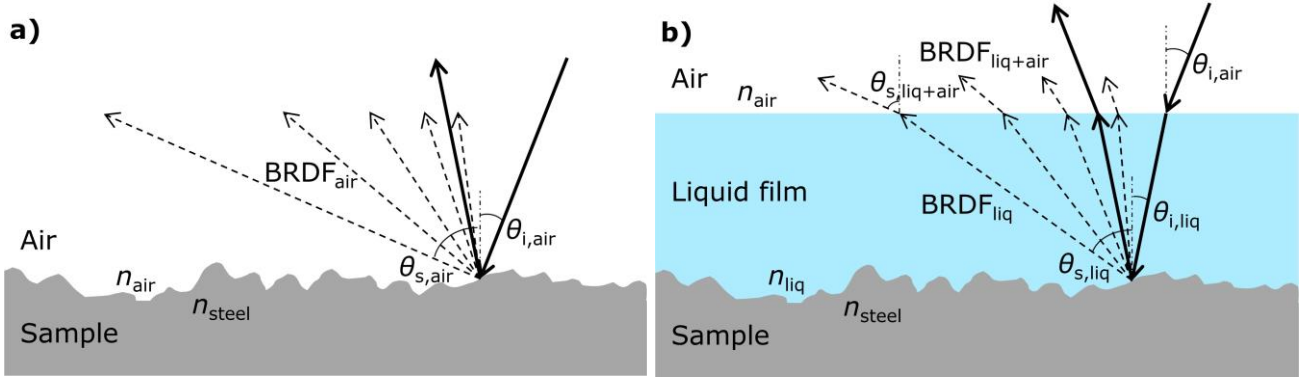


Figure 27: Illustration of scattering from a rough surface. **a)** A clean surface surrounded by air, **b)** the same surface but covered with a liquid film with refractive index above 1. For clarity, reflections at the liquid-air interface are not shown.

With a liquid interface layer between the air and sample the interesting spectrum is  $BRDF_{liq+air}$  since this is the observable spectrum one would measure for the sample. The changes to  $BRDF_{liq+air}$  compared to  $BRDF_{air}$  can be divided into field and angular effects, where the angular effects are comprised of two main factors: The liquid scattering angles,  $\theta_{s,liq}$ , decrease due to a compression of the light wavelength inside the liquid, given by:  $\lambda = \lambda_0/n$ , where  $\lambda$  is the wavelength inside the medium,  $\lambda_0$  the wavelength in vacuum, and  $n$  the refractive index of the medium. For a typical metal working liquid with a refractive index of<sup>[105]</sup> 1.45, the wavelength of the light from the OptoSurf instrument changes from 674 nm to 462 nm inside the film. From Equation (18) it is seen that this results in a tapering of the scattering pattern. The second effect, refraction at the liquid-air interface, is governed by Snell's law:

$$\sin(\theta_{air}) \cdot n_{air} = \sin(\theta_{liq}) \cdot n_{liq}, \quad (19)$$

which for  $n_{\text{liq}} > n_{\text{air}}$  results in increased angles, hence a broadening of the scattering spectrum. Conveniently, the tapering and broadening of the spectrum cancels each other out, as seen when combining Equation (18) and (19):

$$\sin(\theta_{s,\text{liq+air}}) = \sin(\theta_{s,\text{liq}}) \cdot n_{\text{liq}} = \sin\left(\sin^{-1}\left[\frac{\lambda_0}{n_{\text{liq}}} f - \sin(\theta_{i,\text{liq}})\right]\right) \cdot n_{\text{liq}} = \lambda_0 f - \sin(\theta_{i,\text{air}}) \quad (20)$$

This shows that the observed scattering angles are not affected by a liquid film on the sample. However, if the film contains contaminants such as particles or emulsion droplets, these will scatter the light independently of the surface and lead to an overestimated roughness value. The liquid must also have a flat surface parallel to the sample plane, otherwise the refraction angles will be different. Even though the final scattering angles  $\theta_{s,\text{liq+air}}$  are identical to  $\theta_{s,\text{air}}$ , the detection position will change slightly due to the smaller horizontal displacement when traveling in the liquid. However, if the layer is thin compared to the detector-sample distance this effect is negligible.

The two main factors influencing the intensity changes are: reflection losses at the interfaces, and absorption in the liquid. The reflection losses at the air-liquid and liquid-air interfaces are determined from the Fresnel equations, while the change in reflection intensity from the sample is calculated from the change in Q factor (a more general form of the Fresnel reflection, see detailed description in<sup>[36,52]</sup>). Transmission through the liquid is given by Beer–Lamberts law:  $T = 10^{-\mu l}$ , where  $\mu$  is the attenuation coefficient of the liquid, and  $l$  the path length. All three factors are angular dependent, although the angular variation is small as seen in Figure 28. The total intensity relative to the intensity reflected from a clean surface,  $r_{\text{total}}$ , is determined as<sup>[109]</sup>:

$$r_{\text{total}}(\theta_s) = \frac{R_{\text{liq}}(\theta_s) T_{\text{liq}}(\theta_s)}{R_{\text{air}}(\theta_s)} = \frac{R_{\text{air,liq}} + T_{\text{air,liq}} Q_{\text{liq,steel}}(\theta_s) T_{\text{liq,air}}(\theta_s)}{Q_{\text{air,steel}}(\theta_s)} T_{\text{liq}}(\theta_s) \quad (21)$$

where  $R_i$  and  $T_i$  are the Fresnel reflectance and transmittance,  $Q_i$  the Q-factors, while the subscripts refer to the interfaces.

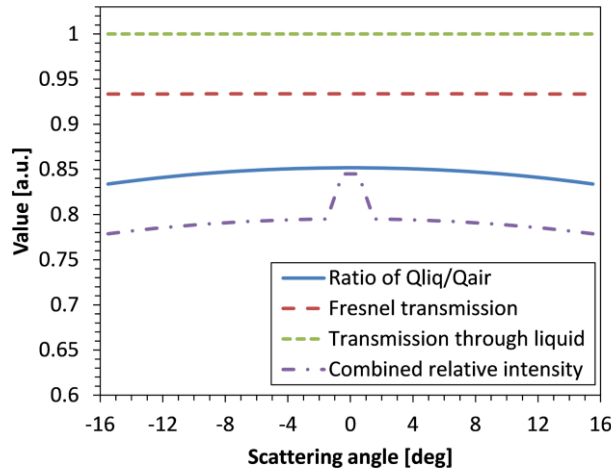


Figure 28: Illustration of the angular dependency of the three intensity factors. The solid blue line is the ratio of Q factors, the long dashed red line is  $T_{\text{air,liq}} \cdot T_{\text{liq,air}}$ , the short dashed green line is the transmission through the liquid, and the purple dash-dot line is the total relative transmittance,  $I_{\text{liq}}/I_{\text{clean}}$ . Parameters used for calculations:  $n_{\text{liq}}=1.45$ ,  $t_{\text{liq}}=300 \mu\text{m}$ ,  $\lambda_0=674 \text{ nm}$ ,  $\mu=3 \cdot 10^{-4} \text{ cm}^{-1}$ ,  $\theta_i=0^\circ$ .

## Experiments

### Aq-Rq relation

The BRDF spectrum of the clean samples are measured with two instruments: a laboratory scatterometer which can measure one side of the scattering spectrum with a resolution of  $0.01^\circ$  (termed the “BRDF instrument”), and a small commercial scatterometer to be referred to as the OptoSurf, which evaluates the range from  $-16^\circ$  to  $16^\circ$  from specular, but only with  $1^\circ$  resolution. For detailed description of both instruments and the samples, we refer to<sup>[107]</sup>. From the high resolution BRDF spectrum the roughness parameter Rq is calculated based on the Rayleigh-Rice theory<sup>[36]</sup>, and this value is compared to the Aq value measured with the OptoSurf. Previously we have shown the correlation between the BRDF Aq and BRDF Rq values<sup>[107]</sup>, while here we present a relation between the BRDF Rq and the OptoSurf Aq values, see Figure 29. This relation is probably more interesting, as an efficient setup would be to use the rapid measuring OptoSurf to determine the Aq values and then calculate the corresponding Rq values. The correlation is composed of two linear regimes: one for smooth surfaces with  $Aq < 4.5$  and one for rougher surfaces with  $Aq \geq 4.5$ . The reason for the two regimes is not known, but might be due to a transition from mainly specular to more diffuse scattering. Both regimes are fitted with linear relations ( $y=ax+b$ ) using least squares, with the resulting coefficients:  $a_{\text{smooth}} = 5.38$ ,  $b_{\text{smooth}} = -7.68$ ,  $a_{\text{rough}} = 0.258$ ,  $b_{\text{rough}} = 19.7$ . As expected, the coefficients are similar to the ones obtained in<sup>[107]</sup>.

The complete conversion from the OptoSurf Aq value to the Rq value, including extrapolation of Aq values as described in<sup>[107]</sup>, is performed with a mean absolute deviation of 2.4 nm for the smooth and 6.6 nm for the rough regime, corresponding<sup>[110]</sup> to 95 % confidence intervals of  $\pm 4.3$  nm and  $\pm 14$  nm. The input OptoSurf Aq values are measured in the range  $\pm 16^\circ$ , while the final Rq values correspond to a bandwidth of spatial surface wavelengths from  $0.8 \mu\text{m}$  to  $25 \mu\text{m}$ . Since the analyzed samples are made of various grades of steel and using several different fabrication methods, the relations are expected to be valid for most steel surfaces with one dimensional structures, such as the parallel grooves produced from milling or uni-directional polishing.

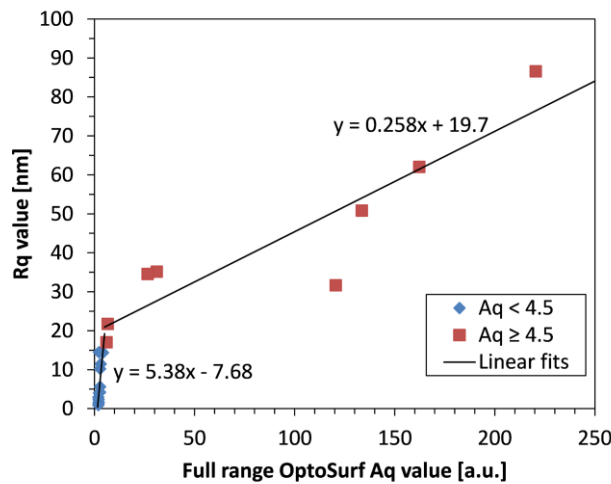


Figure 29: Correlation between Rq and Aq values. The Rq values cover a bandwidth of  $0.8 \mu\text{m}$  to  $25 \mu\text{m}$ , while the full range Aq values cover the range of  $\pm 80^\circ$ , and are extrapolated from the measured values as described in<sup>5</sup>.

### Liquid interface layer

To determine the effects of a liquid interface layer, the scattering intensity of the exact same position on each sample was measured, with and without a liquid film. Measurements in the same position were achieved by fixing the OptoSurf above the sample, and then measuring the angular scattering distribution of the clean surface and after applying a thin layer of liquid. Two liquids were used: pure distilled water with a refractive index of<sup>[111]</sup> 1.33 at 674 nm, and a glycerol-water mixture of 86 wt% with a refractive index of<sup>[111]</sup> 1.45 at 674 nm, as this corresponds to typical metal working fluids<sup>[105]</sup>. Since stainless steel is naturally only weakly hydrophilic, the samples were made more hydrophilic by oxygen activation, achieved with a 90 s exposure to oxygen plasma (Plasma Cleaner Atto, Diener electronic GmbH, Germany), which resulted in a good spreading of the liquids. In an industrial setup, this treatment could easily be circumvented by covering the entire sample surface with liquid to provide a flat surface. The samples G1-G3 were covered with the glycerol-water mixture, while W1-W3 was covered with the water film.

Figure 30a shows the raw scattering intensities from four typical samples, with and without a liquid film, while Figure 30b shows the ratio  $I_{\text{liq}}/I_{\text{clean}}$ . A substantial intensity change is seen due to the liquid film, much larger than the approximately 20 % anticipated from Figure 28. The decrease is significantly larger in the center compared to the wider scattering angles, and for most samples the angular intensity actually increases for the larger angles. These data reveal that other effects must be present, besides the reflection and transmission losses already considered. One possible effect is intensity changes could be due to interference in the liquid film, which would occur if the film is thinner than the coherence length of the light source. To test this, the thickness of the liquid film,  $t_{\text{liq}}$ , was estimated from confocal measurements (Sensofar PLu Neox, Sensofar Tech, Spain) to 300  $\mu\text{m}$ , although this value might change drastically between experiments. The coherence length of the OptoSurf LED light source was determined to<sup>[112]</sup>:  $L_c = 2\ln(2)/\pi \cdot \lambda^2/\Delta\lambda_{\text{FWHM}} = 8.5\mu\text{m}$ , with  $\lambda$  and  $\Delta\lambda_{\text{FWHM}}$  measured using a spectrometer (USB2000+VIS-NIR-ES, Ocean Optics Inc., USA). For  $t_{\text{liq}} \gg L_c$  interference patterns should not occur in the film, and for interference effects one would also expect more gradual intensity changes than e.g. seen from sample G1 in Figure 30b.

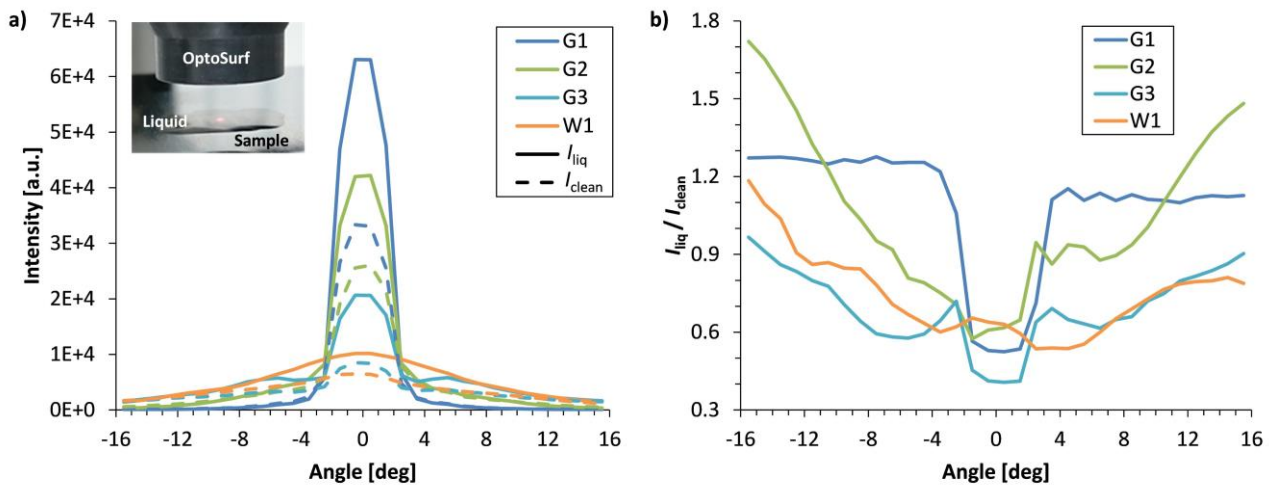


Figure 30: **a)** Typical angular scattering intensities measured for clean surfaces (solid lines) and with a liquid film (dashed lines). The corresponding Aq values are seen in Table 1. The insert is a photograph of the measurement setup, showing the OptoSurf and sample with the liquid film. **b)** Ratio between  $I_{\text{liq}}$  and  $I_{\text{clean}}$  for the samples.

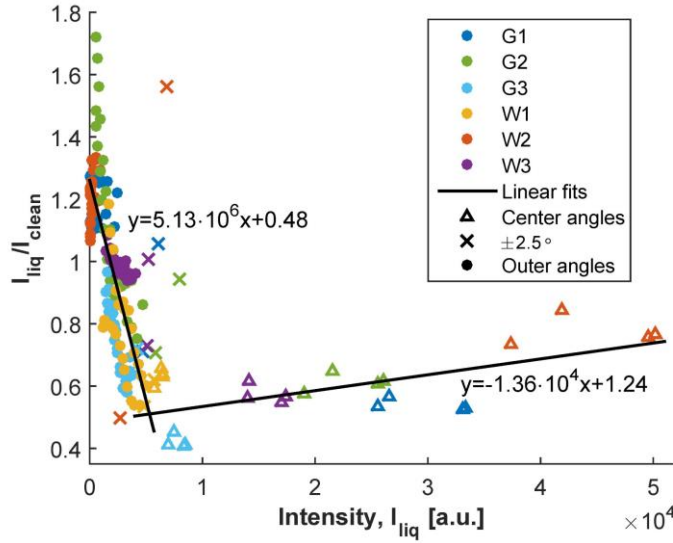


Figure 31: Graph illustrating the empirical relationship between the measured intensity,  $I_{liq}$ , and the intensity ratio  $r_{liq/clean} = I_{liq}/I_{clean}$ . Marker colors represent samples, while shapes relate to angular positions. The data in this graph include both samples with water and with glycerol-water films. The two regimes are fitted with linear relations using least square.

Since the theory cannot explain the measured intensity changes, it might be due to unknown effects in the OptoSurf instrument. The  $r_{liq/clean}$  ratio seems to follow the shape of the spectrum, and when comparing  $r_{liq/clean}$  and the  $I_{liq}$  value for each point we notice a tendency for the data points, see Figure 31. For the most intense points, corresponding to the center angles of  $-1.5^\circ$  to  $1.5^\circ$ ,  $r_{liq/clean}$  is generally small compared to the less intense points at larger angles, and there is a slight linear increase with intensity. The outer angles also follow a linear trend from the intensity, although with a different slope. Such correlations should not arise from interference, instead it is suspect that the two regimes relate to the beam shape of the light emitted from the OptoSurf. We previously found<sup>[107]</sup> that the OptoSurf beam did not resemble a single Gaussian beam, but instead matched a superposition of three Gaussian functions. Two of the functions described an intense center beam while the third function described a broader and less intense beam. In Figure 31 the center beam and the broad outer beam is seen as two regimes of linear correlation, and then the transient points at  $\pm 2.5^\circ$  which are outliers. By fitting both regimes with linear relations, a conversion equation to compensate for the liquid film and reconstruct the scattering spectrum of the clean surface is found. The conversion consists of three equations: for the center and for outer beam and the intermediate points at  $\pm 2.5^\circ$  which are compensated with the average factor from the two linear relations. The complete equations are:

$$\begin{aligned}
 I_{comp,center} &= \frac{I_{liq}}{r_{liq/clean}} = \frac{I_{liq}}{5.13 \cdot 10^{-6} \cdot I_{liq} + 0.48}, \text{ for } |\varphi| \leq 1.5^\circ \\
 I_{comp,outer} &= \frac{I_{liq}}{r_{liq/clean}} = \frac{I_{liq}}{-1.36 \cdot 10^{-4} \cdot I_{liq} + 1.24}, \text{ for } |\varphi| \geq 3.5^\circ \\
 I_{comp,2.5} &= \frac{I_{liq}}{r_{liq/clean}} = \frac{I_{liq}}{2 \left( \frac{1}{5.13 \cdot 10^{-6} \cdot I_{liq} + 0.48} + \frac{1}{-1.36 \cdot 10^{-4} \cdot I_{liq} + 1.24} \right)}, \text{ for } |\varphi| = 2.5^\circ
 \end{aligned} \tag{22}$$

where  $I_{\text{liq}}$  is the intensity measured with a liquid film,  $I_{\text{comp},x}$  the compensated intensity corresponding to a clean surface, and  $\varphi$  the detection angle in the OptoSurf.

Using these relations the liquid measured intensities is converted to the corresponding clean values, and from this the “true” Aq value of the clean surface determined. Figure 32 shows the clean and compensated angular intensities for the six samples, while Table 1 compares the corresponding Aq values. Most of the compensated intensities match reasonably well with the clean measurements, although S1 deviates significantly in the center values. However, the compensated Aq values,  $Aq_{\text{comp}}$ , are all close to the measured  $Aq_{\text{clean}}$  values, within an uncertainty of  $5.7 \% \pm 6.1 \%$  (mean deviation  $\pm$  one standard deviation). However, it should be noted that this is only a preliminary investigation of the effects due to a liquid film, and more experiments are needed to confirm the conversion equation. In this study the conversion equation is also fitted and evaluated on the same data, and therefore biased towards a low deviation.

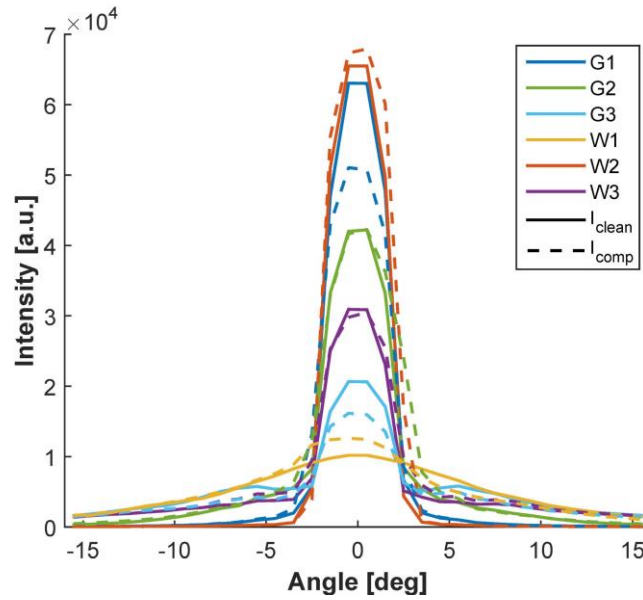


Figure 32: Scattering intensities measured for clean surfaces and the compensated values using the relations presented in Equation (22). Solid lines are the clean measurements while dashed are the compensation, colors represent samples.

Table 2: Comparison of the Aq values for the clean and compensated intensities shown in Figure 32, and for the original liquid intensities. The relative difference is found as:  $(Aq_{\text{clean}} - Aq_{\text{comp}})/Aq_{\text{clean}}$ .

	$Aq_{\text{clean}}$	$Aq_{\text{liq}}$	$Aq_{\text{comp}}$	$Aq_{\text{clean}} - Aq_{\text{comp}}$	Relative difference
G1	4.34	7.30	5.04	-0.70	-16 %
G2	16.9	25.8	17.3	-0.39	-2.3 %
G3	48.2	63.4	48.0	0.22	0.5 %
W1	54.1	64.2	48.6	5.60	10.0 %
W2	2.71	3.38	2.80	-0.09	-3.3 %
W3	36.5	49.0	35.8	0.64	1.8 %

## Conclusion

An updated relation between the Aq and Rq values was presented, see Figure 29, for previous version see<sup>[107]</sup>. Here the Rq-to-Aq relations are based on Aq values obtained with the OptoSurf instrument instead of the high resolution BRDF setup. This relation provides a more accurate conversion from the OptoSurf Aq values.

Furthermore, this manuscript has studied the changes in scattering intensities when measured on a surface with a thin liquid film,  $I_{\text{liq}}$ , compared to a clean surface,  $I_{\text{clean}}$ . To remove effects due to sample inhomogeneity, the two measurements were conducted in the exact same positions on the sample. The results showed an intensity change due to the liquid film, expected to relate to the shape of the beam emitted by the OptoSurf. The relation between  $I_{\text{liq}}$  and  $I_{\text{clean}}$  was determined, to hereby compensate for the liquid film and restore  $I_{\text{clean}}$  from  $I_{\text{liq}}$ . This enables the determination of the Aq value corresponding to a clean surface, from the angular scattering intensities of a surface covered with a thin liquid film, or another interface layer. Two liquids with different refractive indices were analyzed, and the presented compensation equation covers both liquids, since there were no notably differences between the two datasets. Hence the refractive index of the interface film does not seem to influence the conversion.

The compensation equation is two linear relations, one for the center beam corresponding to the angular range  $-1.5^\circ$  to  $1.5^\circ$ , and one for the outer angles from  $\pm 16^\circ$  to  $\pm 3.5^\circ$ . The values at  $\pm 2.5^\circ$  are the crossover points and are compensated using the average value from the two equations. The complete relations are seen in Equation (22). The compensated Aq values are within 5.7 %  $\pm$  6.1 % of the measured clean values, where 6.1 % represent one standard deviation. However, more experiments are needed to verify this correlation.

- - - End of paper reprint - - -

### 2.3.2 Motivation for dividing the beam into segments

The division of the correction equation into three different angular ranges is only briefly mentioned in Paper 2, in the section *Liquid interface layer*. The division is motivated by an analysis of the OptoSurf beam profile, described in Paper 1 in the section *BRDF and rBRDF comparison*. The conclusion is that the beam shape corresponds to a superposition of three Gaussian functions, obtained by fitting to the scatter distribution from a smooth sample. The sample is a clean silicon wafer, which is almost atomically flat; hence, the obtained distribution is very close to a perfect reflection of the incident beam. The diameter of the three fits, given by their  $1/e^2$  widths, suggests a narrow and intense center beam along with a wide and much weaker beam, see Figure 33 and Table 3. The fitted width of  $\sim 5^\circ$  for the wide beam corresponds well with the transition angles of  $\pm 2.5^\circ$  in Equation (22). The beam shape is expected to result from the lenses focusing the light from the LED.

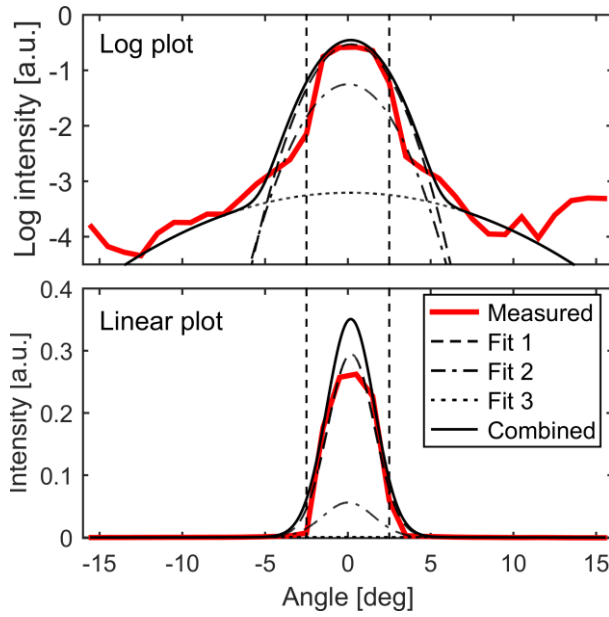


Figure 33: Plot of the Gaussian fits to the OptoSurf beam. The transition angles of  $\pm 2.5^\circ$  are indicated by vertical dashed lines.

Fit	a	$\mu$	$\sigma$	$1/e^2$ width
1	0.29	$0.20^\circ$	$1.4^\circ$	$5.6^\circ$
2	0.056	$0.020^\circ$	$1.5^\circ$	$6.1^\circ$
3	$6.2E-4$	$0.10^\circ$	$5.5^\circ$	$22^\circ$

Table 3: Parameters for the Gaussian functions in Figure 33. The function form is:  $(x) = a \exp\left(-\frac{(x-\mu)^2}{(2\sigma)^2}\right)$ .

### 2.3.3 Validity of assumptions

For the theoretical analysis of the interface layer, a few assumptions are applied to the layer. This section will evaluate how well they might be fulfilled in actual production environments, and the implications if they are not.

#### 2.3.3.1 Transmission

The layer is assumed transparent for the probe wavelength, which it obviously has to be, at least partially. If typical metalworking fluids absorb in similar wavelength bands, the probe wavelength can be chosen to optimize the transmission.

#### 2.3.3.2 Homogeneous liquid

The layer is assumed completely homogeneous to ensure it does not contribute to the scattering of light. However, this might prove difficult to fulfill in real environments, as metalworking processes typically generate many particles. The simplest cleaning method would be to rinse the

sample thoroughly with clean working fluid, hereby avoiding an actual cleaning step and only use one liquid in the setup. However, most metalworking fluids are water based oil emulsions, with the oil phase dispersed as small droplets in the water, stabilized by various surfactants and solvents<sup>[105]</sup>. Such droplet emulsion does not constitute a homogeneous liquid, as the droplets will scatter the light. Depending on the ratio between droplet size and the probe wavelength, different physical effects govern the scattering process. If the size is much larger than the wavelength of the light, they are in the geometric regime where normal refraction and reflection occurs at the interfaces. Due to the large number of interfaces a typical ray interacts with, the light will be scattered into a broad range of angles, resulting in a milky appearance<sup>[113]</sup>. On the other hand, if the droplet size is much smaller than the wavelength, the scattering is dominated by Rayleigh scattering, where light scatters into both the forward and backward direction, though only a smaller fraction of the light is scattered, hereby providing a rather clear liquid<sup>[113]</sup>. Lastly, if the size is comparable to the wavelength, the scattering properties are governed by Mie scattering. Here the light is mainly scattered in the forward direction, with a scattering probability largely determined by the particle size<sup>[113]</sup>. This will most likely also result in an unclear and milky appearance. The three regimes are roughly categorized based on the particle size parameter:  $x = 2\pi r/\lambda$ , where  $r$  is the radius of the particle, and  $\lambda$  the wavelength of the light. The divisions between the three regimes are approximately:

$$\begin{aligned} x \ll 1 & : \text{Rayleigh scattering,} \\ x \sim 1 & : \text{Mie scattering,} \\ x \gg 1 & : \text{Geometric scattering.} \end{aligned} \tag{23}$$

With droplet sizes typically in the range  $0.1 \mu\text{m} - 2 \mu\text{m}$ <sup>[105]</sup>, the scattering is described by Mie and geometric scattering. To be in the Rayleigh regime, where the liquid is still mostly clear, the droplet radius would have to be below 10 nm. Hence, the liquid has to be homogeneous and not contain emulsion droplets.

#### 2.3.3.3 Layer thickness

The interface layer is assumed thin compared to the distance between sample and sensor, as this ensures minimal changes to the scattering angles. If the thickness becomes comparable to the distance between the sample and sensor, the reduced scattering angle inside the liquid, resulting from the larger refractive index, will generate a smaller horizontal displacement, see Figure 34. This causes the rays to hit the detector in another position, hereby providing a different scattering angle.

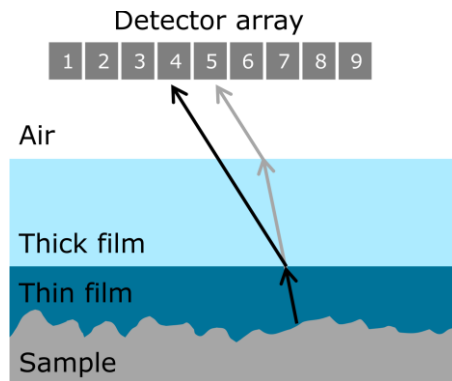


Figure 34: Illustration of light scattering for two different film thicknesses. For a thin film (in dark blue) the scattered ray hits pixel number 4, while for a thick film (light blue) the same scattering ray will hit pixel number 5.

The actual film thickness was determined to approximately 300  $\mu\text{m}$ , using a confocal microscope (Sensofar PLu Neox, Sensofar Tech, Spain). In comparison to the 5 mm between sample and detector, this is considered a thin layer.

#### 2.3.3.4 Normal incidence

The incident beam is assumed to be at normal incidence. The OptoSurf device already assumes this condition, and it is easily verified from the position of the specular peak in the scattering distribution. Hence, this assumption can always be expected to be fulfilled.

#### 2.3.4 Future work

The reported findings are mainly intended as a preliminary study, where further investigations should be conducted to increasing the understanding of the setup. The observed intensity changes of the scattering distributions would be a good candidate for future research, as these are still unexplained.

In the present study, the scattering distributions were only evaluated using the rather simple OptoSurf scatterometer. This instrument has little control over the setup parameters and data acquisition, and it is not completely clear if the exported data is raw or processed. For a detailed investigation of the scattering distributions, a more configurable setup with higher angular resolution would be beneficial. A setup similar to the laboratory scatterometer would probably be optimal. Unfortunately, this setup cannot be used for liquid films, as the samples have to be mounted vertically. Another parameters which would benefit from more control is the film thickness. In this study, the film thickness and scattering distributions are evaluated on different films. Being able to measure the thickness of the same film as the scattering distribution is measured on, will enable an analysis of thickness dependent effects, such as interference in the film.

# Chapter 2.4

## Paper 3, Replication of surface roughness

---

The focus of the two previous papers was on methods for in-line (or in-machine) evaluation of roughness. Another problem for roughness evaluation is that the surface can often be difficult, or even impossible, to position in the instrument. The sample might be too large, too heavy, or the surface might not face outwards. In many cases, the solution is to form a molded replica of the surface and evaluate this instead<sup>[114]</sup>. Typically, a two-component polymer is applied to the surface where it solidifies while in contact with the structures. To ensure a good replication, the polymer must fill all micro- and nanostructures on the surface, and the structures not break or elongate when demolded. If the structures are not fully replicated, the replica might get a smoother surface than the original, resulting in an artificial low roughness that does not represent the original surface.

Several factors influence the replication quality, and in this study, we investigate one factor, namely the lateral shrinkage of the replica during curing. The analysis is performed using the silicon-based polymer PDMS. It is important to know the shrinkage ratio, as the dimensions measured on the replica have to be corrected with this factor. Even though PDMS is widely used in academia<sup>[115]</sup>, a thorough investigation of the shrinkage ratios has not been published. Several smaller studies exist, but these only cover a small range of the curing temperatures and monomer ratios that are typically used. Furthermore, the studies often find different values, and as they do not present the associated uncertainties, it is difficult to draw any general conclusions. Hence, the aim of this study is to investigate many combinations of curing temperatures and monomer ratios, and also provide the uncertainties on the final shrinkage ratios.

### 2.4.1 Paper reprint

Published as a technical note in *Journal of Micromechanics and Microengineering* (IOP) in October 2014.

The article has currently received 3 citations (according to Scopus), and has been downloaded 347 times (according to the journal webpage).

Citation:

M. H. Madsen\*, N. A. Feidenhans'l\*, P.-E. Hansen, J. Garnæs, and K. Dirscherl, Accounting for PDMS shrinkage when replicating structures, *Journal of Micromechanics Microengineering*, vol. 24, no. 12, p. 127002, dec. 2014.

\*Equal contributions

The published version is available online at: <http://dx.doi.org/10.1088/0960-1317/24/12/127002>

#### Title

Accounting for PDMS Shrinkage when Replicating Structures

#### Abstract

Polydimethylsiloxane (PDMS) is a widely used material for fabrication of microfluidic devices and for replication of micro- and nanotextured surfaces. Shrinkage of PDMS in the fabrication process can lead to leaking devices and poor alignment of layers. However, corrections to the mold master are seldom applied to counteract the shrinkage of PDMS. Also, to perform metrological measurements using replica techniques one has to take the shrinkage into account. Thus we report a study of the shrinkage of PDMS with several different mixing ratios and curing temperatures. The shrinkage factor, with its associated uncertainty, for PDMS in the range 40 °C to 120 °C is provided. By applying this correction factor, it is possible to replicate structures with a standard uncertainty of less than 0.2 % in lateral dimensions using typical curing temperatures and PDMS mixing ratios in the range 1:6 to 1:20 (agent:base).

#### Keywords

PDMS, Polydimethylsiloxane, shrinkage, replica, replication, microfluidic

### Introduction

In the research area of lab-on-a-chip systems, polydimethylsiloxane (PDMS) is a popular fabrication material for small scale production of fluidic systems<sup>[116]</sup> and for replication of surfaces<sup>[117]</sup>. Some of the advantages of PDMS are: low cost compared to other materials<sup>[118]</sup>, chemical resistant to many solvents<sup>[118]</sup>, optically transparent down to near-UV<sup>[119]</sup>, and easy fabrication using commercial kits<sup>[116]</sup>.

The fabrication of PDMS devices is done by replica molding. Here, a liquid PDMS mixture is prepared from two components, poured onto a previously fabricated mold, and cured while in the mold. The PDMS hereby replicates the surface structures of the mold, on both the micro and nano-scale<sup>[114,116]</sup>. PDMS is a thermosetting polymer, specified for curing at both room temperature and temperatures up to 150 °C<sup>[120]</sup>, though most lab-on-a-chip fabrication is performed in the range 60 °C – 80 °C<sup>[117,121–123]</sup>. However, it is well-known that PDMS shrinks compared to the mold dimensions, mainly due to curing of PDMS at elevated temperatures<sup>[124,125]</sup>. Unfortunately, this temperature induced shrinkage is very seldom included in the design, even though it

might cause leakage from channels or bad alignment between layers. We attribute this issue to the lack of reliable values for the degree of contraction.

Several studies have investigated the shrinking ratio and found a broad range of values ranging from 0.7 % at 80 °C to ~3 % at 60 °C<sup>[121,124,126]</sup>. In a study by Lee et al.<sup>[127]</sup> the PDMS shrinkage has been investigated, but only in a narrow range of curing temperatures, and no measurement uncertainties are given. One group also had success with circumventing the shrinkage problem, by curing the PDMS while attached to a rigid substrate<sup>[126]</sup>. Unfortunately, this method complicates the curing procedure and introduces an additional fabrication step, which is regrettable since the easy fabrication process is one of PDMS's advantages.

Besides the use of PDMS in microfluidic systems, PDMS replicas can also be used for nondestructive surface characterization, where a small surface area is replicated to e.g. allow imaging of objects which physically do not fit under the microscope<sup>[114]</sup>. In the area of surface metrology replications are typically made using replication kits, based on a two component polymer which is mixed in the spout while applying the polymer<sup>[128,129]</sup>. According to one manufacturer, their polymer is optimized to produce high resolution replicas (down to 0.1  $\mu\text{m}$ ) with only negligible shrinkage (the value is not stated)<sup>[128]</sup>. Hence, these commercial replica kits are not well suited for replication of nanoscale structures. For such small structures, PDMS replicas are preferred since these has been demonstrated to replicate down to 10 nm wide lines<sup>[130]</sup>, and even smaller features in combination with hard-PDMS<sup>[117,131]</sup>. However, to perform metrological measurements of surface structures, the non-negligible shrinkage of PDMS has to be taken into account.

In this paper, the influence of curing temperature and mixing ratio to the shrinkage of PDMS is investigated. Compared to previous studies<sup>[127]</sup>, a broader range of variations are investigated, with the range of curing temperatures spanning from 8 °C to 120 °C, and several mixing ratios are used. We estimate a correction factor for adjusting the master's dimensions to account for shrinkage in relation to the curing conditions. The master structures used for the replications are two 2D checkerboard gratings, classified as transfer standards for use in metrological measurements.

## Experimental methods

### Master structure

For the masters, two 2D checkerboard silicon gratings (manufactured by Ibsen Photonics, Denmark) with a nominal pitch of 3000 nm and 10000 nm was used. The surface of the gratings is covered with chromium and platinum, which ensure an easy release of the cured PDMS. The patterned area covers an area of 2.5 mm  $\times$  2.5 mm positioned in the center of a silicon chip of 7 mm  $\times$  5 mm  $\times$  0.5 mm (width, length, height). The nominal depth of the structures is 100 nm. Their periods in the  $x$ - and  $y$ -direction have been measured to  $(3001.1 \pm 1.5) \text{ nm} \times (3001.9 \pm 1.5) \text{ nm}$  and  $(10.002 \pm 0.005) \mu\text{m} \times (10.008 \pm 0.005) \mu\text{m}$ , where the values after  $\pm$  indicate the standard uncertainties given at the 68 % confidence level ( $k=1$ ). The periods were determined by traceable diffraction measurements<sup>[132]</sup>, hereby certifying the gratings as metrological transfer standards.

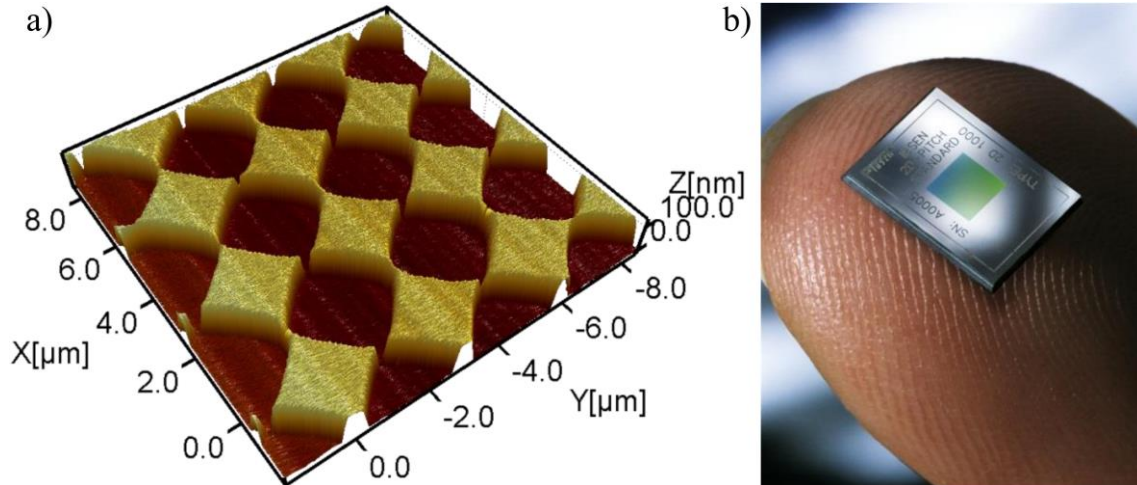


Figure 35: The transfer standard used as a master. **a)** AFM image of the 3  $\mu\text{m}$  master, showing the 2D checkerboard grating. **b)** Photograph showing a master grating positioned on a finger.

### Fabrication of PDMS replica

The PDMS was prepared from a Sylgard 184 silicone elastomer kit (Dow Corning, USA), which consist of two components: a base (Part A) and a curing agent (Part B). These were mixed in weight ratios of 1:6, 1:10 and 1:20 (curing agent:base). The two components were thoroughly mixed, put under vacuum for a few minutes, and stored for at least 30 min to remove air bubbles. The two mold masters were placed in a container and gently covered with the liquid PDMS mixture, to prevent trapping of air pockets. After curing, the PDMS replicas were trimmed with a pair of scissors to fit under the microscope.

For curing at elevated temperature, the container was placed on a hotplate (VWR VHP-C4, VWR, US-PA), preheated to the desired temperature. The total height of container, mold, and PDMS layer was approximately 5 mm, which is thin enough to safely assume a constant temperature for the entire volume of PDMS. For the room temperature curing, the container was put on a desk in a temperature monitored room. For lower temperatures, the container was put in a refrigerator set to the specified temperature. For a complete list of all curing conditions, see Table 4. The curing times were selected such that it was guaranteed the PDMS was completely hardened<sup>[120]</sup>. The mold was cooled to room temperature before the master and PDMS were split. The final PDMS replicas were approximately 3 mm thick. Relevant as the thickness may slightly influence the shrinkage<sup>[127]</sup>.

Mixture	1:6	1:10	1:20
Temperature			
8 °C		12 days	
21 °C	65 hours	60 hours	60 hours
40 °C		16 hours	
60 °C		4 hours	9 hours
70 °C		3 hours	
80 °C	2 hours	2 hours	
100 °C	70 min	80 min	130 min
120 °C	30 min	40 min	80 min

Table 4: Overview of the curing times associated with each curing temperature and mixing ratio (curing agent:base). At least two replicas were fabricated for each set of conditions, one with a 3  $\mu\text{m}$  pitch and one with a 10  $\mu\text{m}$  pitch.

### Shrinkage measurements

Shrinkage of the PDMS replicas were investigated using a confocal microscope (Sensofar PLu neox, Sensofar-Tech, Spain) equipped with a 50x objective (N.A. 0.80). For each replica a 3D surface profile in the center of the grid was acquired by a z-stack, and covering an area of 255  $\mu\text{m}$  x 191  $\mu\text{m}$ . A typical topographic image is shown in Figure 37 for a PDMS replica of the 10  $\mu\text{m}$  grating. The master is shown in Figure 35 and as the grating has 50 % filling factor, it is difficult to distinguish the master and the inverse replica. The height was extracted from the confocal imaging and used to correct for an overall tilt of the sample, which is not possible by conventional imaging. To correct for tilt of the samples, the images were initially flattened using a first order plane correction. However, this correction projects the lateral length scales down on to the plane without any correction, see Figure 36. Thus one has to correct the length scales with a factor of  $1/\cos(\theta_x)$  and  $1/\cos(\theta_y)$  for the x- and y-scale, respectively.

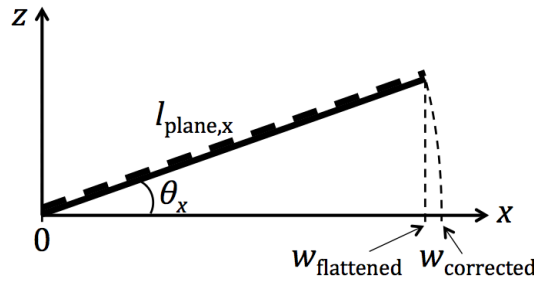


Figure 36: Illustration of how flattening of a tilted sample requires scaling of the image width and height, due to how the flattening projects each pixel onto the  $x,y$ -plane. This illustration only shows the effect on the  $x$ -axis.

The measurements were performed in a temperature monitored room at 23 °C. The dimensions of the master structures were determined using the same microscope, under the same conditions, also in the center of the grid. The replicas and masters were always positioned with the same orientation in relation to the objective, within a few degrees. The replica dimensions were then compared relative to the master dimensions, hereby ensuring that any systematic errors, e.g. from aberrations in the optics, affected the measurements identically. An average unit cell of the entire grid was estimated using the Fast Fourier Transform (FFT) of the image. The pitch along both directions of the grid is then found directly from the length of the unit vectors spanning the unit cell. To validate the quality of the estimate, the unit cell is replicated over the entire image, and the deviations between this unit cell grid and the actual image determined, see Figure 38. The analysis was done using the image processing software SPIP (SPIP 6.2.7, Image Metrology, Denmark). The percentage-wise shrinkage was determined as:  $r_{\text{shrinkage}} = -\frac{l_{\text{replica}} - l_{\text{master}}}{l_{\text{master}}} \cdot 100 \%$ .

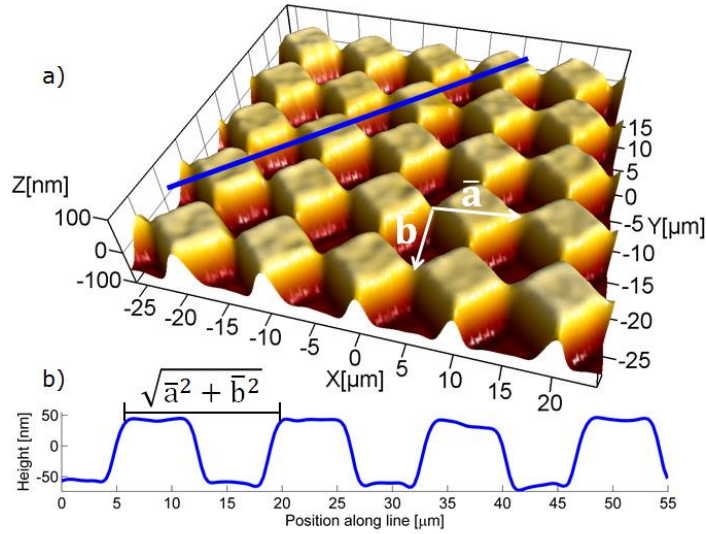


Figure 37: Confocal microscopy imaging. **a)** Typical 3D surface profile of PDMS replica, illustrating the periodic grid on the master. Illustrated with white arrows, are the unit-vectors ( $\vec{a}$  and  $\vec{b}$ ) which spans the unit cell of the grid. **b)** Line profile along blue line in a. The distance indicated in the profile is  $\sqrt{2}$  times the period, due to the orientation of the unit vectors.

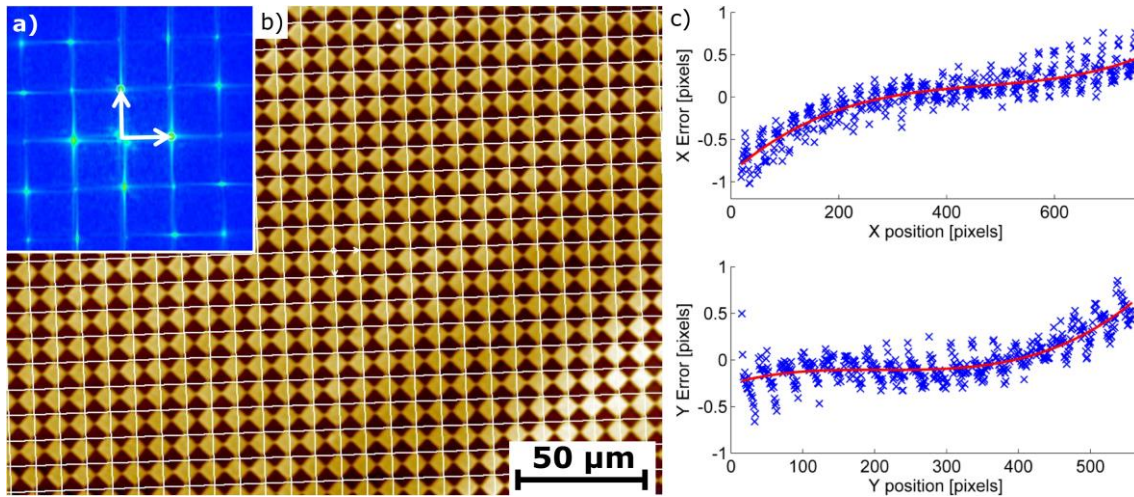


Figure 38: Graphical output from unit cell analysis. **a)** 2D Fourier transform of the image with two white arrows indicating the unit vectors in Fourier space. **b)** Confocal image of a 10  $\mu\text{m}$  sample overlaid with a white grid showing the unit cells determined from the Fourier transform. **c)** The error between the estimated unit cell and the structures.

## Results and discussion

### Reproducibility

The reproducibility of the replication process was investigated by repeating the same molding several times, see Figure 39. Both the 3  $\mu\text{m}$  and 10  $\mu\text{m}$  master grating were replicated 8 times with PDMS 1:10 at a curing temperature of 80  $^{\circ}\text{C}$ . The shrinkage compared to the master was measured in both  $x$ - and  $y$ -direction for each replica, yielding a total of 32 measurements. The mean relative shrinkage are found to  $(1.94 \pm 0.05) \%$  and  $(1.91 \pm 0.08) \%$  for the 3  $\mu\text{m}$  and 10  $\mu\text{m}$  grating, respectively, where the values after  $\pm$  indicate in these cases the spread of the measurement data, which is the standard deviation (SD). The larger value of the SD for the 10

$\mu\text{m}$  grating can be attributed to the lower number of grating periods within the field of view of the microscope compared to the  $3\ \mu\text{m}$  grating. The mean relative shrinkage for all replicas of the two masters is found to  $(1.92 \pm 0.07)\%$ . Their SD will be used as an estimate for the standard uncertainty of the reproducibility.

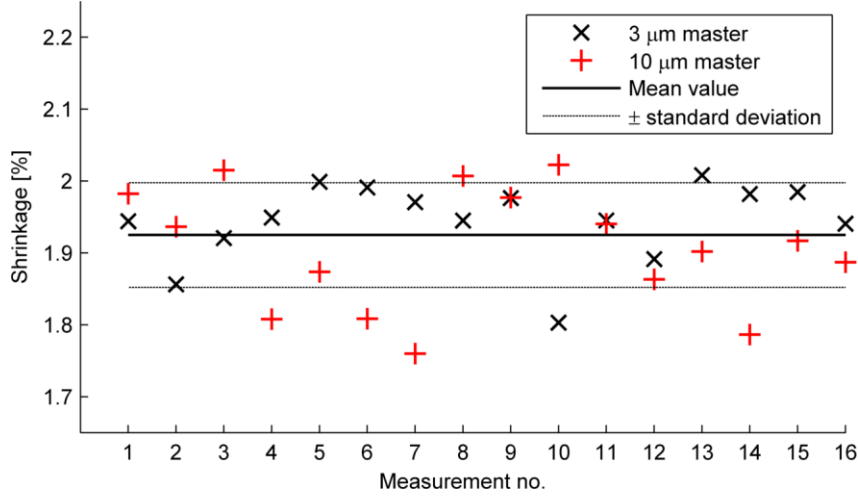


Figure 39: Reproducibility of PDMS replication when molded under identical conditions. Two masters,  $3\ \mu\text{m}$  and  $10\ \mu\text{m}$ , were replicated 8 times with 1:10 PDMS at  $80\ ^\circ\text{C}$  for 2 hours. The mean value of all 16 replicas is  $1.92\%$  with a standard deviation of  $0.07\%$ .

### Shrinkage

The shrinkage of PDMS replicas prepared as described in Table 4 was investigated using the unit cell analysis presented in the Experimental methods section. The results are shown in Figure 40, with the percent-wise shrinkage for all the replicas as a function of the curing temperature. The shrinkage here is identical to a negative expansion. Each point is an average over at least four measurements, comprised of two values from both of the  $3\ \mu\text{m}$  and  $10\ \mu\text{m}$  masters, one along each direction of the grid. The y-errorbars indicate the standard error of the mean (SEM) and the x-errorbars are the estimated temperature uncertainties. The SEM is found by combining the standard deviation (SD) of the four measurements and the uncertainty found from the reproducibility experiment, see Figure 39. The uncertainty on the reproducibility accounts for the fact that the replicas were molded in pairs of two, and thus not completely independent experiments. The x-errorbars are the standard uncertainty estimated from temperature stabilities of  $\pm 5\ ^\circ\text{C}$  on the hotplate,  $\pm 2\ ^\circ\text{C}$  in the refrigerator, and  $\pm 1\ ^\circ\text{C}$  related to at the room temperature. All temperature uncertainties are assumed to follow a rectangular distribution<sup>[83]</sup>.

The data from  $40\ ^\circ\text{C}$  to  $120\ ^\circ\text{C}$  is fitted with a first order polynomial,  $y = \alpha T + \beta$ , using weighted least squares. The fitting parameters are found to:  $\alpha = 0.0180\ ^\circ\text{C}^{-1}$ , and  $\beta = 0.46$ , with the standard uncertainties  $u(\alpha) = 0.0015\ ^\circ\text{C}^{-1}$  and  $u(\beta) = 0.13$ .

The combined standard uncertainty of the fit is indicated with dotted lines in Figure 40, and estimated using the equation:

$$u(y) = \sqrt{(T \cdot u(\alpha))^2 + (\alpha \cdot u(T))^2 + (u(\beta))^2} \quad , \quad (24)$$

where  $u(\alpha)$  and  $u(\beta)$  are the standard uncertainties of the fitting parameters, and  $T$  is the curing temperature with its associated standard uncertainty  $u(T)$ .

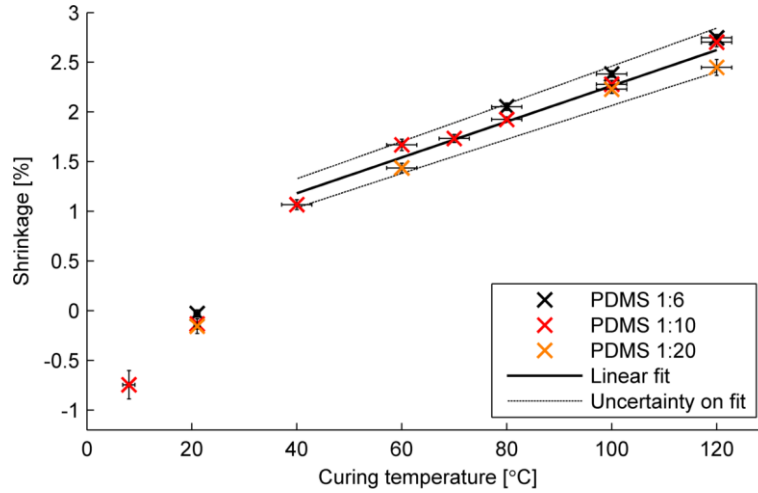


Figure 40: Shrinkage of PDMS after curing under the conditions specified in Table 4. A positive shrinkage corresponds to a negative expansion, thus PDMS replicas cured above room temperature are smaller than the master. The equation of the linear fit is:  $y = 0.0180 \cdot T + 0.46$ , with an standard uncertainty indicated by the dotted lines, ranging from  $\pm 0.15$  to  $\pm 0.22$ . Each data point is an average of between four and sixteen measurements, with errorbars indicating the standard error on the mean.

Curing temperature	Shrinkage [%]			Lee & Lee shrinkage
	1:6	1:10	1:20	
8 °C		$-0.75 \pm 0.14$		
21 °C	$-0.03 \pm 0.04$	$-0.13 \pm 0.05$	$-0.16 \pm 0.07$	
40 °C		$1.07 \pm 0.05$		
60 °C		$1.67 \pm 0.06$	$1.44 \pm 0.05$	1.06 (PDMS 1:9)
70 °C		$1.73 \pm 0.04$		
80 °C	$2.05 \pm 0.04$	$1.92 \pm 0.03$		1.52 (PDMS 1:9), 1.46 (PDMS 1:6)
100 °C	$2.38 \pm 0.03$	$2.28 \pm 0.04$	$2.23 \pm 0.04$	1.94 (PDMS 1:9)
120 °C	$2.75 \pm 0.03$	$2.70 \pm 0.05$	$2.45 \pm 0.08$	

Table 5: List of the determined shrinkage for each set of curing conditions, including a comparison with the ones obtained by Lee and Lee<sup>[127]</sup>. Note the slightly different ratios for their PDMS. The values after  $\pm$  indicate the standard error on the mean.

Figure 40 reveal a correlation between curing temperature and shrinkage ratio, with shrinkage ratios of around 2 % in the typical temperature range of 60 °C – 80 °C. All the ratios in this study are larger than the ones obtained by Lee and Lee<sup>[127]</sup>, see Table 5. This difference can be explained by the thickness of the PDMS layer, which differs from approximately 5 mm in this study to only around 1 mm in the study by Lee and Lee. The difference in observed shrinkage could also be caused by the smaller length scale investigated in this study, although one would expect the shrinkage to be uniform over length scales.

Shrinking of the PDMS during curing arises mainly due to thermal contraction of the PDMS after curing, but polymer may also experience density changes during the curing step due to reconfiguration of the monomers<sup>[133]</sup>. Dow Corning provides a linear coefficient of thermal expansion (CTE) for cured PDMS of  $310\text{E-}6 \text{ }^{\circ}\text{C}^{-1}$ , although without any specifications of uncertainty level or temperature range<sup>[120]</sup>. Since this value is only valid for cured PDMS, it cannot be used for correction when molding but only to determine the expansion of a PDMS device when heated or cooled during experiments. The slope,  $\alpha$ , of the fit corresponds to the

CTE for the curing process. However, the offset,  $\beta$ , cannot directly be explained. As seen from the figure, the shrinkage is also not linear over the entire temperature range, which could be due to a phase change or similar, although it does not match the glass transition temperature of PDMS, which is  $-125\text{ }^{\circ}\text{C}$ <sup>[134]</sup>. Nevertheless, since the vast majority of PDMS is cured in the range around  $60\text{ }^{\circ}\text{C} - 80\text{ }^{\circ}\text{C}$ , the focus should be on this range.

One of the goals of this study is to provide a correction equation for scaling of dimensions when molding in PDMS. For this reason, a linear fit is only performed in the range  $40\text{ }^{\circ}\text{C} - 120\text{ }^{\circ}\text{C}$ , which thoroughly encompasses the essential range. Focusing solely on this range, will make the correction less general, but instead provide a better estimate of the shrinkage for majority of users.

Since no significant correlation is found for the shrinkage depending on the mixing ratios, the linear fit is applicable for all three mixing ratios. Thermal expansion of the mold masters have been neglected in the analysis, as these are made of silicon which has a CTE of  $3.0 \cdot 10^{-6}\text{ }^{\circ}\text{C}^{-1}$ <sup>[135]</sup>, around 100 times smaller than the table value of PDMS. The analysis further assumes that the PDMS device is used at near room temperature, here defined as  $23\text{ }^{\circ}\text{C}$ .

Since the shrinkage is seen to depend significantly on the curing temperature, this effect is important to consider when making microfluidic devices in PDMS. To ensure reproducible molding of devices, the PDMS should always be cured at the same temperature, and e.g. not raised to speed up the curing process. If the design feature dimensions with small tolerances, the PDMS shrinking should be considered and compensated for when designing the mold master. To correct the design dimensions of a master for PDMS molding, one can use:

$$l_{\text{corrected}} = l_{\text{original}} \cdot (1 + \gamma(T_{\text{cure}})) = l_{\text{original}} \cdot (1 + 0.0180 \cdot T_{\text{cure}} + 0.46) \quad , \quad (25)$$

where  $l_{\text{original}}$  is the original dimension,  $l_{\text{corrected}}$  is the dimension corrected for shrinkage of PDMS when cured at the temperature  $T_{\text{cure}}$ . Based on the presented experiments, the formula is at a minimum valid for microscale dimensions in the range  $3\text{ }\mu\text{m} - 10\text{ }\mu\text{m}$ , at curing temperatures from  $40\text{ }^{\circ}\text{C}$  to  $120\text{ }^{\circ}\text{C}$ .

If redesigning the PDMS mold is not possible, one can instead decide on a tolerable level of shrinkage, and then use the shrinkage values presented in Figure 40 and Table 5 to determine an appropriate curing temperature which satisfy this tolerance. Also, if the device is to be used at elevated temperatures, the expansion at these temperatures should be considered. It should also be noted, that when choosing a curing temperature one should also consider the effect on the mechanical properties of PDMS, as parameters such as Young's Modulus and tensile strength have been shown to depend on the curing temperature<sup>[136]</sup>.

## Conclusion

The shrinkage of PDMS is important for both fabrication of devices and for metrological measurements. The shrinkage has been studied in the range from  $8\text{ }^{\circ}\text{C}$  to  $120\text{ }^{\circ}\text{C}$  by replication of 2D gratings with periods of  $3\text{ }\mu\text{m}$  and  $10\text{ }\mu\text{m}$ . To avoid shrinkage, the curing can take place at room temperature. However, this will increase the curing time from around an hour to more than two days. Instead the curing can be performed at an elevated temperature and then corrected for the shrinkage. For temperatures ranging from  $40\text{ }^{\circ}\text{C}$  to  $120\text{ }^{\circ}\text{C}$ , we have found that the shrinkage can be described by a first order polynomial,  $y = ax + \beta$ , where  $\alpha = 0.0180\text{ }^{\circ}\text{C}^{-1}$ , and  $\beta = 0.46$  with associated standard uncertainties of  $u(\alpha) = 0.0015\text{ }^{\circ}\text{C}^{-1}$  and  $u(\beta) = 0.13$ . By using this correction factor, the standard uncertainty on the dimensions due to shrinkage will be

less than 0.2 % at typical curing temperatures. Also when fabricating microfluidic devices, one should take shrinkage into account when designing the master structure.

### **Acknowledgements**

The authors acknowledge the support from the Danish National Advanced Technology Foundation through the project NanoPlast and the FI project 'Documentation of micro- and nanotextured products'. NAF further acknowledges financial support from the Danish Ministry of Higher Education and Science through the Industrial PhD Programme.

- - - End of paper reprint - - -

## 2.4.2 Thickness dependency

The comparison with Lee and Lee<sup>[127]</sup> reveals that our shrinkage ratios are consistently below theirs. In the paper, this is attributed to the differences in thickness of the PDMS replicas, with theirs being between 1.2 mm and 2.4 mm while ours are around 5 mm. In this paragraph, we expand on the possible thickness dependency.

Lee and Lee investigated the influence of several variables, namely: monomer ratio, curing temperature, and replica thickness, but only include a few samples for each parameter. They only comment on the variations with curing temperature; but based on the published shrinkage ratios, we can perform an analysis of the correlation with the two other variables. The difference in monomer ratio does not seem to have a significant effect, in agreement with our study. On the other hand, the replica thicknesses and shrinkage ratio does appear to correlate, as shown from Figure 41. The figure shows an indication of a linear correlation between the two parameters, although it is not possible to state a definite conclusion with this few data points. Such correlation could potentially explain some of the difference between the reported values, which range from 0.7 % to ~3 %<sup>[121,124,126]</sup>. However, a more detailed study is definitely needed. This would be an interesting study, as PDMS is used for molding components with thicknesses ranging from a few micrometers to centimeters<sup>[137,138]</sup>.

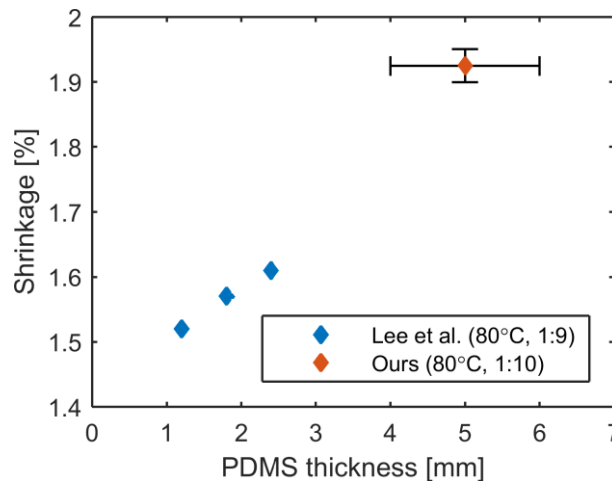


Figure 41: Shrinkage ratio of PDMS replicas as a function of the replica thickness. The data is combined from<sup>[127]</sup> and the presented paper. Error bars indicate the standard error of the mean.

## 2.4.3 Outlook

### 2.4.3.1 Other materials

PDMS is a well-studied material due to its wide use in academia<sup>[115]</sup>. Unfortunately, the long curing time of several hours renders it less suitable for industrial replications, especially if the master cannot be heated. For these cases, commercially available replication kits are often better suited. Two of such possibilities are the RepliSet kit from Struers<sup>[128]</sup> and AccuTrans from Coltene<sup>[129]</sup>. Both are two-component polymers where the base and curing agent are mixed in a syringe immediately before application, and the curing time is only in the order of minutes. Another advantage is that they are designed to reduce uncertainties from thermal expansions, with curing at room temperature and the polymer having negligible thermal expansion<sup>[128]</sup>. On the other hand, the polymers in these kits often have high viscosities (thick flowing), hence requiring an external force to penetrate fully into surface structures and provide a good replication. This might influence the reproducibility uncertainty, and it could prove difficult to force

the polymer into nanostructures. Hence, a thorough analysis of the replication fidelity and reproducibility is needed before using such kits.

#### 2.4.3.2 Other structures

The paper only analyzes the replication of rather artificial structures, namely the metrological transfer standards with well-defined square pillars arranged in a 2D grating. These structures are mainly useful models for resembling molding of microfluidic structures, but to validate the replication fidelity of surfaces roughness, a study with random roughness patterns would be interesting. Such study could be done by evaluating the 3D surface profile on both master and replica, e.g. with AFM or confocal microscopy. However, it is often difficult to locate the exact same areas, as these high-resolution microscopes have small fields of view. One would also have to consider the inverted tip convolution for the original and replica.



# Part 3

## COLOR SCATTEROMETRY

As mentioned in the introduction, a future commercialization of nanostructured products requires new types of characterization instruments, which can provide automated and high-speed quality control for the high volume fabrication methods employed. Part 3 investigates the use of fixed-angle scatterometry for characterization of micro- and nanoscale gratings, as these gratings can be added to a design and work as quality control indicators.

This part is based on a paper presenting this method, reprinted in Chapter 3.2. Preceding the paper is a more comprehensive introduction, and it is followed by a more detailed presentation of the experimental setup and the simulations.

Short summary of the paper:

Paper 4: The paper presents a new characterization method for periodic nanostructures, based on spectroscopic scatterometry. The method works by analyzing the color of the structures, obtained with a color camera. It is tested on polymer line gratings, and is shown to provide uncertainties not significantly larger than more advanced imaging scatterometers. The acquired images comprise a surface area of several mm<sup>2</sup>, which enables an evaluation of the grating dimensions for many small regions independently.

# Chapter 3.1

## Introduction

---

### 3.1.1 Scatterometry

Where the angular scatterometry in Part 2 was used for characterization of random roughness features, the scatterometry techniques in Part 3 concerns the evaluation of well-defined periodic structures. The structures are all on the same length scale as the visible light, and the scattering caused by diffraction. The most obvious example of diffraction is the pattern of periodic dots, resulting from a laser and a binary grating, described by the well-known diffraction grating equation<sup>[36]</sup>:

$$m\lambda = d(\sin \theta_m + \sin \theta_i) \quad , \quad (26)$$

where  $m$  is the diffraction order,  $\lambda$  the wavelength of the light,  $d$  the grating period,  $\theta_m$  the diffraction angle of the  $m$ 'th order, and  $\theta_i$  the incident angle.

The concept of evaluating the position of the diffraction orders is called *angular scatterometry* and is well suited for determining the grating period<sup>[139]</sup>. The setup is conceptually identical to the setup used in Part 2, only the data analysis differs. The power of scatterometry is the possibility to determine several parameters, such as the structure height, sidewall slope, and corner roundness<sup>[140]</sup>. The concept is identical to measuring the diffraction angles and determine the grating period from Equation (26), but scatterometry often relies on more advanced methods for calculating the theoretical diffraction pattern. Typically, numerical simulations are used, which can include more parameters for defining the grating profile, and provides more variables to measure<sup>[140]</sup>. The term *diffraction efficiency* covers the efficiency of both reflected and transmitted orders; however, as this report only considers non-transparent samples, the term *reflection efficiency* is often used interchangeably with *diffraction efficiency*.

When including many structural parameters in the simulations, they often take many hours to perform and are often performed before the actual measurement, using the expected grating dimensions as a-prior information. The measured reflection efficiencies are then fitted to the previously generated simulation database, and the grating dimensions determined from the best matching simulation, typically defined as the minimum chi-square value. To obtain good fitting confidence many efficiency values need to be determined, for example by evaluating several diffraction orders or by varying the incident angle<sup>[140]</sup>. This study focuses on *spectroscopic*

*scatterometry*, where the reflection efficiencies are evaluated for a range of wavelengths, but the incident and detection angles fixed to evaluate only the specular reflection<sup>[140]</sup>.

The advantages of scatterometry are that it is a non-destructive optical technique, and it can evaluate grating features far below the diffraction limit<sup>[140]</sup>. Compared to scanning probe microscopy, it is significantly faster as the evaluation of one sample typically takes below one second<sup>[140]</sup>. Scanning probe methods such as AFM and SEM often have better resolutions on some axis, but generally, cannot evaluate the same range of dimensions as scatterometry<sup>[140]</sup>. A drawback of scatterometry is the generation of the simulation database, where the refractive index along with the approximate grating dimensions must be known a-prior. For this reason, scatterometry cannot be used to evaluate unknown samples. Scatterometry can also provide misleading results, as it only provides the global minimum *with-in* the simulation database. If the actual structures deviate significantly from the expectations, the best fit might be unreliable. Though this problem should be indicated by a noticeably high chi-square value; however, it is also possible that two very different structures can provide similar reflections efficiencies.

Currently, scatterometry is mainly used for quality control in semiconductor processes, in combination with critical dimension SEM (CD-SEM)<sup>[140–143]</sup>. Compared to normal SEM instruments, CD-SEM instruments are typically more stable and better calibrated, to provide sub-nanometer measurement uncertainties<sup>[144]</sup>. Where scatterometry can evaluate the full 3D profile of the structures, CD-SEM is best suited for evaluating planar dimensions from top-down images, although this gap is being closed by tilted CD-SEM<sup>[142]</sup>. A future potential of scatterometry is for in-situ measurements and end-point detection, where the structures formed by an etch process can be evaluated in real time<sup>[145]</sup>. This is similar to the current use of ellipsometry for in-situ monitoring of thin film processes<sup>[146]</sup>. Other optical methods similar to scatterometry are ellipsometry<sup>[147]</sup> and Mueller polarimetry<sup>[148]</sup>. These methods are conceptually similar, by determining structural parameters from the correlation between theoretical and measured light interactions. The difference is that ellipsometry and Mueller polarimetry mainly focus on the polarization changes of the light for determining the refractive index and film thicknesses, while scatterometry evaluates the intensity changes and focuses on 3D structures<sup>[140,142]</sup>.

### 3.1.2 Color perception

In principle, only three things are needed to evaluate a color: a light source, an object, and an observer, nevertheless, human perception of colors is a complicated process<sup>[149]</sup>. The light source and object are fully described by the emission spectrum and the reflection spectrum. The complex part is the observer, as human color interpretation is not a direct function of the received spectra. The basis of human color vision the light interacting with three cone receptors positioned in the retina on the inside of the human eye<sup>[149]</sup>. Even though the spectral sensitivities of the cones has been determined<sup>[150]</sup>, the later post-processing performed by the brain can make identical spectra appear different, depending on factors such as the light intensity, previous stimuli, color of surrounding objects, and the object size<sup>[149]</sup>. Due to many of these effects not being well understood, the evaluation of human color vision is based on a set of well-defined setups, defined by the International Commission on Illumination (abbreviated CIE from its French name). These definitions comprise a set of standard illuminants and standard observers, the main ones being the *CIE Standard Illuminant D65* that resembles the daylight spectrum at noon, and the *CIE 1931 2° Standard Observer* that is the empirically determined response of a set of test persons under specific viewing conditions<sup>[149]</sup>. The 2° refers to the visual angle and

corresponds to a circular area of 1.8 cm in diameter with a viewing distance of 50 cm. The observed color is then calculated as<sup>[149]</sup>:

$$\begin{aligned} X &= k \sum_{i=1}^N S(\lambda_i) R(\lambda_i) \bar{x}(\lambda_i) \Delta\lambda \\ Y &= k \sum_{i=1}^N S(\lambda_i) R(\lambda_i) \bar{y}(\lambda_i) \Delta\lambda \\ Z &= k \sum_{i=1}^N S(\lambda_i) R(\lambda_i) \bar{z}(\lambda_i) \Delta\lambda \quad , \end{aligned} \quad (27)$$

where  $X$ ,  $Y$ , and  $Z$  are the color coordinates in XYZ space,  $k$  is a normalization constant,  $S(\lambda_i)$  is the light source spectrum,  $R(\lambda_i)$  is the reflectance of the object,  $\Delta\lambda$  is the wavelength interval, and  $\bar{x}$ ,  $\bar{y}$ ,  $\bar{z}$  are the color matching functions of the CIE 1931 2° Standard Observer, see Figure 42.

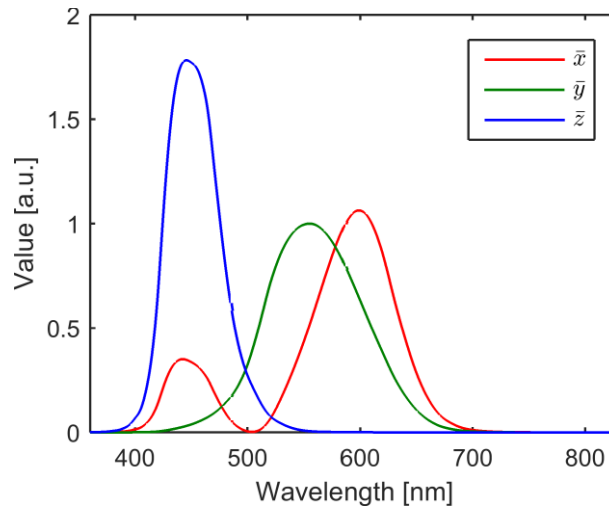


Figure 42: Color matching functions of the CIE 1931 2° Standard Observer. Data obtained from<sup>[151]</sup>.

The XYZ color space is one of the standardized coordinate systems for describing colors. Other systems include the  $L^*a^*b^*$  and sRGB spaces. The XYZ space is important due to the correlation with the standard observers, described by Equation (26).  $L^*a^*b^*$  is a non-linear conversion of the XYZ values, to provide a more perceptual uniform color space<sup>[149]</sup>. The asterisks are used to distinguish it from the original “Hunter Lab” space, but in this thesis, it will be referred to as “Lab”. In Lab space, the colors are described by the lightness ( $L$ ) ranging from a value of 0 for completely dark to a value of 1 for perfect white, and the actual color defined on a red-green axis (a) and a yellow-blue axis (b). An important property is that the color values are device independent; hence, this space is often used for color-critical applications, e.g. when transferring image data from one device to another. The Lab space is also used for calculating color differences, either given by the Euclidian distance or by the CIEDE2000 formula, which corrects for the space not being completely perceptual uniform<sup>[152]</sup>. The sRGB space was designed by HP and Microsoft in 1995 to provide a standardized color space optimized for computer monitors<sup>[153]</sup>. It is now considered the default color space for computer graphics<sup>[154]</sup> and officially standardized by the International Electrotechnical Commission (IEC)<sup>[155]</sup>. A conversion to the sRGB space is needed when a color has to be displayed on a screen.

Besides the mathematical descriptions with coordinate systems, colors are often described with words, although the terminology is not strictly defined<sup>[149]</sup>. Generally, three quantities describe a color: hue, lightness, and saturation, with the following terminology used throughout this thesis. The *hue* is the basic color such as blue or red, and can be thought of as corresponding to the color of a single wavelength. Altering the *lightness* of a given hue, tones the color to lighter or darker shades. The *saturation* describes how vibrant or colorful the color is. A low saturation corresponds to the gray nuances, while highly saturated colors are vivid and intense.

The previous was a short introduction to human color perception, for in-depth descriptions we refer to the books by Georg Klein<sup>[149]</sup> and Robert W. G. Hunt<sup>[154]</sup>. However, since this thesis employs a camera for all color characterization, things are a little different. The color calculation is identical to Equation (27), and similar to the post-processing performed by the human brain, modern cameras typically apply a significant amount of image correction algorithms<sup>[156]</sup>. Fortunately, with cameras, it is possible to extract the raw RGB values of each pixel, before any post-processing, and these values correlate linearly with the received spectrum. This type of unmodified images is called RAW images and is intended for (semi)professional photographers that prefer to optimize the post-processing algorithm manually.

### 3.1.3 Simulation of reflection efficiencies

As previously mentioned, scatterometry relies on a previously generated database of simulated reflection efficiencies. The calculations are performed with a numerical solver, and typically last several hours, depending on the size of the database. The size is determined by the number of varied grating parameters, together with the range and step size of each. The step sizes are determined from the change in reflection efficiency with that parameter, while the range is based on the certainty on the a-prior expected values. The simulation time is proportional to the power of the number of parameters since all combinations of all parameters are simulated. As each grating can be solved independent, the computation is well suited for parallel computing.

Different numerical solvers exist, and they vary with respect to accuracy and computational speed<sup>[157]</sup>. The most widely used method for scatterometry is rigorous coupled wave analysis (RCWA)<sup>[140]</sup>, while other methods include the finite element method (FEM) and the finite-difference time-domain (FDTD). In RCWA, the structure is divided into three regions: an infinite substrate below the grating, the grating region, and an infinite superstrate above the grating. The grating itself is defined as a stack of horizontal layers, resulting in a staircase approximation of slanted sidewalls. For each layer, Maxwell's equations are solved with the boundary conditions of continuous parallel electromagnetic fields and continuous perpendicular electromagnetic flux densities<sup>[2,158]</sup>. The simulation output is the reflection and transmission efficiencies of each diffraction order. In FEM the grating, substrate, and superstrate are all defined by a mesh of small finite elements, typically triangles for 2D and tetrahedrals for 3D simulations. In FEM the real physical problem described by partial differential equations is approximated with numerical model equations that can be solved numerically for each node in the mesh<sup>[157]</sup>. The greater flexibility in meshing averts the staircase approximation in RCWA. FEM is a more versatile technique than RCWA and provides more output information than simply the reflection efficiencies<sup>[157]</sup>. However, it also requires longer simulation times. FDTD uses finite differences in both the spatial and time domain to approximate the derivatives in Maxwell's equation. Similar to FEM, FDTD can also model arbitrarily shaped structures, however, it is more demanding on the computational resources<sup>[157]</sup>. RCWA will be used for all

simulation in this thesis, as it is fully adequate for describing the employed gratings, and it has a high computational efficiency.

### 3.1.3.1 RCWA simulations

RCWA originates back to the 60's but has continuously been improved through the years. For a review of the major breakthroughs, see Section 3.2 in Madsen & Hansen<sup>[140]</sup> and Chapter VI in Nevière and Popov<sup>[159]</sup>. In this work, the commercially available RCWA package “GD-Calc” (KJ Innovation, CA-USA) is used. This implementation is based on a generalized variant of RCWA, where the electromagnetic fields and the permittivity of each horizontal slab are described in terms of Fourier series, and the propagation of Fourier coefficients through the slabs determined by a set of differential equations<sup>[158]</sup>. It applies a variant of the scattering matrix approach<sup>[160]</sup>, where each slab is treated as a “black box”, described by the amplitudes of the reflected and transmitted field<sup>[158]</sup>. The structures are defined by dividing each horizontal slab into parallel lines, and each line designated a permittivity to specify whether it belongs to the grating or the superstrate. Slanted sidewalls are imitated by increasingly narrower lines towards the top layer. For bi-periodic gratings, the lines can be further divided into blocks<sup>[158]</sup>. The incident field is defined from the vacuum wavelength and the propagation direction defined by the polar ( $\theta$ ) and the azimuthal angles ( $\varphi$ ) in a spherical coordinate system. For an illustration of a typical line grating with a staircase approximation of slanted sidewalls, see Figure 43.

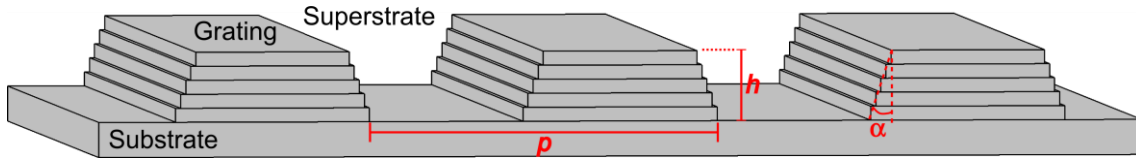


Figure 43: Typical line grating setup in an RCWA simulation. Sidewall slopes ( $\alpha$ ) are approximated by a staircase arrangement of five horizontal slabs. The three full periods are only shown for visual purposes, for simulations the unit cell is a single period ( $p$ ).

The simulation output is the reflection and transmission coefficients of the electric field for each diffraction order, along with the propagation vectors of each order<sup>[161]</sup>. Four coefficients are provided for the reflection and transmission of each order, corresponding to the reflection matrix ( $\mathbf{r}_{\text{sample}}$ ):

$$\mathbf{E}_{\text{reflected}} = \mathbf{r}_{\text{sample}} \mathbf{E}_{\text{incident}} \Leftrightarrow \begin{bmatrix} E_{\text{reflected}, s} \\ E_{\text{reflected}, p} \end{bmatrix} = \begin{bmatrix} r_{s \rightarrow s} & r_{p \rightarrow s} \\ r_{s \rightarrow p} & r_{p \rightarrow p} \end{bmatrix} \begin{bmatrix} E_{\text{incident}, s} \\ E_{\text{incident}, p} \end{bmatrix}, \quad (28)$$

where  $E_i$  are the reflected and incident intensity for  $s$ - and  $p$ -polarization, and  $r_i$  are the complex reflection coefficients for each polarization. The subscript  $j \rightarrow k$  means incident  $j$  polarization reflected as  $k$  polarization. The intensity reflection efficiencies are determined as:  $R_i = |r_i|^2$ , and the light intensity as:  $I_i = (\mathbf{E}_i^*)^T \mathbf{E}_i = |E_{i,s}|^2 + |E_{i,p}|^2$ , where  $*$  denotes the complex conjugate,  $T$  the matrix transpose, and  $|x|$  the modulus.

Typically when evaluating surface reflections, only the diagonal terms of  $\mathbf{r}$  are considered, since for all isotropic materials (and anisotropic materials at normal incidence) the off-diagonal terms with polarization conversion vanish. For the presented color scatterometry setup, the off-diagonal terms are essential, as these are found to provide stronger color variations in relation to the grating dimensions. For a typical simulation output of reflection efficiencies, see Figure 44. The RCWA simulation setup will be described in more detail in Section 3.4.1.

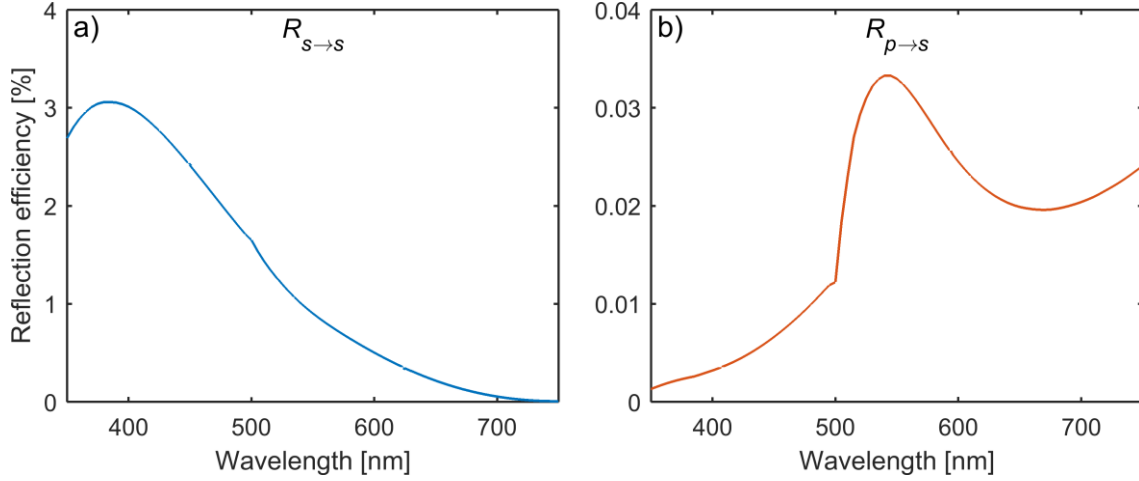


Figure 44: Typical RCWA simulation output. Showing the reflection efficiencies,  $R_{s \rightarrow s}$  in **a)** and  $R_{p \rightarrow s}$  in **b)**, for the grating presented in Figure 43 under normal incidence and linear polarization rotated  $45^\circ$  with respect to the grating vector. Only two of the matrix components are shown, as the other two have identical values.

### 3.1.4 State of the art

Scatterometry is a well-known method for determining subwavelength structures using visible light. The research is mainly focused on characterization of structures in the semiconductor industry<sup>[143,162–164]</sup>, and several of the large companies within semiconductor metrology are developing scatterometers for process control applications, e.g. ASML<sup>[165]</sup>, IBM<sup>[166]</sup>, and KLA-Tencor<sup>[167]</sup>. It is mainly focused on high accuracies<sup>[163]</sup> and the determination of many grating parameters<sup>[168]</sup>.

The advantages of scatterometry are that it is non-destructive, and it can evaluate sub-wavelength features, meaning that visible light can be used to resolve feature sizes an uncertainty of a few nanometers<sup>[169]</sup>. An abundance of methods similar to scatterometry exists, all utilizing the changes to intensity/polarization/phase of light after interacting with the sample, and a theoretical model that links the structure dimensions with these properties. Besides the range of scatterometry techniques mentioned in<sup>[140]</sup>, other examples are: scatterfield microscopy<sup>[170,171]</sup>, ellipsometry<sup>[148]</sup> and Fourier scatterometry<sup>[172–174]</sup>.

The use of colors for structural characterization is largely unexplored and has mainly been applied to simple structures such as thin films. For a single thin film, it is well-known that the thickness can be evaluated from the reflected color<sup>[175,176]</sup>. By using a setup with well-defined viewing conditions, it has been shown that humans can determine the thickness of titanium dioxide thin films on fused silica with an accuracy of only a few nanometers<sup>[177]</sup>. The same concept has been automatized, using a standard flatbed scanner for obtaining the colors<sup>[178]</sup>. A similar application, aimed at identifying single and few-layer graphene flakes, has also been developed based on colors obtained by optical microscopy<sup>[179,180]</sup>. Besides thin film characterization, the human color vision has also been applied for characterization of fused silica gratings from the transmitted colors<sup>[181]</sup>, though with uncertainties significantly larger than obtained for thin films<sup>[177]</sup>.

# Chapter 3.2

## Paper 4 reprint

---

Article submitted as a Letter to *Optica* (OSA) on the 11<sup>th</sup> of August 2016.

The paper is currently under review.

Citation:

N. A. Feidenhans'l, S. Murthy, M. H. Madsen, J. C. Petersen, and R. Taboryski, "Spatial characterization of nanotextured surfaces by visual color imaging," *Applied Optics*, 2016.

The supporting information is found in Appendix A3.

### Title

Spatial characterization of nanotextured surfaces by visual color imaging

### Abstract

We present a method for characterization of nanostructures from the visual color of the structures, obtained with an ordinary color camera. The method provides a macroscale overview image from which micrometer sized regions can be analyzed independently, hereby revealing long-ranged spatial variations of the structures. The method is tested on injection molded polymer line gratings, and the height and filling factor determined with confidence intervals similar to more advanced imaging scatterometry setups.

### Introduction

The development of structured functional surfaces is currently receiving increased focus, with applications such as generating color effects<sup>[182,183]</sup> or altering wetting behaviors<sup>[184,185]</sup>. Simultaneously several groups have demonstrated the fabrication of such micro- and nanostructures using large-scale production methods like injection molding<sup>[20]</sup> and roll-to-roll manufacturing<sup>[18,19,186,187]</sup>. However, with high volume production methods, characterization of the structures is becoming an increasing issue. The current workhorses for characterization of micro/nano-scale structures are atomic force microscopy (AFM) and scanning electron microscopy (SEM)<sup>[140]</sup>. AFM is excellent for evaluating structure heights and period, but the recording of each image takes many minutes and the field of view is limited ( $<100\text{ }\mu\text{m}$ ). SEM has a larger field of view, but evaluation of vertical structures is difficult and the sample size restricted by

the instrument vacuum chamber. For adoption of structured functional surfaces into mass produced products, faster characterizations techniques are needed.

In the semiconductor industry, scatterometry is increasingly being employed for critical dimension metrology<sup>[140,163]</sup>. Scatterometry is an optical characterization technique for periodic structures, where the structure dimensions are determined by fitting the measured reflection efficiencies to a simulation database, as the reflection efficiencies depends on the structure dimensions. To obtain good fitting confidence several values are obtained for each sample, typically by including multiple diffraction orders, or by varying parameters such as the wavelength, polarization, or incident angle of the probe light<sup>[140]</sup>. For generating the simulation database, the approximate structure dimensions must be known a priori. The current approaches are mainly targeting precise measurements of the very high quality samples produced by the semiconductor industry<sup>[163,169]</sup>. However, for industrial polymer production single nanometer precision is not needed, as the samples cannot be expected to have perfectly well defined shapes.

We present a new method, based on scatterometry, which can determine the height, filling factor, and sidewall slope of nanoscale 1-dimensional (1D) line gratings, simply by evaluating the color of the sample. The use of visual colors in scatterometry has previously been reported, but only with focus on the human ability to distinguish colors<sup>[175,177,181]</sup>. In the presented setup, the color is determined as the RGB values obtained with an ordinary camera, and the method is named “color scatterometry”. The motivation is that such gratings can be added for quality control purposes in areas of no significance for the products functionality. The advantage over other scatterometry methods, such as spectroscopic scatterometry, is that it provides an overview image of several mm<sup>2</sup> from which smaller areas subsequently can be analyzed independently. This is similar to imaging scatterometry<sup>[188]</sup>, where hyper-spectral imaging is used to obtain the reflection spectrum for each pixel in an image. However, where hyper-spectral requires around 50 images obtained at different wavelengths, color scatterometry only requires a single image acquisition, hereby providing significantly shorter evaluation times.

## Methods

Polymer test samples were manufactured by polymer injection molding, as described in the Supplement Section S1. The samples consist of a single polymer disc with seven areas of 4.5 x 4.5 mm<sup>2</sup>, patterned with rectangular shaped line gratings of different periods, as shown in Figure 45a-d. The design dimensions were: height  $h = 210$  nm, projected area filling factor  $f = 0.50$ , sidewall slope  $\alpha = 0^\circ$ , and periods  $p$  of 600, 800, 1000, 1200, 1400, 2000 and 5000 nm. The dimensions were chosen to provide high reflection efficiencies, but not with respect to the detection sensitivity. The actual dimensions of each sample were determined by a combination of AFM and focused ion-beam electron microscopy (FIB SEM), see Supplement Section S2. Two methods were employed, as none of them alone could evaluate the full range of dimensions obtained by color scatterometry. AFM is superior for measuring heights, but not well suited for sidewall slopes or filling factors, due to tip convolution. With FIB milling a trench was cut perpendicular to the grating, hereby revealing a cross section of the profile, from which the filling factor and slope was determined from SEM images. The final reference values were obtained as the mean of several grating profiles, and the 95 % confidence intervals (CI) determined as:  $\mu \pm t_{n-1} \cdot SE$ , where  $\mu$  is the mean value,  $SE$  is the standard error of the mean, corrected for small sample bias by Cochran’s theorem<sup>[189]</sup>, and  $t$  is the Student’s  $t$ -distribution for  $n$  samples ( $n = 2$  to  $9$ , typically  $4$  or  $5$ ).

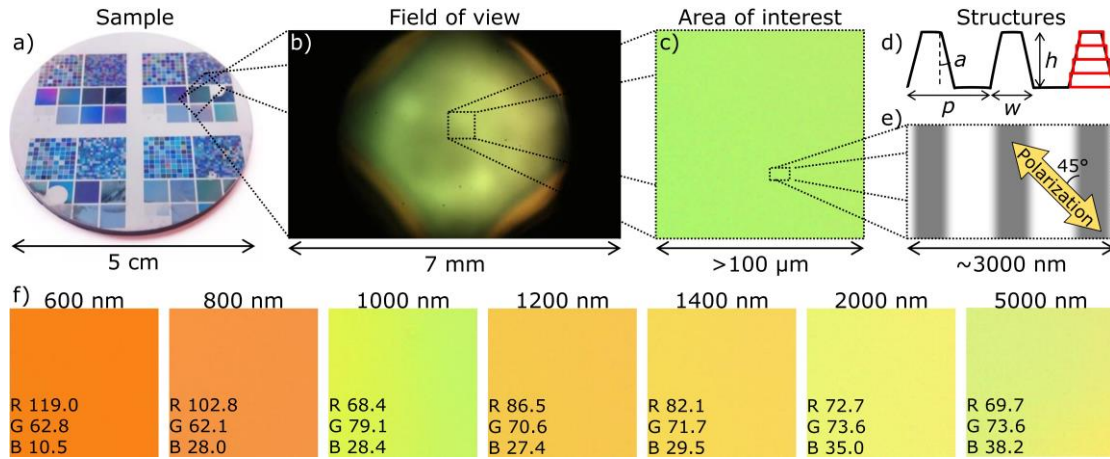


Figure 45: Color scatterometry. **a)** Photograph of a nano-textured polymer disc. **b)** Typical color image acquired by the setup, showing one sample area. **c)** Region cropped from **b)** and corrected for light non-uniformities by scaling with the RGB intensity. **d)** Sketch of grating profile, with red boxes illustrating the RCWA simulation setup. **e)** Illustration of the orientation between line grating and incident polarization. **f)** Color images of each sample and the corresponding average RGB values. The side lengths are 1 mm.

The colors reflected from each sample were evaluated with a custom-built setup consisting of: a broadband LED lamp, three irises, a polarizing beamsplitter, and a RGB color camera, see Figure 46ab. The lamp provides unpolarized light, partially collimated by two irises, while the last iris blocks higher order diffractions. The polarizing beamsplitter effectively functions as a crossed polarizer and analyzer, by blocking the dominant reflection of unchanged polarization, and only transmits light that is rotated from *s*- to *p*-polarization. This polarization setup provides significantly larger color changes with respect to the grating dimensions, and outperforms typical scatterometry setups that use non-polarizing 50/50 beamsplitters<sup>[140,169,188]</sup>. However, as all light from non-structured samples is blocked, it was not possible to reference-correct the reflection spectra as normally done in scatterometry<sup>[140,169,188]</sup>. Instead the spectral properties of each component were calibrated independently, see Supplement Section S4. For a line grating to provide polarization conversion, the incident polarization must be angled with respect to the grating vector, with an angle of 45° providing maximum conversion while other angles yield identical spectra but with lower efficiencies<sup>[190,191]</sup>. The combination of no focus plane, a larger field of view of 5 x 7 mm<sup>2</sup>, and rotational independent colors, makes color scatterometry very stable with respect to vibrations and sample misalignments.

Theoretical reflection spectra were simulated by rigorous coupled-wave analysis (RCWA), which is a computationally efficient technique for calculating reflection efficiencies of periodic structures<sup>[140]</sup>. In RCWA, the structures are defined as horizontal slabs, for which Maxwell's equations are solved with appropriate boundary conditions between each slab to obtain the grating diffraction efficiencies, see Figure 45d<sup>[140,158]</sup>. For each sample a range of reflection spectra for different grating dimensions were simulated, and a database of corresponding camera RGB values calculated as described in element S3. By fitting the measured RGB values to the database, the grating dimensions were determined from the best matching simulation, defined by a minimum chi-square value. The 95 % CI on the dimensions were obtained from constant chi-square boundaries, and the final dimensional value obtained as the midpoint of the CI<sup>[140,192]</sup>.

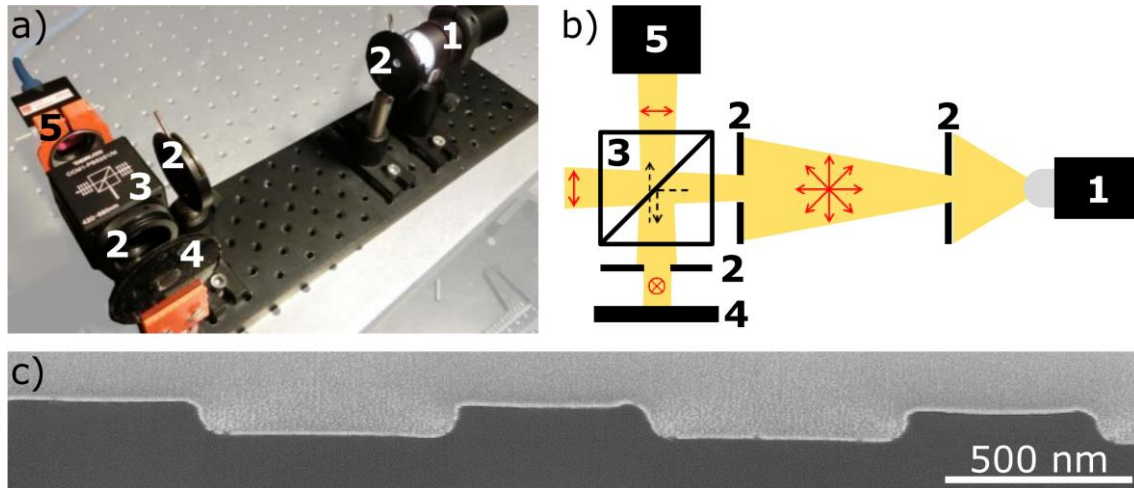


Figure 46: Experimental setup. **a)** Photograph of the setup, highlighted by a faded background. **b)** Sketch of setup with the main polarization orientations shown in red. **c)** FIB SEM images of typical grating profile. Numbers in a) and b) indicate: 1: LED lamp, 2: iris, 3: beamsplitter, 4: sample, 5: camera.

## Results and discussion

The reference values obtained by AFM and FIB SEM are shown in Figure 47a. All samples have similar heights and projected area filling factors, indicating good mold filling during fabrication. Only the 600 nm sample deviates with slightly lower values, which is attributed to micro-loading effects in the silicon etch process<sup>[193]</sup>. Three samples (1000, 2000, and 5000 nm) have large CIs on the slope values, due to demolding damages in the injection molding process, caused by thermal contraction of the polymer that results in scratched sidewalls<sup>[194]</sup>. Due to spatial variations of the damages, the CIs on the reference values indicate the variation of the grating profile across the sample, and not the accuracy of the reference instrument. Since scatterometry evaluates a mean value covering a larger area, the determined values must overlap the reference range.

The dimensions determined by color scatterometry are compared to the reference values in Figure 46a, and a good correlations for all three dimensions is seen. The color is obtained as the average color of a  $1 \times 1 \text{ mm}^2$  region for each sample, see Figure 45bcf. Only the 600 nm sample deviates in the filling factor. The height and filling factor are determined with average precisions of 7 % and 9 %, respectively, corresponding to 14 nm in the height and 3.5 percentage points in the filling factor. Compared to imaging scatterometry with corresponding values of 3.4 % and 3.0 %, the CIs are only two to three times larger<sup>[188]</sup>. Hence, when considering the significantly shorter measurement time for the presented method, the decrease in precision should not be prohibitive for quality control applications. The slope, however, is not as well defined, with CIs typically ranging from  $0^\circ$  to  $30^\circ$ . This is a fundamental limitation of scatterometry being a volume sensitive technique, where the slope only slightly affects the spectrum<sup>[188]</sup>. The 600 nm sample matches the reference height and slope, but deviates significantly in the filling factor. The bad fit is also indicated by a significantly larger chi-square value of 0.2, compared to typically  $\sim 0.01$  for the other samples. This single deviation is attributed to the small grating period, resulting in smooth spectra with small color variations. The period is an important parameter for light-structure interactions, and it cannot be expected that a given scatterometry technique covers all<sup>[140,195]</sup>.

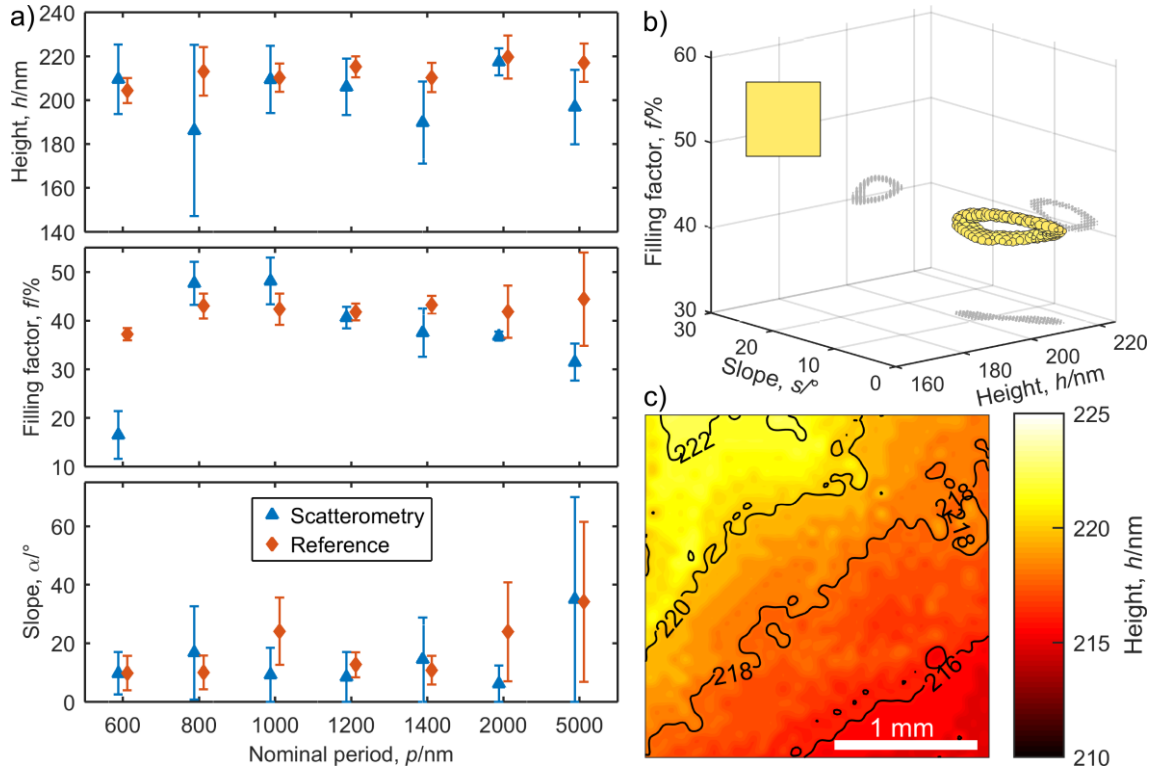


Figure 47: Experimental data. **a)** Grating dimensions determined for each sample by color scatterometry, and the corresponding reference values obtained with AFM and FIB SEM. Error bars indicate 95 % CIs. **b)** Illustration of raw fitting output for the 1200 nm sample. Each dot corresponds to a match between simulated and measured color, within the 95 % CI. Insert shows the measured color, while the markers are colored with the simulated RGB values. **c)** Contour plot of the fitted height variation over a 6 mm<sup>2</sup> sample area, obtained by dividing the image into 1300 individual regions.

The raw fitting is illustrated as a 3D graph in Figure 47b. The database covers the dimensional ranges shown by the  $x, y, z$ -axis, in total 15.500 different grating geometries. Each dot indicates a match between simulation and measurement, and the CIs in Figure 47a are determined as the smallest and largest value in each dimension. The marker color corresponds to the simulated color, while the insert shows the sample color. The gray dots illustrate plane projections of the 3D shape.

For some samples, a slight color change is seen across the surface, see Figure 45f. These long-ranged variations can be analyzed by dividing the image into small independent regions, instead of obtaining a single average value as done for Figure 47a. Such analysis is shown in Figure 47c, where a sample area of 2.5 mm x 2.5 mm is divided into regions of 10 x 10 pixels, and the color of each fitted independently to the RGB database. The analysis reveals a generally increasing height going from the upper left towards the lower right, hereby illustrating the possibilities of analyzing millimeter-sized areas with nanometer precision. The smallest possible crop region is 2 x 2 pixels, corresponding to a physical size of 11  $\mu$ m x 11  $\mu$ m. However, the actual imaging resolution is currently limited to 100  $\mu$ m due to limited collimation of the light. The resolution can easily be increased by applying a better collimation, or alternatively, by including a focusing lens.

Generally, the color scatterometry and reference precisions are similar, as illustrated by the confidence intervals in Figure 47a. However, a few samples deviate with much larger or smaller confidence intervals, e.g. the height for 800 nm and the filling factor for 2000 nm. The precision

depends mainly on the gradient of color change, where slowly varying colors result in a low precision due to redundancy effects, where a wide range of e.g. heights is equally probable, while on the contrary very, a drastic color changes yield a higher precision. The color gradient varies very irregularly with the grating dimensions, and can form strange shapes as seen from Figure 47b. Hence, to increase the precision in quality control applications, the control structures should be designed with dimension in high gradient regimes. The structures can also be designed to avoid duplicate colors within the range of possible dimensional values, since with the camera acquiring 12-bit RGB values; 69 billion different colors can be distinguished.

## Conclusions

In conclusion, we have presented a new method for optical characterization of nanoscale gratings, which we call “color scatterometry”. Color scatterometry is based on spectrographic scatterometry, but instead of obtaining a broad wavelength spectrum, it only evaluates the visual color of the sample, obtained with a single exposure by a RGB color camera. It can evaluate an area of several mm<sup>2</sup> in less than a second, and determine the grating dimension with nanometer precision. The height and filling factor are typically obtained with an accuracy of  $\pm 8\%$  (95 % CI), while the sidewall slope is within  $\pm 15^\circ$ . The method is tested on polymer samples with non-perfect grating profiles; hence, the presented confidence intervals should reflect realistic values obtainable in actual production environments. So far, color scatterometry has only been validated for line gratings, but adaption to 2D gratings should be straightforward since these structures also influence the specular reflected spectrum<sup>[188]</sup>.

## Funding

The Danish Agency for Science, Technology and Innovation (Industrial PhD Programme and the Advanced Technology Group (GTS)).

- - - End of paper reprint - - -

# Chapter 3.3

## Experimental setup

---

### 3.3.1 Imaging resolution

The lateral resolution of a microscope is often stated as the diffraction limit, also called the Rayleigh criterion<sup>[196]</sup>. The limit is based on the Airy disks arising from the diffraction of a point source, and the minimum resolvable distance defined as the distance from the peak to the first minimum<sup>[196]</sup>. The distance ( $d_0$ ) depends on the wavelength of the light ( $\lambda$ ) and the numerical apertures of the microscope ( $NA_{\text{objective}}$ ,  $NA_{\text{condenser}}$ ):

$$d_0 = \frac{1.22\lambda}{NA_{\text{objective}} + NA_{\text{condenser}}} . \quad (29)$$

However, since the color scatterometer performs lens-less imaging that relies on collimated light, it does not make sense to define a numerical aperture. Instead, the lateral imaging resolution is determined from the smallest distinguishable feature in an actual image. This test is shown in Figure 48, performed on an image of the logo of NIL Technology (Kongens Lyngby, Denmark). The intensity profile in Figure 48c reveals that the three black regions of the letter “N” are clearly distinguishable as valley 2, 3, and 4. From Figure 48b, the width of the bright regions between these three valleys is seen to be 50  $\mu\text{m}$ . However, this value is a bit uncertain, and it would be better to estimate the resolution from more simple structures, such as a point-like feature or parallel straight lines. Nevertheless, we are confident that the resolution is below 100  $\mu\text{m}$ .

For future work, the resolution can easily be improved by providing a better collimation of the light, though this will also result in a lower light intensity, hereby decreasing the signal to noise ratio due to longer exposure times of the camera.

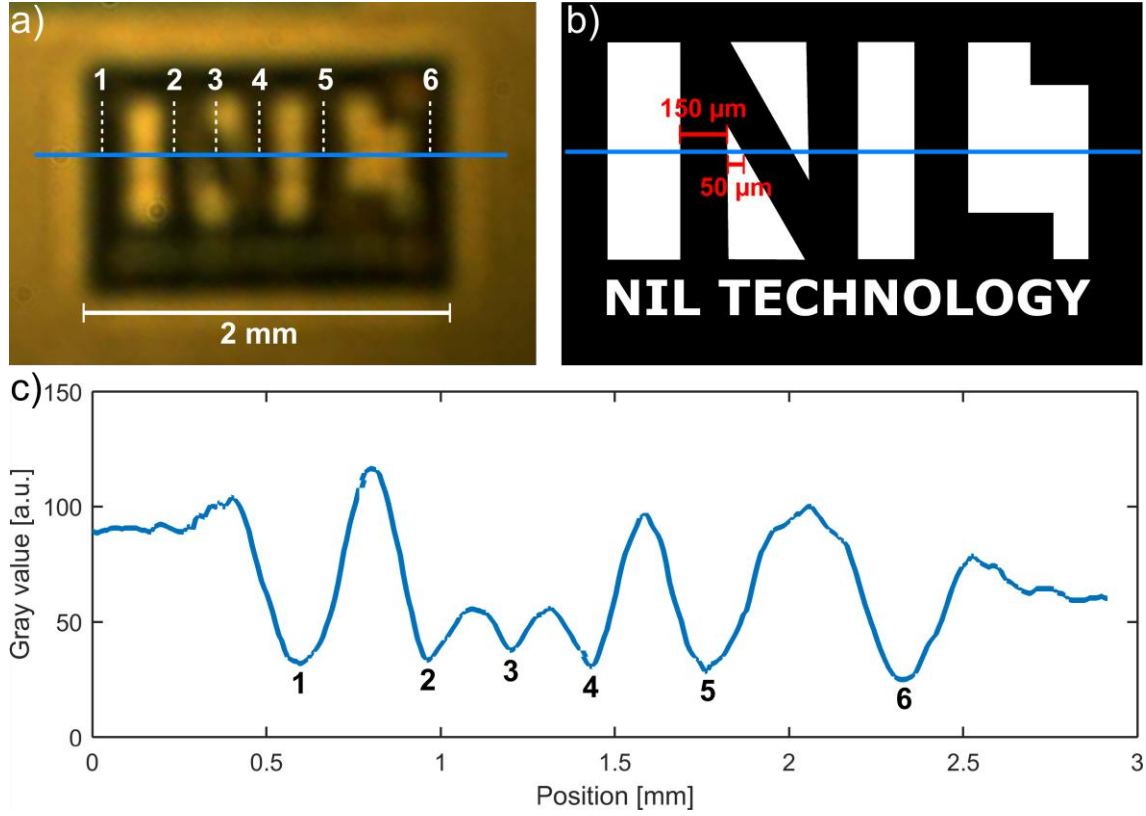


Figure 48: Evaluation of imaging resolution. **a)** Image acquired with color scatterometer depicting the NIL Technology logo. **b)** Illustration of the binary pattern defining the logo in **a)**. **c)** Intensity profile along the blue lines indicated in **a)** and **b)**. The numbers highlight the correlation between features in **a)** and **b)**.

### 3.3.2 Polarization conversion

As mentioned in the paper, a significant portion of the light reaching the camera is generated by polarization conversion on the sample. This design was chosen to provide a better sensitivity on the grating dimensions, since the off-diagonal matrix components in Equation (28) on page 76 were found to be more sensitive to changes in the grating dimensions, hereby resulting in larger color variations. Figure 49 illustrates the increased color variation with respect to the filling factor. The following will expand on the concept of polarization conversion.

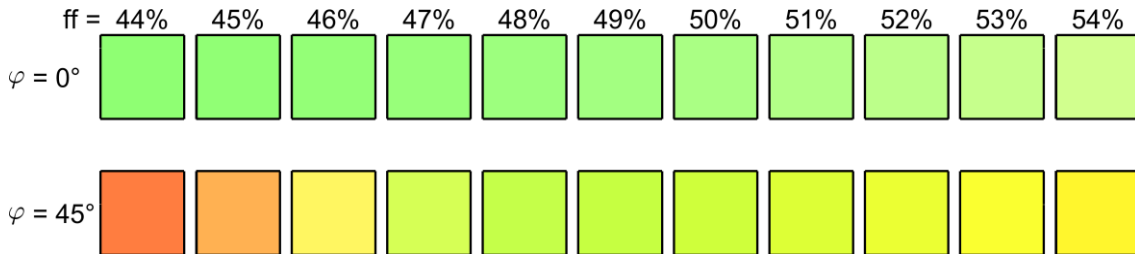


Figure 49: Color variations with respect to filling factor (ff) for incidence light of pure *s*-polarization ( $\varphi = 0^\circ$ ), and the angled incidence ( $\varphi = 45^\circ$ ) providing polarization conversion. The grating dimensions are: period = 1000 nm, height = 200 nm, sidewall slope =  $10^\circ$ .

The orientations of the two orthogonal polarization components are defined with respect to the plane of incidence, spanned by the surface normal and the propagation vector of the incident light. *S*-polarization has the electric field perpendicular to the plane (from the German word

*senkrecht*), while  $p$ -polarization has the electric field parallel to the plane, see Figure 50. The two orientations are also named trans-electric (TE) and trans-magnetic (TM), respectively. In the color scatterometer, the plane of incidence is not well defined due to the surface normal and propagation vector being parallel. Instead, the plane is spanned by the grating normal and the  $p$ -polarization vector, see Figure 50b.

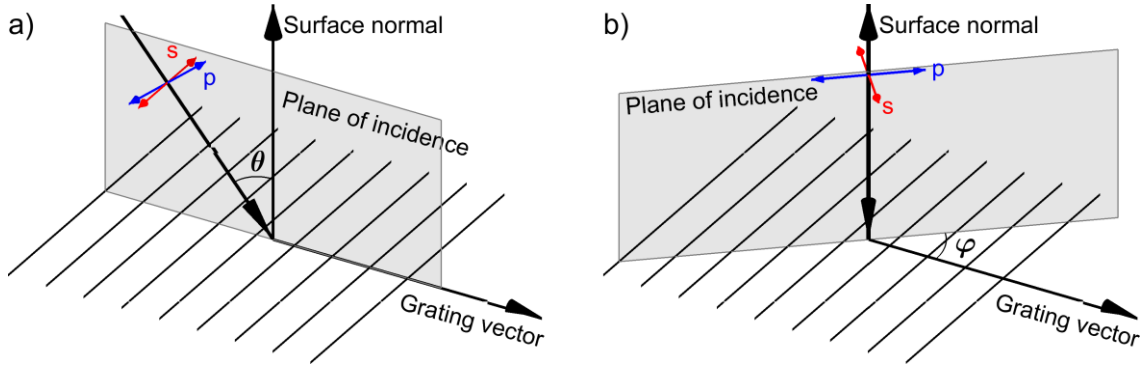


Figure 50: Coordinate system for light incident on a grating. **a)** Polarization aligned with grating lines ( $\varphi = 0^\circ$ ). **b)** Normal incidence ( $\theta = 0^\circ$ ) and polarization angled with respect to the grating vector.

When the incident light is polarized either parallel or perpendicular to the grating vector, the reflected light does not exhibit polarization conversion, due to the off-diagonal terms in Equation (28) being zero. However, if the incident polarization is angled with respect to the grating vector, as shown in Figure 50b, the reflected light will be a combination of both  $s$ - and  $p$ -polarization. The spectral reflection efficiencies for various azimuth angles ( $\varphi$ ) are shown in Figure 51. We see that for the pure incident polarizations of  $\varphi = 0^\circ$  ( $s$ ) and  $\varphi = 90^\circ$  ( $p$ ), the cross polarization terms ( $R_{s \rightarrow p}$  and  $R_{p \rightarrow s}$ ) vanish, while for all other angles, polarization conversion occurs. The conversion efficiency has a maximum at  $\varphi = 45^\circ$ , while other angles have identical spectral shapes but lower intensities. The intensity decrease from  $45^\circ$  to  $50^\circ$  is only around 2 %; hence, the setup is stable with respect to misalignments. The symmetry results in  $R_{s \rightarrow p}$  and  $R_{p \rightarrow s}$  always being identical and symmetric around  $45^\circ$ , while  $R_{s \rightarrow s}$  and  $R_{p \rightarrow p}$  are identical with respect to the rotation from  $0^\circ$  and  $90^\circ$ , respectively. We also see that the efficiencies of the polarization conversion terms are around 100 times smaller than the reflections of unchanged polarization.

With the polarizing beamsplitter, the purpose is to mainly evaluate the  $R_{s \rightarrow p}$  component. However, the reflected light from the beamsplitter is only around 99%  $s$ -polarized, hence also containing  $\sim 1\%$   $p$ -polarization, see calibration in Section 3.5.3. Since the  $R_{p \rightarrow p}$  efficiency is around 100 times greater than  $R_{s \rightarrow p}$ , the small amount of incident  $p$ -polarization actually provides a significant contribution to total intensity after reflection from the sample. Consequently, the final spectrum at the camera will be close to an equal combination of the  $R_{s \rightarrow p}$  and the  $R_{p \rightarrow p}$  spectra.

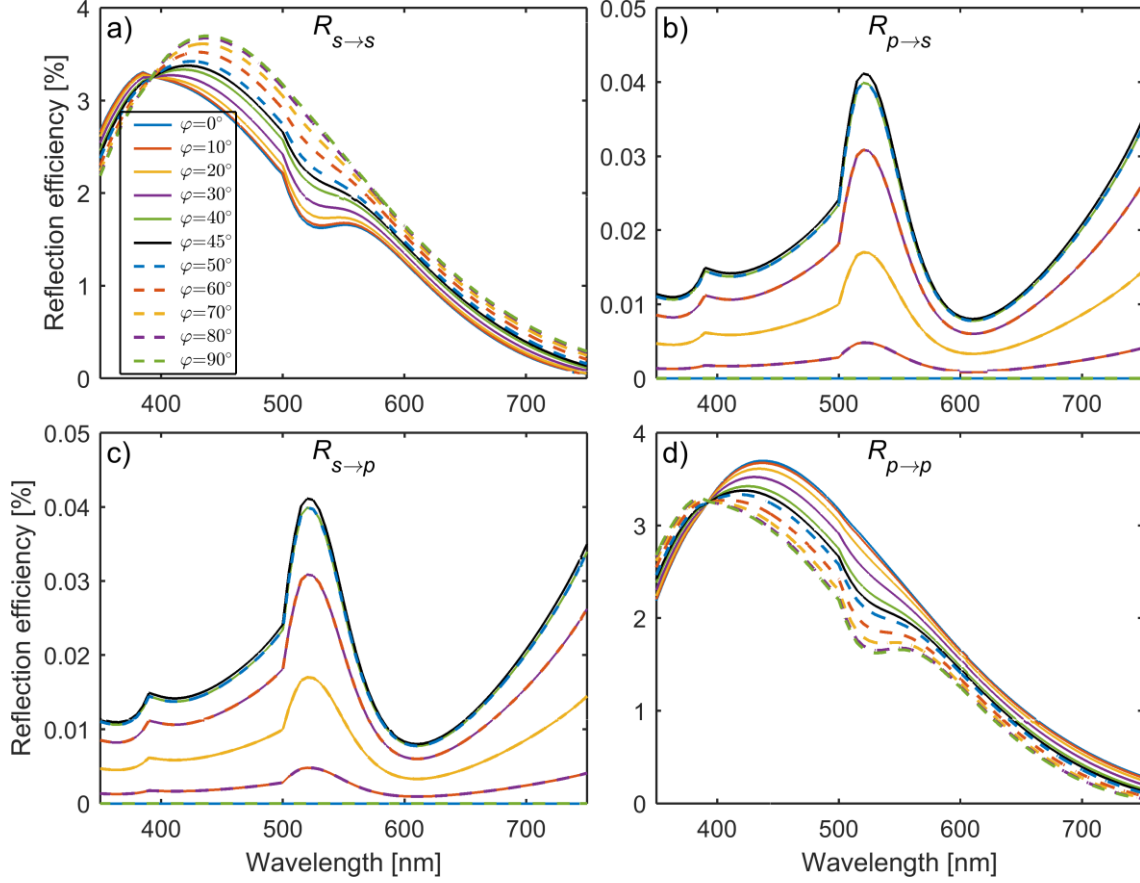


Figure 51: Reflection efficiencies of a typical line grating for different azimuthal angles of the incident polarization. **a)** Shows the efficiency of  $R_{s \rightarrow s}$ , **b)** of  $R_{p \rightarrow s}$ , **c)** of  $R_{s \rightarrow p}$ , and **d)** of  $R_{p \rightarrow p}$ , see Equation (28) on page 76. The legend and the axis labels refer to all figures.

The concept of structured surfaces providing polarizing effects is also known as “form birefringence” and was first described by Sir C. V. Raman in 1950<sup>[197]</sup>. The setup with the incidence polarization angled with respect to the grating normal, is often termed “conical mounting”, due to the diffraction orders forming a cone shape instead of being distributed in the plane of incidence<sup>[190,198]</sup>. Form birefringence is similar to the bulk birefringence of crystals<sup>[147]</sup>, but instead of an anisotropic crystal structure the anisotropic surface pattern provides the birefringence. The effect has mainly been studied for metal gratings<sup>[198–201]</sup>, probably due to the significantly higher efficiency than for dielectrics, with reported conversion efficiencies of up to 100 % for certain configurations<sup>[202]</sup>.

### 3.3.3 Relative scaling of colors

The simulated color of each grating might not only differ in the actual hue, but also in the total reflection efficiency, resulting in a different lightness and saturation of the color. However, as described in the paper, all colors are scaled individually and the intensity information lost. The scaling is required as the setup is not absolute calibrated, hence only the relative spectral shape of the spectrum reaching the camera can be determined from the simulations. The simulated RGB values are scaled with the intensity, given as the sum of the three channels:

$$R_{\text{scaled}} = \frac{R_{\text{original}}}{R_{\text{original}} + G_{\text{original}} + B_{\text{original}}} , \quad (30)$$

with similar equations for the green and blue channels.

The scaling effectively reduces the number of variables from three to two, resulting in increased CIs on the fitted grating dimension, as illustrated in Figure 52. This figure shows the output of two fitting routines using the same database and measured RGB values. In Figure 52a the colors are scaled individually by Equation (30), as in Paper 4, while in Figure 52b the colors are all scaled by a common value, to simulate the use of absolute color intensities. The plotted colors correspond to the simulated color for a given height and filling factor, but where Figure 52a features equally bright colors for all simulations, the absolute colors in Figure 52b also show a spatial intensity variation, seen as brighter and darker regions. The different CIs in the two graphs, indicated by the black lines, show how the color scaling reduces the fitting confidence and significantly increase the CIs on the determined grating dimensions.

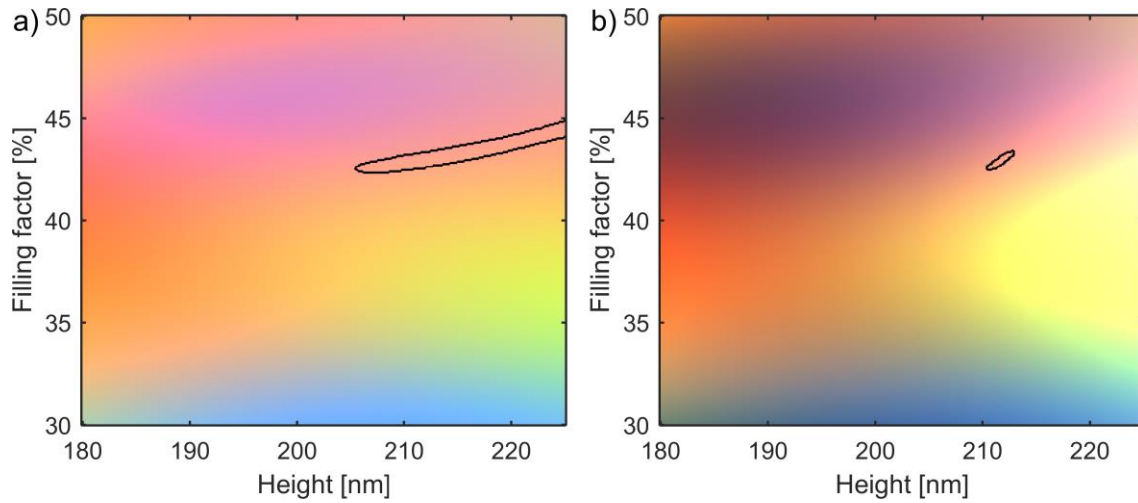


Figure 52: Effect of color scaling. A fit of measured RGB values to the simulated RGB database with **a)** colors scaled by Equation (30), and **b)** colors scaled to a common value to simulate the use of absolute colors. Black lines indicate the 95 % CIs of the fitting process.

For obtaining an absolute calibration of the setup, the light source spectrum should be evaluated in terms of the power per steradian per wavelength (W/sr/m), meaning the number of photons at each wavelength emitted into any given solid angle. From this, the spectral irradiance incident on the sample could be calculated from the collimation loss and the beamsplitter reflectance. After also accounting for the beamsplitter transmittance, the absolute RGB value would be determined by multiplying the final spectrum with the quantum efficiency of the camera, and taking the sum of this spectrum. The quantum efficiency is the percentage of photons striking a pixel that is converted to an electric signal. Such calibrations could be achieved with an absolute calibrated spectrophotometer, although it would require more controlled calibration setups, with precise knowledge of the distances between light sources and detectors, along with the sensor sizes and acceptance angles of all detectors.

# Chapter 3.4

## Simulations

---

### 3.4.1 Simulation setup

The generation of the simulation database is a central part of scatterometry, and it is important that the simulations describe the physical system as accurately as possible. For an RCWA simulation, four main factors must be defined: the grating geometry, the refractive index of the grating, the number of terms included in the Fourier series, and the number of slabs in the staircase approximation. RCWA simulations can be performed with an arbitrary level of accuracy, by increasing the number of terms included in the Fourier series ( $n$ )<sup>[157]</sup>. However, including more terms also increases the memory requirements and the simulation time, which approximately scale with  $n$  to the power of four and six, respectively<sup>[203]</sup>. Another factor affecting the accuracy is the density of slabs in the staircase approximation, as shown in Figure 43 on page 76. Increasing the number of slabs ( $m$ ) also increases the visual resemblance with a smooth sidewall; however, the accuracy of the simulated diffraction efficiencies does not necessarily follow the same trend. The electric field experiences large gradients along the edge regions, and as these increase with a higher density of slabs, the truncation of the Fourier series becomes more important, and the value of  $n$  needs to be increased simultaneously<sup>[159,203]</sup>. To determine the appropriate number of Fourier terms and slabs that yield a sufficient accuracy with a reasonable simulation time, a convergence test must be performed for the actual gratings simulated.

#### 3.4.1.1 Convergence test

A convergence test is performed with multiple simulations of the same grating, but using different values of  $m$  and  $n$ . The resulting efficiencies compared to the “true” reflection efficiencies, obtained from a simulation with a large value of  $m$  and  $n \gg m$ . The convergence test for  $m$  is seen in Figure 53, and we see that both  $R_{s \rightarrow s}$  and  $R_{s \rightarrow p}$  vary significantly with the value of  $m$ . Figure 53cd reveals that, for some wavelengths, the deviation exceeds 10 %. To stay within a deviation of approximately  $\pm 1$  %, the number of slabs should be at least  $m = 20$ . Similar test were performed for grating periods of 600 nm and 5000 nm and these supported the same conclusion, see Appendix A2.

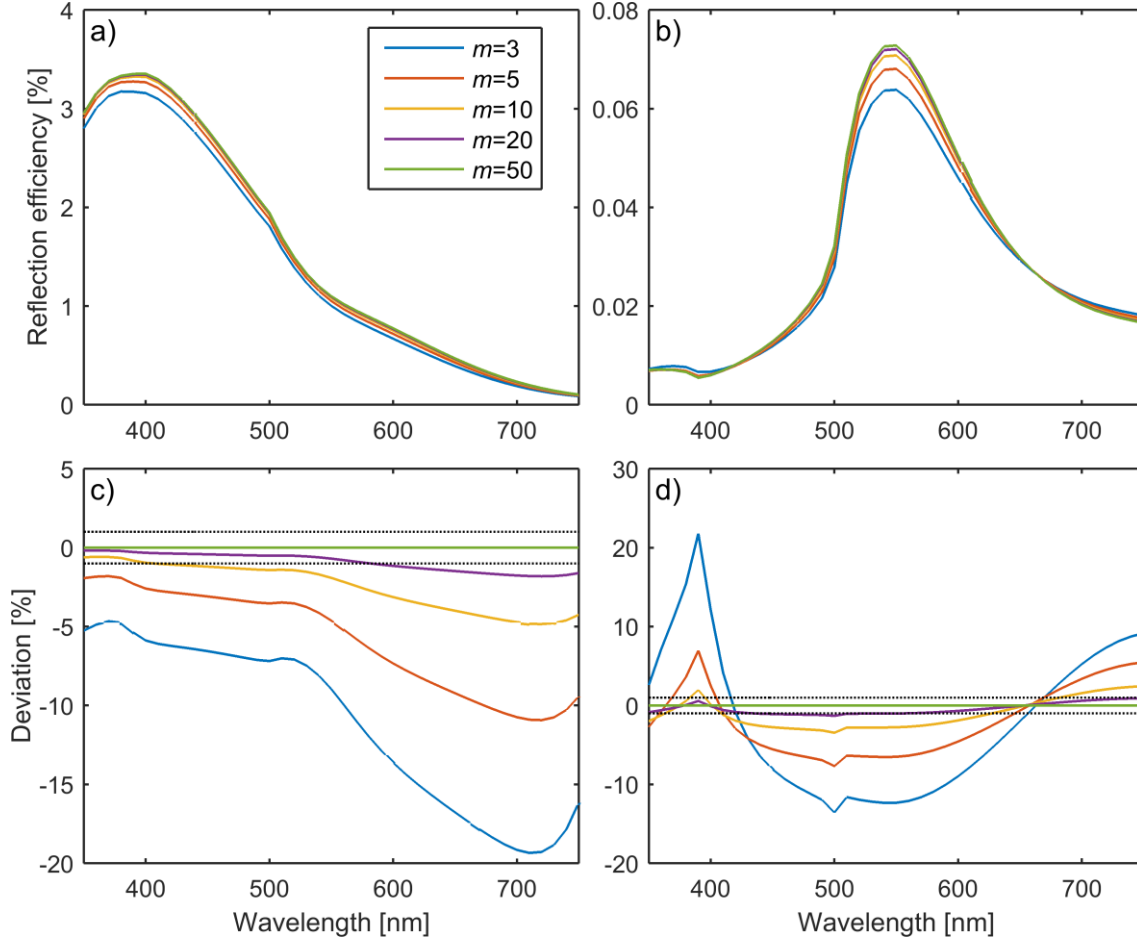


Figure 53: Convergence test for the number of slabs ( $m$ ). **a)** and **b)** show the reflection efficiencies for  $R_{s \rightarrow s}$  and  $R_{s \rightarrow p}$ , respectively. **c)** and **d)** show the corresponding deviations from the  $m = 50$  spectrum. The dotted lines indicate deviations of  $\pm 1\%$ . The grating dimensions are: period = 1000 nm, height = 200 nm, filling factor = 50 %, sidewall slope =  $10^\circ$ , while the incident field has  $\theta = 0^\circ$  and  $\varphi = 45^\circ$ . For all simulations  $n = 10m$ .

A similar test is performed for  $n$ , and the results are shown in Figure 54. We see that the  $R_{s \rightarrow s}$  spectrum is sufficiently modeled with  $n = 10$ , while  $R_{s \rightarrow p}$  requires  $n = 40$ , to stay within a deviation of approximately  $\pm 1\%$ . However, the same test performed for the 5000 nm grating revealed a requirement of at least  $n = 80$ . Hence this number should be used for longer periods while for shorter periods  $n = 40$  is sufficient. The tests for periods of 600 nm and 5000 nm are shown in Appendix A2. To reduce the simulation times, the actual simulation databases were performed with  $m = 10$  and  $n = 40$  for all sample periods, as this provides an adequate accuracy within most of the spectrum.

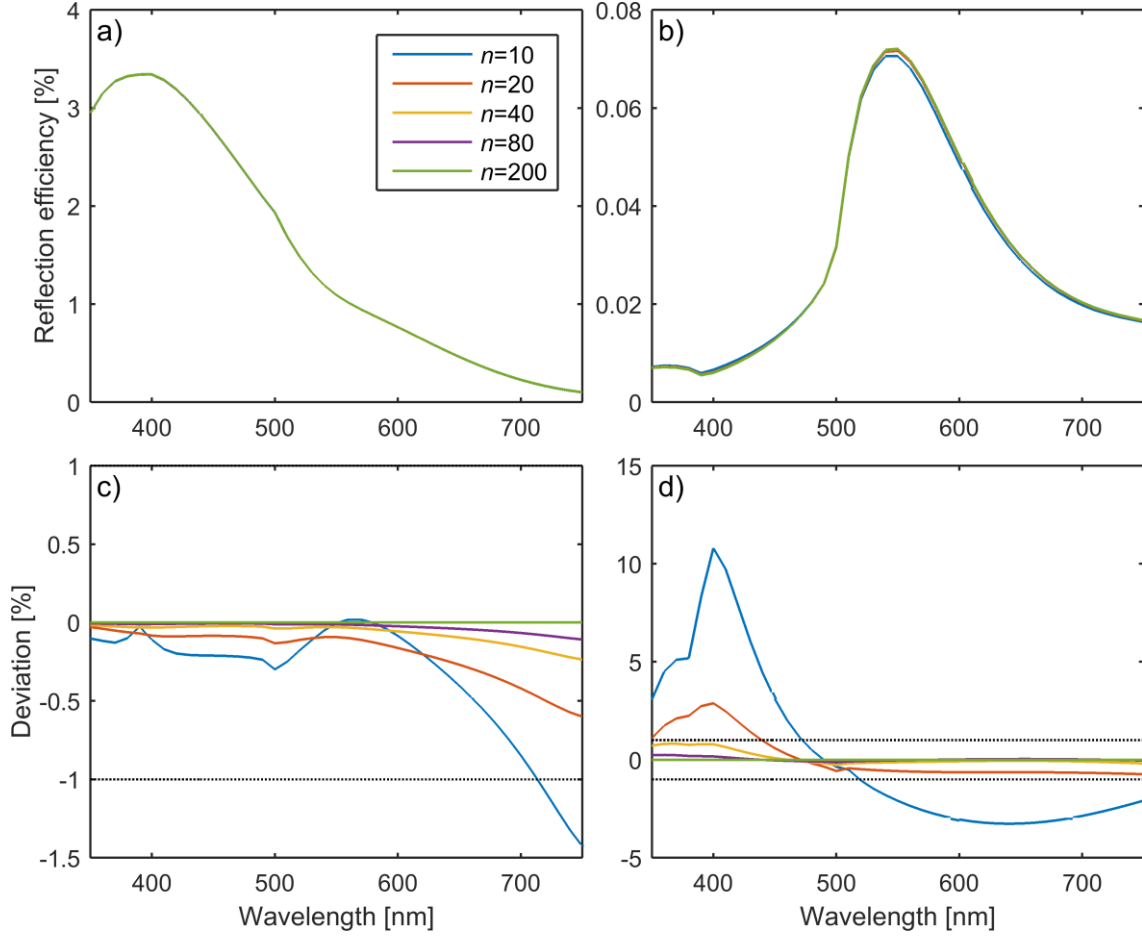


Figure 54: Convergence test for the number of included terms in Fourier series ( $n$ ). **a)** and **b)** show the reflection efficiencies for  $R_{s \rightarrow s}$  and  $R_{s \rightarrow p}$ , respectively. **c)** and **d)** show the corresponding deviations from the  $n = 200$  spectrum. The dotted lines indicate deviations of  $\pm 1\%$ . The grating dimensions are: period = 1000 nm, height = 200 nm, filling factor = 50 %, sidewall slope =  $10^\circ$ , while the incident field has  $\theta = 0^\circ$  and  $\varphi = 45^\circ$ . For all simulations  $m = 20$ .

### 3.4.1.2 Comparison with FEM

Besides the validation of adequate precision, the RCWA simulations are validated with respect to the accuracy by a comparison with FEM simulations. The FEM simulations are performed using COMSOL Multiphysics (COMSOL 5.2, COMSOL Inc., Sweden), and the grating simulated as a 2D structure using the Electromagnetic waves module. Only one grating period is defined, and Floquet periodic boundary conditions applied to model an infinite grating. To accurately model the diffracted energy, an input and output port is defined for each diffraction order, and the mesh element size is approximately one tenth of the shortest wavelength, see setup in Figure 55. The grating dimensions are identical to the ones used in Figure 53 and Figure 54, but the incident field is simulated for pure  $s$ -polarization and pure  $p$ -polarization, corresponding to  $\varphi = 0^\circ$  and  $\varphi = 90^\circ$ , respectively.

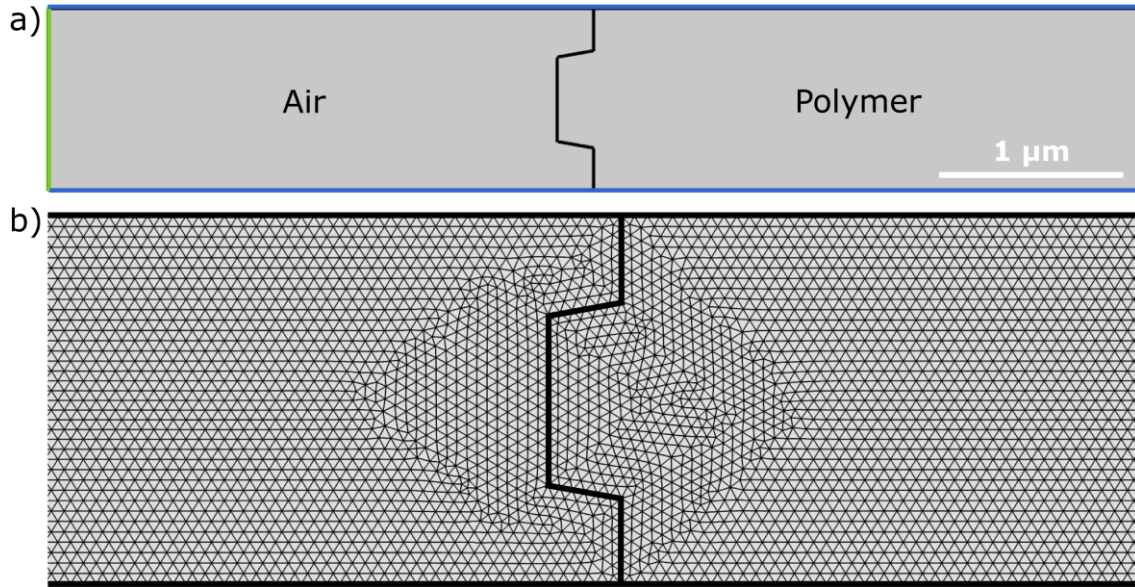


Figure 55: FEM simulation setup. **a)** The geometry with color indications of the boundary conditions: input port (green), output port (red), Floquet boundaries (blue). **b)** Illustration of the mesh in the central grating region.

The FEM and RCWA simulations are compared in Figure 56, which shows a good correlation between the two methods. A small numerical instability is seen for the FEM simulation at short wavelengths, where it fluctuates around the RCWA values. Probably due to the mesh not being fine enough for these wavelengths. To illustrate the computational efficiency of RCWA, the computational time for the FEM simulations was 14 min, while the RCWA simulations only took 5 s.

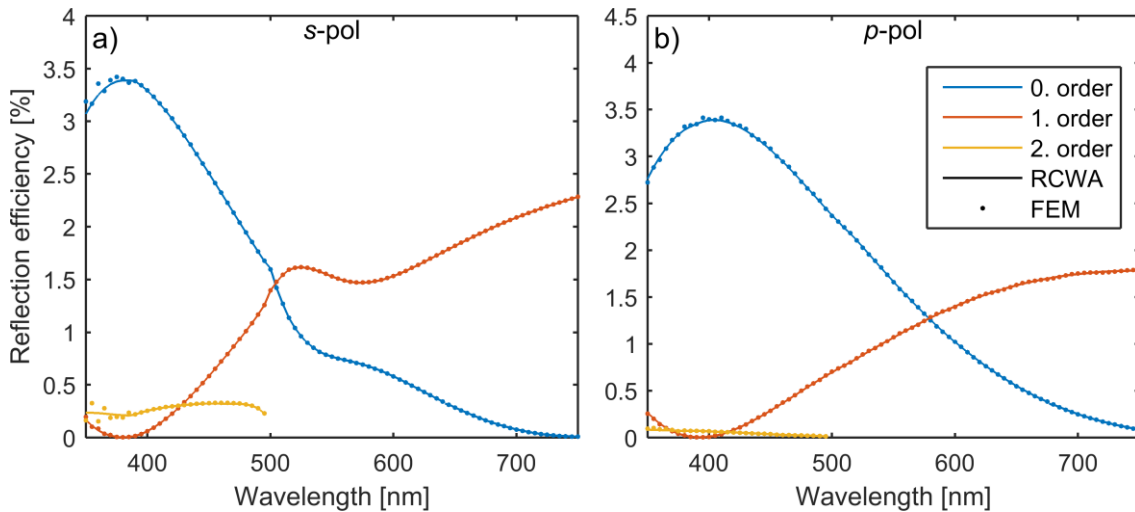


Figure 56: Comparison of FEM and RCWA simulations. **a)** The reflection efficiencies simulated for incident and detected *s*-polarization, and **b)** for *p*-polarization. The legend and the axis labels refer to both figures.

### 3.4.2 Calculation of colors

For the generation of the RGB database, the simulated reflection spectrum for each grating is converted to the corresponding color evaluated by the camera. The correlation between the spectrum reaching the camera and the detected color was described in Section 3.1.2; instead, this section describes how the final spectrum reaching the camera is determined.

The RCWA simulation output is the amplitude reflection coefficients for the electromagnetic fields, as described in Section 3.1.3.1. A practical theoretical framework for working with electromagnetic fields is the Jones matrix formalism<sup>[148]</sup>, also called Jones calculus. In this formalism, the electromagnetic field is described by a two-column vector of the *s*- and *p*-polarization, and each optical component described by a 2 x 2 matrix. The interaction between the field and a component is determined by the product between the corresponding vector and matrix<sup>[148]</sup>. Before reaching the camera, the light interacts with three components: reflection in the beamsplitter ( $\mathbf{R}_B$ ), reflection of the sample ( $\mathbf{r}_{\text{sample}}$ ), and transmission through the beamsplitter ( $\mathbf{T}_B$ ), resulting in the equation:

$$\begin{aligned} \mathbf{E}_{\text{final}} &= \mathbf{T}_B \mathbf{r}_{\text{sample}} \mathbf{R}_B \mathbf{E}_{\text{incident}} \Leftrightarrow \\ \begin{bmatrix} E_{\text{final}, s} \\ E_{\text{final}, p} \end{bmatrix} &= \begin{bmatrix} T_s & 0 \\ 0 & T_p \end{bmatrix} \begin{bmatrix} r_{s \rightarrow s} & r_{p \rightarrow s} \\ r_{s \rightarrow p} & r_{p \rightarrow p} \end{bmatrix} \begin{bmatrix} R_s & 0 \\ 0 & R_p \end{bmatrix} \begin{bmatrix} E_{\text{inc}, s} \\ E_{\text{inc}, p} \end{bmatrix} \\ &= \begin{bmatrix} (E_{\text{inc}, s} r_{s \rightarrow s} R_s + E_{\text{inc}, p} r_{p \rightarrow s} R_p) T_s \\ (E_{\text{inc}, s} r_{s \rightarrow p} R_s + E_{\text{inc}, p} r_{p \rightarrow p} R_p) T_p \end{bmatrix}. \end{aligned} \quad (31)$$

The camera does not evaluate the E-fields but the light intensity, hence the final spectrum is determined as:

$$\begin{aligned} I_{\text{final}} &= \begin{bmatrix} E_{\text{final}, s}^* & E_{\text{final}, p}^* \end{bmatrix} \begin{bmatrix} E_{\text{final}, s} \\ E_{\text{final}, p} \end{bmatrix} \\ &= (E_{\text{inc}, s} r_{s \rightarrow s} R_s + E_{\text{inc}, p} r_{p \rightarrow s} R_p) (E_{\text{inc}, s}^* r_{s \rightarrow s}^* R_s + E_{\text{inc}, p}^* r_{p \rightarrow s}^* R_p) T_s^2 \\ &\quad + (E_{\text{inc}, s} r_{s \rightarrow p} R_s + E_{\text{inc}, p} r_{p \rightarrow p} R_p) (E_{\text{inc}, s}^* r_{s \rightarrow p}^* R_s + E_{\text{inc}, p}^* r_{p \rightarrow p}^* R_p) T_p^2, \end{aligned} \quad (32)$$

where \* denotes the complex conjugate. This calculation is carried out in Matlab for all simulated spectra, using the reflection and transmission properties for the beamsplitter, and the emission spectrum of the light source, see calibrations in Chapter 3.5.

The RGB color evaluated by the camera is then determined as:

$$R = \int_{350\text{nm}}^{750\text{nm}} I_{\text{final}}(\lambda_i) S_{\text{cam}, R}(\lambda_i) d\lambda, \quad (33)$$

where  $R$  is the value of the “red” pixels,  $S_{\text{cam}, R}$  the camera spectral sensitivity for the red channel (R), and  $\lambda_i$  the wavelength of the light. The integration limits of 350 nm and 750 nm ensure that the full sensitivity range of the camera is included. Similar equations were used for the green (G) and blue (B) camera channels. The integral is performed in Matlab using the “trapz” function, which uses trapezoids to perform a numerical integration.

### 3.4.3 Database resolution

When generating the simulation database the range and the step size of each grating parameter have to be resolved. The range is typically determined by the range of expected values, while the color gradients determine the step size. A typical database for the presented experiments contains 15.000 different grating geometries, corresponding to approximately 25 different values for each of the three parameters. However, the step sizes are optimized individually for each parameter and each grating, to ensure a sufficient resolution of the color changes, while also considering the total simulation time. For an illustration of the color changes and the relation between dimensions and the color change, see Figure 57. This graph shows smoothly varying colors with respect to the filling factor, and the variations nicely resolved by the step size of 0.5 percentage points. The largest gradient in this plot is  $\sim 10\%$ , and this value was chosen as a rough limit for determining the step sizes of each parameter. To analyze the gradient distribution of the entire database, three histograms of the color gradients along each grating parameter is seen in Figure 58. We see that almost all gradients are below the 10 % limit. Only the slope deviates with around half of the gradients above this value, indicating that the step size should be decreased by a factor of 2. However, as the slopes were always determined with rather large uncertainties, the gradients on this parameter is not that critical, and they were often allowed to exceed the 10 % limit, to help reduce the database size and simulation time.

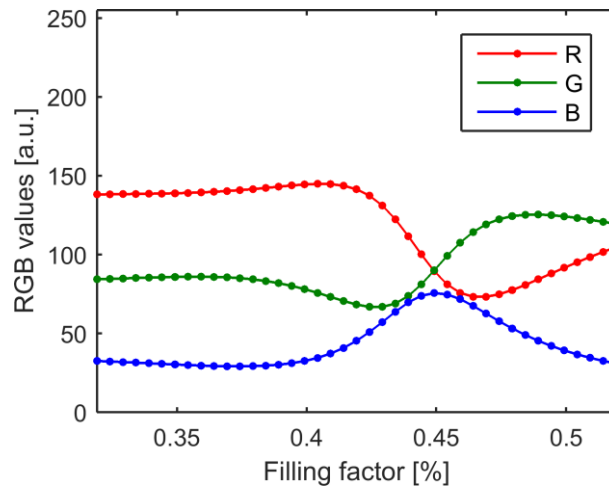


Figure 57: Illustration of a typical relation between the RGB values and the grating filling factor. The filling factor steps size is 0.5 percent points, while the fixed grating dimensions are: period = 1000 nm, height = 220 nm, slope =  $5^\circ$ . The RGB values are shown in the 8-bit range from 0 to 255.

Even though the curves in Figure 57 are smoothly varying, the difference between adjacent RGB values is up to 11 a.u. Hence, if the measured color has RGB values in-between two simulations, the fitting process might not deem these grating a good fit. This problem can be resolved by decreasing the step sizes to a level where the RGB values do not change more than e.g. 1 a.u. between each simulation. Unfortunately, such detailed simulations are not realistic, as this would require  $\sim 14$  times the number of simulations, resulting in a total simulation time of  $\sim 10$  days, for the database analyzed in Figure 57 and Figure 58.

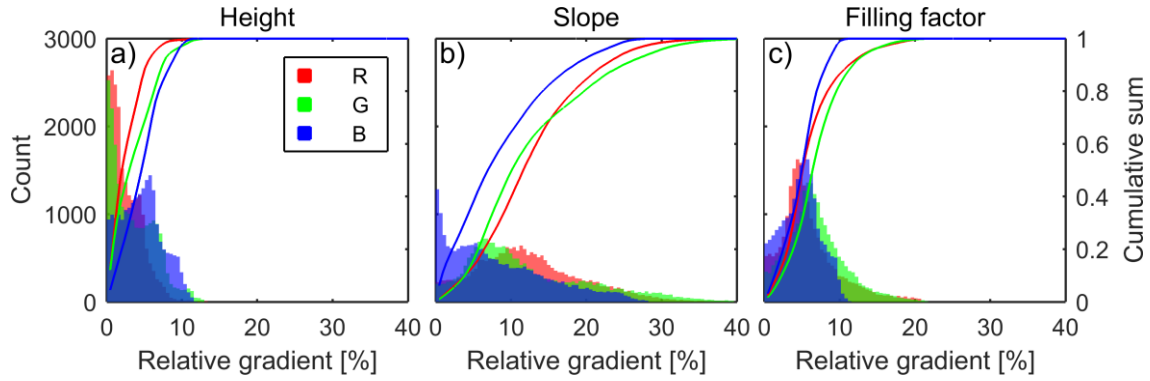


Figure 58: Histograms of color gradients, along with the cumulative sum for each channel. The gradients are determined along each of the three grating parameters, **a)** the height, **b)** the side-wall slope, and **c)** the filling factor. The step sizes are: height = 2.5 nm, slope = 2.5°, filling factor = 0.5 percentage points. Legend and y-axis labels refer to all graphs.

However, since the color changes are smoothly varying functions, the intermediate points can be interpolated, as shown in Figure 59. We see that the interpolation provides significantly more positive matches, not only centered closely around the initial points in a), but it also finds the intermediate points and more clearly defines the shape of the matching region. Considering the region around (5°, 200 nm, 45 %) that has very few positive fits in a), this region probably contains steep color gradients with gaps between the adjacent RGB values. By interpolating the intermediate colors, these gaps are closed, and the fitted points show a much smoother relation. As long as the databases are confirmed not to contain steep gradients, as done in Figure 58, the interpolation provides a more accurate representation of the matching gratings, without needing an excessive amount of simulations. The interpolation is performed linearly between adjacent values, using the Matlab function “griddedInterpolant”.

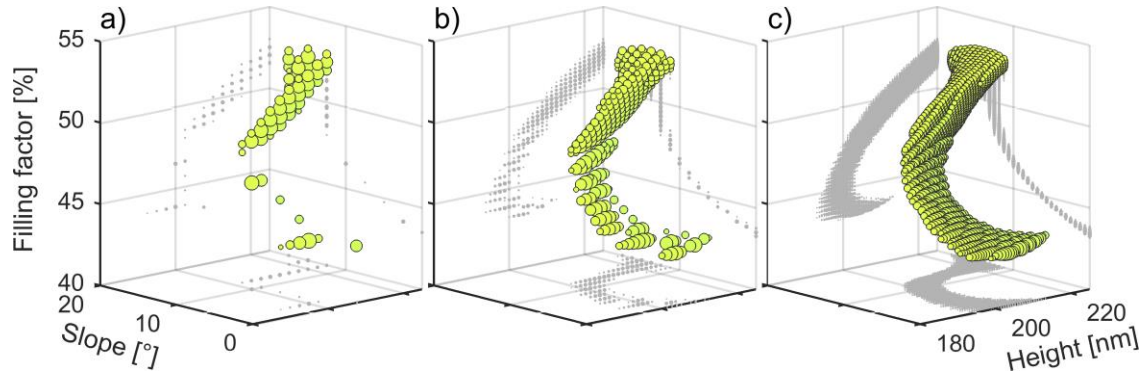


Figure 59: Illustration of the interpolation of data points. **a)** The original simulation data, **b)** with the step sizes decreased by a factor of two, and **c)** the step sizes decreased by a factor of four. The gray dots illustrate the projection onto each axis. The axis labels refer to all three plots.

# Chapter 3.5

## Calibrations

---

For spectroscopic scatterometry, the setup is continuously referenced by scaling the sample spectrum with a reference spectrum, obtained from a known sample such as a mirror or silicon wafer<sup>[140]</sup>. Unfortunately, such internal referencing is not possible with the color scatterometer, due to the polarizing beamsplitter effectively blocking all light reflected from smooth surfaces. Instead, the final spectrum recorded by the camera is determined from Equation (32) and (33) on page 93. To perform these calculations, each component in the setup is calibrated with respect to the spectral and polarizing properties

### 3.5.1 Camera

The camera is a CMOS color camera (BFLY-U3-23S6C, Point Grey Research, Inc., USA), with 2.3 megapixels and a pixel size of 5.86  $\mu\text{m}$ . The pixel values are saved in 16-bit format, though the analog to digital conversion is only performed at 12-bit. The manufacturer provides detailed test results of the camera performance, though only typical values for the camera model and they do not provide a value of the expected inter-camera variations. This section presents our calibration of the spectral sensitivity, while the warmup time is presented in Appendix A4.

A camera is a complex device where many components influence the spectral sensitivity. The main ones in relation to this analysis are the color filters and the pixels. The color filters consist of an infrared filter covering the entire sensor, and a color filter array (CFA) arranged in a Bayer filter pattern. The Bayer CFA is also termed an “RGGB” filter because it is composed of three filters a red (R), a green (G), and a blue (B), arranged in a 2 x 2 unit cell with G repeated twice. This is the most common CFA layout for digital cameras<sup>[204]</sup>, though for our application, a chip with four different colors would be beneficial, as this provides more information on the spectral distribution. In the early days of digital photography, some manufacturers experimented with four-color CFAs also contained cyan (C), yellow (Y), or magenta (M). With time the Bayer CFA replaced all others, and the last consumer camera with a different filter was produced more than ten years ago<sup>[205–207]</sup>.

Since the camera features a CMOS sensor where each pixel contains an amplifier, each pixel should be calibrated individually, as there might be small differences in the efficiency of each circuit. However, since the camera values are only used as average values of many pixels, these small variations are assumed negligible.

### 3.5.1.1 Spectral sensitivity

The absolute spectral sensitivity of a camera is given by the quantum efficiency of each channel. However, for this calibration, we will determine the *relative* spectral sensitivity for each channel. The spectral sensitivity is determined as described in the industry standard by the European Machine Vision Association (EMVA), called EMVA Standard 1288<sup>[208]</sup>. The standard is intended to ease the comparison of cameras from different manufacturers, and it describes the calibration procedures for several camera performance values. For a quick introduction see reference<sup>[209]</sup>. Point Grey also uses this standard to obtain the camera data they provide. The general concept is the well-established method of acquiring images of monochromatic light, and scaling the pixel value for each wavelength with the reference intensity obtained with a calibrated photodetector<sup>[210]</sup>. The EMVA standard does take it a bit further, by requiring two images and two dark images at 50 different exposure times for each wavelength, and from these determines the wavelength dependent responsivity ( $R$ ), gain ( $K$ ), and quantum efficiency ( $\eta = R/K$ ). The responsivity and gain are determined as the slopes of two linear fits to the irradiation versus pixel value, and pixel value versus pixel variance, see Figure 60. For a relative calibration, the irradiation in photons per pixel is substituted with the camera exposure time, as these values are proportional. The motivation is presumably to obtain better statistics, by fitting to the response of 50 images instead of a single one. The relation for  $\eta$  is based on a linear model of the camera, with the mean ( $\mu$ ) and variance ( $\sigma^2$ ) of the pixel values given by<sup>[208]</sup>:

$$\mu_{\text{exp}} = \mu_{\text{dark}} + K\eta n_{\text{photons}} \quad (34)$$

$$\sigma_{\text{exp}}^2 = \sigma_{\text{dark}}^2 + K(\mu_{\text{exp}} - \mu_{\text{dark}}) \quad , \quad (35)$$

where  $n_{\text{photons}}$  is the number of photons striking each pixel (proportional to the exposure time), and  $R = K\eta$ . The subscripts of  $\mu$  and  $\sigma$  refer to whether the values are obtained from the dark images or the ones exposed to monochromatic light. The dark corrected values in Figure 60 corresponds to:  $\mu_{\text{exp}} - \mu_{\text{dark}}$  and  $\sigma_{\text{exp}}^2 - \sigma_{\text{dark}}^2$ .

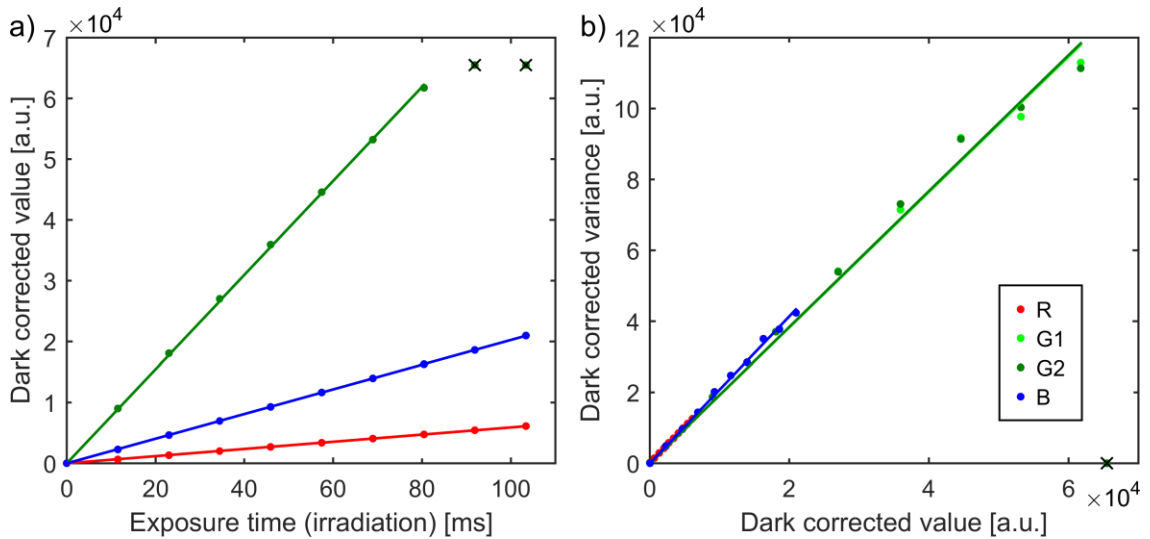


Figure 60: Graphs from the camera calibration at 520 nm. **a)** The linear fit used to obtain the responsivity ( $R$ ), and **b)** the fit to obtain the gain ( $K$ ). The fits are performed for each channel and are shown as solid lines. The two images with exposure times above 90 ms are saturated in the green channel and are omitted from the analysis.

The setup consists of a broadband light source (HPX2000, Ocean Optics Inc., USA), a computer-controlled monochromator (CM110 1/8 m Monochromator, Spectral Products, USA) with 0.3 mm slits to provide sharp spectral peaks, a glass diffuser to ensure a homogeneous illumination, a calibrated spectrometer (see Appendix A4), and the camera, both computer controlled. The monochromator scans the light from 350 nm to 750 nm in 2 nm intervals, while the spectrometer acquires the reference intensities, the peak wavelengths, and the peak full width at half maximum (FWHM) for each wavelength setting. The spectrometer is then replaced by the camera, and images acquired for the identical wavelength settings. For our calibration, the recommended 50 exposures per wavelength are reduced to 10, to shorten the evaluation time and the required computer storage. Otherwise, with 50 exposure settings of 2 images and 2 dark images each, the total file size would be around 80 GB. The lamp, spectrometer, and camera had all warmed up for several hours, and the reference spectrums were measured several times both before and after the image acquisitions, to confirm the monochromator output is stable with respect to both intensity and peak wavelength. For each wavelength setting, the peak is fitted with a Gaussian function to obtain the sub-pixel wavelength and intensity values. A stability test is presented in Figure 61a-b, by comparing the values obtained before and after the actual image acquisition. A good correlation is seen, with the intensity difference below 1 % for almost the entire spectral range, and wavelength differences below 0.05 nm. The FWHM (not shown) varies from 3.0 nm to 2.6 nm.

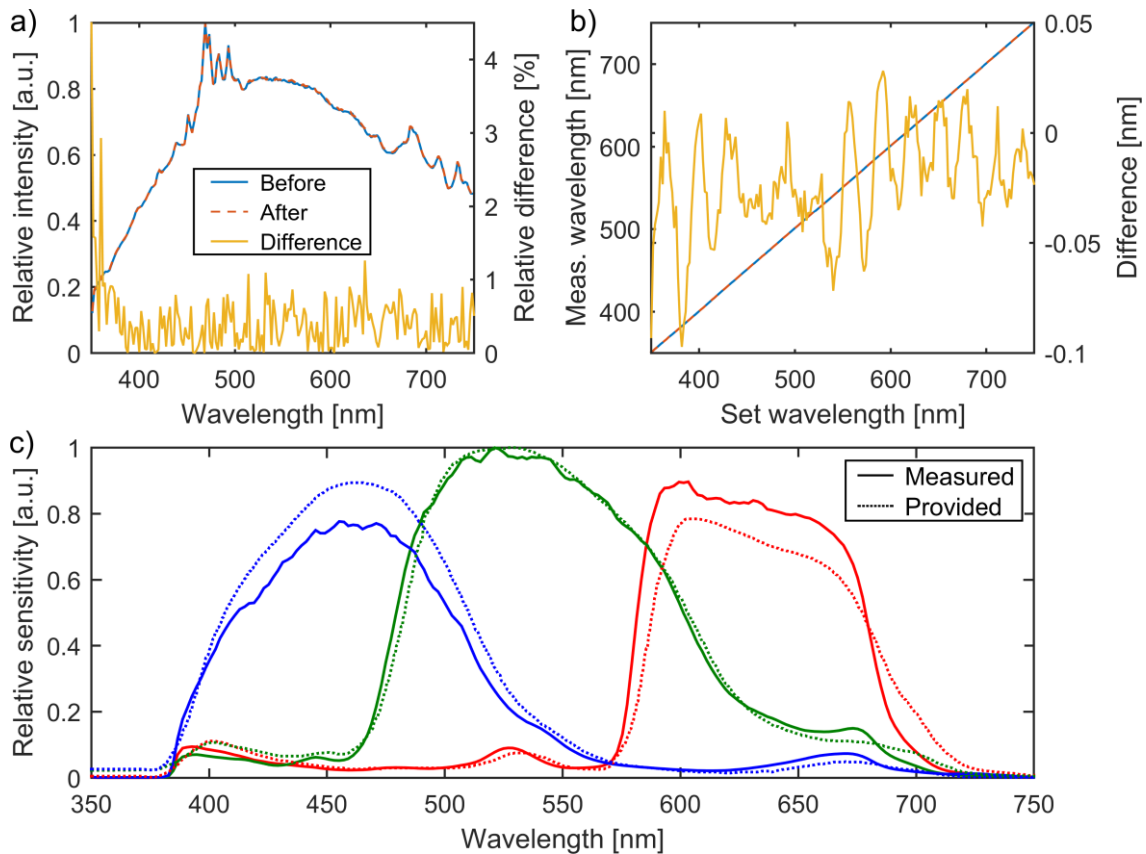


Figure 61: Camera spectral sensitivity calibration, including a stability test. The stability test is performed by comparing two spectral sweeps, before and after the image acquisition. **a)** Shows the comparison of the peak intensities, while **b)** shows a comparison of the peak wavelength. Legend refers to both figures. **c)** Final camera sensitivity functions, compared to the values provided by the manufacturer.

The obtained camera spectral sensitivities are seen in Figure 61c and compared to the values provided by Point Grey. The green channels match well with the provided calibration, while the red and blue channels have similar shapes, but deviates in the overall values. The resulting RGB values obtained when calculating the color of a typical spectrum are (184, 255, 175) and (163, 255, 197), for our and Point Grays calibration, respectively. Hence, the deviations result in significant differences in the RGB values, illustrating how sensitive the color analysis is to the camera calibration.

The two green channels in the RGGGB layout are calibration individually, but the sensitivities are almost identical and cannot be distinguished in Figure 61c. Hence, for the actual color measurements, the average value of the two green channels is used.

### 3.5.2 Light source

The main light source used for the experiments is a broadband LED (MWWHL3, Thorlabs Inc., USA). For some of the calibrations a xenon light source was used (HPX2000, Ocean Optics Inc., USA), as this has a broader emission spectrum. Only the calibration of the LED is presented, as the lamps are calibrated by identical procedures. For a calibration of the lamp warmup time, see Appendix A4.

#### 3.5.2.1 Spectrum

The spectrum of the light source is provided by the manufacturer but is also evaluated with the spectrometer calibrated in Appendix A4. The intensity is controlled by adjusting the current, and the spectrum is found to vary with around 10 % depending on the intensity setting, see Figure 62. For all measurements, the LED was used at the maximum intensity with the current setting at position 6. Since the spectrum is evaluated by the intensity, the electric field amplitudes used in the color calculations are determined as:

$$E_{\text{inc, s}} = E_{\text{inc, p}} = \sqrt{\frac{1}{2} I_{\text{incident}}} . \quad (36)$$

This provides the real components of the E-field, without any phase information. Since only linearly polarized light is used, the relative phase difference is zero and the complex part of the fields vanishes.

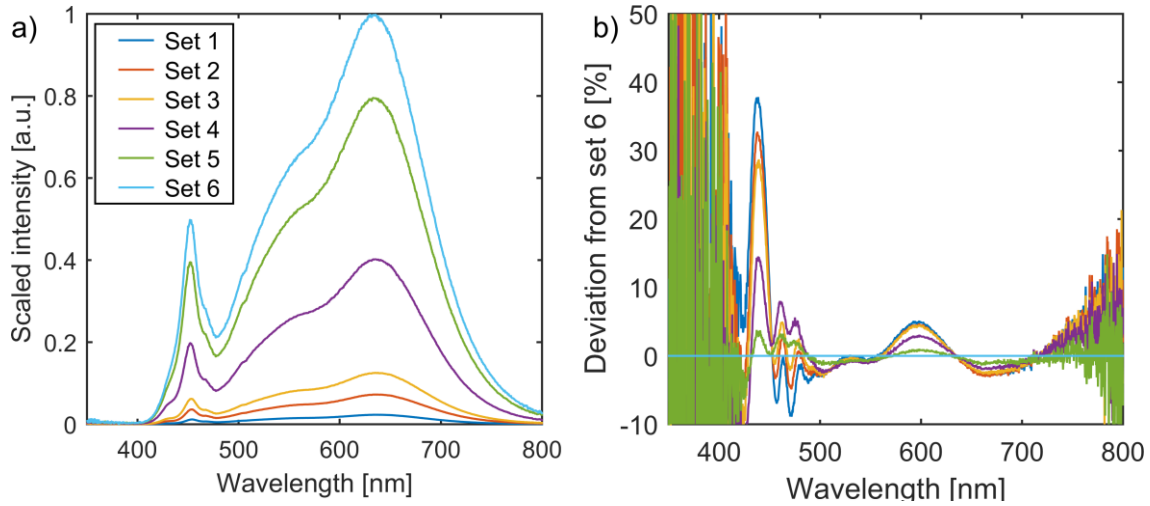


Figure 62: Spectrum of LED light source. **a)** The spectrum of six current settings normalized to the maximum value. **b)** The deviation of each spectrum compared to setting 6, hereby illustrating the differences between each spectrum. The fluctuations below 420 nm and above 720 nm are due to noise.

### 3.5.3 Beamsplitter

The polarizing beamsplitter (CCM1-PBS251/M, Thorlabs Inc., USA) directs the incident light onto the sample and transmits the reflected light to the camera. It is designed to reflect *s*-polarization and transmit *p*-polarization, but some *p*-polarization is also reflected along with the *s*-polarization. Similarly, some of the *s*-polarization reflected from the sample is transmitted and detected by the camera. As described in Section 3.3.1, this non-perfect behavior is important for determining the final spectrum reaching the camera.

#### 3.5.3.1 Reflectance and transmittance

The polarization dependent reflection and transmission properties of the beamsplitter were determined with the setup illustrated in Figure 63. The light source is unpolarized, and by rotating the polarizer (GT10-A, Thorlabs Inc., USA) the reflection and transmission spectra are evaluated for both *s*- and *p*-polarization, by repositioning the polarizer and spectrometer, as shown in Figure 63. The reflectance and transmittance were determined relative to the lamp spectral intensity, obtained by a straight through measurement without the beamsplitter but including the polarizer. The distance between the spectrometer fiber and the beamsplitter was kept identical, within a few millimeters, for the two configurations. The diffuser ensures a more even illumination of the spectrometer fiber. The calibration was performed with the broadband xenon light source (HPX2000, Ocean Optics Inc., USA), to evaluate a larger wavelength range than provided by the Thorlabs LED.

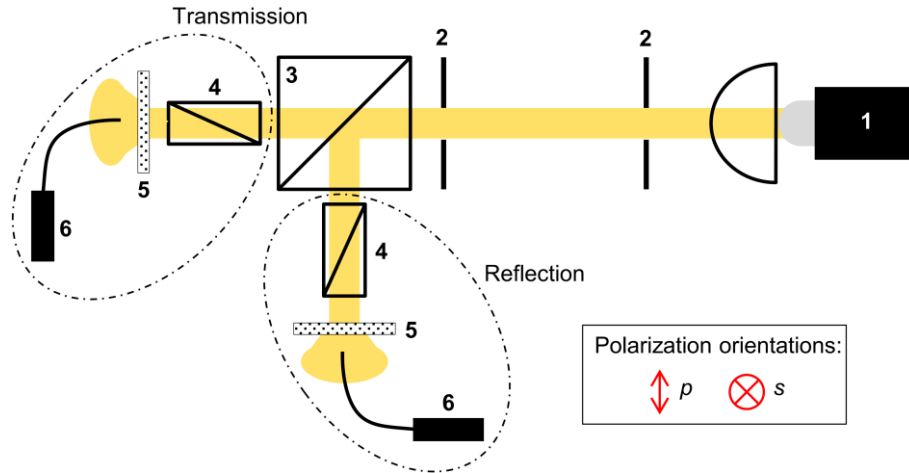


Figure 63: Illustration of the setup for characterizing the beamsplitter. The different configurations for the reflection and transmission setups are indicated with dashed circles. Numbers indicate: 1: light source, 2: iris, 3: beamsplitter, 4: polarizer, 5: diffuser, 6: spectrometer with fiber.

As expected, the calibration shows a high reflectance of  $s$ -polarization and a high transmittance of  $p$ -polarization, see Figure 64. The polarization ratios are around 1000:1 for transmission ( $T_p:T_s$ ) and 200:1 for reflection ( $R_s:R_p$ ), which is similar to the manufacturer specifications<sup>[211]</sup>. The oscillations in the reflected  $p$ -polarization are likely due to interference effects in the polarizing coating. Some values are slightly above 100 %, which is attributed to small discrepancies of the alignment in the different configurations. However, an absolute calibration is not needed, since the color measurements are only performed relatively.

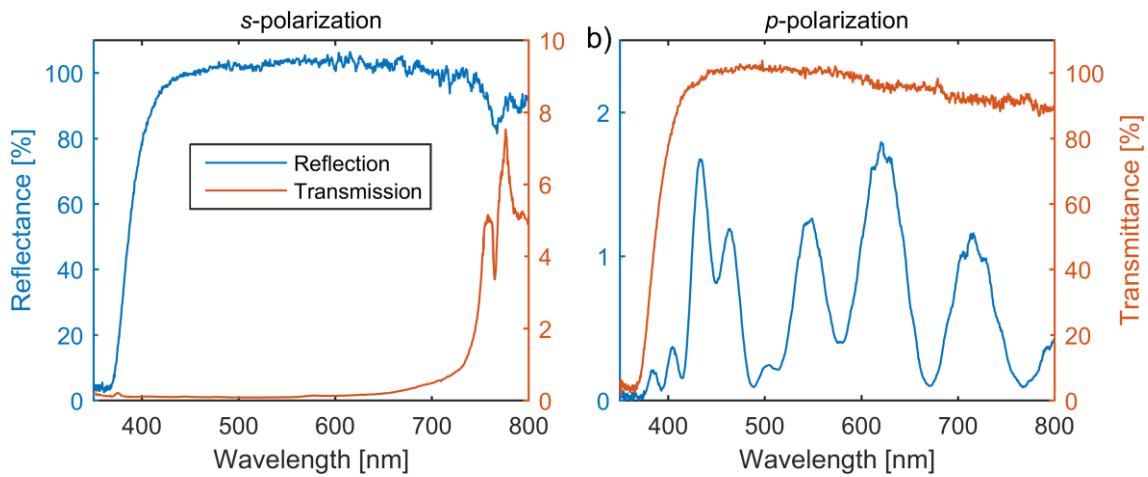


Figure 64: Calibration of the beamsplitter. The reflectance and transmittance spectra through the beamsplitter for a)  $s$ -polarized light, and b)  $p$ -polarized light. The legend and the y-axis labels refer to both graphs.



# CONCLUSION & OUTLOOK

This thesis has presented a study of optical scatterometry methods for characterization of micro- and nanoscale surface structures. The examined structures encompassed both random roughness features and periodic patterns of line gratings.

Part 2 evaluated the use of angular scatterometry for determining the roughness level of polished steel surfaces. The samples featured RMS roughness ( $R_q$ ) values ranging from 0.8 nm to  $\sim 0.1 \mu\text{m}$ , corresponding to  $R_a$  values of approximately 1 nm to  $0.07 \mu\text{m}$ . The study showed that the angular scatterometry technique is capable of evaluating surface roughness, but only for smooth surfaces where the height of the roughness features is in the nanometer regime. For rougher samples with tall structures, the scattering pattern is affected by shadowing from adjacent structures, and the applied Rayleigh-Rice scattering theory breaks down. Other scattering theories, such as the Generalized Harvey-Shack model, have been developed to describe surfaces with larger roughness features. However, these models were not applied, as the study focused on smooth surfaces intended for patterning of nanoscale gratings. The evaluation of rough surfaces might be relevant for the initial phases of a surface finishing process, and since it is advantageous to use the same instrument for the entire process chain, future studies could focus on the application of other theories.

The angular distributions of light scattered from the samples were evaluated with a custom-built setup, and these detailed distributions used to validate the commercial scatterometer “OptoSurf OS 500-32”. The main analysis is presented in Section 2.2.2. The comparison revealed that the OptoSurf instrument provides reliable  $A_q$  values, though only for structures with spatial surface wavelengths above  $2.5 \mu\text{m}$ , limited by the narrow opening angle of the instrument. We showed that the range of evaluated surface wavelengths could be extended without physical modifications to the instrument, by accounting for the light intensity scattered beyond the opening angle. We further determined a relation for converting the  $A_q$  values to the more well-known RMS roughness values. These two enhancements improve the OptoSurf’s performance for in-machine characterization of finely polished surfaces. Preferably, this mathematical post-processing of the scattering data should only be seen as a temporary solution, as the data analysis can be significantly improved by small changes to the instrument hardware. These modifications include a higher resolution CCD sensor along with a larger acceptance angle of the incoming light, as discussed in Section 2.2.5.

A preliminary study was performed to evaluate the use of scatterometry when the surface was not perfectly cleaned, see Chapter 2.3. This was investigated by analyzing the angular scattering distributions with and without a thin liquid film covering the surface roughness. The results were inconclusive, revealing some unexplained intensity changes to the distribution. Unfortunately, it was not possible to further investigate these changes with the available experimental setups. The OptoSurf did not provide sufficient resolution, while the laboratory scatterometer required the sample to be mounted vertically, causing the liquid to flow off. One solution could be to use a solid film, such as cured PDMS, since this also provides a more stable film for consecutive analyses on different instruments.

For evaluation of roughness on hard-to-reach surfaces, the use of polymer replicas was investigated in Chapter 2.4. The thermosetting polymer PDMS was used to replica a 2D checker pattern and the lateral shrinkage ratio determined for a range of curing temperatures and base:harder ratios. The study resulted in the determination of a temperature dependent correction factor, which for curing temperatures in the range 40°C to 120°C ensures a deviation between the master and replica dimensions of less than 0.2 %. Future work should investigate the possible correlation between the shrinkage ratio and the PDMS layer thickness discussed in Section 2.4.2. Such correlation would be important to resolve, as this effect will influence the accuracy of all PDMS moldings, not only regarding surface replicas but also the widespread use in microfluidic chips.

Part 3 concerned the use of fixed-angle scatterometry for characterizing the dimensions of periodic surface structures. A new method was developed, similar to spectroscopic scatterometry, but instead of evaluating the reflected spectrum with a spectrometer, a standard color camera was used to evaluate the visual color. This new scatterometry method was termed “color scatterometry”, and the main features were presented in Chapter 3.2. The method is intended for use in quality control applications, to perform in-line inspection for high volume fabrication of nanoscale surface features. The advantages are that it provides an overview image of the sample, a cheap setup, and a fast evaluation speed of a few seconds. The overview image provides an important feature, as this enables the detection of point defects and spatial variations in the grating dimensions. The current optical resolution of the instrument enables an analysis of regions down to 100  $\mu\text{m}$  x 100  $\mu\text{m}$  across a 35  $\text{mm}^2$  overview area. This region specific analysis enables the use of multiple quality control areas in different positions, for improved monitoring of the production process. As smaller analysis areas often are desired, future work should focus on decreasing the smallest region size, where one possibility is to provide better collimation of the light, as discussed in Section 3.3.1.

The grating dimensions were determined by fitting the measured color to a database of simulated colors, with each simulation corresponding to a different combination of values for the grating dimensions. The simulations were calculated using a freely available RCWA package for Matlab. Color scatterometry was only used to characterize rectangular line gratings, though an extension to 2D patterns should be straightforward, as long as the structures are on a length scale that alters the reflected light. The gratings were characterized by three parameters: the height, the projected-area filling factor, and the sidewalls slope. The height and filling factor were determined with accuracies of  $\sim 8\%$ , based on the 95 % confidence intervals, while the slope was determined with an accuracy of  $\pm 15^\circ$ . The larger uncertainty is due to the slope only slightly affecting the reflection spectrum. These accuracies are larger than for imaging scat-

---

terometry based on hyperspectral imaging, as the RGB values provides less information compared to the full reflection spectrum typically obtained.

Currently, the accuracy is mainly limited by the spectral calibrations of each component, and reducing the reliance on these calibrations could provide better overlap of the confidence interval with the reference dimensions. One approach would be to use a reference sample with known dimensions to continuously reference-correct the setup. This is similar to the current approach in spectroscopic scatterometry, where the reflection spectrum from a mirror or silicon wafer is used to correct for the source spectrum and the setup transmission. However, flat surfaces cannot be used with the presented color scatterometer, as they do not provide polarization conversion. Evaluating the spectrum from a known grating would eliminate the need for calibrating the source and beamsplitter reflection, but the camera spectral sensitivity and beamsplitter transmission would still need to be determined. Characterization of the polarization dependent properties of the beamsplitter would also require the addition of a polarizer in the setup. Another possibility is to perform absolute calibrations of all components. This would enable the intensity information of the colors to be included in the database fitting, resulting in smaller confidence intervals, as discussed in Section 3.3.3.

The analyzed gratings were designed early in the project, and the dimensions were optimized to provide distinct visual colors by having strong first order diffractions. However, this is not optimal for the presented analysis of the specular reflected color. Hence, an obvious possibility for reducing the confidence intervals is instead to optimize the grating dimensions for providing significant changes to the specular reflected color with respect to small variations in the dimensions. Other possibilities include the use of UV or IR wavelengths. However, this would mainly be for increasing the interactions with smaller or larger structures. Additionally, if the overview image is not needed for spatial analysis, the exposure time can be reduced by a sensor with larger pixels that captures more light, and the analysis time shortened by only evaluating a single region.

However, the future of color scatterometry does not solely depend on the achieved accuracy or speed of the instrument. More importantly, it depends on whether the future will bring a widespread adoption of nanostructures in high-volume plastic manufacturing. So far, only a few companies have utilized these functional nanostructures, and they typically prefer a bit larger structures, e.g. in the range of several micrometers, as these are easier to manufacture and characterize. Many plastic manufacturers are also not accustomed to high-tech characterization equipment, as the quality control of macroscale products often can be performed manually with calipers and micrometers. These companies might reject new instruments, especially if they do not understand the mechanism for how the work. In contrast to many other scatterometry methods, which mainly provide a comparison of spectral graphs, we believe that color scatterometry can provide a more intuitive understanding, due to the visual analysis of an overview image and the well-known concept of colors.



# BIBLIOGRAPHY

- [1] S. KINOSHITA, S. YOSHIOKA, Structural colors in nature: the role of regularity and irregularity in the structure., *Chemphyschem : A European Journal of Chemical Physics and Physical Chemistry*. 6 (2005) 1442–59. doi:10.1002/cphc.200500007.
- [2] J.S. CLAUSEN, *Nanoscale surface topographies for structural colors*, PhD thesis, Technical University of Denmark, 2014.
- [3] E. HØJLUND-NIELSEN, *Color Metasurfaces in Industrial Perspective*, PhD thesis, Technical University of Denmark, 2016. [http://orbit.dtu.dk/en/projects/structural-colors-in-plastic\(f2502624-7710-4f96-b736-08f0a2a41dd1\).html](http://orbit.dtu.dk/en/projects/structural-colors-in-plastic(f2502624-7710-4f96-b736-08f0a2a41dd1).html).
- [4] W. BARTHOLOTT, C. NEINHUIS, Purity of the sacred lotus, or escape from contamination in biological surfaces, *Planta*. 202 (1997) 1–8. doi:10.1007/s004250050096.
- [5] C.G. BERNHARD, Structural and functional adaptation in a visual system, *Endeavour*. 26 (1967) 79.
- [6] K. AUTUMN, Y.A. LIANG, S.T. HSIEH, W. ZESCH, W.P. CHAN, T.W. KENNY, R. FEARING, R.J. FULL, Adhesive force of a single gecko foot-hair, *Nature*. 405 (2000) 681–685. doi:10.1038/35015073.
- [7] J. CECH, *Nanopatterning of tools for replication of non-planar polymer surfaces*, PhD thesis, Technical University of Denmark, 2013.
- [8] A.B. CHRISTIANSEN, *Nanostructured polymer- and metal surfaces - Antireflective and colour functionality*, PhD thesis, Technical University of Denmark, 2014.
- [9] E. SØGAARD, *Injection molded self-cleaning surfaces*, Technical University of Denmark, 2014.
- [10] N.K. ANDERSEN, *Fabrication of nanostructured polymer surface and characterization of their wetting properties*, PhD thesis, Technical University of Denmark, 2016.
- [11] HYDROBEAD, Water beads on lotus leaf, (2016). <http://www.hydrobead.com/> (accessed 07/15/2016).
- [12] INTEL CORPORATION, Intel® Core™ i7-6800K Processor, (2016). [http://ark.intel.com/products/94189/Intel-Core-i7-6800K-Processor-15M-Cache-up-to-3\\_60-GHz](http://ark.intel.com/products/94189/Intel-Core-i7-6800K-Processor-15M-Cache-up-to-3_60-GHz) (accessed 07/14/2016).
- [13] V. GOODSHIP, ED., *Practical Guide to Injection Moulding*, Rapra Technology Ltd., 2004. ISBN 1-85957-444-0.
- [14] B. JENSEN, P. KJÆRSGÅRD, A.B. RASMUSSEN, T.B. RASMUSSEN, J. JOHANSEN, K. KARBÆK,

- PlastTeknologi*, Erhvervsskolernes Forlag, 2005. ISBN 9788778815507.
- [15] M. MATSCHUK, H. BRUUS, N.B. LARSEN, Nanostructures for all-polymer microfluidic systems, *Microelectronic Engineering*. 87 (2010) 1379–1382. doi:10.1016/j.mee.2009.11.167.
- [16] B. ROCKEY, File:Principe moulage injection polymere.svg, (2010). [https://commons.wikimedia.org/wiki/File:Principe\\_moulage\\_injection\\_polymere.svg](https://commons.wikimedia.org/wiki/File:Principe_moulage_injection_polymere.svg) (accessed 07/14/2016).
- [17] QENOS PTY LTD, Extrusion coating & lamination, (2015). [http://www.qenos.com/internet/home.nsf/\(LUIImages\)/TG4Exco/\\$File/TG4Exco.pdf](http://www.qenos.com/internet/home.nsf/(LUIImages)/TG4Exco/$File/TG4Exco.pdf) (accessed 07/14/2016).
- [18] S. MURTHY, M. MATSCHUK, Q. HUANG, N.K. MANDSBERG, N.A. FEIDENHANS'L, P. JOHANSEN, L. CHRISTENSEN, H. PRANOV, G. KOFOD, H.C. PEDERSEN, O. HASSAGER, R. TABORYSKI, Fabrication of Nanostructures by Roll-to-Roll Extrusion Coating, *Advanced Engineering Materials*. 18 (2016) 484–489. doi:10.1002/adem.201500347.
- [19] S.H. AHN, L.J. GUO, High-Speed Roll-to-Roll Nanoimprint Lithography on Flexible Plastic Substrates, *Advanced Materials*. 20 (2008) 2044–2049. doi:10.1002/adma.200702650.
- [20] M. ZALOKOVSKIJ, L.H. THAMDRUP, K. SMISTRUP, T. ANDÉN, A.C. JOHANSSON, N.J. MIKKELSEN, M.H. MADSEN, J. GARNÆS, T.T. KRISTIANSEN, M. DIEMER, M. DØSSING, D. MINZARI, P.T. TANG, A. KRISTENSEN, R. TABORYSKI, S. ESSENDROP, T. NIELSEN, B. BILENBERG, Smart plastic functionalization by nanoimprint and injection molding, in: *Proc. SPIE 9423, Alternative Lithographic Technologies VII*, 2015: p. 94230T. doi:10.1117/12.2085766.
- [21] J. CECHE, H. PRANOV, G. KOFOD, M. MATSCHUK, S. MURTHY, L.Y. CHEONG, R. TABORYSKI, Nanopatterning planar and non-planar mold surfaces for polymers replication, in: *Nanotechnology 2013: Advanced Materials, CNTs, Particles, Films and Composites*, 2013: pp. 638–641.
- [22] L.J. GUO, Nanoimprint Lithography: Methods and Material Requirements, *Advanced Materials*. 19 (2007) 495–513. doi:10.1002/adma.200600882.
- [23] H. BECKER, U. HEIM, Hot embossing as a method for the fabrication of polymer high aspect ratio structures, *Sensors and Actuators A: Physical*. 83 (2000) 130–135. doi:10.1016/S0924-4247(00)00296-X.
- [24] M. HECKELE, W.K. SCHOMBURG, Review on micro molding of thermoplastic polymers, *Journal of Micromechanics and Microengineering*. 14 (2004) R1–R14. doi:10.1088/0960-1317/14/3/R01.
- [25] L. PILNÝ, *Process monitoring for intelligent manufacturing processes*, PhD thesis, Technical University of Denmark, 2015. [http://orbit.dtu.dk/en/publications/process-monitoring-for-intelligent-manufacturing-processes--methodology-and-application-to-robot-assisted-polishing\(87c94744-7055-40f6-ba92-e95555a66fc6\).html](http://orbit.dtu.dk/en/publications/process-monitoring-for-intelligent-manufacturing-processes--methodology-and-application-to-robot-assisted-polishing(87c94744-7055-40f6-ba92-e95555a66fc6).html).
- [26] T.L. CHRISTIANSEN, *Design and Development of a Microfluidic Chip for Electrical Measurements on Biological Cells*, Master thesis, Technical University of Denmark, 2012.
- [27] M. MATSCHUK, *All-Polymer Microfluidic Systems with integrated Nanostructures for Cell Handling*, PhD thesis, Technical University of Denmark, 2011. [http://orbit.dtu.dk/en/publications/allpolymer-microfluidic-systems-with-integrated-nanostructures-for-cell-handling\(9fe8aaae-fc1c-4dfc-a940-a98cfa9e34db\).html](http://orbit.dtu.dk/en/publications/allpolymer-microfluidic-systems-with-integrated-nanostructures-for-cell-handling(9fe8aaae-fc1c-4dfc-a940-a98cfa9e34db).html).
- [28] K. TURNER, P. HARTWELL, Experimental Characterization Techniques for Micro/Nanoscale Devices, in: *Springer Handbook of Nanotechnology*, Springer Berlin Heidelberg, Berlin, Heidelberg, 2007: pp. 1639–1662. doi:10.1007/978-3-540-29857-1\_51.
- [29] B. BHUSHAN, O. MARTI, Scanning Probe Microscopy – Principle of Operation, Instrumentation, and Probes, in: *Springer Handbook of Nanotechnology*, Springer Berlin Heidelberg, Berlin, Heidelberg, 2007: pp. 591–636. doi:10.1007/978-3-540-29857-1\_22.
- [30] NANOSENSORS, SSS-NCLR, (2014). <http://www.nanosensors.com/SuperSharpSilicon-Non-Contact-Tapping-Mode-Long-Cantilever-Reflex-Coating-afm-tip-SSS-NCLR> (accessed 07/18/2016).

- 
- [31] J.P. KAPUR, D.P. CASASSENT, Geometric correction of SEM images, in: *Proc. SPIE 4044, Hybrid Image and Signal Processing VII*, 2000: pp. 165–176. doi:10.1117/12.391928.
  - [32] S. INOUÉ, Foundations of Confocal Scanned Imaging in Light Microscopy, in: *Handbook Of Biological Confocal Microscopy*, Springer US, Boston, MA, 2006. doi:10.1007/978-0-387-45524-2\_1.
  - [33] P. HARIHARAN, Chapter 12 – White-Light Interference Microscopy, in: *Basics of Interferometry*, 2007: pp. 105–110. doi:10.1016/B978-012373589-8/50014-6.
  - [34] P.E. MURPHY, C.A. HALL, Considerations in the evaluation and correction of mid-spatial frequency surface features, in: *Proc. SPIE 9633, Optifab 2015*, 2015: p. 96330F. doi:10.1117/12.2197037.
  - [35] OPTOSURF GMBH, *Data sheet OS 500-32*, 2009. <http://www.optosurf.de/images/Datenblaetter/en/Data-Sheet-OS-500.pdf> (accessed 02/23/2015).
  - [36] J.C. STOVER, *Optical Scattering: Measurement and Analysis*, 3. Edition, SPIE Press, 2012. ISBN 9780819492517.
  - [37] SENSO FAR-TECH, *Sensofar Plu Neox Brochure*, 2009. [http://www.sensofar.com/sensofar/pdf/PLu\\_neox.pdf](http://www.sensofar.com/sensofar/pdf/PLu_neox.pdf) (accessed 02/13/2015).
  - [38] INTERNATIONAL ORGANIZATION FOR STANDARDIZATION, *ISO 4287: Geometrical Product Specifications (GPS) - Surface texture: Profile method: Terms, definitions and surface texture parameters*, Geneva, Switzerland, 1998.
  - [39] INTERNATIONAL ORGANIZATION FOR STANDARDIZATION, *ISO 25178-2:2012: Geometrical product specifications (GPS) - Surface texture: Areal - Part 2: Terms, definitions and surface texture parameters*, 2012.
  - [40] L. DE CHIFFRE, P. LONARDO, H. TRUMPOLD, D. A. LUCCA, G. GOCH, C. A. BROWN, J. RAJA, H.N. HANSEN, Quantitative Characterisation of Surface Texture, *CIRP Annals - Manufacturing Technology*. 49 (2000) 635–652. doi:10.1016/S0007-8506(07)63458-1.
  - [41] G.T. SMITH, *Industrial Metrology: Surfaces and Roundness*, Springer Science & Business Media, 2013. ISBN 1447138147.
  - [42] INTERNATIONAL ORGANIZATION FOR STANDARDIZATION, *ISO 3274:1996: Geometrical Product Specifications (GPS) -- Surface texture: Profile method -- Nominal characteristics of contact (stylus) instruments*, 1996.
  - [43] J.E. HARVEY, S. SCHRÖDER, N. CHOI, A. DUPARRÉ, Total integrated scatter from surfaces with arbitrary roughness, correlation widths, and incident angles, *Optical Engineering*. 51 (2012) 013402. doi:10.1117/1.OE.51.1.013402.
  - [44] P. BECKMANN, A. SPIZZICHINO, *The scattering of electromagnetic waves from rough surfaces*, Pergamon Press, 1963.
  - [45] K.E. TORRANCE, E.M. SPARROW, Theory for Off-Specular Reflection From Roughened Surfaces, *Journal of the Optical Society of America*. 57 (1967) 1105. doi:10.1364/JOSA.57.001105.
  - [46] H. LI, K.E. TORRANCE, An experimental study of the correlation between surface roughness and light scattering for rough metallic surfaces, in: *Proc. SPIE 5878, Advanced Characterization Techniques for Optics, Semiconductors, and Nanotechnologies II*, 2005: p. 58780V. doi:10.1117/12.617637.
  - [47] I.G.E. RENHORN, T. HALLBERG, D. BERGSTRÖM, G.D. BOREMAN, Four-parameter model for polarization-resolved rough-surface BRDF, *Optics Express*. 19 (2011) 1027–36. doi:10.1364/OE.19.001027.
  - [48] B.G. HOOVER, V.L. GAMIZ, Coherence solution for bidirectional reflectance distributions of surfaces with wavelength-scale statistics, *Journal of the Optical Society of America A*. 23 (2006) 314. doi:10.1364/JOSAA.23.000314.
  - [49] T.M. ELFOUHAILY, C.-A. GUÉRIN, A critical survey of approximate scattering wave theories from random rough surfaces, *Waves in Random Media*. 14 (2004) R1–R40. doi:10.1088/0959-

7174/14/4/R01.

- [50] A. KRYWONOS, J.E. HARVEY, N. CHOI, Linear systems formulation of scattering theory for rough surfaces with arbitrary incident and scattering angles, *Journal of the Optical Society of America. A, Optics, Image Science, and Vision*. 28 (2011) 1121–1138. doi:10.1364/JOSAA.28.001121.
- [51] J.E. HARVEY, *Light Scattering Characteristics of Optical Surfaces*, University of Arizona, 1976.
- [52] E.L. CHURCH, H.A. JENKINSON, J.M. ZAVADA, Relationship between Surface Scattering and Microtopographic Features, *Optical Engineering*. 18 (1979) 125–136. doi:10.1117/12.7972337.
- [53] H. YAMEI, R. POTTS, Y. BAORYIN, G. ZHENG TANG, A. DEINO, W. WEI, J. CLARK, X. GUANGMAO, H. WEIWEN, Mid-Pleistocene Acheulan-like Stone Technology of the Bose Basin, South China, *Science*. 287 (2000) 1622–1626. doi:10.1126/science.287.5458.1622.
- [54] L. DE CHIFFRE, H. KUNZMANN, G.N. PEGGS, D.A. LUCCA, Surfaces in Precision Engineering, Microengineering and Nanotechnology, *CIRP Annals - Manufacturing Technology*. 52 (2003) 561–577. doi:10.1016/S0007-8506(07)60204-2.
- [55] R.J. HOCKEN, N. CHAKRABORTY, C. BROWN, Optical Metrology of Surfaces, *CIRP Annals - Manufacturing Technology*. 54 (2005) 169–183. doi:10.1016/S0007-8506(07)60025-0.
- [56] P.M. LONARDO, D.A. LUCCA, L. DE CHIFFRE, Emerging Trends in Surface Metrology, *CIRP Annals - Manufacturing Technology*. 51 (2002) 701–723. doi:10.1016/S0007-8506(07)61708-9.
- [57] D.J. WHITEHOUSE, *Handbook of Surface and Nanometrology*, 2nd ed., CRC Press, 2011. doi:10.1201/b10415.
- [58] R. LEACH, *Optical Measurement of Surface Topography*, Springer Berlin Heidelberg, 2011. doi:10.1007/978-3-642-12012-1.
- [59] D.J. WHITEHOUSE, *Handbook of Surface Metrology*, IOP Publishing Ltd, 1994. ISBN 0-7503-0039-6.
- [60] C.Y. POON, B. BHUSHAN, Comparison of surface roughness measurements by stylus profiler, AFM and non-contact optical profiler, *Wear*. 190 (1995) 76–88. doi:10.1016/0043-1648(95)06697-7.
- [61] A. DUPARRÉ, J. FERRE-BORRULL, S. GLIECH, G. NOTNI, J. STEINERT, J.M. BENNETT, Surface characterization techniques for determining the root-mean-square roughness and power spectral densities of optical components., *Applied Optics*. 41 (2002) 154–171. doi:10.1364/AO.41.000154.
- [62] S. SCHRÖDER, S. GLIECH, A. DUPARRÉ, Sensitive and flexible light scatter techniques from the VUV to IR regions, in: *Proc. SPIE 5965, Optical Fabrication, Testing, and Metrology II*, 2005: p. 59651B. doi:10.1117/12.625780.
- [63] C. RUPPE, A. DUPARRÉ, Roughness analysis of optical films and substrates by atomic force microscopy, *Thin Solid Films*. 288 (1996) 8–13. doi:10.1016/S0040-6090(96)08807-4.
- [64] C. DEUMIÉ, R. RICHIER, P. DUMAS, C. AMRA, Multiscale roughness in optical multilayers: atomic force microscopy and light scattering., *Applied Optics*. 35 (1996) 5583–5594. doi:10.1364/AO.35.005583.
- [65] A. VON FINCK, T. HERFFURTH, S. SCHRÖDER, A. DUPARRÉ, S. SINZINGER, Characterization of optical coatings using a multisource table-top scatterometer., *Applied Optics*. 53 (2014) A259–69. doi:10.1364/AO.53.00A259.
- [66] R.N. YOUNG WORTH, B.B. GALLAGHER, B.L. STAMPER, An overview of power spectral density (PSD) calculations, *Proc. SPIE*. 5869 (2005) 58690U–58690U–11. doi:10.1117/12.618478.
- [67] V. V. AZAROVA, V.G. DMITRIEV, Y.N. LOKHOV, K.N. MALITSKII, Measuring the roughness of high-precision quartz substrates and laser mirrors by angle-resolved scattering, *Journal of Optical Technology*. 69 (2002) 125. doi:10.1364/JOT.69.000125.
- [68] T. HERFFURTH, S. SCHRÖDER, M. TROST, A. DUPARRÉ, A. TÜNNERMANN, Comprehensive nanostructure and defect analysis using a simple 3D light-scatter sensor., *Applied Optics*. 52 (2013) 3279–87. doi:10.1364/AO.52.003279.

- 
- [69] J.C. STOVER, *Optical Scattering: Measurement and Analysis, section 5.1*, 3. Edition, SPIE Press, 2012. ISBN 9780819492517.
- [70] HALLE PRÄZISIONS-KALIBRIERNORMALE GMBH, Products, (2015). <http://www.halle-normale.de/framesets/englisch/products/products.html> (accessed 07/22/2016).
- [71] L. PILNÝ, G. BISSACCO, L. DE CHIFFRE, Validation of in-line surface characterization by light scattering in Robot Assisted Polishing, in: *3rd International Conference on Virtual Machining Process Technology (VMPT)*, 2014. <http://forskningbasen.deff.dk/Share.external?sp=S02aae26c-933d-4e12-a161-a7c9cb654eb6&sp=Sdtu>.
- [72] VERBAND DER AUTOMOBILINDUSTRIE E.V. (VDA), *VDA 2009:2010-07 - Angle-resolved light scattering measurement*, Berlin, Germany, 2010. [http://www.vda.de/de/publikationen/publikationen\\_downloads/detail.php?id=1120](http://www.vda.de/de/publikationen/publikationen_downloads/detail.php?id=1120).
- [73] G. UDUPA, M. SINGAPERUMAL, R.S. SIROHI, M.P. KOTHIYAL, Characterization of surface topography by confocal microscopy: I. Principles and the measurement system, *Measurement Science and Technology*. 11 (2000) 305–314. doi:10.1088/0957-0233/11/3/320.
- [74] F. MAUCH, W. OSTEN, Model-based approach for planning and evaluation of confocal measurements of rough surfaces, *Measurement Science and Technology*. 25 (2014) 105002. doi:10.1088/0957-0233/25/10/105002.
- [75] H.-J. JORDAN, M. WEGNER, H. TIZIANI, Highly accurate non-contact characterization of engineering surfaces using confocal microscopy, *Measurement Science and Technology*. 9 (1999) 1142–1151. doi:10.1088/0957-0233/9/7/023.
- [76] R. BRODMANN, M. ALLGAUER, Comparison Of Light Scattering From Rough Surfaces With Optical And Mechanical Profilometry, in: *Proc. SPIE 1009, Surface Measurement and Characterization, 111*, 1989: pp. 111–118. doi:10.1117/12.949161.
- [77] R. BRODMANN, J. SEEWIG, Non-Contact Surface Metrology by Means of Light Scattering, in: *Encyclopedia of Tribology: SpringerReference*, Springer-Verlag Berlin Heidelberg, 2013. <http://www.springerreference.com/docs/html/chapterdbid/332811.html>.
- [78] R. BRODMANN, G. THURN, Roughness measurement of ground, turned and shot-peened surfaces by the light scattering method, *Wear*. 109 (1986) 1–13. doi:10.1016/0043-1648(86)90247-4.
- [79] R. BRODMANN, O. GERSTORFER, G. THURN, Optical Roughness Measuring Instrument For Fine-Machined Surfaces, *Optical Engineering*. 24 (1985) 243408. doi:10.1117/12.7973497.
- [80] D. HÜSER, T. RINDER, H. ROTHE, Comparison of PSD measurements using stray light sensors with PSD curves evaluated from topography of large AFM scans, *Proceedings of SPIE - The International Society for Optical Engineering*. 3426 (1998) 262–272. doi:10.1117/12.328475.
- [81] R.-S. LU, G.Y. TIAN, On-line measurement of surface roughness by laser light scattering, *Measurement Science and Technology*. 17 (2006) 1496–1502. doi:10.1088/0957-0233/17/6/030.
- [82] J.C. STOVER, *Optical Scattering: Measurement and Analysis, section 1.5*, 3. Edition, SPIE Press, 2012. ISBN 9780819492517.
- [83] JOINT COMMITTEE FOR GUIDES IN METROLOGY, *Evaluation of measurement data — Guide to the expression of uncertainty in measurement (JCGM 100:2008)*, 2008. <http://www.bipm.org/en/publications/guides/gum.html>.
- [84] J.C. STOVER, *Optical Scattering: Measurement and Analysis, section 1.2*, 3. Edition, SPIE Press, 2012. ISBN 9780819492517.
- [85] M.G. DITTMAN, K-correlation power spectral density & surface scatter model, in: *Proc. SPIE 6291, Optical Systems Degradation, Contamination, and Stray Light: Effects, Measurements, and Control II*, 2006: p. 62910R. doi:10.1117/12.678320.
- [86] K. HIRAYAMA, E.N. GLYTSIS, T.K. GAYLORD, Rigorous electromagnetic analysis of diffraction by finite-number-of-periods gratings, *Journal of the Optical Society of America A*. 14 (1997) 907. doi:10.1364/JOSAA.14.000907.
- [87] S.O. RICE, Reflection of electromagnetic waves from slightly rough surfaces, *Communications on*

- Pure and Applied Mathematics*. 4 (1951) 351–378. doi:10.1002/cpa.3160040206.
- [88] J.E. HARVEY, A. KRYWONOS, J.C. STOVER, Unified scatter model for rough surfaces at large incident and scatter angles, in: *Proc. SPIE 6672, Advanced Characterization Techniques for Optics, Semiconductors, and Nanotechnologies III*, 2007: p. 66720C. doi:10.1117/12.739139.
- [89] J.M. BENNET, L. MATTSSON, *Introduction to Surface Roughness and Scattering*, 2nd ed., Optical Society of Amer, 1999. ISBN 978-1557526090.
- [90] J.C. STOVER, S. SCHRÖDER, T. A. GERMER, Upper roughness limitations on the TIS/RMS relationship, *Proc. SPIE*. 8495 (2012) 849503–1–7. doi:10.1117/12.930770.
- [91] J.C. STOVER, *Optical Scattering: Measurement and Analysis, section 4.3*, 3. Edition, SPIE Press, 2012. ISBN 9780819492517.
- [92] B. KARLSSON, C.G. RIBBING, Optical constants and spectral selectivity of stainless steel and its oxides, *Journal of Applied Physics*. 53 (1982) 6340–6. doi:10.1063/1.331503.
- [93] D.E. ASPNES, A.A. STUDNA, Dielectric functions and optical parameters of Si, Ge, GaP, GaAs, GaSb, InP, InAs, and InSb from 1.5 to 6.0 eV, *Physical Review B*. 27 (1983) 985–1009. doi:10.1103/PhysRevB.27.985.
- [94] T.Y. LIN, L. BLUNT, K.J. STOUT, Determination of proper frequency bandwidth for 3D topography measurement using spectral analysis. Part I: isotropic surfaces, *Wear*. 166 (1993) 221–232. doi:10.1016/0043-1648(93)90265-N.
- [95] P. PAWLUS, Digitisation of surface topography measurement results, *Measurement: Journal of the International Measurement Confederation*. 40 (2007) 672–686. doi:10.1016/j.measurement.2006.07.009.
- [96] M. KARAMEHMEDOVIĆ, P.-E. HANSEN, T. WRIEDT, An efficient rough-interface scattering model for embedded nano-structures, *Thin Solid Films*. 541 (2013) 51–56. doi:10.1016/j.tsf.2012.11.048.
- [97] S. SCHRÖDER, A. DUPARRÉ, L. CORIAND, A. TÜNNERMANN, D.H. PENALVER, J.E. HARVEY, Modeling of light scattering in different regimes of surface roughness, *Optics Express*. 19 (2011) 9820–35.
- [98] A.M. NILSSON, J.C. JONSSON, Light-scattering properties of a Venetian blind slat used for daylighting applications, *Solar Energy*. 84 (2010) 2103–2111. doi:10.1016/j.solener.2010.09.005.
- [99] BREAUULT RESEARCH ORGANIZATION INC., *Scattering in ASAP*, 2012. ISBN 0819419346.
- [100] E.R. FRENIERE, G.G. GREGORY, R.C. CHASE, L.R. CORPORATION, Interactive Software for Optomechanical Modeling, *Proc. SPIE: Optomechanical Engineering*. 3130 (2004) 128–133. doi:10.1117/12.284054.
- [101] C. ASMAIL, Bidirectional Scattering Distribution Function (BSDF): A Systematized Bibliography, *Journal of Research of the National Institute of Standards and Technology*. 96 (1991) 215–223. [http://nvlpubs.nist.gov/nistpubs/jres/096/jresv96n2p215\\_A1b.pdf](http://nvlpubs.nist.gov/nistpubs/jres/096/jresv96n2p215_A1b.pdf).
- [102] TAYLOR HOBSON, *Form Talysurf Intra Brochure*, 2012. <http://www.taylor-hobson.com/products/14/107.html> (accessed 03/22/2016).
- [103] TAYLOR HOBSON, *Form Talysurf PGI Brochure*, 2012. <http://www.taylor-hobson.com/products/12/107.html> (accessed 04/04/2016).
- [104] SONY, SONY ILX511B brochure, (2003). <http://oceanoptics.com/wp-content/uploads/SONY-ILX511B.pdf> (accessed 09/03/2015).
- [105] B. GLASSE, A. ZERWAS, R. GUARDANI, U. FRITSCHING, Refractive indices of metal working fluid emulsion components, *Measurement Science and Technology*. 25 (2014) 035205. doi:10.1088/0957-0233/25/3/035205.
- [106] L.F. HOYT, New Table of the Refractive Index of Pure Glycerol at 20°C, *Industrial & Engineering Chemistry*. 26 (1934) 329–332. doi:10.1021/ie50291a023.

- 
- [107] N.A. FEIDENHANS'L, P.-E. HANSEN, L. PILNÝ, M.H. MADSEN, G. BISSACCO, J.C. PETERSEN, R. TABORYSKI, Comparison of optical methods for surface roughness characterization, *Measurement Science and Technology*. 26 (2015) 085208. doi:10.1088/0957-0233/26/8/085208.
  - [108] M. EIFLER, F. SCHNEIDER, M. BOHLEY, J.C. AURICH, J. SEEWIG, Contamination of roughness artefacts - impact on the measurement results, in: *Euspen's 15th International Conference*, 2015.
  - [109] J.R. REITZ, F.J. MILFORD, R.W. CHRISTY, *Foundations of Electromagnetic Theory*, Third, Addison-Wesley Publishing Company, 1979. ISBN 0201063417.
  - [110] E.M.J. HERREY, Confidence Intervals Based on the Mean Absolute Deviation of a Normal Sample, *Journal of the American Statistical Association*. 60 (1965) 257–269. doi:10.1080/01621459.1965.10480788.
  - [111] G.M. HALE, M.R. QUERRY, Optical Constants of Water in the 200 nm to 200  $\mu$ m Wavelength Region, *Applied Optics*. 12 (1973) 555. doi:10.1364/AO.12.000555.
  - [112] J.A. IZATT, M.A. CHOMA, Theory of Optical Coherence Tomography, in: *Optical Coherence Tomography - Technology and Applications*, Springer Berlin Heidelberg, 2008: pp. 47–72. doi:10.1007/978-3-540-77550-8\_2.
  - [113] C.F. BOHREN, D.R. HUFFMAN, *Absorption and Scattering of Light by Small Particles*, Wiley-VCH Verlag GmbH, Weinheim, Germany, 1998. doi:10.1002/9783527618156.
  - [114] H.N. HANSEN, R.J. HOCKEN, G. TOSELLO, Replication of micro and nano surface geometries, *CIRP Annals - Manufacturing Technology*. 60 (2011) 695–714. doi:10.1016/j.cirp.2011.05.008.
  - [115] C.F. CARLBORG, T. HARALDSSON, K. ÖBERG, M. MALKOCH, W. VAN DER WIJNGAART, Beyond PDMS: off-stoichiometry thiol-ene (OSTE) based soft lithography for rapid prototyping of microfluidic devices., *Lab on a Chip*. 11 (2011) 3136–47. doi:10.1039/c1lc20388f.
  - [116] B.D. GATES, Q. XU, M. STEWART, D. RYAN, C.G. WILLSON, G.M. WHITESIDES, New approaches to nanofabrication: molding, printing, and other techniques., *Chemical Reviews*. 105 (2005) 1171–96. doi:10.1021/cr030076o.
  - [117] S. ELHADJ, R.M. RIOUX, M.D. DICKEY, J.J. DEYOREO, G.M. WHITESIDES, Subnanometer replica molding of molecular steps on ionic crystals, *Nano Letters*. 10 (2010) 4140–5. doi:10.1021/nl102409d.
  - [118] J.N. LEE, C. PARK, G.M. WHITESIDES, Solvent compatibility of poly(dimethylsiloxane)-based microfluidic devices., *Analytical Chemistry*. 75 (2003) 6544–54. doi:10.1021/ac0346712.
  - [119] V.-M. GRAUBNER, R. JORDAN, O. NUYKEN, T. LIPPERT, M. HAUER, B. SCHNYDER, A. WOKAUN, Incubation and ablation behavior of poly(dimethylsiloxane) for 266 nm irradiation, *Applied Surface Science*. 197-198 (2002) 786–790. doi:10.1016/S0169-4332(02)00415-4.
  - [120] DOW CORNING, *Product information - Sylgard® 184 Silicone Elastomer*, 2014.
  - [121] H. SCHMID, B. MICHEL, Siloxane Polymers for High-Resolution, High-Accuracy Soft Lithography, *Macromolecules*. 33 (2000) 3042–3049. doi:10.1021/ma982034l.
  - [122] E. SOLLIER, C. MURRAY, P. MAODDI, D. DI CARLO, Rapid prototyping polymers for microfluidic devices and high pressure injections, *Lab on a Chip*. 11 (2011) 3752–65. doi:10.1039/c1lc20514e.
  - [123] N.A. FEIDENHANS'L, J.P. LAFLEUR, T.G. JENSEN, J.P. KUTTER, Surface functionalized thiol-ene waveguides for fluorescence biosensing in microfluidic devices, *Electrophoresis*. 35 (2013) 282–288. doi:10.1002/elps.201300271.
  - [124] H. WU, T.W. ODOM, D.T. CHIU, G.M. WHITESIDES, Fabrication of complex three-dimensional microchannel systems in PDMS, *Journal of the American Chemical Society*. 125 (2003) 554–9. doi:10.1021/ja021045y.
  - [125] D.B. WOLFE, J.C. LOVE, G.M. WHITESIDES, Nanostructures Replicated by Polymer Molding, in: *Dekker Encyclopedia of Nanoscience and Nanotechnology*, M. Dekker, 2004: pp. 2657–2667. ISBN 0824750462.
  - [126] C. MORAES, Y. SUN, C. A. SIMMONS, Solving the shrinkage-induced PDMS alignment registration

- issue in multilayer soft lithography, *Journal of Micromechanics and Microengineering*. 19 (2009) 065015. doi:10.1088/0960-1317/19/6/065015.
- [127] S.W. LEE, S.S. LEE, Shrinkage ratio of PDMS and its alignment method for the wafer level process, *Microsystem Technologies*. 14 (2007) 205–208. doi:10.1007/s00542-007-0417-y.
- [128] STRUERS, *RepliSet Brochure*, Denmark, 2008.  
[http://www.struers.com/resources/elements/12/189599/Repliset brochure English.pdf](http://www.struers.com/resources/elements/12/189599/Repliset%20brochure%20English.pdf) (accessed 06/25/2014).
- [129] ACCUTRANS, *Brochure*, Switzerland, 2012.  
[http://www.accutrans.info/fileadmin/dam/DATEN/AccuTrans/downloads/others/9227\\_UK\\_07-12\\_AccuTrans.pdf](http://www.accutrans.info/fileadmin/dam/DATEN/AccuTrans/downloads/others/9227_UK_07-12_AccuTrans.pdf) (accessed 06/25/2014).
- [130] R. GABAI, A. ISMACH, E. JOSELEVICH, Nanofacet Lithography: A New Bottom-Up Approach to Nanopatterning and Nanofabrication by Soft Replication of Spontaneously Faceted Crystal Surfaces, *Advanced Materials*. 19 (2007) 1325–1330. doi:10.1002/adma.200601625.
- [131] F. HUA, Y. SUN, A. GAUR, M. A. MEITL, L. BILHAUT, L. ROTKINA, J. WANG, P. GEIL, M. SHIM, J. A. ROGERS, A. SHIM, Polymer Imprint Lithography with Molecular-Scale Resolution, *Nano Letters*. 4 (2004) 2467–2471. doi:10.1021/nl048355u.
- [132] I.M. AND S.G. AND T.K. AND Y.T. AND N.O. AND J.K. AND F.K. AND M.Y. AND Y.F. AND Y.N. AND K. TAKAMASU, Submicrometre-pitch intercomparison between optical diffraction, scanning electron microscope and atomic force microscope, *Measurement Science and Technology*. 14 (2003) 2065. doi:10.1088/0957-0233/14/12/004.
- [133] H. ISHIDA, H.Y. LOW, A Study on the Volumetric Expansion of Benzoxazine-Based Phenolic Resin, *Macromolecules*. 30 (1997) 1099–1106. doi:10.1021/ma960539a.
- [134] J.C. LÖTTERS, W. OLTHUIS, P.H. VELTINK, P. BERGVELD, The mechanical properties of the rubber elastic polymer polydimethylsiloxane for sensor applications, *Journal of Micromechanics and Microengineering*. 7 (1997) 145–147. doi:10.1088/0960-1317/7/3/017.
- [135] R.B. ROBERTS, Thermal expansion reference data: silicon 300–850 K, *Journal of Physics D: Applied Physics*. 14 (1981) L163–L166. doi:10.1088/0022-3727/14/10/003.
- [136] I.D. JOHNSTON, D.K. MCCLUSKEY, C.K.L. TAN, M.C. TRACEY, Mechanical characterization of bulk Sylgard 184 for microfluidics and microengineering, *Journal of Micromechanics and Microengineering*. 24 (2014) 035017. doi:10.1088/0960-1317/24/3/035017.
- [137] K.S. RYU, C. LIU, Precision Patterning of PDMS Thin Films: A New Fabrication Method and Its Applications, in: *Micro Total Analysis Systems 2002*, Springer Netherlands, Dordrecht, 2002: pp. 112–114. doi:10.1007/978-94-010-0295-0\_37.
- [138] C.A. BICHSEL, S. GOBAA, S. KOBEL, C. SECONDINI, G.N. THALMANN, M.G. CECCHINI, M.P. LUTOLF, Diagnostic microchip to assay 3D colony-growth potential of captured circulating tumor cells, *Lab on a Chip*. 12 (2012) 2313. doi:10.1039/c2lc40130d.
- [139] D. A. CHERNOFF, E. BUHR, D.L. BURKHEAD, A. DIENER, Picometer-scale accuracy in pitch metrology by optical diffraction and atomic force microscopy, in: *Proc. SPIE 6922, Metrology, Inspection, and Process Control for Microlithography XXII*, 2008: p. 69223J. doi:10.1117/12.768429.
- [140] M.H. MADSEN, P.-E. HANSEN, Scatterometry—fast and robust measurements of nano-textured surfaces, *Surface Topography: Metrology and Properties*. 4 (2016) 023003. doi:10.1088/2051-672X/4/2/023003.
- [141] J. FOUCHER, Critical dimension metrology: perspectives and future trends, *SPIE Newsroom*. (2008). doi:10.1117/2.1200811.1345.
- [142] M. LAPEDUS, Searching For 3D Metrology, (2015). <http://semiengineering.com/searching-for-3d-metrology/> (accessed 06/27/2016).
- [143] B. BODERMANN, G. EHRET, J. ENDRES, M. WURM, Optical dimensional metrology at Physikalisch-Technische Bundesanstalt (PTB) on deep sub-wavelength nanostructured surfaces,

- 
- Surface Topography: Metrology and Properties*. 4 (2016) 024014. doi:10.1088/2051-672X/4/2/024014.
- [144] T. IKEGAMI, A. YAMAGUCHI, M. TANAKA, S. TAKAMI, Y. HOJO, A. SUGIMOTO, Evolution and Future of Critical Dimension Measurement System for Semiconductor Processes, *Hitachi Review*. 60 (2011) 203–209. [http://128.241.23.25/rev/field/industrialsystems/\\_\\_\\_icsFiles/afiedfile/2011/09/06/r2011\\_05\\_104.pdf](http://128.241.23.25/rev/field/industrialsystems/___icsFiles/afiedfile/2011/09/06/r2011_05_104.pdf).
  - [145] H.P. KLEINKNECHT, H. MEIER, Optical Monitoring of the Etching of SiO<sub>2</sub> and Si<sub>3</sub>N<sub>4</sub> on Si by the Use of Grating Test Patterns, *Journal of The Electrochemical Society*. 125 (1978) 798–803. doi:10.1149/1.2131551.
  - [146] B.D. JOHS, J. HALE, N.J. IANNO, C.M. HERZINGER, T.E. TIWALD, J.A. WOOLLAM, Recent Developments in Spectroscopic Ellipsometry for in situ Applications, in: *Proc. SPIE 4449, Optical Metrology Roadmap for the Semiconductor, Optical, and Data Storage Industries II*, 2001: pp. 41–57. doi:10.1117/12.450108.
  - [147] H.G. TOMPKINS, E.A. IRENE, *Handbook of Ellipsometry*, William Andrew Inc., 2005. ISBN 978-0-8155-1499-2.
  - [148] D.H. GOLDSTEIN, *Polarized Light*, 3rd ed., CRC Press, 2011. doi:10.1201/b10436.
  - [149] G.A. KLEIN, *Industrial Color Physics*, Springer New York, New York, 2010. doi:10.1007/978-1-4419-1197-1.
  - [150] L.T. SHARPE, A STOCKMAN, H. JÄGLE, H. KNAU, G. KLAUSEN, A REITNER, J. NATHANS, Red, green, and red-green hybrid pigments in the human retina: correlations between deduced protein sequences and psychophysically measured spectral sensitivities., *The Journal of Neuroscience : The Official Journal of the Society for Neuroscience*. 18 (1998) 10053–10069. ISBN 0270-6474 (Print)r0270-6474 (Linking).
  - [151] INSTITUTE OF OPHTHALMOLOGY - UNIVERSITY COLLEGE LONDON, Colour & Vision Research Laboratory, (2016). <http://www.cvgl.org/> (accessed 06/29/2016).
  - [152] G. SHARMA, W. WU, E.N. DALAL, The CIEDE2000 color-difference formula: Implementation notes, supplementary test data, and mathematical observations, *Color Research & Application*. 30 (2005) 21–30. doi:10.1002/col.20070.
  - [153] M. STOKES, M. ANDERSON, S. CHANDRASEKAR, R. MOTTA, *A Standard Default Color Space for the Internet - sRGB*, 1995. <http://www.w3.org/Graphics/Color/sRGB> (accessed 09/02/2015).
  - [154] R.W.G. HUNT, *The Reproduction of Colour*, 6th ed., John Wiley & Sons, Ltd, Chichester, UK, 2004. doi:10.1002/0470024275.
  - [155] INTERNATIONAL ELECTROTECHNICAL COMMISSION (IEC), *IEC 61966-2-1:1999: Multimedia systems and equipment - Colour measurement and management - Part 2-1: Colour management - Default RGB colour space - sRGB*, 1999. <https://webstore.iec.ch/publication/6169>.
  - [156] S. WESTLAND, C. RIPAMONTI, *Computational Colour Science using MATLAB*, John Wiley & Sons, 2004. ISBN 0470845627.
  - [157] K. HAN, C.-H. CHANG, Numerical Modeling of Sub-Wavelength Anti-Reflective Structures for Solar Module Applications, *Nanomaterials*. 4 (2014) 87–128. doi:10.3390/nano4010087.
  - [158] KJ INNOVATION, *Optical Simulation of Grating Diffraction in MATLAB (GD-calc\_Intro.pdf)*, Santa Clara, CA-USA, 2006. <http://kjinnovation.com/GD-Calc.html> (accessed 06/21/2016).
  - [159] M. NEVIÈRE, E. POPOV, *Light Propagation in Periodic Media: Differential Theory and Design*, Marcel Dekker Inc., 2002. ISBN 0-8247-0893-8.
  - [160] R.C. RUMPF, Improved formulation of scattering matrices for semi-analytical methods that is consistent with convention, *Progress In Electromagnetics Research B*. 35 (2011) 241–261. doi:10.2528/PIERB11083107.
  - [161] KJ INNOVATION, *Coupled-Wave Theory for Biperiodic Diffraction Gratings (GD-calc.pdf)*, Santa Clara, CA-USA, 2006. <http://kjinnovation.com/GD-Calc.html> (accessed 06/30/2016).

- [162] R.M. SILVER, R. ATTOTA, M. STOCKER, M. BISHOP, L. HOWARD, T. GERMER, E. MARX, M. DAVIDSON, R. LARRABEE, High-resolution optical metrology, in: *Proc. SPIE 5752, Metrology, Inspection, and Process Control for Microlithography XIX*, 2005: pp. 67–79. doi:10.1117/12.606231.
- [163] H.H. SMILDE, A. DEN BOEF, M. KUBIS, M. JAK, M. VAN SCHIJNDEL, A. FUCHS, M. VAN DER SCHAAR, S. MEYER, S. MORGAN, J. WU, V. TSAI, C. WANG, K. BHATTACHARYYA, K.-H. CHEN, G.-T. HUANG, C.-M. KE, J. HUANG, Evaluation of a novel ultra small target technology supporting on-product overlay measurements, in: *Proc. SPIE 8324, Metrology, Inspection, and Process Control for Microlithography XXVI*, 2012: p. 83241A. doi:10.1117/12.916382.
- [164] C. RAYMOND, Overview of scatterometry applications in high volume silicon manufacturing, *AIP Conference Proceedings*. 788 (2005) 394–402. doi:10.1063/1.2062993.
- [165] A.J. DEN BOEF, M. DUSA, Inspection apparatus and method of inspection, US7315384B2, 2005.
- [166] E.W. CONRAD, D.P. PAUL, Method and apparatus for measuring the profile of small repeating lines, US5963329A, 1997.
- [167] Y. XU, I. ABDULHALIM, Spectroscopic scatterometer system, US6483580B1, 1998.
- [168] J. GARNÆS, P.-E. HANSEN, N. AGERSNAP, J. HOLM, F. BORSETTO, A. KÜHLE, Profiles of a high-aspect-ratio grating determined by spectroscopic scatterometry and atomic-force microscopy, *Applied Optics*. 45 (2006) 3201. doi:10.1364/AO.45.003201.
- [169] M.H. MADSEN, P.-E. HANSEN, M. ZALOKOVSKIJ, M. KARAMEHMEDOVIĆ, J. GARNÆS, Fast characterization of moving samples with nano-textured surfaces, *Optica*. 2 (2015) 301–306. doi:10.1364/OPTICA.2.000301.
- [170] R.M. SILVER, B.M. BARNES, R. ATTOTA, J. JUN, M. STOCKER, E. MARX, H.J. PATRICK, Scatterfield microscopy for extending the limits of image-based optical metrology., *Applied Optics*. 46 (2007) 4248–57. doi:10.1364/ao.46.004248.
- [171] B.M. BARNES, N.A. HECKERT, R. QUINTANILHA, H. ZHOU, R.M. SILVER, Spectroscopic scatterfield microscopy, *AIP Conference Proceedings*. 1173 (2009) 261–265. doi:10.1063/1.3251230.
- [172] P. BOHER, J. PETIT, T. LEROUX, J. FOUCHER, Y. DESIERES, J. HAZART, P. CHATON, Optical Fourier Transform Scatterometry for LER and LWR metrology, *Proc. of SPIE: Metrology, Inspection, and Process Control for Microlithography XIX*. 5752 (2005) 192–203. doi:10.1117/12.594526.
- [173] S. ROY, N. KUMAR, S.F. PEREIRA, H.P. URBACH, Interferometric coherent Fourier scatterometry: a method for obtaining high sensitivity in the optical inverse-grating problem, *Journal of Optics*. 15 (2013) 075707. doi:10.1088/2040-8978/15/7/075707.
- [174] V. FERRERAS PAZ, S. PETERHÄNSEL, K. FRENNER, W. OSTEN, Solving the inverse grating problem by white light interference Fourier scatterometry, *Light: Science & Applications*. 1 (2012) e36. doi:10.1038/lsa.2012.36.
- [175] J. HENRIE, S. KELLIS, S. SCHULTZ, A. HAWKINS, Electronic color charts for dielectric films on silicon., *Optics Express*. 12 (2004) 1464–9.
- [176] G.S. MAY, S.M. SZE, 3.5 Oxide Thickness Characterization, in: *Fundamentals of Semiconductor Fabrication*, 1st ed., Wiley, 2003. ISBN 0-471-23279-3.
- [177] S. PETERHÄNSEL, H. LAAMANEN, J. LEHTOLAHTI, M. KUITTINEN, W. OSTEN, J. TERVO, Human color vision provides nanoscale accuracy in thin-film thickness characterization, *Optica*. 2 (2015) 627. doi:10.1364/OPTICA.2.000627.
- [178] N. BORNEMANN, D. EDGAR, A flatbed scanner for large-area thickness determination of ultra-thin layers in printed electronics, *Optics Express*. 21 (2013) 21897–21911. doi:10.1364/OE.21.021897.
- [179] W. OUYANG, X.-Z. LIU, Q. LI, Y. ZHANG, J. YANG, Q. ZHENG, Optical methods for determining thicknesses of few-layer graphene flakes., *Nanotechnology*. 24 (2013) 505701. doi:10.1088/0957-4484/24/50/505701.

- 
- [180] L. GAO, W. REN, F. LI, H. CHENG, Total color difference for rapid and accurate identification of graphene., *ACS Nano*. 2 (2008) 1625–33. doi:10.1021/nn800307s.
  - [181] S. PETERHÄNSEL, H. LAAMANEN, M. KUITTINEN, J. TURUNEN, C. PRUSS, W. OSTEN, J. TERVO, Solving the inverse grating problem with the naked eye, *Optics Letters*. 39 (2014) 3547–50. doi:10.1364/OL.39.003547.
  - [182] J.S. CLAUSEN, E. HØJLUND-NIELSEN, A.B. CHRISTIANSEN, S. YAZDI, M. GRAJOWER, H. TAHA, U. LEVY, A. KRISTENSEN, N.A. MORTENSEN, Plasmonic metasurfaces for coloration of plastic consumer products, *Nano Letters*. 14 (2014) 4499–4504. doi:10.1021/nl5014986.
  - [183] X.M. GOH, Y. ZHENG, S.J. TAN, L. ZHANG, K. KUMAR, C.-W. QIU, J.K.W. YANG, Three-dimensional plasmonic stereoscopic prints in full colour, *Nature Communications*. 5 (2014) 5361. doi:10.1038/ncomms6361.
  - [184] P. ROACH, N.J. SHIRTCLIFFE, M.I. NEWTON, Progress in superhydrophobic surface development, *Soft Matter*. 4 (2008) 224–240. doi:10.1039/B712575P.
  - [185] E. SØGAARD, N.K. ANDERSEN, K. SMISTRUP, S.T. LARSEN, L. SUN, R. TABORYSKI, Study of Transitions between Wetting States on Microcavity Arrays by Optical Transmission Microscopy, *Langmuir*. 30 (2014) 12960–12968. doi:10.1021/la502855g.
  - [186] S.H. AHN, L.J. GUO, Large-Area Roll-to-Roll and Roll-to-Plate Nanoimprint Lithography: A Step toward High-Throughput Application of Continuous Nanoimprinting, *ACS Nano*. 3 (2009) 2304–2310. doi:10.1021/nn9003633.
  - [187] M. LEITGEB, D. NEES, S. RUTTLOFF, U. PALFINGER, J. GÖTZ, R. LISKA, M.R. BELEGATIS, B. STADLOBER, Multilength Scale Patterning of Functional Layers by Roll-to-Roll Ultraviolet-Light-Assisted Nanoimprint Lithography, *ACS Nano*. 10 (2016) 4926–4941. doi:10.1021/acsnano.5b07411.
  - [188] M.H. MADSEN, P.-E. HANSEN, Imaging scatterometry for flexible measurements of patterned areas, *Opt. Express*. 24 (2016) 1109–1117. doi:10.1364/OE.24.001109.
  - [189] W.G. COCHRAN, The distribution of quadratic forms in a normal system, with applications to the analysis of covariance, *Mathematical Proceedings of the Cambridge Philosophical Society*. 30 (1934) 178. doi:10.1017/S0305004100016595.
  - [190] J.B. HARRIS, T.W. PREIST, E.L. WOOD, J.R. SAMBLES, Conical diffraction from multicoated gratings containing uniaxial materials, *Journal of the Optical Society of America A*. 13 (1996) 803. doi:10.1364/JOSAA.13.000803.
  - [191] G.P. BRYAN-BROWN, S.J. ELSTON, J.R. SAMBLES, Polarization conversion through the excitation of electromagnetic modes on a grating, in: *Proc. SPIE 1545, International Conference on the Application and Theory of Periodic Structures*, 1991: pp. 167–178. doi:10.1117/12.49414.
  - [192] W.H. PRESS, W.T. VETTERLING, S. A TEUKOLSKY, B.P. FLANNERY, *Numerical Recipes in C: The Art of Scientific Computing*, 2. ed., Cambridge University Press, 1992. ISBN 0521431085.
  - [193] J.D. PLUMMER, M. DEAL, P.D. GRIFFIN, *Silicon VLSI Technology*, Prentice Hall, 2000. ISBN 0130850373.
  - [194] G. FU, S.B. TOR, D.E. HARDT, N.H. LOH, Effects of processing parameters on the micro-channels replication in microfluidic devices fabricated by micro injection molding, *Microsystem Technologies*. 17 (2011) 1791–1798. doi:10.1007/s00542-011-1363-2.
  - [195] P.E. HANSEN, L. NIELSEN, Combined optimization and hybrid scalar-vector diffraction method for grating topography parameters determination, *Materials Science and Engineering B: Solid-State Materials for Advanced Technology*. 165 (2009) 165–168. doi:10.1016/j.mseb.2009.09.006.
  - [196] J. PEATROSS, M. WARE, *Physics of Light and Optics*, 2015. ISBN 9781312929272.
  - [197] B.S.I.R.C. V RAMAN, Structural birefringence in amorphous solids, in: *Proceedings of the Indian Academy of Sciences - Section A*, 1950: pp. 207–212. doi:10.1007/BF03046600.
  - [198] M.L. GIGLI, R.A. DEPINE, Conical Diffraction from Uniaxial Gratings, *J. Mod. Opt.* 42 (1995) 1281–1299. doi:10.1080/09500349514551121.

- [199] R. PETTIT, G. TAYEB, About The Electromagnetic Theory Of Gratings Made With Anisotropic Materials, in: *Proc. SPIE 0815, Application and Theory of Periodic Structures, Diffraction Gratings, and Moire Phenomena III*, 1987: pp. 11–16. doi:10.1117/12.941727.
- [200] C.W. HAGGANS, L. LI, T. FUJITA, R.K. KOSTUK, Lamellar Gratings as Polarization Components for Specularly Reflected Beams, *Journal of Modern Optics*. 40 (1993) 675–686. doi:10.1080/09500349314550721.
- [201] R.M.A. AZZAM, N.M. BASHARA, Polarization characteristics of scattered radiation from a diffraction grating by ellipsometry with application to surface roughness, *Physical Review B*. 5 (1972) 4721–4729. doi:10.1103/PhysRevB.5.4721.
- [202] N. PASSILLY, P. KARVINEN, K. VENTOLA, P. LAAKKONEN, J. TURUNEN, J. TERVO, Polarization conversion by dielectric subwavelength gratings in conical mounting, *Journal of the European Optical Society*. 3 (2008). doi:10.2971/jeos.2008.08009.
- [203] KJ INNOVATION, *Demo and Tutorial Guide (GD-calc\_Demo.pdf)*, Santa Clara, CA-USA, 2006.
- [204] D. WU, D.-W. SUN, Colour measurements by computer vision for food quality control - A review, *Trends in Food Science & Technology*. 29 (2013) 5–20. doi:10.1016/j.tifs.2012.08.004.
- [205] DIGITAL PHOTOGRAPHY REVIEW, Nikon Coolpix 5700 Review, (2002). <http://www.dpreview.com/reviews/nikoncp5700/2> (accessed 06/09/2016).
- [206] DIGITAL PHOTOGRAPHY REVIEW, Kodak DCS620x Review, (2000). <http://www.dpreview.com/reviews/kodakdcs620x/> (accessed 06/09/2016).
- [207] DIGITAL PHOTOGRAPHY REVIEW, Sony announce new RGBE CCD, (2003). <http://www.dpreview.com/articles/1471104084/sonyrgbeccd> (accessed 06/09/2016).
- [208] EUROPEAN MACHINE VISION ASSOCIATION, *EMVA Standard 1288 - 3.0: Standard for characterization of Image Sensors and Cameras*, 2012. <http://www.emva.org/standards-technology/emva-1288/emva-standard-1288-downloads/>.
- [209] POINT GREY RESEARCH INC., EMVA 1288 Overview: Imaging Performance, (2016). <https://www.ptgrey.com/point-grey/10931> (accessed 06/09/2016).
- [210] M.M. DARRODI, G. FINLAYSON, T. GOODMAN, M. MACKIEWICZ, Reference data set for camera spectral sensitivity estimation, *Journal of the Optical Society of America A*. 32 (2015) 381. doi:10.1364/JOSAA.32.000381.
- [211] THORLABS INC., Broadband Polarizing Beamsplitter Cubes in 30 mm Cage Cubes, (2015). [https://www.thorlabs.de/newgrouppage9.cfm?objectgroup\\_ID=4137](https://www.thorlabs.de/newgrouppage9.cfm?objectgroup_ID=4137) (accessed 07/22/2016).
- [212] INTERNATIONAL ORGANIZATION FOR STANDARDIZATION, *ISO 5436-1:2000: Geometrical Product Specifications (GPS) -- Surface texture: Profile method; Measurement standards -- Part 1: Material measures*, Geneva, Switzerland, 2000.
- [213] OCEAN OPTICS INC., *Calibrating the Wavelength of the Spectrometer*, 2000. ISBN 1389928896.
- [214] NATIONAL INSTITUTE OF STANDARDS AND TECHNOLOGY (NIST), Strong Lines of Krypton (Kr), (2003). <http://physics.nist.gov/PhysRefData/Handbook/Tables/kryptontable2.htm> (accessed 06/02/2016).
- [215] OCEAN OPTICS INC., *Loading Non-Linearity Correction Coefficients Instructions*, 2015. <http://oceanoptics.com/wp-content/uploads/OOINLCorrect-Linearity-Coeff-Proc.pdf> (accessed 06/02/2016).

# APPENDICES

A1 Detailed description of angular scatterometer setup .....	120
A1.1 Components .....	120
A1.2 Complete measurement workflow .....	121
A2 Convergence tests .....	124
A3 Supporting information for paper 4.....	128
A4 Instrument calibrations.....	133
A4.1 Spectrometer .....	133
A4.2 Camera warmup time .....	136
A4.3 LED warmup time.....	137
A5 Papers not included in thesis.....	138
A5.1 Paper 5.....	138
A5.2 Paper 6.....	145

# A1 Detailed description of angular scatterometer setup

## A1.1 Components

Paper 1 mainly provides an overview description of the laboratory scatterometer. This appendix will describe the setup in more detail, presenting the components in backwards order.

The last component is a silicon photodetector (New Focus Model 2032, Newport, USA) with a gain of  $2 \times 10^6$  and a maximum signal frequency of 150 kHz. The chopper frequency was kept around 380 Hz, safely below the limit. The photodetector generates a voltage proportional to the incident power, which is detected by a lock-in amplifier (SR530, Stanford Research Systems, USA), from which the output voltage is logged as a representation of the light intensity. The lock-in has several sensitivity settings, which are adjusted according to the incident intensity, hereby increasing the dynamic range of the setup. To reduce the noise floor, the lock-in filters in a narrow band around the dc frequency, hereby requiring a long filter time constant of 0.1 s. Unfortunately, this results in a fairly long stabilization time for the lock-in, and a measurement time of around 3 s per data point, or around 2 hours for a full scan.

Immediately before the sample is an iris for shaping the beam. The beam shape is evaluated by a straight through measurement without a sample, and found to closely resemble a Gaussian curve in the center region, see Figure 65. To provide optimal shaping, three additional irises are included throughout the setup.

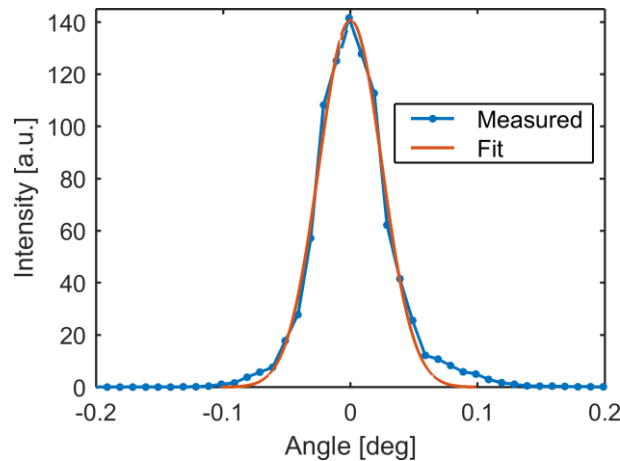


Figure 65: Profile of incident beam obtained from straight through measurement, and compared to a Gaussian fit.

Before the iris is a 500 mm focal length lens (LA4184, Thorlabs Inc., USA), which focuses the beam on the detector. This is important for the detection of long spatial surface wavelengths on the sample, as these scatter into small angles close to specular. The focus point can also be on the sample, as the OptoSurf has, but this result in a larger spot on the detector, hereby degrading the detection limit for long spatial wavelengths. This configuration is only beneficial if a small measurement area is desired, e.g. to increase the resolution of a raster scan.

A Glan-Taylor polarizer (GT10, Thorlabs Inc., USA) ensures that the incident light is *s*-polarized, which simplifies the calculation of the  $Q$  factor. It might be more beneficial to position the polarizer after the lens, as the focusing slightly alters the polarization. However, due to the long focal length and weak focusing, this effect is negligible.

A step neutral-density (ND) filter (NDL-10S-4, Thorlabs Inc., USA) is used to decrease the incident intensity. It is mounted on a translation stage to automatically change the transmission steps during a scan. The ND filter is required due to the high gain setting on the photodetector, as it otherwise saturates for the straight through beam and specular reflections. On the other hand, the high gain is required to detect the weak scatter signals at larger angles, and it is not possible to automatically control the detector gain from the computer. The actual transmission of the five filter steps were calibrated from a straight through scan of each filter, and determined to: 92%, 10%, 1.5%, 0.16%, and 0.022%. Compared to the nominal values provided by the manufacturer, the deviations are: 2%, 2%, 52%, 61%, 128%, respectively.

To correct for variations in the incident intensity, a reference photodetector (New Focus Model 2032, Newport, USA) continuously measures the laser intensity. The scattering intensities are then corrected for the relative change in the laser intensity. The laser stability is generally within 0.5 %, as seen from Figure 66.

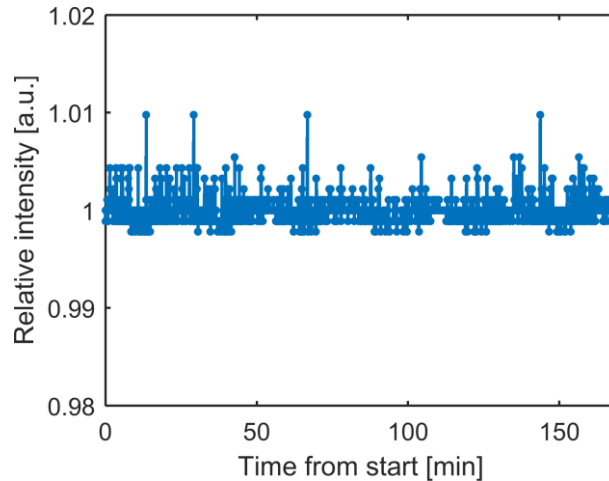


Figure 66: Typical laser stability of the 662 nm diode laser. The values are measured with the reference photodetector and are scaled relative to the initial value.

The first component is the laser, which is a 100 mW diode laser (LBX-660-100-CIR-PP, Oxxius, France), with a wavelength of 662 nm  $\pm$  1 nm determined with a spectrometer (USB2000+VIS-NIR-ES, Ocean Optics Inc., USA).

## A1.2 Complete measurement workflow

This section describes the steps for performing a measurement of the BRDF of a sample, using the laboratory angular scatterometer.

- i. System warmup
  - a. To stabilize all the components, the setup was turned on at least 30 min before commencing experiments.

- ii. ND filter calibration
  - a. The transmission of the ND filters is determined by measuring the straight through beam for each filter, and comparing the peak intensity through filter. To not saturate the detector, it is run in low gain mode.
  - b. The transmittance is determined relative to the uncoated filter step with pure glass. During the sample scans, the software tracks the applied filter for all data point, and corrects with the calibrated transmittance values.
  - c. The filter transmissions were measured several times over a cause of a few weeks. The values was found to change with up to 13 %, hence the uncertainty on these transmission values is a significant contribution to the overall uncertainty.
- iii. Noise floor
  - a. The noise floor was evaluated from a scan without a sample. The noise was then determined as an average over a large angular range of approximately  $40^\circ$ , calculated as the mean value plus two times the standard deviation within this range. We did not determine an angle dependent value, as no significant angle variations were seen.
- iv. Incident beam intensity
  - a. To determine the intensity of the incident beam and ensure it resembled a Gaussian shape, a straight through measurement without a sample was performed. This was done each time the setup was turned on or altered. A typical beam is seen in Figure 65. The peak value of the beam was then used as the incident intensity.
- v. Sample alignment
  - a. The samples were mounted in a holder providing movement in all three rotational axes. It was aligned to normal incidences, by aligning the reflected specular beam to the incident beam, and by positioning the sample an incident angle of  $30^\circ$  or  $60^\circ$ , we ensured that the in-plane scattering coincided with the detector plane.
  - b. Most samples were measured with an angle of incidence of  $8^\circ$ , but to correct for small misalignments, the actual incident angle was determined from the relation between the specular reflection and the straight through beam.
- vi. Acquisition protocol
  - a. The entire process is controlled by a Matlab script, which goes through a setup routine to determine the optimal settings for each intensity measurement. The process is:
    - i. Move detector to the measurement angle and acquire the angle from the stage.
    - ii. Acquire an initial intensity value from the lock-in amplifier.
    - iii. Check if the ND filter should be changed. If so, move the linear stage and acquire new value.

- iv. Check if the lock-in sensitivity should be changed. If so, increase or decrease the sensitivity until the value is within the allowed range of that sensitivity. Each time the sensitivity is changed, the lock-in requires a stabilization period determined by the time constant of the lowpass filter. This stabilization period had previously been determined to 1 s, by evaluating when the output value stabilized.
  - v. Acquire the final intensity value, and query the lock-in for any errors reported.
  - vi. Immediately after the acquisition, the reference value of the laser intensity is measured.
- vii. Post processing
  - a. Before calculating the BRDF distributions, the raw measurement intensities are subtracted with the noise floor, and corrected for variations in the laser intensity and the transmission of the ND filters. The lock-in amplifier already corrects the output voltage for the applied sensitivity. Because the BRDF distribution requires normalization to the incident power, the correction for the reference laser intensity should not be performed individually for each scan, but must account the drift between the straight through measurement and the actual scattering measurement.
  - b. After these corrections, the final BRDF distribution is determined, and this converted to the surface PSD using the Raleigh-Rice theory previously described.

## A2 Convergence tests

Results of convergence tests, as described in Section 3.4.1.1 on page 89.

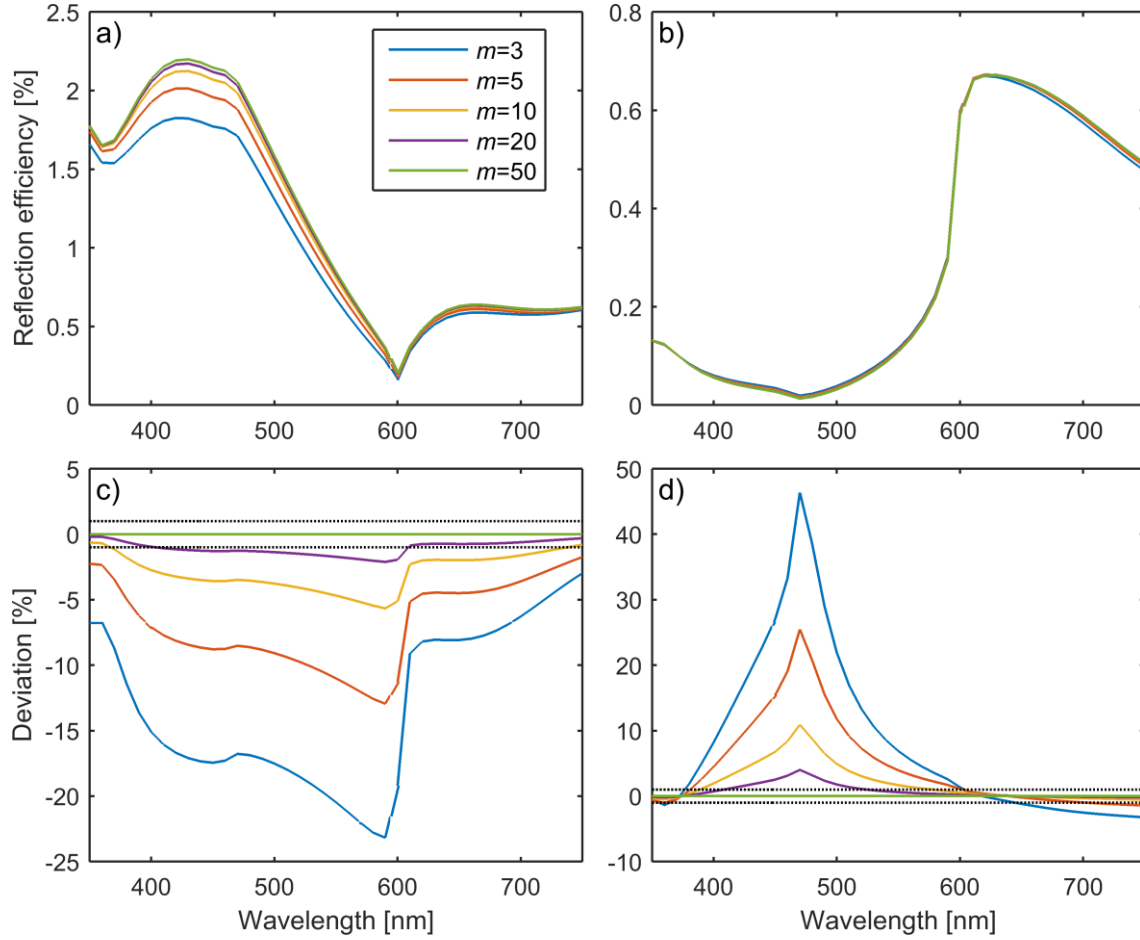


Figure 67: Convergence test for number of slabs ( $m$ ). **a)** and **b)** show the reflection efficiencies for  $R_{s \rightarrow s}$  and  $R_{s \rightarrow p}$ , respectively. **c)** and **d)** show the corresponding deviations from the  $m = 50$  spectrum. The dotted lines indicate deviations of  $\pm 1\%$ . The grating dimensions are: period = 600 nm, height = 200 nm, filling factor = 50 %, sidewall slope =  $10^\circ$ . For all simulations  $n = 10m$ .

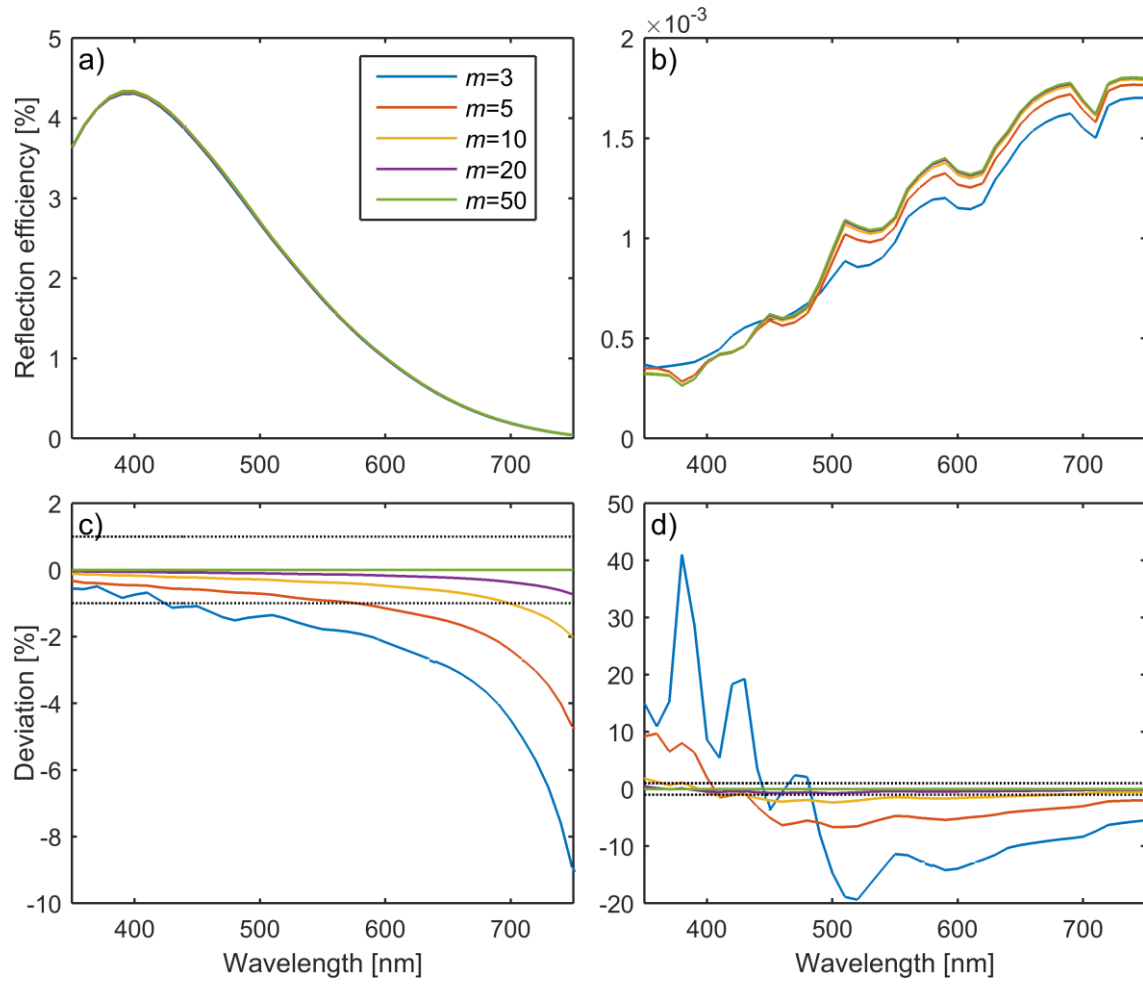


Figure 68: Same as Figure 67, but with period = 5000 nm.

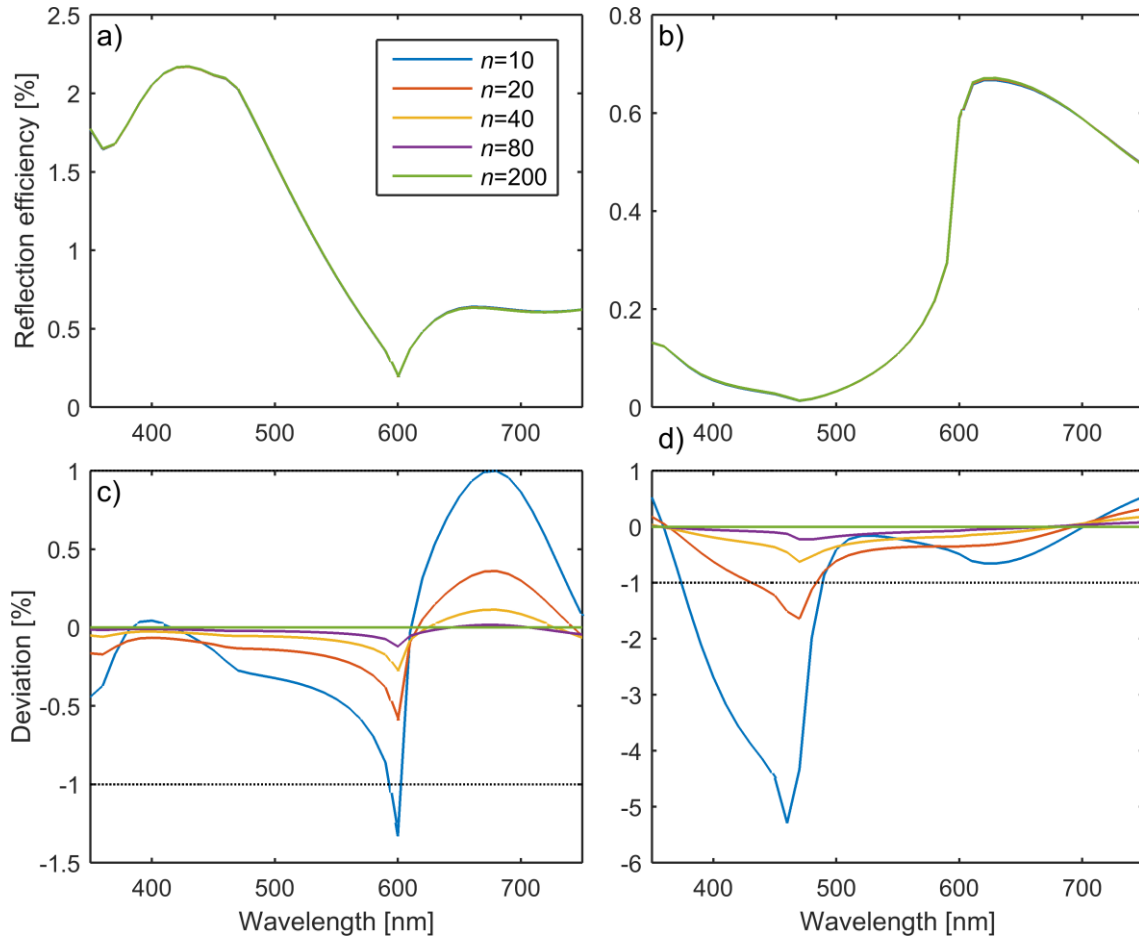


Figure 69: Same as Figure 67, but for number of terms included in Fourier series ( $n$ ). For all simulations  $m = 20$ .

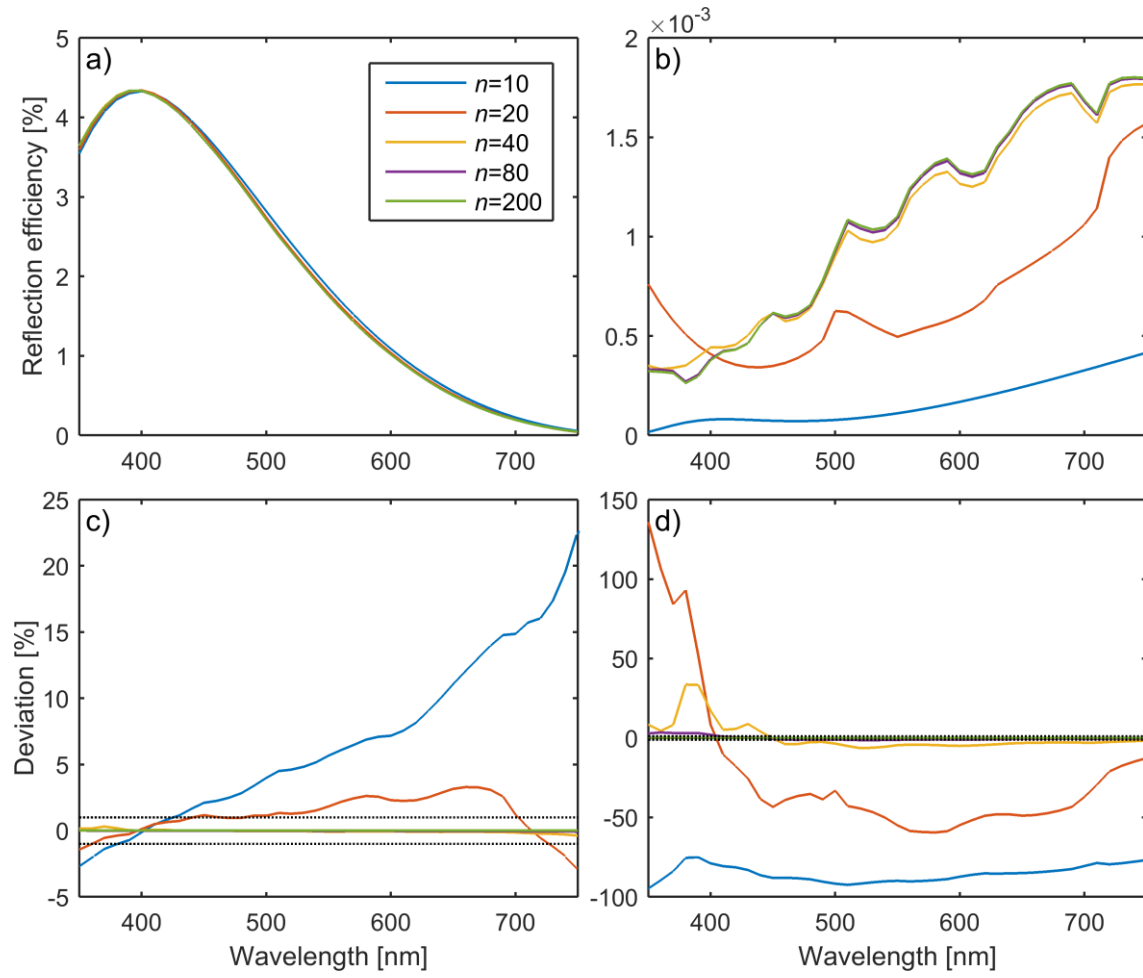


Figure 70: Same as Figure 69, but with period = 5000 nm.

# A3 Supporting information for paper 4

## S1 Fabrication

### Mold master

The mold was a nickel shim electroformed from a silicon master that was fabricated by semiconductor processing techniques. The substrate was a 100 mm silicon wafer (TN443, Topsil Semiconductor Materials Ltd., Denmark). A 350 nm photoresist layer (JSR-M230Y, JSR Corporation, Japan) was spin coated and patterned by deep UV lithography (FPA-3000EX4, Canon Inc., Japan). After development, the gratings were defined in the silicon wafer by deep reactive ion etching (DRIE Pegasus, SPTS Technologies Ltd., USA), using the photoresist as etch mask. Remaining photoresist was removed by an oxygen plasma (PVA Tepla 300, PVA Metrology & Plasma Solutions GmbH, Germany), and a 100 nm nickel-vanadium seed layer was deposited by sputtering (Lesker CMS 18, Kurt J. Lesker Company, USA) to facilitate the electroforming process. A nickel layer of 370  $\mu\text{m}$  was electroformed (Technotrans micro-form.200, Technotrans AG, Germany), and the nickel shim released by dissolving the silicon in a KOH etch. To easy demolding of mold master and polymer, the nickel shim was coated with an anti-stiction monolayer of perfluorodecyltrichlorosilane (FDTS) by molecular vapor deposition (MVD 100, Applied Microstructures Inc., USA). See process illustration in Figure S1.

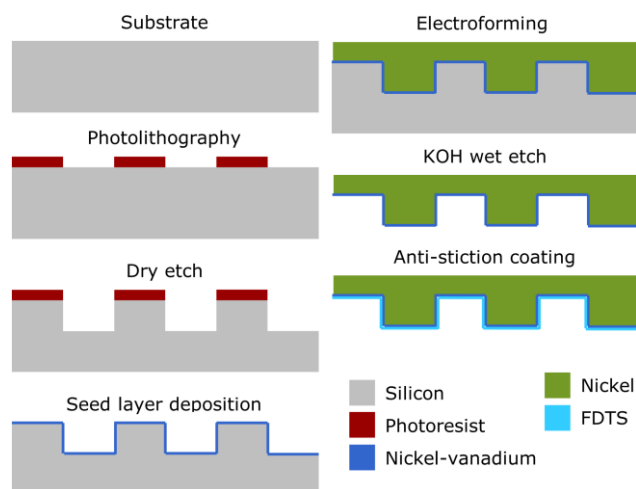


Figure S1: Cross sectional diagrams of the mold master fabrication process.

### Injection molding

Injection molding was performed on an industry grade injection molding machine (Engel Victory Tech 80/45, ENGEL AUSTRIA GmbH, Austria) using a variotherm process, with the main process parameters shown in Table S1. The polymer used was cyclic olefin copolymer (TOPAS5013L-10, TOPAS Advanced Polymers GmbH, Germany) mixed with 1.15 % black pigment (UNS 949227, Gabriel-Chemie Group, Austria). The black pigment provides an enhanced visual appearance of the structured colors, due to a surrounding dark background, but does not affect the structural colors.

Table S1: Main process parameters used in the injection molding process.

Clamp force	450 kN
Switchover pressure	1000 bar
Holding pressure	1000 bar
Injection flow	52 cm <sup>3</sup> /s
Tool temperature	120°C
Mold pause time	145 s
Cooling time	120 s
Plasticizer delay time	90 s

### Refractive index of polymer

The refractive index of the polymer was determined by ellipsometry (VASE, J.A. Woollam Co., USA), on the unstructured center region of the disc. The measurements were performed at three incident angles, and the complex refractive index determined by the instrument software, by fitting each wavelength individually to the ellipsometry model:

$$\frac{r_p}{r_s} = \tan(\Psi) e^{i\Delta}, \quad (S1)$$

where  $r_p$  and  $r_s$  are the Fresnel reflection coefficients of  $p$  and  $s$  polarized light, respectively,  $\Psi$  is the amplitude component, and  $\Delta$  the phase component.

The wavelength depend complex refractive index ( $\tilde{n} = n + ik$ ) is seen in Figure S2.

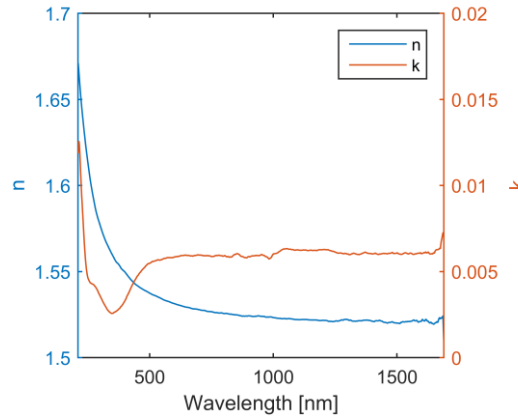


Figure S2: Complex refractive index of polymer, determined with variable angle spectroscopic ellipsometry on the actual sample.

## S2 Reference measurements

AFM measurements were performed on a Park NX20 (Park Systems, South Korea), and the grating heights determined using a ISO 5436 step height analysis<sup>[212]</sup> in SPIP (SPIP 6.5.1 Image Metrology, Denmark). FIB milling was performed on a FEI Helios Nanolab 600 (FEI, USA), and to protect the structures, they were covered with a few micrometers of platinum, before milling with gallium ions. SEM images of the cross-sections were subsequently acquired on a Zeiss Supra VP 40 (Zeiss, Germany), and the grating dimension evaluated manually using ImageJ (US National Institutes of Health, USA).

### S3 Simulations

Rigorous Coupled-Wave Analysis (RCWA) is a widely used method for calculating diffraction efficiencies of periodic structures.<sup>[140,158]</sup> The structures are defines as horizontal slabs, and for each slab the electromagnetic field is represented by a Fourier series, where a set of differential equations are constructed to describe the propagation of the Fourier coefficients through the slabs.<sup>[140,158]</sup> The final output is the far-field diffraction coefficients of an infinite grating.

RCWA simulations were performed using Matlab (Matlab R2014b, MathWorks Inc., USA) and GD-Calc (KJ Innovation, USA). For each grating with a specific height, filling factor, and sidewall slope, the reflection spectra were simulated for wavelengths from 350 nm to 750 nm with 5 nm intervals. The output from a simulation with a single wavelength was a 2 x 2 matrix with the reflection efficiencies for *s*- and *p*-polarized light. The four efficiency values describes both the reflection of unchanged polarization and polarization conversion, with the notation:  $r_{s \rightarrow p}$ , meaning incident *s*-polarization that is reflected as *p*-polarization. The cross-polarization terms are especially important for the presented setup with crossed polarizers, however, the efficiencies are typically 100 times lower than for the reflection of unchanged polarization, see see Figure S3. The values were simulated for wavelengths from 350 nm to 750 nm with 5 nm intervals, and the resulting color calculated as:

$$R = \sum_{i=1}^N I_{\text{lamp}}(\lambda_i) \begin{bmatrix} R_{BS,s}(\lambda_i) \\ R_{BS,p}(\lambda_i) \end{bmatrix} \cdot \begin{bmatrix} r_{s \rightarrow s}(\lambda_i) & r_{s \rightarrow p}(\lambda_i) \\ r_{p \rightarrow s}(\lambda_i) & r_{p \rightarrow p}(\lambda_i) \end{bmatrix} \begin{bmatrix} T_{BS,s}(\lambda_i) \\ T_{BS,p}(\lambda_i) \end{bmatrix} S_{\text{cam},R}(\lambda_i) \Delta\lambda_i, \quad (\text{S2})$$

where  $R$  is the value of the “red” pixels,  $I_{\text{lamp}}$  the lamp spectrum,  $R_{BS,i}$  and  $T_{BS,i}$  the beamsplitter reflectance and transmittance for each polarization, respectively,  $r_{i \rightarrow j}$  the polarization dependent reflection efficiencies of the sample,  $S_{\text{cam},R}$  the camera spectral sensitivity for channel  $R$ ,  $\Delta\lambda$  the wavelength interval, and  $N$  the number of wavelengths. Similar equations were used for the green (G) and blue (B) camera channels.

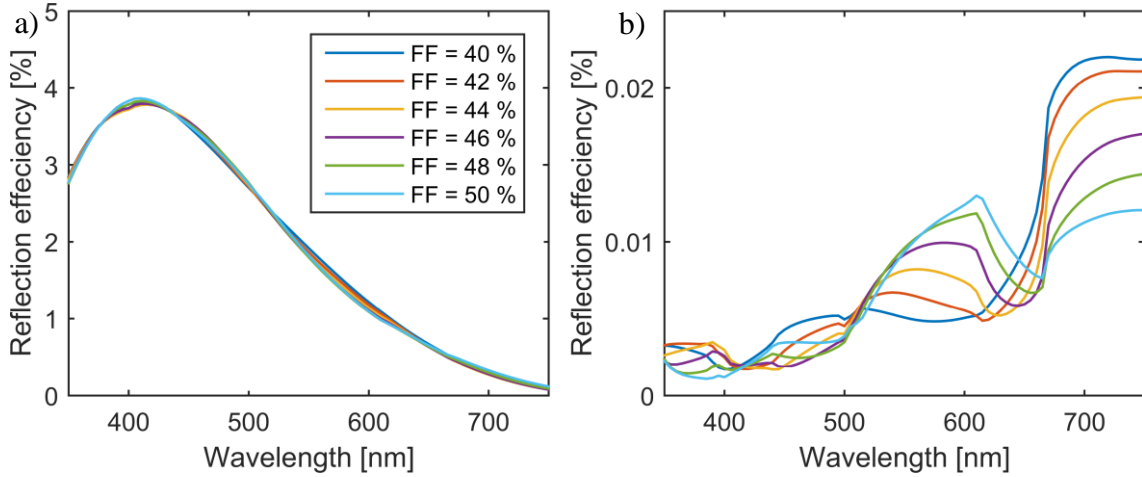


Figure S3: Simulated reflection efficiencies for typical grating. Only the  $r_{s \rightarrow s}$  (a) and  $r_{s \rightarrow p}$  (b) components are shown, since for the incident polarization rotated with  $45^\circ$  with respect to the grating, the  $r_{s \rightarrow s}$  and  $r_{p \rightarrow p}$  are identical, and similarly with the  $r_{p \rightarrow s}$  and  $r_{s \rightarrow p}$ . Legend refers to both graphs a) and b).

A typical RGB database consisted of 20.000 different gratings geometries, and took around 15 hours to simulate on a 20-core computer (IBM NeXtScale nx360 M4, Lenovo Group Inc., China). The dimensional ranges varied slightly for each sample, but were similar to the one shown in Figure 47b in the paper. The ranges were chosen not to restrict the fitted values,

except for the height that was limited to the height of the mold-master, determined to 224 nm with AFM.

A set of typical reflection efficiency spectra is shown in Figure S3, for a grating of  $h=210$  nm,  $p=2000$  nm,  $s=10^\circ$ , and varying filling factors. When comparing the  $r_{s \rightarrow s}$  with the  $r_{s \rightarrow p}$  efficiencies, the values are seen to be around 100 higher for  $r_{s \rightarrow s}$ , meaning that 100 times more light will be reflected with this polarization. However, the six simulated spectra, corresponding to six different filling factors, are seen to be very similar for  $r_{s \rightarrow s}$ , while  $r_{s \rightarrow p}$  feature significantly larger variations. For increased sensitivity with color scatterometry, large spectral variations between different structures are advantageous, as this result in larger color changes and better fitting confidence.

#### S4 Setup calibrations

Typically in scatterometry, the reflection efficiencies of the structures are determined by scaling the sample spectrum with a reference spectrum of the light source, obtained e.g. from the reflection of a mirror.<sup>[140,169,188]</sup> However, this is not possible for color scatterometry, due to the polarizing beamsplitter blocking all light from non-structured samples. Instead, each component had to be calibrated individually, and Equation (S2) applied to relate the sample reflectance to the RGB camera color. The lamp (MWWHL3, Thorlabs Inc., USA) spectrum was evaluated with a calibrated spectrometer, see Figure S4. The reflectance and the transmittance of the beamsplitter (CCM1-PBS251/M, Thorlabs Inc., USA), were determined by comparing the reflection and transmission spectra with a straight through measurement without the beamsplitter, see Figure S5. To evaluate the values independently for  $s$ - and  $p$ -polarization, a polarizer (GT10-A, Thorlabs Inc., USA) was positioned before the spectrometer fiber. The spectral sensitivity of the camera (BFLY-U3-23S6C, Point Grey Research, Inc., USA), was evaluated according to the industry standard EMVA 1288<sup>[208]</sup>, see Figure S6. The camera features a four channel RGGB (red, green, green, blue) color filter array, and each channel were analyzed separately. However, as seen from Figure S6 the two green channels show almost identical responses, hence for the further color analysis the average of both channels was used to only obtain the three RGB values.

As it was only possible to obtain relative calibrations for the components, all measured and simulated colors are scaled with their individual intensities. This results in slightly larger CIs, as the color gradients would be steeper if the intensities were preserved.

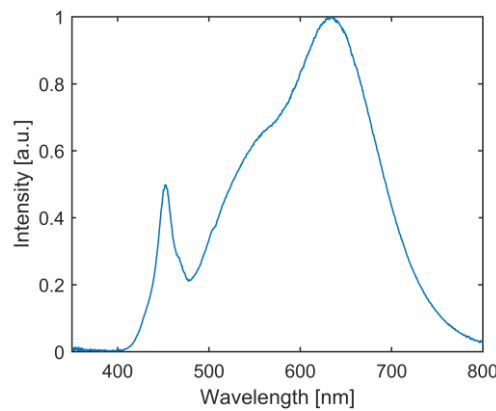


Figure S4: Spectrum of LED light source.

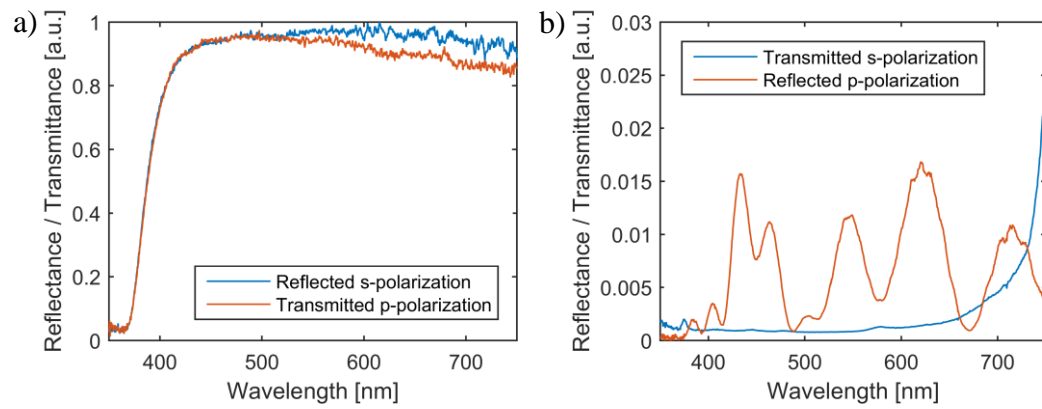


Figure S5: Polarization dependent reflectance and transmittance of beamsplitter.

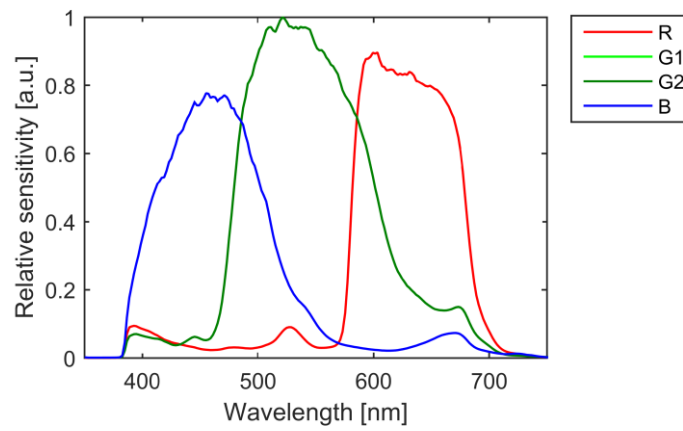


Figure S6: Spectral sensitivity of the four RGGB camera channels. The two green channels show similar responses.

# A4 Instrument calibrations

## A4.1 Spectrometer

The final setup does not include a spectrometer, but this was used for calibration of the other components, and for troubleshooting during the design and test phases.

The spectrometer is a USB2000+VIS-NIR-ES (Ocean Optics Inc., USA), covering a spectral range from 350 nm to 1000 nm with approximately 0.4 nm increments. It features a fiber optic connector fitted with a 600  $\mu\text{m}$  diameter multimode fiber (QP600-2-VIS-BX, Ocean Optics Inc., USA).

### A4.1.1 Spectral sensitivity

Several components in a spectrometer influence the spectral sensitivity, most notably the diffraction grating and the photodetector. The simplest approach is simply to consider the spectrometer a “black box” and determine the combined sensitivity of the entire device. The spectral sensitivity was determined by referencing against a calibrated spectroradiometer (OL 756 Portable UV-VIS Spectroradiometer, Gooch & Housego, FL-USA). The same light source (HPX2000, Ocean Optics Inc., USA) was evaluated with both spectrometers, and from this, the spectral correction factors for the spectrometer determined as the ratio of the two spectrums. The calibration was performed with the optical fiber attached, hence the factors also corrects for spectral variations of the fiber transmission. To avoid thermal drift, the lamp and spectrometer were warmup sufficiently before measuring, see Sections A4.1.4 and A4.3.

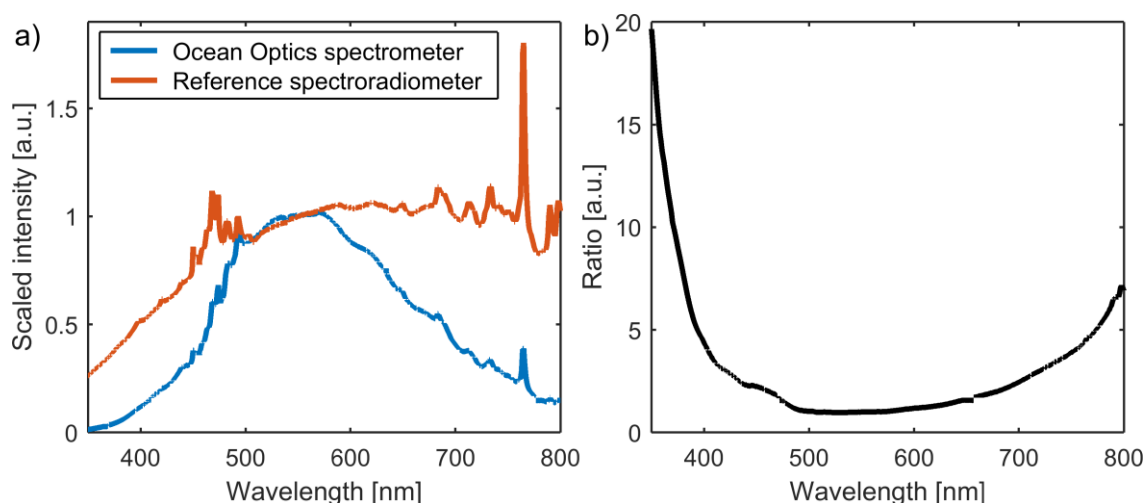


Figure 71: Calibration of spectrometer spectral sensitivity. **a)** Spectrum of light source obtained by spectrometer and reference. **b)** Correction factors for the Ocean Optics spectrometer, determined as the ratio of the spectrums in a).

The calibration results are shown in Figure 71. The importance of such calibration is obvious when comparing the two spectra in Figure 71a. The correction factors in Figure 71b have a smooth shape, even though the two spectra have some distinct peaks as seen from Figure 71a. The steep increase in the correction factors from 400 nm and downwards, is a consequence of the detection limit, which results in the spectrum approaching zero at 350 nm. The combination

of a poor sensitivity and a large correction factor will cause large uncertainties for this range of the spectrum. Fortunately, most of this region is not important since the camera is only sensitive from around 380 nm.

### A4.1.2 Wavelength correlation

Since a spectrometer is simply a grating and a linear photodetector array, a calibration is needed to relate the detector pixel to a physical wavelength. The manufacturer already provides such calibration for the spectrometer, consisting of a third-order polynomial relating the pixel number and wavelength. The calibration is performed on the actual spectrometer, but we performed an analysis to validate the results.

A wavelength calibration is performed by measuring the emission spectrum of a known source, typically a low-pressure gas such as krypton, that provides sharp emission peaks at well-defined wavelengths. By correlating the pixel number and wavelength of each peak, the polynomial coefficients are determined. Ocean Optics provides a detail description of the procedure<sup>[213]</sup>. The spectrum for a krypton-1 calibration source (KR-1, Ocean Optics Inc., USA) was evaluated with the spectrometer using the manufacturer supplied wavelength calibration. A sample of ten peaks was then fitted with Gaussian functions, and the wavelength of the peak apex determined with sub-pixel resolution. The ten peaks were selected based on high intensities, no superpositions with neighboring peaks, and covering wavelengths in the full spectrum. Comparing the obtained wavelengths with the reference values from the National Institute of Standards and Technology (NIST)<sup>[214]</sup> did not reveal a significant difference, hence the manufacturer supplied coefficients were used, see results in Table 6.

Table 6: Peak wavelengths of ten krypton-1 emission peaks, measured with the spectrometer and compared to the reference values from NIST<sup>[214]</sup>.

Reference [nm]	Measured [nm]	Difference [nm]
427.3969	427.3985	-0.0016
431.9579	431.9543	0.0037
450.2354	450.2308	0.0046
587.0916	587.0412	0.0504
785.4823	785.4461	0.0362
805.9505	805.9503	0.0002
819.0057	818.9989	0.0068
850.8873	850.8835	0.0038
892.8693	892.8442	0.0252
975.1761	975.2738	-0.0977

### A4.1.3 Intensity non-linearity

All CCD detectors have a slight non-linear response between light intensity and electric signal, which can be corrected by a post-processing step. Ocean Optics supplies a non-linearity calibration for the spectrometer, in the form of a 7th order polynomial that linearizes the raw intensities. This calibration was validated by the procedure described by Ocean Optics<sup>[215]</sup>.

The procedure is to evaluate the intensity of a stable light source several times using different integration times of the spectrometer, and analyze the results with respect to the counts per

second versus the total count. The total count will increase with increasing integration time, but the counts per second stays constant for a stable light source. The relation can then be fitted with a 7th order polynomial, as shown in Figure 72. When comparing our polynomial with the one provided by Ocean Optics, they are generally very similar and only differ in the boundary regions, close to saturation and the detection limit. Consequently, since the spectra are always acquired with values in the center of the detection range (by adjusting the integration time), the use of either polynomial should not result in significantly different values. This was also observed when analyzing the spectrums. After correction for the non-linearity, the spectrometer response is linear within 0.5 %, compared to around 10 % without the correction.

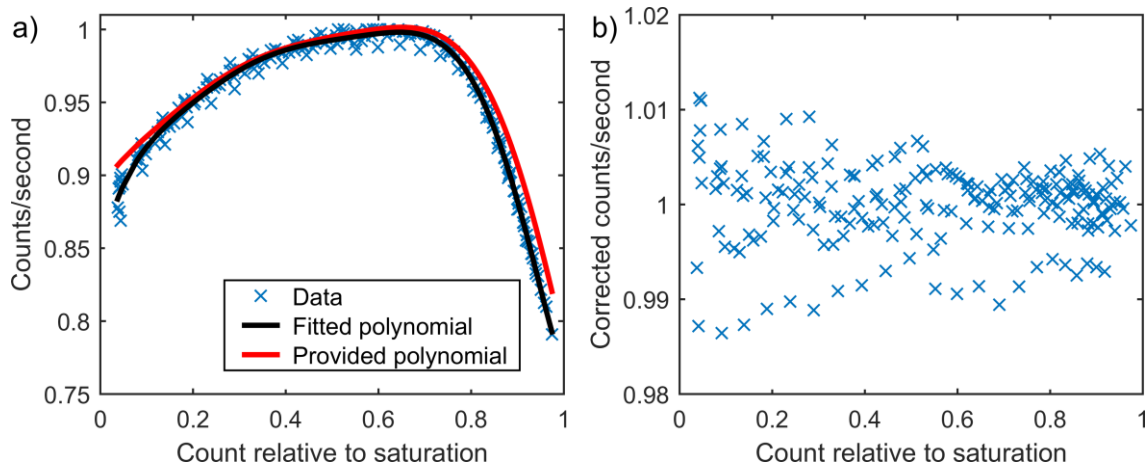


Figure 72: Result of linearity calibration. **a)** Plot of the rate of counts versus total count for various integration times. For a linear response, the rate should stay constant. Also shown is the 7th order polynomial fitted to the data, and for comparison, the polynomial from the provided Ocean Optics calibration. **b)** The data from **a)** after applying the polynomial correction.

#### A4.1.4 Spectrometer warmup time

The spectrometer is neither temperature stabilized nor features a temperature sensor. Hence, to ensure stable and consistent measurements, it needs to warmup and stabilize. To determine how long time is needed, the spectrometer is set to continuously evaluate the spectrum of a light source (MWWHL3, Thorlabs Inc., USA), immediately after being switched on. The light source is assumed to be stable, as it has stabilized for several hours. The intensities of individual pixels are then monitored to determine when they stabilized. The resulting data is shown in Figure 73a, for 10 pixels in the range 430 nm to 720 nm encompassing both high and low intensities. After approximately 40 min the values are stable within ~0.5 %, hence this time is used for the spectrometer warmup period.

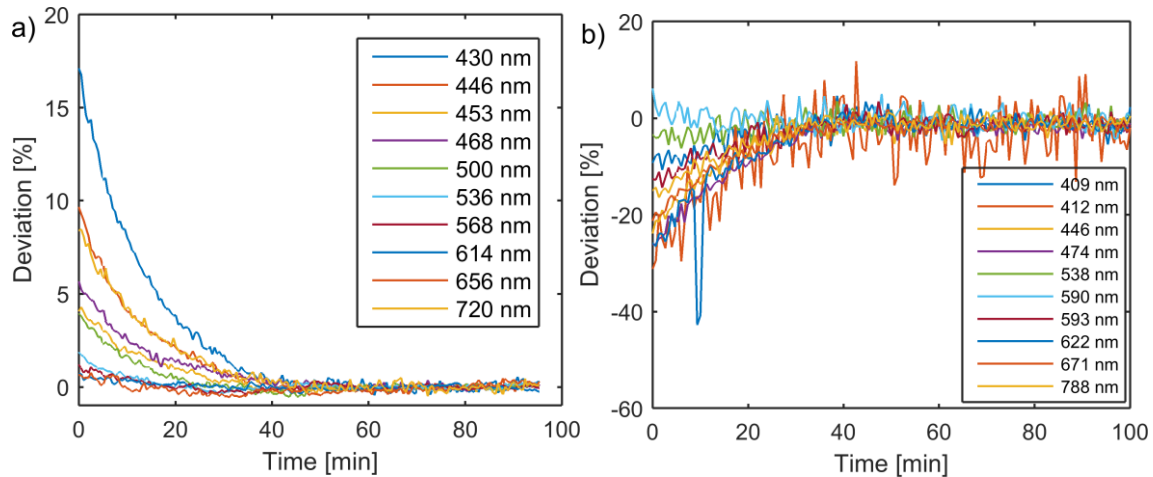


Figure 73: Warmup experiments of spectrometer, showing the drift of ten pixels after the spectrometer is turned on. **a)** When continuously measuring the spectrum of a light source. **b)** When evaluating the dark noise in the spectrometer. The deviations are calculated with respect to the final stable value.

Another method for characterizing the warmup drift is to evaluate the dark noise of the pixels. This is done by continuously acquiring spectrums while the spectrometer entrance is blocked and no light reaches the sensor. When using a long integration time, in this case 10 s, the noise signal can be evaluated. Most pixels are low in noise, fluctuating at around 4 % of the saturation value, but some pixels stand out with much large noise signal. Some of these high-noise pixels are shown in Figure 73b, where the intensity drift immediately after turning on the spectrometer is plotted. The warmup drift is seen to stabilize after around 40 min, identical to the time determined from Figure 73a.

## A4.2 Camera warmup time

The warmup time for the camera is determined similar to the spectrometer. Images are acquired continuously for a stable light source (MWWHL3, Thorlabs Inc., USA), and the intensity changes with respect to time evaluated. Contrary to the spectrometer, the camera features a temperature sensor to monitor the actual temperature inside the camera housing. Figure 74 shows the warmup results as the intensity drift with respect to time in a) and with respect to temperature in b), for each of the four color channels. The drift is seen to be significantly smaller than for the spectrometer, with the maximum change being the R channel with 2.5 %. The difference between the four channels is expected to result from the actual value of the pixels. The color of the light source was (255, 240, 80), hence the R channel also had the highest value. The warmup time is found to be around 30 min, after which the values are stable within 0.1 %. From Figure 74b, the warmup is seen to correlate strongly with the reported camera temperature; hence, the temperature reading can also be used to ensure a sufficient warmup. As with the spectrometer, the warmup time was also evaluated from dark measurements, and this provided similar results.

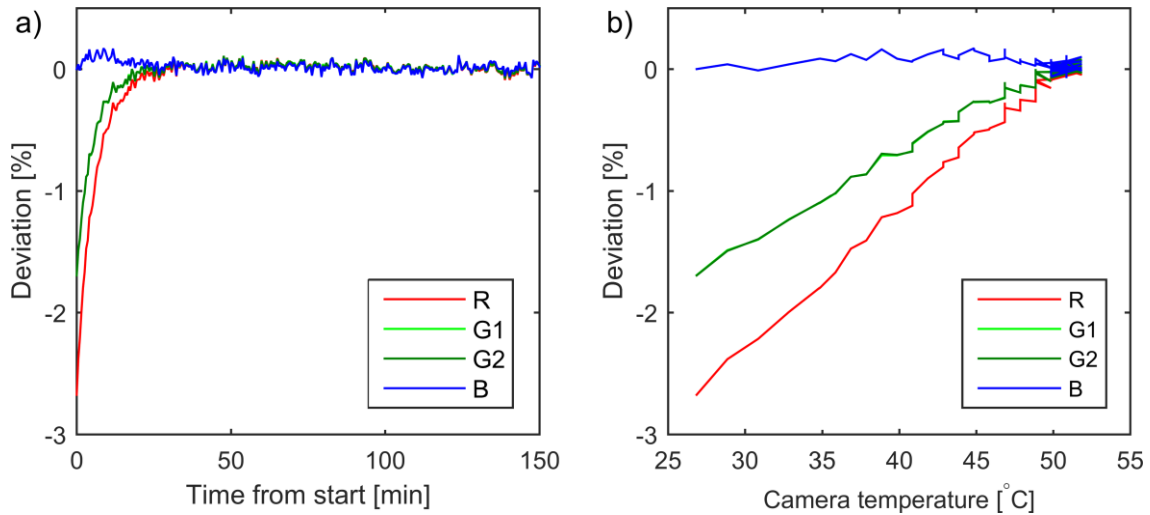


Figure 74: Warmup time of camera. The intensity drift of the pixel values are shown with **a)** respect to the time, and **b)** the on-board camera temperature. The intensities are determined as the mean of 200 x 200 pixels in the center of the image, and the deviations are calculated with respect to the final stable value.

### A4.3 LED warmup time

The lamp warmup time is determined similar to the spectrometer, except now the spectrometer is warmed up initially, and the lamp turned on when the spectrum acquisition commenced. The spectrum is continuously acquired for 2.5 hours with 30 s intervals. The LED is found to be relatively stable with a maximum drift of 5%, and after 40 min all values are stable within 1 %, see Figure 75.

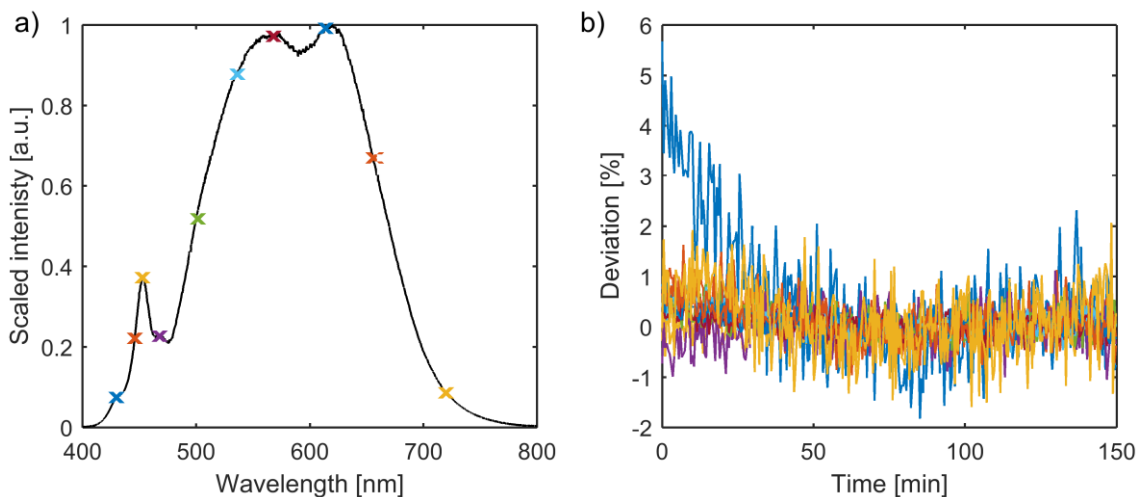


Figure 75: Warmup experiment of LED light source. **a)** The lamp spectrum with crosses indicating the evaluated wavelengths. **b)** The drift of ten wavelengths immediately after the LED is turned on. The line color correlates with the marker color in a). The deviations are calculated with respect to the final stable value.

## A5 Papers not included in thesis

### A5.1 Paper 5

Published as communication in *Advanced Engineering Materials* (Wiley) in September 2015.

The article has yet to be cited (according to Scopus), and the journal webpage does not provide the number of downloads.

Citation:

S. Murthy, M. Matschuk, Q. Huang, N. K. Mandsberg, **N. A. Feidenhans'l**, P. Johansen, L. Christensen, H. Pranov, G. Kofod, H. C. Pedersen, O. Hassager, R. Taboryski, Fabrication of Nanostructures by Roll-to-Roll Extrusion Coating, *Advanced Engineering Materials*, vol. 18, p. 484–489, 2016.

The published version is available online at: <http://dx.doi.org/10.1002/adem.201500347>

DOI: 10.1002/adem.201500347

## Fabrication of Nanostructures by Roll-to-Roll Extrusion Coating\*\*

By Swathi Murthy, Maria Matschuk, Qian Huang, Nikolaj K. Mandsberg, Nikolaj A. Feidenhans'l, Peter Johansen, Lars Christensen, Henrik Pranov, Guggi Kofod, Henrik C. Pedersen, Ole Hassager and Rafael Taboryski\*

The drivers in the development of large area micro- and nanostructuring roll-to-roll (R2R) methods have been hologram security stickers, flexible electronics, graphene electrodes, and organic solar cells.<sup>[1]</sup> In terms of productivity for large-area nanostructuring, the most established technology is roll-to-roll UV-assisted nanoimprint lithography (R2R-UV-NIL), as demonstrated by Ahn et al, who reported replication of 300 nm line gratings using UV-curable imprint resist at a line-speed of  $1 \text{ m min}^{-1}$ .<sup>[2,3]</sup> This method is limited in the choice of materials by the requirement of photo-curability. The throughput for current R2R-UV-NIL systems amounts to  $\approx 0.2 \text{ m}^2 \text{ s}^{-1}$ . Another widely used technology is R2R hot

embossing (R2R-HE), in which a heated structured roller is used to emboss a structure into a thin film in an R2R process.<sup>[4,5]</sup> The full potential of extending R2R techniques to nanostructuring of biomimetic functionalities such as super-hydrophobic,<sup>[6]</sup> anti-reflective,<sup>[7]</sup> structural, and plasmonic color effects,<sup>[8]</sup> is, however, today impeded by the relatively low throughput of R2R-UV-NIL and R2R-HE.<sup>[4,9]</sup> These limitations seem associated with the rheology of polymer flow and the rate of UV-curing processes.<sup>[3]</sup>

This paper investigates a novel R2R process for nano- and microstructuring, potentially having improved productivity with rates exceeding  $5 \text{ m}^2 \text{ s}^{-1}$  (Figure 1). The process is known as roll-to-roll extrusion coating (R2R-EC, in the packaging industry commonly referred to as co-extrusion), which is widely used for production of smooth polymer films. Among benefits of R2R-EC are availability of a wide range of commercial extruders, off-the-shelf extrusion grade polymers, functional additives, polymeric materials with good diffusion barrier properties, and the overall maturity of the technology. However, only few studies have been devoted to this process. Frenkel et al.<sup>[10]</sup> reported replication by R2R-EC of sawtooth microstructures with line-speed of  $10 \text{ m min}^{-1}$ , while Sollogoub et al.<sup>[11]</sup> described the rheological processes associated with standard R2R-EC. To our knowledge, there is no work describing production of nanostructured polymer films by R2R-EC so far.

In R2R-EC, a molten polymer film (melt curtain) is extruded through a flat nozzle, then stretched in air, and finally laminated onto a carrier foil (substrate). The lamination process takes place as the melt curtain is squeezed between a structured cooling roller and a rubber counter roller. A force is exerted on the compliant counter roller to form the so-called nip region where the molten polymer solidifies and adheres to the carrier foil, as shown in Figure 1a. Compared to R2R-UV-NIL and R2R-HE, the extrusion coating process is much faster, mainly due to the fact that the polymer is molten to begin with, and cools rapidly by contact with the cooling roller. When compared to other R2R techniques, R2R-EC resembles R2R-HE, in respect to pressure ranges, but is much less affected by the slow creep-strain effects encountered in R2R-HE.<sup>[4]</sup> R2R-EC can also be compared to the polymer injection molding (IM) process.<sup>[12]</sup> In IM, the polymer is also molten at the onset of relief filling. Important differences between R2R-EC and IM are, however, the pressure and rheological conditions during relief filling. The nip pressure in R2R-EC

[\*] Dr. S. Murthy, Dr. M. Matschuk, Dr. H. Pranov, Dr. G. Kofod  
Inmold A/S, Diplomvej 381, DK-2800 Kongens Lyngby, Denmark  
Dr. S. Murthy, Prof. H. C. Pedersen  
Department of Photonics Engineering, Technical University of Denmark, Frederiksborgvej 399, DK-4000 Roskilde, Denmark  
Dr. Q. Huang, Prof. O. Hassager  
Department of Chemical and Biochemical Engineering, Technical University of Denmark, Søltofts Plads building 229, DK-2800 Kongens Lyngby, Denmark  
Dr. N. A. Feidenhans'l  
Danish Fundamental Metrology A/S, Matematiktorvet 307, Kgs. Lyngby, Denmark  
Prof. R. Taboryski, Dr. N. K. Mandsberg, Dr. N. A. Feidenhans'l  
Department of Micro- and Nanotechnology, Technical University of Denmark, Ørstedes Plads, building 345b DK-2800, Kongens Lyngby, Denmark  
E-mail: rata@nanotech.dtu.dk  
P. Johansen, L. Christensen  
Danapak Flexibles A/S, Strudsbergvej 3, DK-4200 Slagelse, Denmark  
Swathi Murthy and Maria Matschuk contributed equally to this work.

[\*\*] This work is supported by the Danish National Advanced Technology Foundation (HTF) through the "Advanced Technology Project LANI" (grant 011-2011-3), the "Advanced Technology Platform NanoPlast" (grant 007-2010-2), and by The Danish Ministry of Higher Education and Science, through an industrial PhD scholarship for Swathi Murthy (grant 1355-00143). Nis K. Andersen, Freddy Lang, and Nanna Bild are acknowledged for help with the artwork. Supporting Information is available online from Wiley Online Library or from the author.

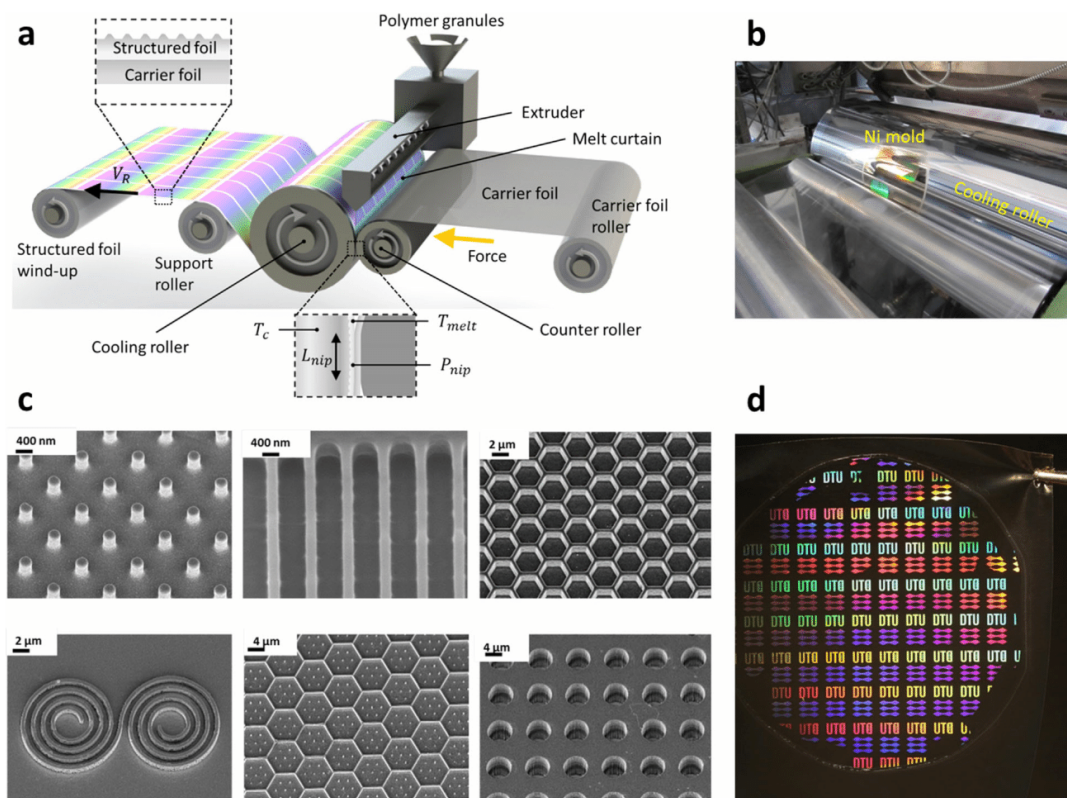


Fig. 1. (a) Schematic of R2R-EC process. (b) Photograph of the cooling roller with the Ni mold mounted. (c) Scanning electron micrographs of structures with various shapes, line-widths ranging from 400 nm to  $\geq 1 \mu\text{m}$ , and aspect ratios  $\geq 1$  replicated in PP by R2R-EC. Images were taken at a  $30^\circ$  tilt angle. (d) Example of an application of the technology; diffraction grading pattern with DTU logo produced by R2R-EC. The pattern was originated from a 100 mm Si wafer, electroformed into a Ni mold, and replicated by R2R-EC on PP foil.

is low ( $\approx 20$  bar), while injection pressures for IM typically reach much higher values ( $\approx 1000$  bar). In addition, for IM, the shear stress typically exceeds the critical value for wall slip,<sup>[13]</sup> whereas this is not the case in R2R-EC, where the shear rate in the nip is practically zero.<sup>[11]</sup> Most extruders have multi-feed nozzles, allowing for, e.g., an adhesion layer to be co-extruded with the structure layer for better adhesion to the carrier foil. If a relief structure is attached to the surface of the cooling roller, the pressure buildup in the nip will force intrusion of the molten polymer into the relief structure, which is the topic of investigation in this paper. R2R-EC is simpler than R2R-UV-NIL, as it does not require any curing step.

We demonstrate large-area replication at high throughput of patterns both on micrometer- (Figure 1b,c) and nanometer scale (Figure 2) in thermoplastic foils using standard industrial R2R-EC equipment and standard thermoplastic polymers. We argue that different regimes of replication exist; a nanostructure regime, where replication is dominated by surface tension of the melt in the nip, and a microstructure regime where microscopic flow is required to fill the deeper microstructures. Nanostructures with typical line-widths in the range of 100–400 nm are best replicated using semi-crystalline polymers such as

polypropylene (PP), running at high roller line-speed  $V_R$ , and high cooling roller temperature  $T_c$  (Figure 2). The best replication of nanopillars (diameter: 120 nm and height: 100 nm in Si master) was obtained for  $T_c = 70^\circ\text{C}$  and the highest line-speed  $V_R = 60 \text{ m min}^{-1}$  (Figure 2a, b), whereas, e.g., at  $T_c = 30^\circ\text{C}$  and  $V_R = 10 \text{ m min}^{-1}$ , the pillars were only 50% replicated in terms of height compared to the Si master (Figure 2c,d, and e). For the used parameter range, this degree of replication at nanoscale was only achieved in PP. Replication in other common polymers like polyethylene (PE) and polystyrene (PS) was not possible for nanostructures.<sup>[14]</sup> Structures with line-widths and depths above ca. 400 nm seem to belong to a different replication regime allowing for a wider range of materials.<sup>[14]</sup> For microstructures (see Figure 1c), we find that process parameters ( $V_R, F, T_c$ ) have to be individually optimized for each pattern, indicating that viscoelastic flow into the relief plays a more important role.<sup>[4]</sup> We believe this difference originates from the thermo-mechanical conditions in the nip, as shown in Figure 3. Both nano- and microstructures require a pressure buildup in the nip for good replication. This is achieved by the compliance of the rubber counter roller. We adapted the theory for contact between two deformable solids to predict the

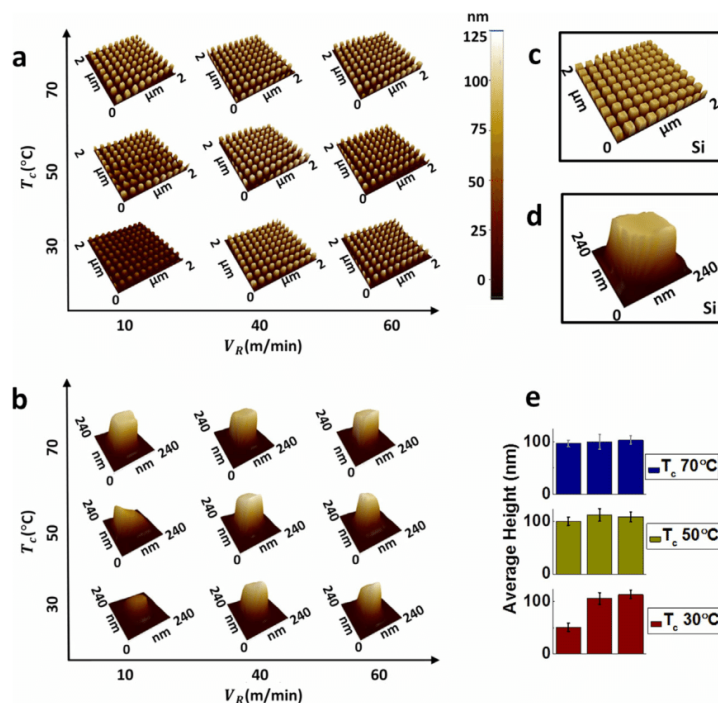


Fig. 2. (a) AFM images of nano-pillar arrays replicated in PP. (b) Single pillar extracted from arrays in (a). (c) and (d) AFM images of the corresponding Si master structures, array (c), and single pillar (d). (e) Average height of the pillars in (a). Error bars represent the standard deviations of heights in the  $2 \times 2 \mu\text{m}^2$  scan-areas.

pressure profile in the nip.<sup>[11,15]</sup> A force  $F$  is applied to the counter roller resulting in a pressure within the nip,

$$P_{\text{nip}} = P_{\text{max}} \sqrt{1 - \left( \frac{L_{\text{nip}} - 2x}{L_{\text{nip}}} \right)^2}, \quad (1)$$

where  $P_{\text{max}} = F/(\pi W L_{\text{nip}})$ ,  $x$  is the distance along the nip from the entrance,  $L_{\text{nip}}$  is the length of the nip region (see Figure 1a), and  $W$  is the width of the rollers. The calculated pressure curves in the nip for three different force values are shown in Figure 3b. According to Equation 1, the maximum pressure is reached at the center of the nip. The carrier foil and the polymer passage in the nip do not significantly affect the pressure in the nip.

We modeled the temperature profile along the nip in a  $100 \mu\text{m}$  thick polymer melt sandwiched between the Ni mold and the polyethylene terephthalate (PET) carrier foil.<sup>[14]</sup> The model simulates the temperature variation at different distances from the mold surface in the polymer along the nip. Our primary interest for this investigation is the cooling rate in the polymer melt near the mold–polymer interface. The model shows that the polymer melt cools very rapidly near the mold surface. In fact, it cools even before entering the nip. The cooling rate is of the order of  $10^7 \text{ K s}^{-1}$  at a distance  $100 \text{ nm}$  from the mold once it enters the nip, while it cools much slower in the bulk of the polymer melt away from the mold surface (Figure 3c). The high rate is due to the high thermal conductivity of Ni as compared to polymer. The line-speed is

an important factor affecting the temperature profile in the nip (Figure 3). At higher line-speed, the polymer solidifies further into the nip and the polymer melt experiences higher nip pressure before solidification of the surface region (Figure 3).

The low pressure and the absence of shear stress in the nip indicate that no-slip boundary conditions are expected to hold for nanopattern filling in the mold.<sup>[13,16]</sup> For a pressure  $\Delta P$  across the melt/air interface, the radius of curvature  $R$  is given by the Young–Laplace formula:

$$R = \frac{-2\gamma(T)\cos\theta_a}{\Delta P}, \quad (2)$$

where  $\gamma(T)$  is the temperature-dependent surface tension, while  $\theta_a$  is the advancing contact angle for the polymer melt intruding into the mold relief. As the antistiction coating<sup>[14,17]</sup> of the roller ensures  $\theta_a \sim 120^\circ$ , and hence  $\cos\theta_a \sim -1/2$ , we argue that feature sizes smaller than  $R \sim \gamma(T)/\Delta P$  cannot be replicated. The surface tension for polymer melts is known to decrease linearly with temperature:<sup>[16,18]</sup>

$$\gamma(T) = \gamma_0 - \alpha T. \quad (3)$$

For PP, we used  $\gamma_0 = 27.734 \text{ mN m}^{-1}$  and  $\alpha = 0.059 \text{ mN (m}^\circ\text{C)}^{-1}$  reported by Yang et al.<sup>[16]</sup> The crystallization temperature obtained by differential scanning calorimetry (DSC) in this work is  $\approx 120^\circ\text{C}$  at a cooling rate of  $10 \text{ K min}^{-1}$ .

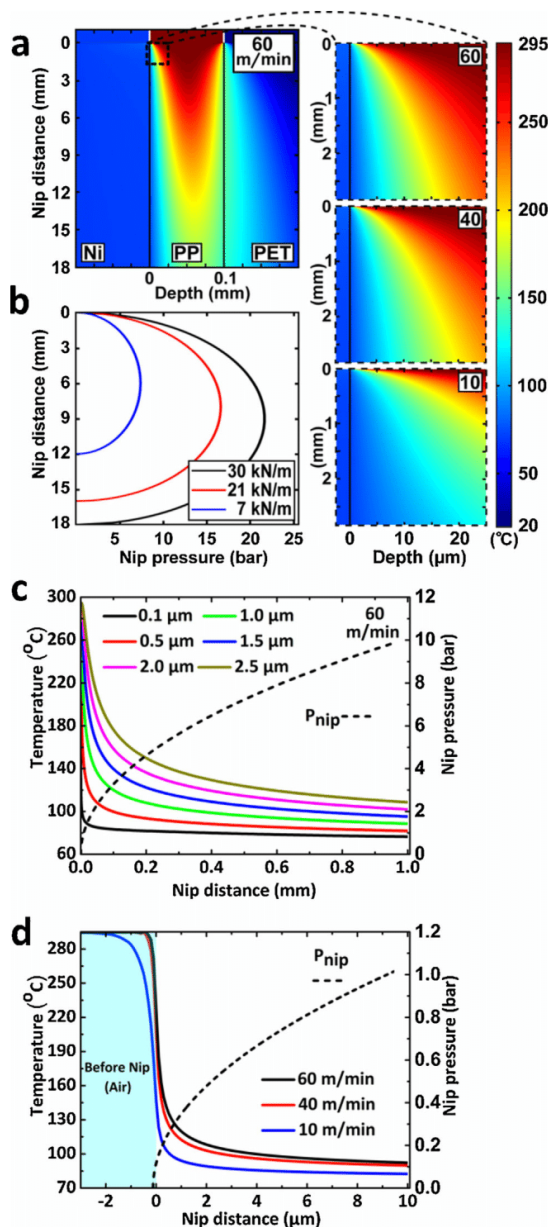


Fig. 3. (a) COMSOL simulation of temperature profile in the nip for  $F/W = 30 \text{ kN m}^{-1}$ ,  $T_c = 70^\circ\text{C}$ , and  $V_R = 60 \text{ m min}^{-1}$ . Right panel shows temperature profiles at nip entry for  $V_R = 60 \text{ m min}^{-1}$ ,  $40 \text{ m min}^{-1}$ , and  $10 \text{ m min}^{-1}$ , respectively. (b) Pressure profile in the nip for different values of  $F/W$  calculated using Equation 1. (c) Temperature profile extracted at different distances from the mold surface from simulation in (a). (d) Temperature profile extracted from simulation in (a) for different  $V_R$  at 100 nm from the mold surface.

However, PP is a semi-crystalline polymer, and we expect considerable crystallization retardation for the extremely high cooling rate ( $\approx 10^7 \text{ K s}^{-1}$ ) near the mold.<sup>[19]</sup> The polymer melt is thus expected to be supercooled and solidify at much lower temperature  $T \gtrsim T_c = 70^\circ\text{C}$ . If we conservatively assume

solidification at the temperature  $120^\circ\text{C}$ , we can follow the  $60 \text{ m min}^{-1}$  curve (100 nm from the mold surface) in Figure 3d to arrive at a distance of  $\approx 1 \mu\text{m}$  inside the nip for  $T = 120^\circ\text{C}$ . At this distance, the nip pressure is  $\approx 0.3 \text{ bar}$ . The characteristic radius of curvature  $R$  for the PP melt under  $0.3 \text{ bar}$  and  $120^\circ\text{C}$  is  $\approx 650 \text{ nm}$  calculated from Equation 2 and 3. In order to completely fill the nanoholes in the mold, including the corners,  $R$  should be smaller than the radius of the nanoholes, i.e.,  $R \lesssim 60 \text{ nm}$  for  $120 \text{ nm}$  pillars (Figure 2). Since smaller pillars were actually replicated at these conditions, this clearly indicates that supercooling of the polymer melt must play an important role in the process. To confirm this hypothesis, we tried to replicate nanopatterns using other polymers, polystyrene (PS), and polyethylene (PE). For PS, the glass transition temperature ( $T_g$ ) is  $\approx 100^\circ\text{C}$ , while the solidification temperature for PE is  $\approx 110^\circ\text{C}$ . PS is an amorphous polymer; it solidifies below  $T_g$  and cannot be supercooled. Indeed, for the parameter range used in this investigation, it was not possible to achieve a visible replication of structures in PS. Though PE is a semi-crystalline polymer and can be supercooled, its crystallization rate is extremely high (compared to PP), which means that PE solidifies quickly below its static solidification temperature ( $110^\circ\text{C}$ ).<sup>[20]</sup> Hence,  $R$  does not become small enough to fill the nanoholes in the mold for PS and PE. From Figure 2, we see that the cooling rate of the PP melt near the mold is  $\approx 10^7 \text{ K s}^{-1}$  at  $V_R = 60 \text{ m min}^{-1}$ . We cannot measure the crystallization rate of PP at such high cooling rate as the maximum cooling rate that presently can be attained by flash DSC is  $\approx 10^4 \text{ K s}^{-1}$ .<sup>[21]</sup> However, the half crystallization time for PP at  $80^\circ\text{C}$  is reported to vary from 0.2 to 10 s.<sup>[21,22]</sup> The polymer takes about 9 ms to reach the center of the nip (9 mm at  $60 \text{ m min}^{-1}$ ), where the pressure is maximum and hence  $R$  is minimum. Since we observe complete replication of nanopillars at  $60 \text{ m min}^{-1}$ , it indicates retardation of solidification of PP by a sufficient amount of time to attain a small enough  $R$ . This explains why the replication of nanopillars (Figure 2) diminishes at lower  $V_R$  and lower  $T_c$ . We observed incomplete replication of  $40 \text{ nm}$  structures and take this as the lower limit for replication in the model.

In conclusion, we have demonstrated replication of micro- and nanostructures in thermoplastic polymers, by a very high throughput, industrial process R2R-EC. Structures of different dimensions, shapes, and aspect ratios have been replicated with high replication fidelity, and productivity up to  $0.45 \text{ m}^2 \text{ s}^{-1}$ . Nanostructures down to  $80 \text{ nm}$  and height  $100 \text{ nm}$  could be replicated in PP at  $V_R = 60 \text{ m min}^{-1}$ . The limiting factors for proper replication of nanostructures were found to be the surface tension induced radius of curvature of the polymer melt and the retardation time for crystallization of the melt. The retardation time limitation leads to the surprising feature of the process, that the replication quality of nanostructures in crystalline polymers becomes better when the higher line-speed is used.

We suggest that the discovery of accurate and high productivity nano- and microscopic replication in thermoplastic

materials could accelerate the integration of nanostructured materials in a broad range of applications, including optical, technical, and functional surfaces and devices. Further possible applications may include cast molding of advanced materials for photo-voltaic, thermo-electric, electro-active, and electro-storage applications, where nanostructuring often leads to improved properties.

### 1. Experimental Section

The nano-microstructured foils were produced by extrusion coating on a pilot roll-to-roll extrusion coating machine, at Danapak Flexibles, Slagelse, Denmark. It consists of a 25 mm extruder (BfA Plastic GmbH), 35 mm extruder (AXON Plastics Machinery AB), and an EPOCH nozzle with a respective three-layer feedblock (Cloeren, Inc.). Micro-nanostructured Ni molds were fabricated by a dry etching, electroplating, and molding (DEEMO) process.<sup>[14,23]</sup> The Ni molds were simply glued to the cooling roller (width  $W = 45$  cm, diameter  $D_{\text{cool}} = 27.2$  cm) with double-sided adhesive tape. The cooling roller is cooled by water, and its temperature  $T_c$  was kept below the solidification temperature of the polymer. The counter roller (diameter  $D_{\text{counter}} = 12.5$  cm) consisted of a metal core wrapped with a  $\approx 10$  mm thick layer of silicone rubber, making it flexible on the surface. The counter roller was maintained at room temperature using cooling water. The nip length  $L_{\text{nip}}$  was measured by running a deformable tape through the nip at different applied force  $F$  and measuring the length of the deformation in the tape. The force across the nip is exerted by two hydraulic pistons attached to the counter roller.  $F$  is calculated by multiplying the measured oil pressure  $P_{\text{oil}}$  in the pistons with the surface area of the pistons. The rollers are not motorized; their drive is supplied by the substrate drawn by the winder, creating a line tension, and resulting in a line-speed  $V_R$ . PP was co-extruded with a polyethylene (PE) adhesion layer material at 295 °C and laminated onto a polyethylene terephthalate (PET) carrier foil.

The solidification temperature was measured by differential scanning calorimetry (DSC) (DSC-Q1000, TA Instruments) (Figure S7).<sup>[14]</sup>

We investigated the nano-microreplication ability of various polymers, like pure PP (WF420HMS, Borealis), low-density polyethylene (LDPE-3020D, LyondellBasell), polyethylene-modified polypropylene (hereafter, referred to as polyolefin, PO), polymethylpentene, polystyrene (PS: BASF PS 158 K), and cyclic olefin copolymer (Topas 8007  $\times$  4, Topas Advanced Polymers GmbH).<sup>[14]</sup> Different sets of processing parameters were investigated to assess their influence on the replication fidelity.<sup>[14]</sup> Specifically, the influence of cooling roller temperature  $T_c$  (30 °–70 °C), line-speed  $V_R$  (10–60 m min<sup>−1</sup>), and nip force  $F$  (7–30 kN m<sup>−1</sup>) were explored separately, while keeping all other parameters constant.<sup>[14]</sup> For the parametric analysis, extruder output, melt temperature, feed rate, die-gap, and air-gap height were kept constant. For each set of process parameters, several hundred meters of

polymer foil were produced. The replication was assessed and compared for samples across different parameter sets. Several samples were cut from the same foils to assess the homogeneity of replication. The structures shown in this paper were characterized either by scanning electron microscopy (SEM - Zeiss Supra) or by atomic force microscopy (AFM - Park Systems Corporation XE-150). Prior to SEM, the polymer foils were coated with a  $\approx 10$  nm thin film of gold-palladium.

Article first published online: September 19, 2015

Manuscript Revised: September 1, 2015

Manuscript Received: July 9, 2015

- [1] a) K. J. Baeg, M. Caironi, Y. Y. Noh, *Adv. Mater.* **2013**, *25*, 4210; b) S. Bae, H. Kim, Y. Lee, X. F. Xu, J. S. Park, Y. Zheng, J. Balakrishnan, T. Lei, H. R. Kim, Y. I. Song, Y. J. Kim, K. S. Kim, B. Ozyilmaz, J. H. Ahn, B. H. Hong, S. Iijima, *Nat. Nanotechnol.* **2010**, *5*, 574; c) F. C. Krebs, J. Fyenbo, M. Jørgensen, *J. Mater. Chem.* **2010**, *20*, 8994; d) S. R. Forrest, *Nature* **2004**, 428, 911.
- [2] a) S. H. Ahn, L. J. Guo, *Adv. Mater.* **2008**, *20*, 2044; b) S. Ahn, M. Ganapathisubramanian, M. Miller, J. Yang, J. Choi, F. Xu, D. J. Resnick, S. V. Sreenivasan, "Roll-to-Roll Nanopatterning Using Jet and Flash Imprint Lithography", presented at *Conf. Altern. Lithographic Technol. IV*, San Jose, CA **2012**; c) C. Stuart, Y. Chen, *ACS Nano* **2009**, *3*, 2062; d) J. John, Y. Tang, J. P. Rothstein, J. J. Watkins, K. R. Carter, *Nanotechnology* **2013**, 24.
- [3] S. H. Ahn, L. J. Guo, *ACS Nano* **2009**, *3*, 2304.
- [4] Y. Deng, P. Yi, L. Peng, X. Lai, Z. Lin, *J. Micromech. Microeng.* **2015**, *25*, 065004.
- [5] M. D. Fagan, B. H. Kim, D. Yao, *Adv. Polym. Technol.* **2009**, *28*, 246.
- [6] a) K. Koch, B. Bhushan, Y. C. Jung, W. Barthlott, *Soft Matter* **2009**, *5*, 1386; b) E. Søgaard, N. K. Andersen, K. Smistrup, S. T. Larsen, L. Sun, R. Taboryski, *Langmuir* **2014**, *30*, 12960.
- [7] A. B. Christiansen, J. Clausen, N. A. Mortensen, A. Kristensen, *Appl. Phys. Lett.* **2012**, *101*, 131902.
- [8] a) J. Clausen, A. B. Christiansen, J. Garnaes, N. A. Mortensen, A. Kristensen, *Opt. Express* **2012**, *20*, 4376; b) K. Kumar, H. G. Duan, R. S. Hegde, S. C. W. Koh, J. N. Wei, J. K. W. Yang, *Nat. Nanotechnol.* **2012**, *7*, 557; c) J. S. Clausen, E. Højlund-Nielsen, A. B. Christiansen, S. Yazdi, M. Grajower, H. Taha, U. Levy, A. Kristensen, N. A. Mortensen, *Nano Lett.* **2014**, *14*, 4499.
- [9] H. Tan, A. Gilbertson, S. Y. Chou, *J. Vac. Sci. Technol. B* **1998**, *16*, 3926.
- [10] R. Frenkel, B. Kim, D. Yao, *Machines* **2014**, *2*, 299.
- [11] C. Sollogoub, E. Felder, Y. Dernay, J. F. Agassant, P. Deparis, N. Mikler, *Polym. Eng. Sci.* **2008**, *48*, 1634.
- [12] S. Tanzi, P. F. Østergaard, M. Matteucci, T. L. Christiansen, J. Cech, R. Marie, R. Taboryski, *J. Micromech. Microeng.* **2012**, *22*, 115008.

- [13] D. G. Yao, B. Kim, *J. Micromech. Microeng.* **2002**, 12, 604.
- [14] See Supporting Information.
- [15] H. Hertz, *J. Reine und Angewandte Mathematik* **1882** 92, 156.
- [16] D. Yang, Z. Xu, C. Liu, L. Wang, *Colloids Surf. a-Physicochem. Eng. Asp.* **2010**, 367, 174.
- [17] M. Matschuk, N. B. Larsen, *J. Micromech. Microeng.* **2013**, 23.
- [18] D. Y. Kwok, L. K. Cheung, C. B. Park, A. W. Neumann, *Polym. Eng. Sci.* **1998**, 38, 757.
- [19] A. Gradys, P. Sajkiewicz, A. A. Minakov, S. Adamovsky, C. Schick, T. Hashimoto, K. Saijo, *Mater. Sci. Eng. a-Struct. Mater. Prop. Microstruct. Process.* **2005**, 413, 442.
- [20] a) J. T. Xu, P. J. Ding, Z. S. Fu, Z. Q. Fan, *Polym. Int.* **2004**, 53, 1314; b) A. J. Peacock, *J. Macromol. Sci. – Polym. Rev.* **2001**, C41, 285.
- [21] J. E. K. Schawe, *J. Therm. Anal. Calorim.* **2014**, 116, 1165.
- [22] C. Vasile, *Handbook of Polyolefins*, Marcel Dekker, Inc., New York **2002**.
- [23] a) J. Elders, H. V. Jansen, M. Elwenspoek, W. Ehrfeld, *Micro Electro Mechanical Systems – IEEE Proceedings, DEEMO: A New Technology for the Fabrication of Microstructures*, **1995**, p. 238; b) S. Tanzi, P. F. Østergaard, M. Matteucci, T. L. Christiansen, J. Cech, R. Marie, R. Taboryski, *J. Micromech. Microeng.* **2012**, 22, 115008; c) M. Matschuk, H. Bruus, N. B. Larsen, *Microelectron. Eng.* **2010**, 87, 1379.

## A5.2 Paper 6

Submitted as Article to *Scientific Reports* (Nature) on the 17<sup>th</sup> of August 2016.

The paper is currently under review, and first revision has been resubmitted.

Citation:

L. Schneider, N. A. Feidenhans'l, A. Telecka, R. Taboryski, One-step Maskless Fabrication and Optical Characterization of Silicon Surfaces with Antireflective Properties and a White Color Appearance, *Scientific Reports*, 2016.

### Title

One-step Maskless Fabrication and Optical Characterization of Silicon Surfaces with Antireflective Properties and a White Color Appearance

### Abstract

We report a simple one-step maskless fabrication of inverted pyramids on silicon wafers by reactive ion etching. The fabricated surface structures exhibit excellent anti-reflective properties: The total reflectance of the nano inverted pyramids fabricated by our method can be as low as 12% without any anti-reflective layers, and down to only 0.33% with a silicon nitride coating. The results from angle resolved scattering measurements indicate that the existence of triple reflections is responsible for the reduced reflectance. The surfaces with the nano inverted pyramids also exhibit a distinct milky white color.

### Introduction

Silicon is abundant in nature, and has been widely used in the semiconductor industry. By texturing silicon surfaces, it is possible to obtain samples of dual- or multi-functions that are attractive in many fields. Recently, there has been increasing interest in using “black silicon” fabricated by reactive ion etching (RIE) to enhance the light trapping efficiency of photovoltaic devices.<sup>1-6</sup> The RIE fabricated silicon typically consists of needle-like or cone-shape structures that scatter the incident light, which is the reason for the black or brownish color of the surface.<sup>3,7-11</sup> Though highly anti-reflective, the black silicon suffers from high surface recombination losses caused by its extremely high surface area, which as a result limits the increase of the external quantum efficiency of photovoltaic devices.<sup>12-13</sup> Recently, Savin et al. reported that it is possible to chemically and electrically passivate the black silicon to reduce the charge recombination by depositing an alumina layer.<sup>14</sup> Alternatively, it has been reported that inverted pyramids have lower surface areas than upright pyramids, yet still good light trapping properties.<sup>12-13,15-20</sup> These inverted pyramids are typically fabricated either by colloidal lithography,<sup>21-22</sup> or by combining interference lithography and wet silicon etching.<sup>13,16-17,19</sup> Both methods are complex and require masks or templates for the fabrication, which increases the fabrication costs. Wang et al. recently reported on using a maskless copper assisted acid etching method to fabricate micro inverted pyramids on a silicon surface.<sup>20</sup> Nonetheless, as copper is a deep donor for silicon, the use of copper could potentially cause contamination to the fabricated samples and other processes performed in the same cleanroom.

In this letter we report a simple one step maskless method to fabricate semi-periodic nano inverted pyramids on silicon wafer surfaces by RIE. RIE is a dry etching technique that can be used to structure silicon surfaces through the combined effect of a corrosive gas ( $\text{SF}_6$  or  $\text{CH}_4$ )

and a passivating gas ( $O_2$ ) without additional masks.<sup>7-8</sup> We will show that by fine tuning the etching parameters, we are able to fabricate nano inverted pyramids of different sizes and regularities. The total reflectance of the inverted pyramids fabricated by our method can be as low as 12% without any anti-reflective layers, and down to only 0.33% with silicon nitride ( $SiN_x$ ) coatings. The surfaces with the uncoated nano inverted pyramids also exhibit a very interesting milky white color, which to the best of our knowledge has not been reported yet. As reactive ion etching (RIE) is widely used in the semi-conducting industry, our technique will have high potential not only in the photovoltaic but also other industries, where surfaces of special optical properties are desired. Moreover, this technique will lead towards cost-effective large-scale productions of inverted pyramidal structures.

The structure fabricated by RIE is determined by complex reactions happening inside the RIE chamber, which according to many studies depend mainly on the gas ratio, chamber temperature, chamber pressure, and the platen power.<sup>2-3,5,10-11,23-26</sup> The absolute gas flow on the other hand does not seem to have much influence on the formed structures. However, in most of the aforementioned studies, the change of the gas flow rate is only within 10%, which perhaps is too small to influence the structure formation. To better understand the parameter influence and better control the etched structures, in this study we fixed the chamber temperature ( $-19^\circ C$ ), chamber pressure (38 mTorr), and the platen power (6 W), and varied the flow rates  $Q$  (in sccm) of  $SF_6$  and  $O_2$  and the etching time  $t$  (in min). The total gas flow rate can be 12 times higher for the batches with the highest rate than for those with the lowest rate. For simplification, we denote our samples of different etching parameters as  $Q_{SF_6} - Q_{O_2} - t$ .

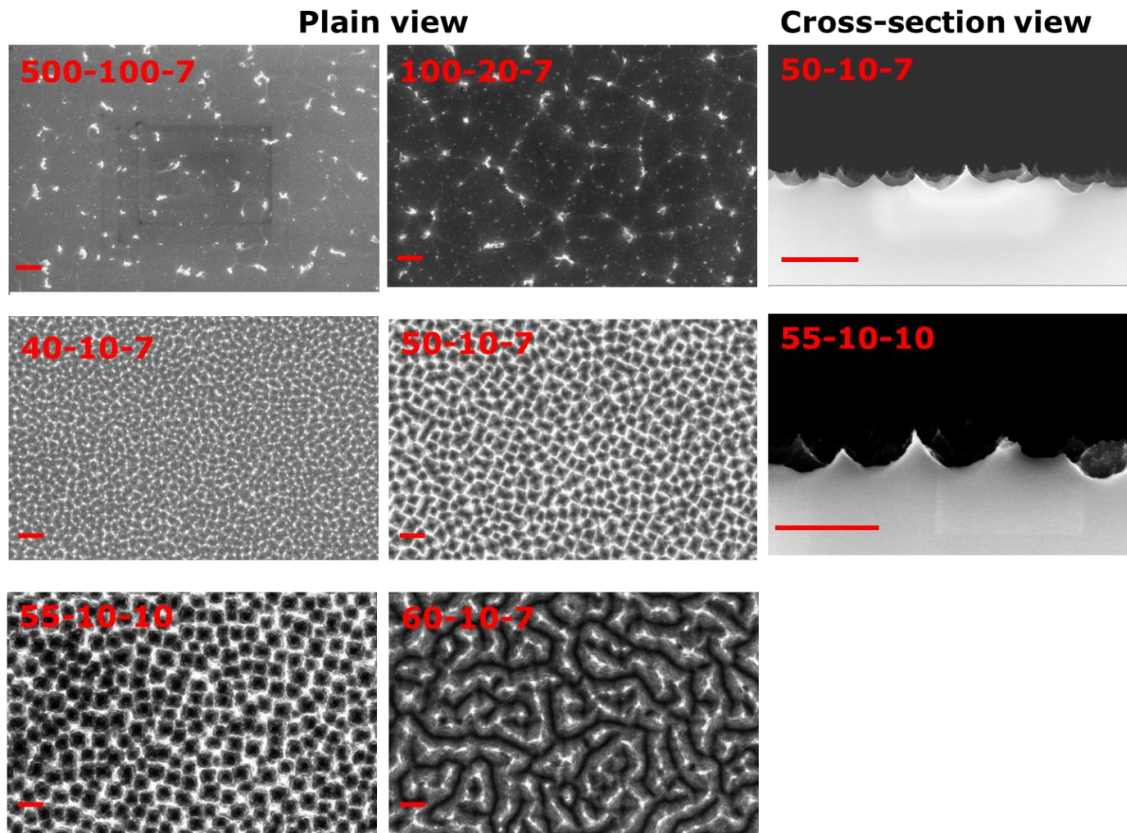


**Figure 1.** SEM images of structures fabricated at different gas flow rates and etching times. The scale bars are 1  $\mu m$ .

By changing the  $\text{SF}_6$  and  $\text{O}_2$  flow rates and the etching time, we are able to obtain waferscale samples of very different surface structures with good reproducibility (samples 55-10-10, 50-10-15, and 50-10-20 were reproduced five times), as presented in **Figure 1**. The fabricated structures range from flat surfaces with random particles (500-100-7 and 100-20-7), winding micro-trenches (60-10-7), non-periodic holes (40-10-7), to semi-periodic inverted pyramids (50-10-7 and 55-10-10). It is worth mentioning that the gas ratio  $Q_{\text{SF}_6}:Q_{\text{O}_2}$  and the etching time  $t$  of samples 500-100-7 and 50-10-7 are the same, while the resulting structures of the two samples are very different: the surface of sample 500-100-7 is almost flat with only some random particles of irregular shape; while the surface of sample 50-10-7 already has inverted pyramidal holes. Apparently, in our study the influence of the total flow rate on the structure formation can be substantial. The dominant effect seems to be the residence time of the gas molecules in the active etching zone, where the plasma is generated. The average residence time  $\tau$  of a gas inside the RIE chamber can be defined as:  $\tau = pV/Q$ ,<sup>26</sup> where  $p$  is the pressure inside the chamber,  $V$  the plasma volume, and  $Q$  the gas flow rate. As we used fixed chamber pressures in all experiments, the throttle valve opened more for higher gas flow rates to maintain the chamber pressure than the lower ones. For a comparison, the average gas residence time of sample 500-100-7 is only 0.02 s (**Figure S2**), while  $\tau$  of sample 50-10-7 is 0.21 s. Hence, for the high gas flow rates, gases pass the active etching zone so fast that there is not enough time for them to dissociate and react with the sample surface in the chamber, leading to an almost flat surface (sample 500-100-7). The Similar observations were also reported by Jansen *et al.*<sup>26</sup>

**Figure 2b** and **2c** are representative spectra of the specular and total reflectance of all fabricated types. Three samples with inverted pyramidal structures (50-10-15, 50-10-20, and 55-10-10) are among those of the lowest specular and total reflectance (**Figure 2a** and **2b**). The total reflectance of sample 55-10-10 (without anti-reflective coating) is lower than 20% at shorter wavelength, and as low as 12% at near IR, which is lower than many reported values of uncoated nano/micro inverted pyramids made by more complex methods.<sup>17,22,27</sup> The inverted pyramids of this sample (55-10-10) are almost arranged in a hexagonal array, and yet with a predominantly quadratic base having side lengths of around 600 nm and a pitch distance of around 700 nm, much smaller than those reported by Wang *et al.*<sup>20</sup> The total reflection of these three samples is further reduced down to only 0.33% after coating with the anti-reflective layer (~80 nm, **Figure 2c**), which is also used as a passivation layer to reduce the surface recombination rate and to increase the effective carrier lifetime in photovoltaic devices.<sup>13,28-30</sup>

**Figure 2d** shows the angle resolved scattering (ARS) spectra of sample 55-10-10 without and with  $\text{SiN}_x$  coating. The solid-dash lines are the respective cosine fittings of the scattered intensity at angle  $\theta_s$ ,  $\text{ARS} = A \cdot \cos(\theta_s)$ . Here  $A$  is a prefactor, and  $\theta_s$  is the angle between the detector and the plane normal to the sample surface (sample normal). The ARS curve of the uncoated 55-10-10 fits well at large angles but deviates from the cosine function at small angles. There are two peaks at  $\theta_s \approx -46^\circ$  and  $\theta_s \approx -21^\circ$ , which could result from double and triple reflections of incoming beam rays by the facets of the inverted pyramids, as illustrated in **Figure 2e**. The average plane inclination of the inverted pyramids is  $\alpha \approx 56.5^\circ$ , as measured by Image J on SEM images. This angle is close to the well-known angle of  $54.7^\circ$  usually obtained for anisotropic wet etching of  $\langle 100 \rangle$  Si surfaces with potassium hydroxide (KOH). By simple trigonometry, the angle of the second reflection to the sample normal can be derived  $\beta \approx 46^\circ$ , and the angle of the third reflection to the sample normal  $\gamma \approx 21^\circ$ . The values of these two angles fit well with the positions of the two peaks observed in **Figure 2d**. The intensity difference between the two peaks can have two origins: 1. The reflection fraction of flat silicon surfaces varies at different angles of incidence according to the Fresnel equation; 2. For an

inverted pyramid of  $D \approx 609$  nm and  $\alpha \approx 56.5^\circ$  as presented in **Figure 2e**, only 15% of the incoming beam (per facet) falls in an area, where a third reflection could happen; the rest would be either reflected out of the inverted pyramid or absorbed by the pyramid (refracted). Similar hypothesis of triple reflections of inverted pyramids was also suggested by other groups.<sup>17,20</sup> Due to the restriction of our experimental setup, light scattered to angles lower than  $17^\circ$  to the sample normal could not be measured, which makes it difficult numerically to fit the two peaks or calculate their integral precisely. However, the  $\text{ARS} \sim \theta_s$  curves of the coated surfaces fit the cosine function very well (**Figure 2d** and **S4**). It is worth mentioning that structures fabricated by RIE are not defect free, which might introduce additional recombination sites when compared to defect free structures.<sup>31</sup> Nonetheless, the decrease in the surface area, and the possibility to passivate the surface by introducing alumina or  $\text{SiN}_x$  still makes the inverted pyramids fabricated by our method promising for photovoltaic applications.

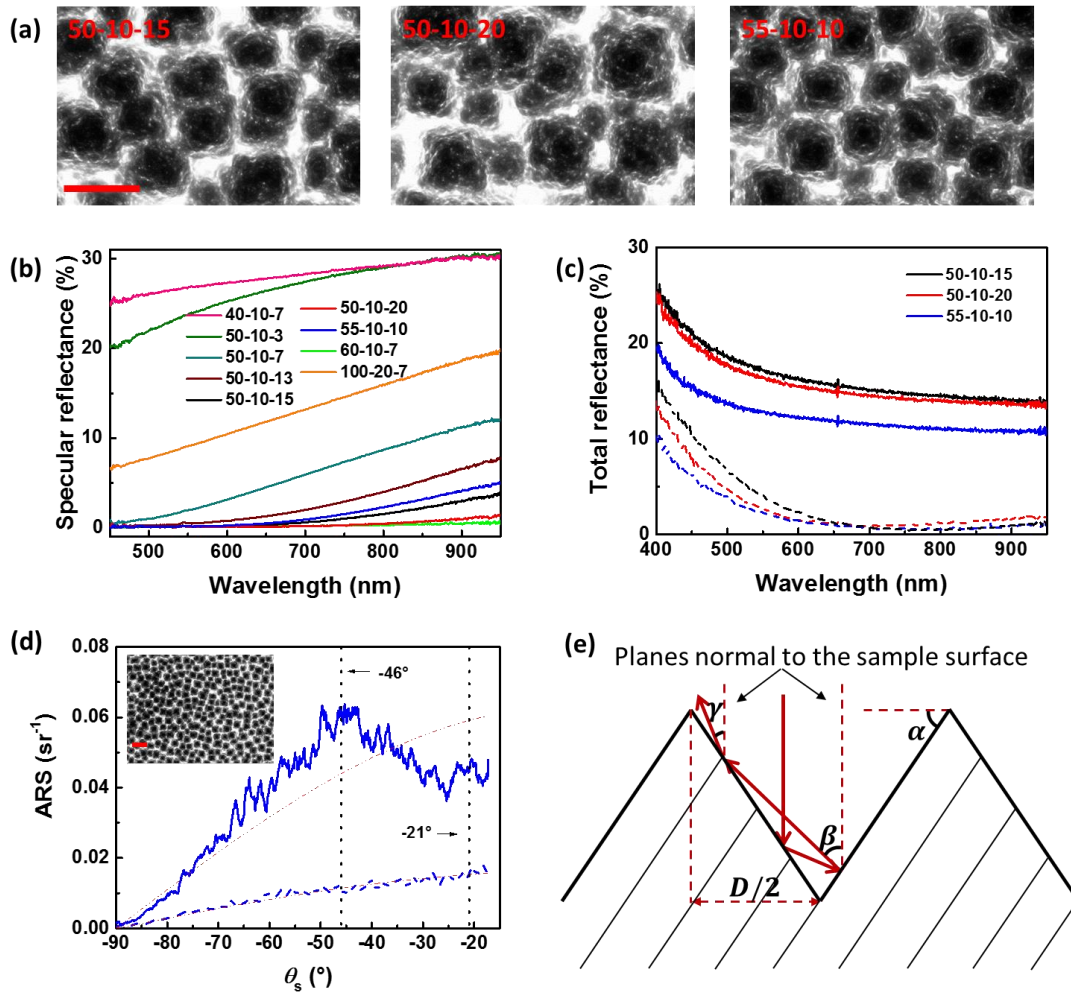


**Figure 2.** (a) SEM images of uncoated inverted pyramids. (b) Specular reflectance of uncoated samples measured at normal incidence. (c) Total reflectance of inverted pyramids without (solid line) and with (dash line)  $\sim 80$  nm  $\text{SiN}_x$  coating measured with an integrating sphere. (d) Angle resolved scattering (ARS) spectra of sample 55-10-10 without (blue solid line) and with (blue dash line)  $\text{SiN}_x$  coating measured by a diode laser of 488 nm. The red dash-dot lines are cosine fittings of the corresponding ARS curves. Inset: SEM image of uncoated 55-10-10. (e) Sketch of possible reflections of the incident light beam by one inverted pyramid. The scale bars are 1  $\mu\text{m}$ .

In addition to being anti-reflective, some of our inverted pyramids appear “white” or greyish, which is distinctly different from the classical black or brownish silicon wafers made by RIE.<sup>3,7,25-26</sup> A clear demonstration of the special color of these nano inverted pyramids is presented by a photo of a white “DTU logo” (approx. 3 mm x 4 mm) on a black background (**Figure 3a**). The white DTU logo was fabricated using the same parameters as sample 55-10-10 on a black silicon wafer of nano spikes. The detailed fabrication procedure and parameters can be found in the experimental section and the supporting information. The SEM image in the white area clearly shows the inverted pyramids are fabricated, though a bit larger (pitch distance up to  $1\mu\text{m}$ ) than the structures fabricated on the polished silicon wafer (**Figure 1, 3c** and **S5**), which might be caused by the incomplete removal of nanograss on the black silicon surface. The color of the logo clearly appears white to human eyes, as compared to the white A4 paper under the sample. The intensity profiles (extracted by Image J) of the RGB colors (**Figure 3d**) along the red line on **Figure 3b** (and **Figure 3e**) overlap well with each other, which further verifies the white color of the DTU logo.<sup>32</sup> There are some oscillations (period  $\sim 14\mu\text{m}$ ) on the color intensity profile, which might stem from defects of similar period in the area (**Figure S5**). These defects might be caused by the inhomogeneous removal of the pre-etched nano spikes in the logo area by RIE, as no such structural irregularities are observed on samples fabricated directly from polished Si wafers (**Figure 1**).

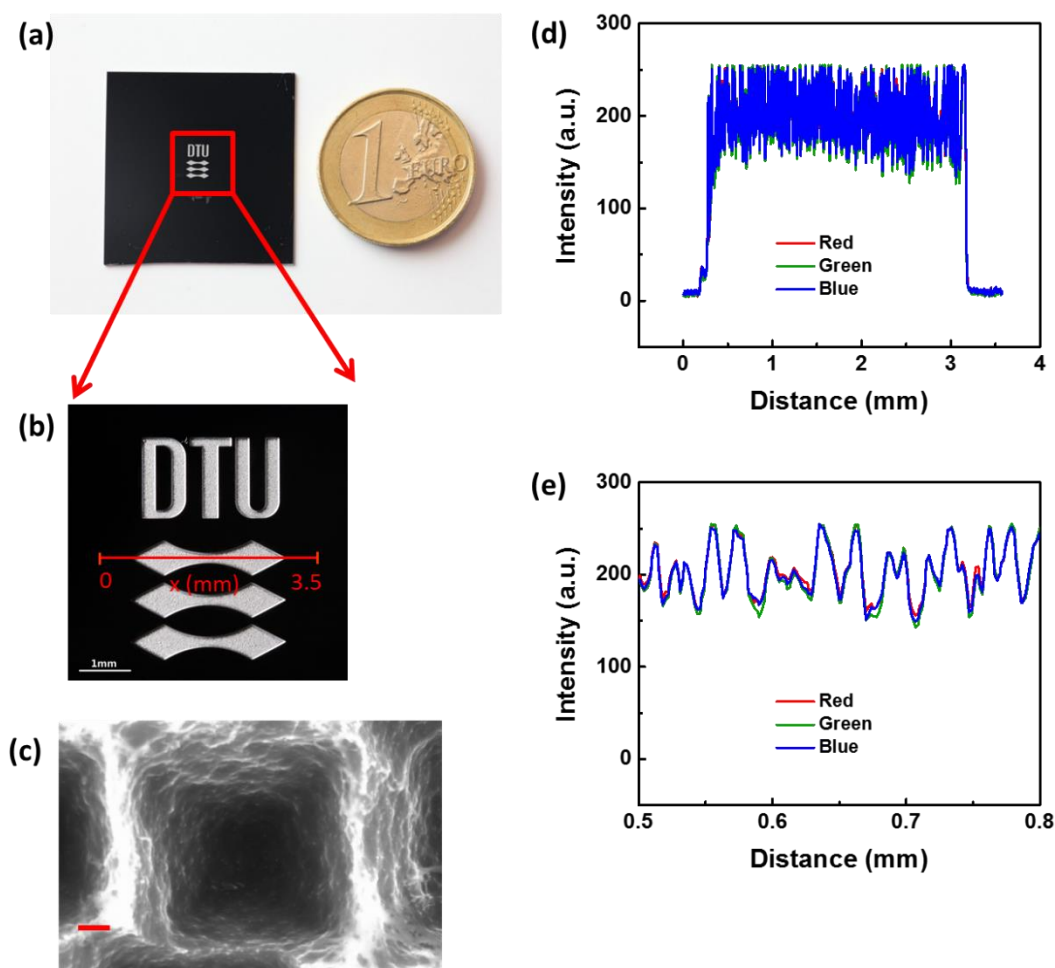


**Figure 3.** (a) Photo of a black silicon wafer with the as fabricated white DTU logo, in reference to a one EUR coin. Both the wafer and the coin were placed on a white A4 paper for color ref-

erence. (b) The zoomed photo of the logo area. (c) SEM image of one single inverted pyramid in the DTU logo area. The scale bar is 200 nm. (d) The intensity profile of RGB colors (red, green, and blue) along the red line indicated on **Figure 3b**. (e) The zoomed intensity profile of RGB colors at  $x = 0.5 - 0.8$  mm.

In summary, we have demonstrated a maskless one-step method to fabricate nano inverted pyramids on silicon wafers by RIE. These structures are very sensitive to the parameters used in RIE, and the total gas flow rate can be substantial to the structure formation. The uncoated inverted pyramids have the lowest specular and total reflectance among all fabricated samples. The low total reflectance of these inverted pyramids is probably caused by a third reflection of the incoming beam by the pyramid facet. The total reflectance of the inverted pyramids is further reduced by an order of 40 after coated with a layer of  $\text{SiN}_x$ , which makes the inverted pyramid fabricated by RIE very promising for photovoltaic applications. As demonstrated by the white DTU logo, some of the inverted pyramids have a milky white color, which could be interesting in other industries. As RIE is an industrialized standardized silicon dry etching technique, our method will pave the way to large scale, cost-effective mass production of nano inverted pyramids.

## Experimental Section

### Silicon surface texturing

All samples were textured by reactive ion etching (RIE, Pegasus D-RIE, STS, UK) on crystal-line 100 mm silicon wafers (n-doped (phosphorous), resistivity 10-100  $\Omega\text{cm}$ , (100)), at different  $\text{SF}_6$  and  $\text{O}_2$  flow rates, platen power, temperature, and etching time. The white DTU logo with black background was fabricated by RIE on a pre-etched black silicon substrate coated with patterned photoresist of the DTU logo. The detailed fabrication parameters and process flow can be found in the supporting information. After RIE, all samples were cleaned by  $\text{N}_2/\text{O}_2$  plasma ( $\text{N}_2$  400 sccm,  $\text{O}_2$  70 sccm, power 1000 W) for 30 min. For the coated samples, a layer of approx. 80 nm silicon nitride ( $\text{SiN}_x$ ) was immediately deposited on the structured surface by plasma enhanced chemical vapor deposition (PECVD, SPTS, UK) after the plasma cleaning. The film thickness of  $\text{SiN}_x$  was tested by ellipsometry (Ellipsometer VASE, J.A. Woollam Co., Inc, USA) on a parallel plain wafer coated with the same parameters.

### Structure characterization

All samples were characterized by scanning electron microscopy (SEM, Supra 40 VP, Carl Zeiss AG, Germany) at both cross-sectional and surface views. The dimension of the structures was measured by ImageJ (version 1.49s).

### Optical characterization

The specular reflection was measured by multiple angle reflectometry (Film Tek 4000, scientific computing international, Carlsbad, USA) at normal and  $70^\circ$  incidence. The total reflectance was measured by optical spectrometer (OE65000, Ocean Optics spectrometer, USA) with an integrating sphere of  $8^\circ$  incidence (AvaSphere-50, Avantes, UK). The total reflectance measurement was calibrated by a white Lambertian scatter (SRS-99-020, LabSphere, USA). The scattering distribution of the samples was measured with an angular scatterometer, where a photodetector (New Focus Model 2032, Newport, USA) was rotated in a circular arc around the sample and the scattering intensity was evaluated in steps of  $0.1^\circ$ . A 40 mW argon-ion laser of 488 nm (60X, American Laser Corporation, USA) was used as the incident light source. The detailed description of the setup can be found in a previous publication.<sup>33</sup> Canon EOS 5D Mark

II camera was used to shoot the photos of the white DTU logo on the black silicon wafer. Except for the auto white balance function, no further post processing was used on the photos. The RGB profile of the photo was extracted by Image J.

The silicon surface texturing, SEM characterizations, and the specular reflection measurements were carried out in a class 10-100 cleanroom (Danchip, DTU, Denmark).

## Funding Sources

This work was supported by EU's 7 Frame Work Program, through the FoF.NMP.2012-7 project "Plast4Future", with grant agreement number 314345.

## Acknowledgements

The authors thank Mr. Suhith Hemanth for providing the photomask; Dr. Carsten Dam-Hansen for sharing the equipment; Mr. Nikolaj Kofoed Mandsberg for providing Matlab scripts; and Dr. Holger Schneider for inspiring discussion and valuable suggestions.

## References

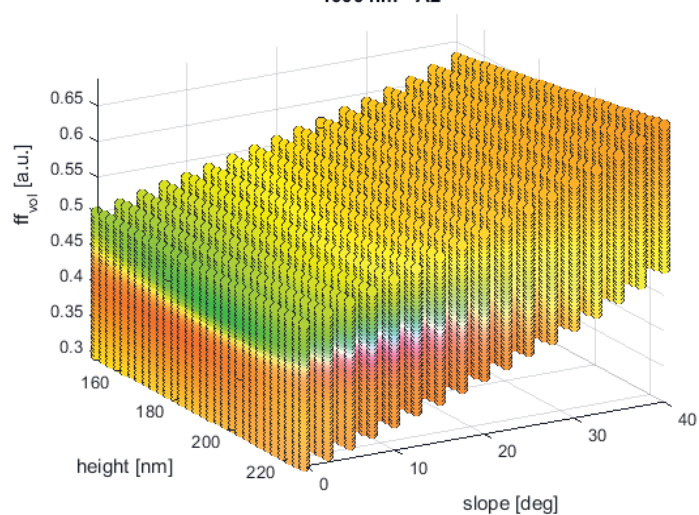
- (1) Koenderink, A. F.; Alù, A.; Polman, A., Nanophotonics: Shrinking light-based technology. *Science* **2015**, *348* (6234), 516-521.
- (2) Nguyen, K. N.; Abi-Saab, D.; Basset, P.; Richalot, E.; Malak, M.; Pavy, N.; Flourens, F.; Marty, F.; Angelescu, D.; Leprince-Wang, Y.; Bourouina, T., Study of black silicon obtained by cryogenic plasma etching: approach to achieve the hot spot of a thermoelectric energy harvester. *Microsyst. Technol.* **2012**, *18* (11), 1807-1814.
- (3) Nguyen, K. N.; Basset, P.; Marty, F.; Leprince-Wang, Y.; Bourouina, T., On the optical and morphological properties of microstructured Black Silicon obtained by cryogenic-enhanced plasma reactive ion etching. *J. Appl. Phys.* **2013**, *113* (19), 194903.
- (4) Campbell, P.; Green, M. A., High performance light trapping textures for monocrystalline silicon solar cells. *Sol. Energ. Mat. Sol. Cells* **2001**, *65* (1-4), 369-375.
- (5) Liu, X.; Coxon, P. R.; Peters, M.; Hoex, B.; Cole, J. M.; Fray, D. J., Black silicon: fabrication methods, properties and solar energy applications. *Energy Environ. Sci.* **2014**, *7* (10), 3223-3263.
- (6) Ingenito, A.; Isabella, O.; Zeman, M., Nano-cones on micro-pyramids: modulated surface textures for maximal spectral response and high-efficiency solar cells. *Prog. Photovolt.: Res. Appl.* **2015**, *23* (11), 1649-1659.
- (7) Jansen, H.; de Boer, M.; Burger, J.; Legtenberg, R.; Elwenspoek, M., The black silicon method II: The effect of mask material and loading on the reactive ion etching of deep silicon trenches. *Microelectron. Eng.* **1995**, *27* (1-4), 475-480.
- (8) d'Agostino, R.; Flamm, D. L., Plasma etching of Si and SiO<sub>2</sub> in SF<sub>6</sub>-O<sub>2</sub> mixtures. *J. Appl. Phys.* **1981**, *52* (1), 162-167.
- (9) Cho, S. J.; An, T.; Kim, J. Y.; Sung, J.; Lim, G., Superhydrophobic nanostructured silicon surfaces with controllable broadband reflectance. *Chem. Commun.* **2011**, *47* (21), 6108-6110.

- (10) Christiansen, A. B.; Caringal, G. P.; Clausen, J. S.; Grajower, M.; Taha, H.; Levy, U.; Asger Mortensen, N.; Kristensen, A., Black metal thin films by deposition on dielectric antireflective moth-eye nanostructures. *Sci. Rep.* **2015**, *5*, 10563.
- (11) Yue, Z.; Shen, H.; Jiang, Y., Antireflective nanostructures fabricated by reactive ion etching method on pyramid-structured silicon surface. *Appl. Surf. Sci.* **2013**, *271* (0), 402-406.
- (12) Branham, M. S.; Hsu, W.-C.; Yerci, S.; Loomis, J.; Boriskina, S. V.; Hoard, B. R.; Han, S. E.; Chen, G., 15.7% Efficient 10- $\mu$ m-Thick Crystalline Silicon Solar Cells Using Periodic Nanostructures. *Adv. Mater.* **2015**, *27* (13), 2182-2188.
- (13) Mavrokefalos, A.; Han, S. E.; Yerci, S.; Branham, M. S.; Chen, G., Efficient Light Trapping in Inverted Nanopyramid Thin Crystalline Silicon Membranes for Solar Cell Applications. *Nano Lett.* **2012**, *12* (6), 2792-2796.
- (14) Savin, H.; Repo, P.; von Gastrow, G.; Ortega, P.; Calle, E.; Garín, M.; Alcubilla, R., Black silicon solar cells with interdigitated back-contacts achieve 22.1% efficiency. *Nat Nano* **2015**, *10*, 624-628.
- (15) Han, S. E.; Chen, G., Optical Absorption Enhancement in Silicon Nanohole Arrays for Solar Photovoltaics. *Nano Lett.* **2010**, *10* (3), 1012-1015.
- (16) Sivasubramaniam, S.; Alkaisi, M. M., Inverted nanopyramid texturing for silicon solar cells using interference lithography. *Microelectron. Eng.* **2014**, *119*, 146-150.
- (17) Chen, H.-Y.; Lu, H.-L.; Ren, Q.-H.; Zhang, Y.; Yang, X.-F.; Ding, S.-J.; Zhang, D. W., Enhanced photovoltaic performance of inverted pyramid-based nanostructured black-silicon solar cells passivated by an atomic-layer-deposited Al<sub>2</sub>O<sub>3</sub> layer. *Nanoscale* **2015**, *7* (37), 15142-15148.
- (18) Kumar, K.; Khalatpour, A.; Nogami, J.; Kherani, N. P. In *Optimizing inverted pyramidal grating texture for maximum photoabsorption in thick to thin crystalline silicon photovoltaics*, Photovoltaic Specialist Conference (PVSC), 2014 IEEE 40th, 8-13 June 2014; **2014**; pp 0605-0607.
- (19) Schuster, C. S.; Bozzola, A.; Andreani, L. C.; Krauss, T. F., How to assess light trapping structures versus a Lambertian Scatterer for solar cells? *Opt. Express* **2014**, *22* (S2), A542-A551.
- (20) Wang, Y.; Yang, L.; Liu, Y.; Mei, Z.; Chen, W.; Li, J.; Liang, H.; Kuznetsov, A.; Xiaolong, D., Maskless inverted pyramid texturization of silicon. *Sci. Rep.* **2015**, *5*, 10843.
- (21) Trompoukis, C.; Massiot, I.; Depauw, V.; El Daif, O.; Lee, K.; Dmitriev, A.; Gordon, I.; Mertens, R.; Poortmans, J., Disordered nanostructures by hole-mask colloidal lithography for advanced light trapping in silicon solar cells. *Opt. Express* **2016**, *24* (2), A191-A201.
- (22) Gao, P.; He, J.; Zhou, S.; Yang, X.; Li, S.; Sheng, J.; Wang, D.; Yu, T.; Ye, J.; Cui, Y., Large-Area Nanosphere Self-Assembly by a Micro-Propulsive Injection Method for High Throughput Periodic Surface Nanotexturing. *Nano Lett.* **2015**, *15* (7), 4591-4598.
- (23) Schneider, L.; Laustsen, M.; Mandsberg, N.; Taboryski, R., The Influence of Structure Heights and Opening Angles of Micro- and Nanocones on the Macroscopic Surface Wetting Properties. *Sci. Rep.* **2016**, *6*, 21400.

- (24) Sainiemi, L.; Jokinen, V.; Shah, A.; Shpak, M.; Aura, S.; Suvanto, P.; Franssila, S., Non-Reflecting Silicon and Polymer Surfaces by Plasma Etching and Replication. *Adv. Mater.* **2011**, *23* (1), 122-126.
- (25) Abi Saab, D.; Basset, P.; Pierotti, M. J.; Trawick, M. L.; Angelescu, D. E., Static and Dynamic Aspects of Black Silicon Formation. *Phys. Rev. Lett.* **2014**, *113* (26), 265502.
- (26) Jansen, H. V.; Boer, M. J. d.; Unnikrishnan, S.; Louwerse, M. C.; Elwenspoek, M. C., Black silicon method X: a review on high speed and selective plasma etching of silicon with profile control: an in-depth comparison between Bosch and cryostat DRIE processes as a roadmap to next generation equipment. *J. Micromech. Microeng.* **2009**, *19* (3), 033001.
- (27) Lin, Q.; Leung, S.-F.; Lu, L.; Chen, X.; Chen, Z.; Tang, H.; Su, W.; Li, D.; Fan, Z., Inverted Nanocone-Based Thin Film Photovoltaics with Omnidirectionally Enhanced Performance. *ACS Nano* **2014**, *8* (6), 6484-6490.
- (28) Zhao, J.; Wang, A.; Altermatt, P. P.; Wenham, S. R.; Green, M. A., 24% efficient per silicon solar cell: Recent improvements in high efficiency silicon cell research. *Sol. Energ. Mat. Sol. Cells* **1996**, *41-42*, 87-99.
- (29) Narasimhan, V. K.; Hymel, T. M.; Lai, R. A.; Cui, Y., Hybrid Metal-Semiconductor Nanostructure for Ultrahigh Optical Absorption and Low Electrical Resistance at Optoelectronic Interfaces. *ACS Nano* **2015**, *9* (11), 10590-10597.
- (30) Hoex, B.; van Erven, A. J. M.; Bosch, R. C. M.; Stals, W. T. M.; Bijker, M. D.; van den Oever, P. J.; Kessels, W. M. M.; van de Sanden, M. C. M., Industrial high-rate (~5 nm/s) deposited silicon nitride yielding high-quality bulk and surface passivation under optimum anti-reflection coating conditions. *Prog. Photovolt.: Res. Appl.* **2005**, *13* (8), 705-712.
- (31) Nakakubo, Y.; Eriguchi, K.; Ono, K., Characterization of Plasma Process-Induced Latent Defects in Surface and Interface Layer of Si Substrate. *ECS J Solid State SC* **2015**, *4*, N5077-N5083.
- (32) Klein, G. A., *Industrial Color Physics*. 1 ed.; Springer-Verlag New York: New York, **2010**; Vol. 154, p XIV, 509.
- (33) Feidenhans'l, N. A.; Hansen, P.-E.; Pilný, L.; Madsen, M. H.; Bisscco, G.; Petersen, J. C.; Taboryski, T., Comparison of optical methods for surface roughness characterization. *Meas. Sci. Technol.* **2015**, *26* (8), 085208.

- - - End of paper reprint - - -

1000 nm - A2



Copyright: Nikolaj Agentoft Feidenhans'l  
All rights reserved

Published by:  
DTU Nanotech  
Department of Micro- and Nanotechnology  
Technical University of Denmark  
Ørstedes Plads, building 345C  
DK-2800 Kgs. Lyngby